CONJUGATED POLYMERS IN MESOPOROUS HOSTS

by

ANDRAS GEZA PATTANTYUS-ABRAHAM

B. Sc., Queen's University, 1996
B. Sc., Queen's University, 1997

A THESIS SUBMITTED IN PARTIAL FULFILLMENT OF
THE REQUIREMENTS FOR THE DEGREE OF

DOCTOR OF PHILOSOPHY

in

THE FACULTY OF GRADUATE STUDIES

(Department of Chemistry)

We accept this thesis as conforming
to the required standard

THE UNIVERSITY OF BRITISH COLUMBIA

September 2003

Abstract

The subject of this thesis is the synthesis and characterization of composite materials based on electroluminescent conjugated polymers in mesoporous hosts. These materials were studied with the goal of producing a structure in which the electrical properties on encapsulated conjugated polymer chains could be measured. Towards this goal, both the creation of thin film hosts with oriented and ordered mesopores and new methods for the incorporation of polymers into mesoporous hosts are described, along with characterization techniques for showing the polymer distribution on the nanometre scale.

The preparation of the conjugated polymer poly(1,4-phenylene vinylene) (PPV) inside the 3.1 nm channels of a hexagonally ordered mesoporous silica material, MCM-41, is described. The MCM-41 surface was first derivatized with an organic base. Subsequent introduction of monomer dissolved in ethanol resulted in base-initiated polymerization in the pores of MCM-41. A pore size reduction of 0.3 nm was seen in the composite material by nitrogen physisorption. Electron-energy loss spectroscopy (EELS) showed that the composite had a distinct loss signal related to the π-electron system on the polymer. Energy-filtered transmission electron microscopy (EFTEM) with 200 keV electrons showed that the polymer was evenly distributed throughout the composite material through mapping of the π-electron losses near 6 eV. A polymer mass content of ~8 % indicated the presence of approx. 6 polymer chains in each pore. The photophysical properties of PPV inside the composite were found to be similar to bulk PPV.

For the preparation of mesoporous thin films with channels oriented normally to the surface, three literature approaches were investigated: the self-assembly of mesoporous silica films with the SBA-2 structure, the thermal oxidation of FeO/SiO_2 films, and the anodic oxidation of aluminum substrates. The latter approach, carried out at low temperature, is shown to yield alumina films with the desired pore structure. Films with a pore size of 4 ± 1 nm are created with an applied potential of 15 V in 1.2 M sulfuric acid (in 1:1 water:methanol) at -39 °C.

EELS and EFTEM were applied to the analysis of composite materials created by the adsorption of a thin layer of poly[2-methoxy-5-(2′-ethylhexyloxy)-1,4-phenylene vinylene] (MEH-PPV) on the surface of porous alumina membrane with 60 nm pore diameter. The measurements were carried out with a 200 keV electron beam travelling parallel to the pores of the host membrane. The π-electron losses of the polymer could not be discerned in this

geometry. Strong surface losses were present at 8, 13 and 18 eV. A long-range loss mode not associated with bulk or surface losses appeared at 7.0 eV, up to 30 nm from the pore surface. Both these loss modes interfered with the detection of the π-electron losses and the polymer distribution could not be confirmed.

The origin of the long-range loss mode was identified as the Cherenkov effect. EELS with 120 keV electrons shifted the peak energy of this loss mode to 8.3 eV, which indicated a dependence on the electron speed. Samples with different pore diameters but a fixed interpore spacing also showed shifts in the peak position. Theoretical modelling of the loss spectrum of a cylindrical pore suggested that these observations arise from the interaction of the generated Cherenkov radiation with the nearby pores in the membrane. This introduces the possibility of studying photonic nanostructures by EELS.

Different methods for introducing the conjugated polymer into an oriented porous host are explored. The idea of creating surface-grafted conjugated polymers on silicon substrates through step polymerization is investigated; as proof of concept, a surface-grafted dimer is synthesized through the Wadsworth-Horner-Emmons reaction. It is further shown that simple centrifugation of a polymer solution, while allowing solvent evaporation, provides a sufficient driving force for polymer insertion into the host. This composite is investigated by electron microscopy. EELS and EFTEM analysis were also applied to ultramicrotomed thin sections of this material, with the electron beam perpendicular to the pore axis. The results showed that relativistic effects may also be important in this geometry, effectively masking the distribution of the π-electron losses associated with the polymer.

Possible routes to the preparation of a light-emitting device (LED) based on porous alumina films are described. The use of the underlying aluminum substrate as electron-injecting electrode was investigated but devices prepared in this manner did not show electroluminescence. The formation of porous alumina films on conductive substrates such as silicon, indium tin oxide and gold was also investigated and the encountered experimental difficulties are reported.

Table of Contents

List of Tables

List of Figures

List of Abbreviations and Symbols

Abbreviation/Symbol	Description
°	degree, unit of angle
a	pore radius, nm
α	beam convergence semi-angle
Å	Ångstrom, unit of length, 10^{-10} m
AMPEL	Advanced Materials and Process Engineering Laboratories
β	spectrometer collection semi-angle
β	ratio of particle speed to the speed of light in vacuum
BET	Brunauer-Emmett-Teller
BJH	Barret-Joyner-Halenda
c	speed of light in vacuum, 3.00×10^8 m s^{-1}
C	Coulomb, unit of charge
°C	degrees Celsius, unit of temperature
CCD	charge-coupled device
cm	centimetre, unit of length, 10^{-2} m
d	pore spacing
d_{hkl}	interplanar spacing
D	pore diameter
DC	direct current
ε	dielectric function
ε_1	real part of the dielectric function
ε_2	imaginary part of the dielectric function
EDX	energy dispersive x-ray spectroscopy
EELS	electron energy loss spectroscopy
EFTEM	energy-filtered transmission electron microscopy
e.g.	(exempli gratia, Latin) for example
et al.	(et alii, Latin) and co-workers
etc.	(et cetera, Latin) and others
eV	electron-Volt, unit of energy, 1.602×10^{-19} J
ex situ	(Latin) outside, external

FIB	focused ion beam
FT-IR	Fourier transform infrared
FWHM	full width at half-maximum
g	gram, unit of mass
GIF	Gatan imaging filter
h	hour, unit of time, 3600 s
i.e.	(id est, Latin) as in
in situ	(Latin) inside, internal
IR	infrared
ITO	Indium Tin Oxide
IUPAC	International Union of Pure and Applied Chemistry
J	Joule, unit of energy, kg m^2 s^{-2}
K	degrees Kelvin, unit of temperature
keV	kilo-electron-Volt, 1.602×10^{-16} J
kg	kilogram, unit of mass, 10^3 g
λ	wavelength
L	pore spacing
LED	light-emitting device
m	metre, unit of length
M	molar, unit of concentration, mol L^{-1}
MCM	Mobil Composition of Matter
MEH-PPV	poly[2-methoxy,5-(2′-ethylhexyloxy)-1,4-phenylene vinylene]
min	minute, unit of time, 60 s
mmol	millimol, 10^{-3} mol
mol	mole, constant of value 6.02×10^{23}
mrad	milliradian, 10^{-3} rad
ms	millisecond, unit of time, 10^{-3} s
N	newton, unit of force, kg m s^{-2}
n-D	n-dimensional
nm	nanometre, unit of length, 10^{-9} metre
p	pressure
p_o	standard pressure

pH	hydrogen ion concentration on logarithmic scale, $-\log_{10}[H^+]$
PL	photoluminescence
NMR	nuclear magnetic resonance
PPV	poly(1,4-phenylene vinylene)
θ_c	Cherenkov angle
Q	magnitude of scattering vector
rad	radian, unit of angle, π rad = 180°
ref.	reference
RF	radio-frequency
RIE	reactive ion etching
RPM	revolutions per minute
s	second, base unit of time
s	impact parameter, nm
SACT	small-angle cleavage technique
sat	saturated solution
SBA	Santa Barbara
sccm	surface cubic centimetre per minute, unit of flow rate
SEM	scanning electon microscopy
STEM	scanning transmission electron microscopy
STM	scanning tunnelling microscopy
t	thickness of adsorbed layer
T	Tesla, unit of magnetic flux density
TBA	tetrabutyl ammonium
TEM	transmission electron microscopy
TGA	thermogravimetric analysis
THF	tetrahydrofuran
Torr	unit of pressure, 1 Torr = 1 mm Hg = 133 kg m^{-1} s^{-2}
UV/Vis	ultraviolet/visible
V	Volts, J C^{-1}
XPS	x-ray photoelectron spectroscopy
ω	particle energy in electron-Volts
wt.	weight

Acknowledgements

I would like to acknowledge foremost my supervisor, Prof. Mike Wolf, for all the help and support he provided during the course of this thesis. My fellow Canadians have also supported me generously through the Natural Sciences and Engineering Research Council.

This work drew on the expertise of many talented staff members, students and professors at UBC. and elsewhere. A number of graduate students helped my work in important ways. The members of the Wolf group were generous and tolerant of my ways, and I would like to thank Dr. Olivier Clot and Dr. Cerrie Rogers especially for tutoring me on the finer points of organic synthesis. Dr. Katja Rademacher, Keri Kwong, Glen Kurokawa and Josh Edel also worked on similar projects and their collaboration was very useful. Darren Brouwer and Jim Sawada from the Fyfe group helped with the analysis of my porous materials.

Among the departmental staff, I would like to thank especially the mech shop staff - Brian Snapkauskas, Cedric Neal, Des Lovrity, Ron Marwick, Ken Love and Razvan Neagu - for their work on my project and their friendship. Brian Ditchburn provided custom glassware with superior helpfulness.

Andre Wong, from the Faculty of Dentistry, taught me ultramicrotomy of hard materials and helped with the very early electron microscopy work. Mary Mager, from Metals and Materials Engineering, provided similar help with sample preparation and electron microscopy. Elaine Humphrey and Garnett Huygens, from the Bioimaging facility, ran a great facility with fabulous microscopes and provided lots of advice as well.

Jeff Young and Murray W. McCutcheon, in the Physics Department, carried out the variable-temperature luminescence studies reported in chapter 3.

The most important results of this thesis can all be traced back to the expert help of Prof. Gianluigi Botton, with whom I started the work on electron energy-loss spectroscopy. The initial

help he provided proved invaluable for completing this work. Further on, Richard Humphrey at the University of Calgary helped with measurements, and Prof. Karen Kavanagh at Simon Fraser University gave access to her new microscope for the most important measurements.

The investigation into the Cherenkov effect was helped immensely by a collaboration with Profs. Alberto Rivacoba, F. Javier Garcia de Abajo and Nerea Zabala at Euskal Herriko Unibersitatea in Spain. Their theoretical insight into the problem guided the investigation and established the significance of the results.

On the fabrication side, Alina Kulpa, Doug Wong and Jim Mackenzie assisted in various ways. I particularly appreciated the great help Al Schmalz provided, and his friendship just as much. Dr. Ken Wong and Dr. Philip Wong carried out all the X-ray photoelectron spectroscopy on my samples.

Lastly, I would like to acknowledge the Green College community for three fulfilling (and thesis-delaying!) years, which have marked me as much as any experience in my life.

CHAPTER 1 Introduction

The three challenges of materials chemistry are synthesis, characterization and understanding. All of these have seen rapid progress in the past decades, largely due to advances in experimental methods and instrumention for investigating materials on the nanometre scale. This follows from the importance of interactions on this scale: the properties of all materials, from atom clusters to the bulk, whether homogeneous or not, are governed by interactions on the nanometre level. Understanding and exploiting these interactions has thus become centrally important in materials chemistry. Consequently, the development of new tools for structural characterization on this scale is of equal importance.

For crystalline materials, the tools for complete characterization on the atomic level have been available for a long time through X-ray diffraction. Yet this technique only provides an average picture of the material and may overlook structural features which may dominate material function, such as interfaces and defects. Furthermore, amorphous materials and materials with structure on a different scale are also excluded from investigation by diffraction. Structural analysis of such materials can only be done by high resolution microscopy, and this area remains in development for organic materials.

This thesis describes the preparation of composite materials consisting of conjugated polymers within mesoporous hosts. In this case, the material properties of interest – charge transport and luminescence in the conjugated polymer – could not be investigated further without first establishing the detailed structure of the composite. As this structure varied on the

nanometre scale, the characterization was not trivial and the development of the appropriate techniques became the focus of this work. In a larger context, this reflects the need for proper material characterization before property studies can be undertaken. The methods followed in this work should be readily applicable to other nanostructured systems with conjugated polymer components.

In this chapter, the properties of conjugated polymers are introduced along with a description of their main application in light-emitting devices. The motivation for introducing such polymers into porous host materials is discussed, and the literature on this developing field is reviewed. Finally, the scope of this thesis is presented along with a short summary of each chapter.

1.1 Conjugated Polymers: Organic Conductors and Semiconductors

The optical and electrical properties of molecular crystals of conjugated molecules have been the subject of study since the 1940's,[1] while the study of conjugated polymers began in the 1970's. Organic polymers with an electron system delocalized over the complete chain are of interest for a number of reasons, including the novelty of charge transport in polymers, theoretical interest in 1-D conductors, the useful mechanical properties of polymeric materials, and their simple and inexpensive processing.

Very significant breakthroughs have occurred in the study of conjugated polymers over the past 30 years. These polymers have been used as the active material in a number of applications, including sensors,[2,3] transistors,[4-6] light-emitting devices,[7-9] photovoltaic devices,[10] and lasers.[11,12] Electroactive polymers are also playing a role[13] in the development of molecular electronics.[14,15]

1.1.1 Organic Molecules with Conjugated π-Electron Systems

In many organic molecules, interesting and useful electrical properties arise from the presence of delocalized π-electron systems. These systems are referred to as conjugated π-electron systems. From the organic chemist's point of view, such a system is recognized in a chemical structure as a sequence of alternating single and double bonds between carbon atoms (Figure 1.1(a)). Electrons on other atoms, such as oxygen, sulfur and nitrogen, can also participate in a conjugated system. From the physical chemist's point of view, a conjugated π-electron system can be defined as a set of adjacent, parallel, half-filled *p* electron orbitals on a molecule (Figure 1.1(b)). In the framework of molecular orbital theory, these *p* orbitals combine to form molecular orbitals that are spread over the chain of interacting atoms (Figure 1.1(c)). Aromatic molecules are a special case where $4N + 2$ conjugated π-electrons form a ring, which imparts additional stability to the molecule.

The highest occupied molecular orbital (HOMO) is a π bonding orbital, and the lowest unoccupied molecular orbital (LUMO) is a π antibonding (or π^*) orbital. In large conjugated electron systems, the bonding orbitals have a quasi-continuous set of energy levels, which is referred to as the valence band. Analogously, the antibonding orbitals form the conduction band. Most importantly, the electrons in the conjugated system are delocalized over the extent of the

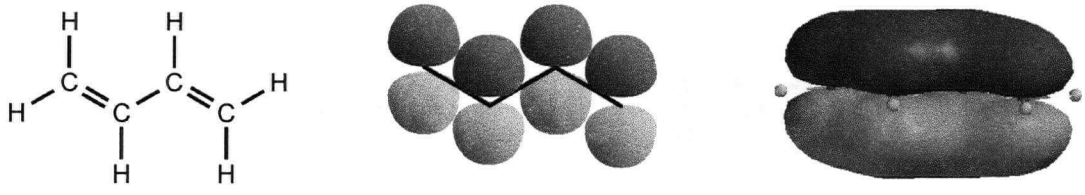

A **B** **C**

Figure 1.1 Butadiene, a simple conjugated molecule: (a) chemical structure, (b) *p*-orbitals forming conjugated system, (c) lowest energy (of four) π molecular orbital.

conjugated bonds. A conjugated molecule may therefore act as a pathway for charge transport if a charge carrier is introduced into the HOMO or LUMO. This can be accomplished by either oxidizing or reducing the molecule, either chemically (also known as doping) or electrochemically.

1.1.2 Conjugated Molecules in the Solid State

The electrical properties of a material depend largely on the distribution of available energy states above the highest occupied state. This is the energy difference between the conduction band and the valence band, which determines the amount of energy required to promote an electron from the HOMO to the LUMO. The size of the band gap is used to classify a material as a conductor, semiconductor or insulator. In conjugated molecules, the band gap is determined by the size of the conjugated system, and in most cases it falls in the range of semiconductors.

The electronic properties of conjugated molecules in the solid state (i.e., as a material) are altered by the effects of interactions between neighbouring molecules. Electronic processes, such as charge transport, are then a combination of intra- and intermolecular processes. For small molecules, intermolecular processes are necessarily important. For larger molecules, in particular polymers, the relative importance of these processes varies from material to material.

1.1.3 Organic Conjugated Polymers

Since the 1970's, molecules with long extensions of conjugated π-electrons have been the subject of scientific pursuit, as a result of interest in their electrical and optical properties. The concept of organic molecules as molecular wires has seen significant development.[16,17] In

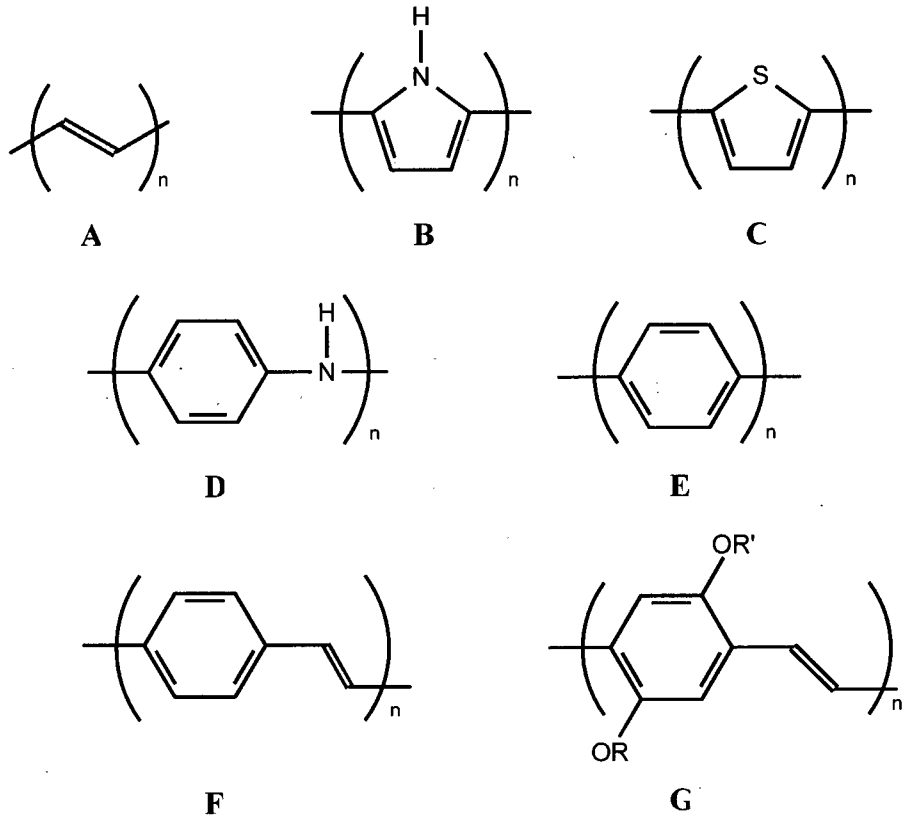

Figure 1.2 Conjugated polymers: (a) polyacetylene, (b) polypyrrole, (c) polythiophene, (d) polyaniline, (e) poly(1,4-phenylene), (f) poly(1,4-phenylene vinylene) (PPV), (g) poly[2-methoxy,5-(2′-ethylhexyloxy)-1,4-phenylene vinylene] (R = Me, R′ = 2-ethylhexyl) (MEH-PPV).

particular, polymers with conjugated π-electron systems extending along the whole length have been investigated. These are semiconductors in the pristine state. The simplest such polymer, polyacetylene (Figure 1.2(a)), was reported to be a conductor when doped by Shirakawa, Heeger and MacDiarmid in 1977.[18] The doped polymer exhibits an electrical conductivity that can reach metallic levels (Table 1.1). The conductivity of polyacetylene was an enormously important scientific discovery that earned the Nobel Prize for chemistry in 2000. The physics associated with the excited states on the polymer chain also proved to be very rich.[19]

The incorporation of aromatic subunits (benzene, thiophene, pyrrole, etc. – see Figure 1.2) allows control over the structure and properties of the polymer. These aromatic subunits may be chemically modified to adjust their electrical and optical properties,[20] and to impart other

Table 1.1 Electrical conductivity of polymers and some common materials.[21]

Conductivity ($S\ cm^{-1}$)	Polymer	Other Materials
10^{5}	doped polyacetylene, or	copper, iron
1	doped polypyrrole,	graphite,
	polythiophene, etc.	doped silicon
10^{-5}	*trans*-polyacetylene	indium,
		tin, silicon
	cis-polyacetylene	water
10^{-10}		diamond
	polythiophene, polypyrrole	
10^{-15}		nylon
10^{-20}	Teflon	quartz

desirable properties such as solubility. The incorporation of metal centres into the polymer chain is also an area of active research but falls outside the scope of this thesis. In general, the incorporation of functional units that interact with the conjugated π-system can be used to make the conductivity sensitive to the presence of external stimuli.[2,3,6]

The structures of conjugated polymers in solution and in the bulk can vary significantly. On short length scales, the chain structure is usually planar for optimal conjugation. On a longer scale, the polymer may deviate significantly from the ideal of a molecular wire and exist in a coiled-up configuration. This structure is difficult to determine in the solid state but may be investigated in solution by dynamic light-scattering measurements.[22]

The conductivity of doped polymers was found to degrade significantly through environmental exposure.[23,24] As undoped semiconductors, they are somewhat more stable and this area has become the main focus of work in the past decade.

1.2 Luminescence in Conjugated Molecules

The process of light emission by a molecule in an excited state is termed luminescence, and many conjugated molecules are highly luminescent. The excited state may be a spin singlet or a spin triplet, while the ground state is normally a singlet in organic molecules. The transition from the excited state to the ground state can occur through both radiative and non-radiative processes.

A radiative decay process in which spin angular momentum is conserved (also called a spin-allowed transition, e.g. between two singlet states or two triplet states) is termed fluorescence. This is a rapid process, with a typical lifetime on the nanosecond scale. A spin-forbidden radiative transition (e.g. from a triplet to a singlet state) is much slower (on the microsecond scale) in organic molecules and is called phosphorescence. The singlet ground state causes fluorescence to be the normal emission process in organic molecules.

A typical non-radiative decay process takes the molecule to a very highly excited vibrational level of the ground state, and the excess vibrational energy is dissipated eventually as heat. This mechanism may dominate if the radiative pathway is slow; for this reason, phosphorescence is not usually observed in organic conjugated molecules.

The initial excited state can be generated in a number of different ways, and this is used to distinguish different types of luminescence: photoluminescence from optical excitation, electroluminescence from electrical excitation, and chemiluminescence from chemical reaction. These modes of excitation may each be important for different applications; they may also differ significantly in the number of singlet and triplet states that they initially create. For conjugated polymers, the most important of these processes is electroluminescence.

1.3 Electroluminescence in Conjugated Polymers

Electroluminescent materials are of special importance in display technology. Electroluminescence is described as the emission of light from condensed matter under the action of an electric field.[25] This phenomenon was reported for small conjugated organic molecules in 1987.[26] It was first reported for a conjugated polymer, poly(1,4-phenylene vinylene) (PPV), in 1990 by Friend and co-workers.[27] A simple polymer-based device is shown in Figure 1.3: the active polymer layer is sandwiched between a metallic cathode and a transparent anode.

While the performance of these devices has been continously improved, the main barrier to commercialization has been device degradation.[6] Conjugated polymers are very susceptible to photo-oxidation; the oxidized molecules then serve as low-energy traps for electrons, which reduces the luminescence efficiency.[28,29] Other routes to device degradation also exist.[30,31]

1.3.1 Electroluminescence Processes in Conjugated Polymers

The technological importance of electroluminescence has made understanding the various electronic processes in these devices an important objective. The mechanism of electroluminescence in polymers has been widely investigated and reviewed in detail.[9,19,25] The

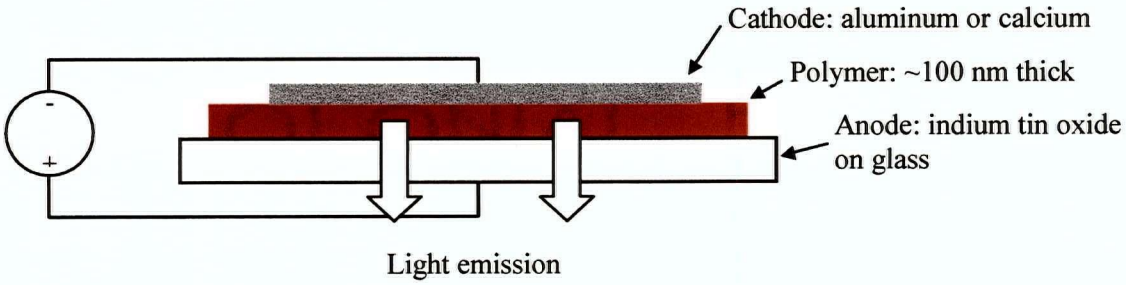

Figure 1.3 Structure of a simple conjugated polymer-based electroluminescent device.

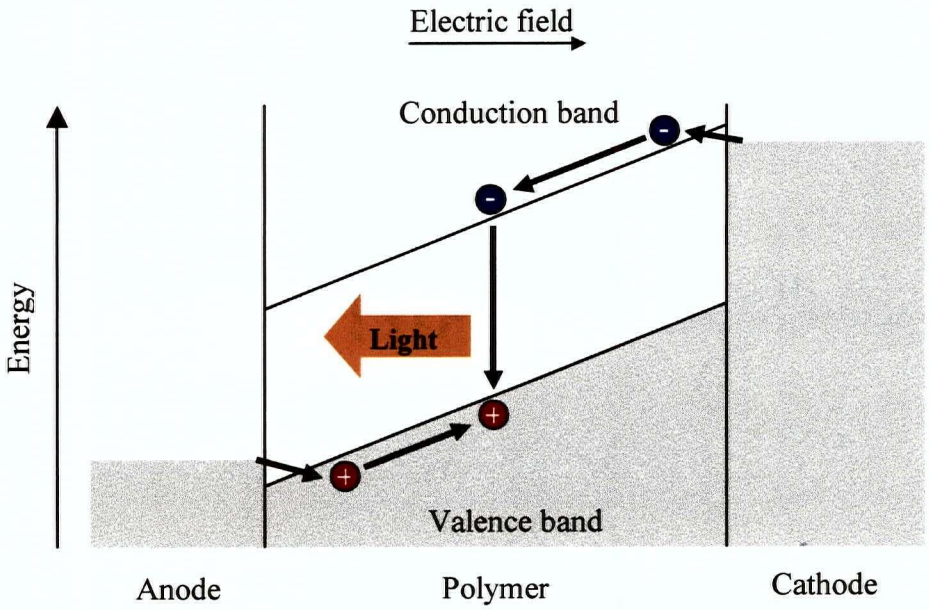

Figure 1.4 Electroluminescence processes in a simple polymer device.

key processes, illustrated in Figure 1.4, are charge injection, transport, recombination and de-excitation.

Under the action of the applied electric field, the polymer is oxidized at the anode (indium tin oxide (ITO) or gold), which introduces a positive charge by removing an electron from the HOMO (valence band). This species is referred to as a hole. At the cathode, the polymer is reduced, which places an electron into the LUMO (conduction band). The work function of the cathode material is chosen to match the polymer LUMO level as closely as possible; aluminum and calcium are used commonly. If there is substantial mismatch, the injection process does not proceed efficiently. It follows that the devices do not conduct under reverse bias.

These charges migrate towards each other through the material due to the applied field through a combination of intrachain and interchain transport. When a hole and an electron meet within the polymer, they may recombine to create either a singlet or triplet excited state. As discussed above, the singlet state will usually decay radiatively, completing the electroluminescence process. The triplet state usually decays non-radiatively; it may be

converted to a singlet state through the addition of a sensitizer;[32,33] the triplet state energy may also be converted to light through phosphorescence.[34,35]

The excited state may be localized on one polymer chain or spread over adjacent chains. In the latter case, it has been found that the radiative lifetime is substantially longer,[22,36] which can then favour non-radiative processes.

1.3.2 Electroluminescence Efficiency

The power efficiency of an electroluminescent device is very important for many applications, as it determines the brightness and power consumption of the device. Important progress has been made in improving this efficiency following the discovery of electroluminescence in conjugated polymers.[9] Many factors affect the power efficiency, and here only the internal quantum efficiency is discussed. This is defined as the number of photons created per injected electron.[9] The overall internal quantum efficiency is determined principally by the photoluminescence yield and the singlet yield.

The photoluminescence efficiency, which can be measured separately, places an upper limit on electroluminescence efficiency. Optical excitation of the polymer creates an excited state identical to the one produced by the charge recombination process. Since optical excitation creates only singlet states, this allows the relative importance of radiative and non-radiative processes to be investigated. The presence of interchain interactions is important in this respect, as an excited state with a slow radiative decay can be more susceptible to non-radiative quenching. In the device, the higher mobility of holes relative to electrons in the polymer causes recombination to occur close to the cathode interface. This interface is known to have many chemical defects at which non-radiative decay can occur,[37,38] which reduces the photoluminescence efficiency relative to the pristine material.

In electroluminescence, the singlet yield corresponds to the fraction of excited states generated as singlets. The creation of the non-radiative triplet states during recombination reduces this yield. Based on simple spin statistics, the singlet spin fraction is expected to be one quarter, and this was long believed to be the limiting factor of organic electroluminescent devices. However, some recent experimental[39-42] and theoretical[43,44] results have indicated that the probabilities of singlet and triplet formation may not be the same, and that singlet creation is favoured in polymeric materials (as opposed to small molecules). Hence the singlet fraction may approach unity in conjugated polymers.

More sophisticated device structures provide higher efficiency: multi-layer devices are used to eliminate the problem of higher hole mobility[45] and the injection processes can be improved by optimizing the cathode material[46] or by modification of the anode interface by ultrathin polymer layers.[47] The complex chemistry of evaporated metal contacts has limited the understanding of processes at the cathode interface.[46]

1.3.3 An Ideal Device Structure

The electronic processes in conjugated polymer devices are difficult to study due to the amorphous nature of the polymer film. The disorder in these films gives rise to complicated 2- and 3-D phenomena despite the 1-D nature of the polymer chain. It is then of scientific interest to develop systems where interchain processes are eliminated, thereby allowing the intrachain properties to dominate. This amounts to electrical isolation of individual polymer chains.

It is clear that complete isolation of each chain would eliminate all charge transport, and therefore a functional device can only be achieved if each polymer chain is in electrical contact with both electrodes (Figure 1.5). An ordered and oriented encapsulant is necessary to achieve such a structure. An ideal device design would also include chemically well-defined interfaces to

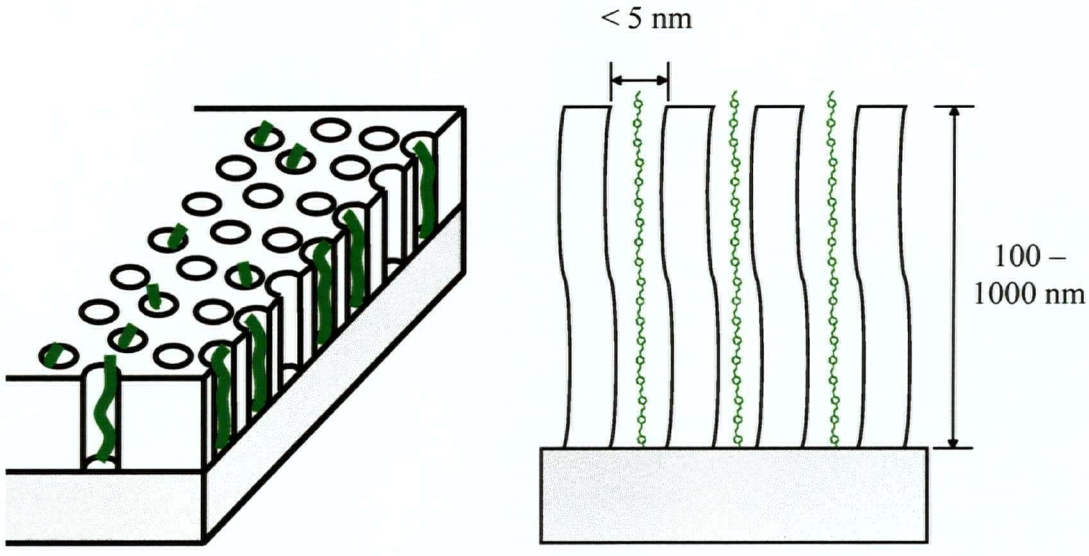

Figure 1.5 Ideal device structure consisting of oriented and isolated polymer chains.

the cathode and anode, such that the charge injection processes could be studied more rigourously. This area has already seen important progress through the study of conjugated molecules self-assembled on metal interfaces.[17,48]

The goal of measuring single polymer chain electrical properties thus serves to introduce the theme of encapsulation. A list of desirable properties may be generated based on the premise that the host material should be present only to induce the desired ordering of the conjugated polymer guest and otherwise not interfere with measurements being made on the guest (Table 1.2). In practice, it must be recognized that host-guest interactions cannot be entirely avoided, and may be difficult to account for.

1.4 Encapsulated Conjugated Polymers

Encapsulation can be generally defined as the preparation of materials in which there is a reduced degree of interaction between the guest molecule and its surroundings. There are two fundamental motivations behind the goal of producing encapsulated conjugated polymers. First, as discussed above, the study of single polymer chains isolated in the solid state is expected to reveal the fundamental photophysical and electrical behaviour of the conjugated polymer chain, without any effects due to aggregation with other polymer chains.[49] Second, a suitable encapsulant would provide protection against environmental agents, most importantly oxygen, which would allow devices to operate for longer periods of time under ambient conditions. In this context, encapsulation implies the reduction of chemical and electrical interactions of the polymer chains.

1.4.1 Approaches to Encapsulation

The photophysics of isolated chains can be studied by dispersing the polymer in an inert

Table 1.2 Properties of the ideal host material for conjugated polymers.

Property	Basis
1. Aligned channels normal to the substrate	Allow good electrical transport
2. Narrow pores (< 5 nm)	Minimize number of polymer chains per pore, ideally only one per pore (guaranteed if diameter is < 2 nm)
3. Optical transparency	Allow optical characterization of polymer guest
4. Electrical insulator	Measure only guest electrical properties, Minimize interchain processes
5. Chemically inert	Minimize interactions with the polymer guest
6. Easily prepared as thin film (controlled thickness, defect-free)	Allow light-emitting device fabrication
7. Good "analytical contrast"	Ease of characterization

polymer matrix.[50,51] However, this approach does not preclude effects due to interactions among

different segments of the same chain, if the polymer is in a coiled configuration. Possible phase segregation of the polymer is also an issue in these materials, and cannot be excluded without detailed microstructural analysis of the dispersed polymer. Similarly, dilute polymer solutions can be studied. In this way, the intrachain hole mobility has been measured for isolated polymer chains[52] and the effect of interchain interactions on photophysical behaviour has been determined.[22]

These approaches to encapsulation are useful but afford a degree of encapsulation which prevents direct electrical measurements on the isolated chains. Furthermore, a degree of disorder remains on the level of the polymer chain conformation. For this reason, novel approaches to encapsulation are desirable and one can look to ordered porous materials. Many of the requirements of Table 1.2 can be satisfied by porous materials based on silica and alumina.

1.4.2 Ordered Porous Materials as Encapsulants

The synthesis of conjugated polymers within ordered host materials has been reviewed extensively in recent years,[21,53,54] and a brief overview is given here. Further details on various host materials are given in chapters 3 and 4.

In the late 1980's, the initial work on the synthesis of polyacetylene within the channels of zeolites (crystalline, microporous aluminosilicate materials) was carried out by Bein and Enzel. They incorporated polypyrrole,[49] polythiophene,[55] and polyaniline[56] into different zeolites. This work was then extended to produce conjugated polymers within the channels of a mesoporous silica material.[57-59] These results provided the first indications about the behaviour of conjugated polymers in a confined environment: microwave conductivity measurements indicated that the confined polymers could be more conductive than in the bulk.[60] The

composite materials were in powder form, which precluded achieving any macroscopic orientation of the samples.

Martin *et al.* developed oriented, encapsulated materials based on porous alumina and track-etch membranes.[61-63] The pore diameters in these membranes were in all cases larger than 10 nm, which allowed for convenient preparation of polymer microtubules but did not allow any polymer confinement effects to be observed.

Substantial progress towards the goal of encapsulating conjugated polymer chains into oriented hosts was reported in the literature during the course of this thesis. The work by the groups of Tolbert and Schwarz at the University of California, Santa Barbara[64-68] and the work by the group of Gin at the University of California, Berkeley[69-75] represent the most significant developments in this field. They prepared host-guest systems where the conjugated polymer guest was encapsulated in very narrow channels, and their evidence suggested that interactions between different polymer chains were eliminated. This was accomplished through investigation of the time-resolved optical properties of the composite material. However, the goal of measuring the electrical properties of single conjugated polymer chains directly has not been achieved to date; the nearest result describes the hole mobility on single conjugated polymer chains in solution.[52]

These and other relevant results are reviewed here to provide a perspective on the field of encapsulated conjugated polymers.

1.4.3 Oriented Mesoporous Silica Encapsulant

The use of a large external magnetic field to align the channels of a surfactant-templated mesoporous silica material was pioneered by Firouzi *et al.*[76] This method may be used to produce solid samples with an overall channel orientation parallel to the applied magnetic field, with a lattice spacing of 3.5 nm and a diameter of 2.2 nm.[77] It was then shown that a soluble PPV derivative, poly[2-methoxy,5-(2′-ethylhexyloxy)-1,4-phenylene vinylene] (MEH-PPV, Figure 1.2(g)), could be introduced into the channels of such a host following proper chemical functionalization of the channel surfaces (diameter reduced to ~ 1.7 nm).[64] The polymer loading was simply accomplished by placing the host in a heated polymer solution for some time (Figure 1.6), then following an optimized solvent washing sequence to maximize removal of external polymer. The initial evidence for polymer incorporation was based on measurements of the fluorescence polarization. It was recognized that at least some unencapsulated polymer was present in larger cavities in the host material, but its effect could be minimized through selective oxidation. It was further argued on geometrical considerations (the polymer packing radius is 0.8 - 0.9 nm in the solid state) that only one polymer chain could be present in each pore.

Investigation of the photoluminescence polarization dynamics indicated that initial excitation energy localized on the unencapsulated polymer migrated quickly to the lower-energy

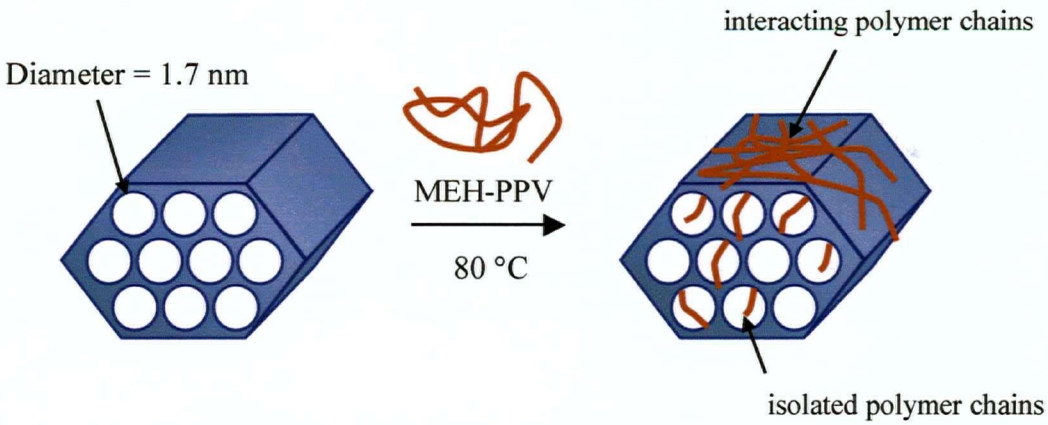

Figure 1.6 Incorporation of MEH-PPV into oriented mesoporous silica.

encapsulated chains.[65,66] Further energy migration along the encapsulated chain was a slower process. The measurement of transient absorption dynamics in the femtosecond regime allowed the encapsulated polymer to be distinguished very clearly, based on comparisons with MEH-PPV in dilute solution and as a thin film.

Overall, these results provided very compelling arguments for the presence of isolated MEH-PPV chains in the pores of the silica host. The single chains were not observed directly in the host channels, but the photophysical behaviour of the composite indicated that chain isolation had been achieved. The determination of the microwave conductivity of the sample, which would give a value for the conductivity of a single conjugated polymer chain, was reportedly under way[64] but has not yet been published.

1.4.4 Liquid Crystal Encapsulant

The use of lyotropic liquid crystals as a host material was pursued by Smith *et al.*, using a polymerizable mesogen to form an inverse hexagonal matrix (Figure 1.7).[69] They initially used a water-soluble PPV precursor (Figure 1.8), which was expected to segregate into the aqueous phase of the liquid crystal. Cross-linking of the matrix stabilized the liquid crystal host, after which the PPV precursor could be converted to the final form by heating under vacuum. The interpore distance was 4.0 nm and the pore diameter ~1.5 nm. The resulting composite showed a blue-shifted photoluminescence spectrum relative to bulk PPV. There was a large increase in the photoluminescence intensity, and the absolute photoluminescence efficiency was reported as 30%, substantially larger than for other samples in the same study (5-20%)[73] but comparable to other values reported for bulk PPV (27%).[78]

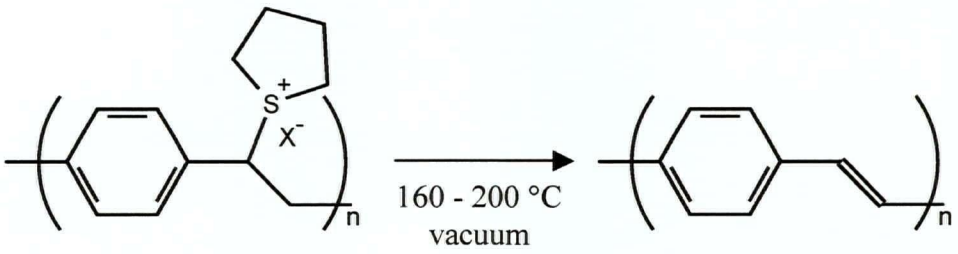

Figure 1.8 High-temperature conversion of a water-soluble precursor polymer to PPV.

The photoinduced absorption spectrum was also shifted to higher energy and showed an excitation intensity dependence consistent with interchain energy transfer inhibition.[74] Photoluminescence-detected magnetic resonance measurements showed that the composite material behaved similarly to conjugated polymer dispersed in an inert matrix.[72] The femtosecond photoluminescence dynamics were not investigated, though this would have provided the best evidence for polymer chain isolation. The difficulty with all the above comparisons is that it is not known whether the polymer precursor conversion step proceeds in the composite in the same manner as in the bulk.

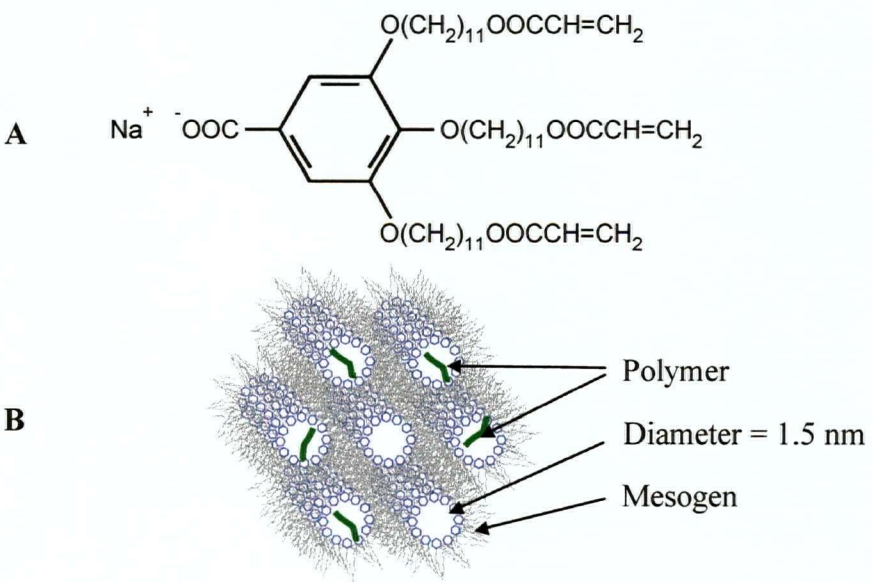

Figure 1.7 (a) Structure of liquid crystal mesogen, (b) structure of lyotropic liquid crystal with polymer guest.

Subsequent work with a water-soluble PPV derivative[79] (Figure 1.9) allowed more definitive experiments: the polymer could be extracted from the composite after synthesis and the photophysical properties of the encapsulated and free polymer chains could be compared directly.[75] This showed that the local dielectric environment of the matrix, which is highly polar due to the carboxylate groups of the mesogen, had little effect on the observed differences. It was also argued (without direct evidence, due to low polymer content in the composite) that the effective conjugation length of the polymer was unaffected by the encapsulation process. This left the isolation of the polymer chains as the only remaining factor responsible for the observed differences. However, it is not clear whether the behaviour of this PPV derivative can be generalized to PPV itself.

The composite material could also be prepared as an oriented film, with the channels reportedly running perpendicular to the substrate,[71] by pressing the liquid crystal between two glass plates. The alignment was induced by the interactions at the glass/liquid crystal interface. However, no direct evidence of this alignment was provided. With such an oriented film, it was claimed that a nearly ideal device structure was produced. The electrical properties of this device structure were investigated, and it was found that both the polymer and the stacked benzene rings of the matrix conducted electricity. Electroluminescence was detected and it was found to originate from both the matrix and the polymer. Thus the electroluminescence behaviour of the isolated chains could not be investigated by this approach.

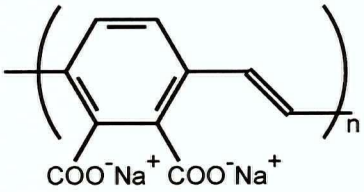

Figure 1.9 Water-soluble PPV derivative.[79]

1.4.5 Clay Encapsulant

Recently, O. O. Park and co-workers reported the successful intercalation of MEH-PPV between the layers of an organoclay material (Figure 1.10).[80,81] The incorporation of some polymer was evidenced by an increase in the spacing of the clay layers, as determined by X-ray diffraction. No further details of the structure of the composite were reported. While the layered structure of the organoclay does not allow full isolation of the polymer chains, the experimental results seemed to indicate that there was a large enhancement of photoluminescence intensity (18×; absolute efficiencies were not reported). The absolute photoluminescence efficiency of MEH-PPV is known to be 10-15%;[78] therefore the claimed increase may be considered somewhat suspect.

Electroluminescent devices could be fabricated using this composite material as the active

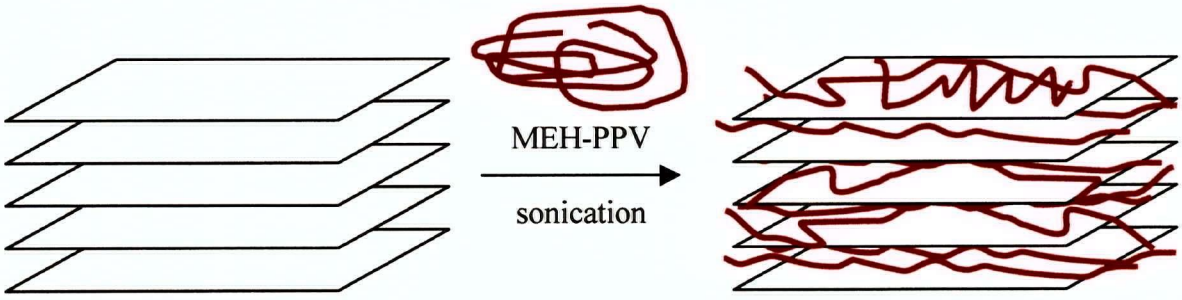

Figure 1.10 Preparation of MEH-PPV/Clay composite material.

layer between ITO and aluminum electrodes. The electroluminesence efficiency of these devices was enhanced. This increase was attributed to the confinement of the charged species. The hole mobility in the composite was also reduced relative to bulk MEH-PPV, which may have led to a better balancing of the hole and electron distribution. Surprisingly, the device operated equally well in reverse bias, indicating that the choice of electrode material was not affecting device operation. However, this fact was not discussed in any detail. Clearly, this material exhibited some very novel behaviour, but the limited characterization did not allow the origin of this behaviour to be identified. Some further work has been carried out on the incorporation of PPV into layered host materials.[82,83]

1.4.6 Cyclodextrin Encapsulant

Anderson *et al.* have shown that luminescent conjugated molecules encapsulated in cyclodextrin have substantially enhanced photostability.[84,85] They have extended this approach to polymers by synthesizing water-soluble conjugated polymer chains threaded inside stacked β-cyclodextrin rings (Figure 1.11).[84] Sufficiently large capping groups at the end of the polymer chain prevent dethreading. This produces polymer chains which are very tightly encapsulated. Direct investigation of thin film morphology by atomic force microscopy allowed the encapsulated polymer strands to be resolved, which indicated that there was substantial reduction in interactions between chains. The absolute photoluminescence efficiency of the polymer chain was shown to increase[86] by 3 - 4× but the photostability of these polymers was not discussed.

The encapsulation provided by these macrocycles is not complete, which still allows the intermolecular charge transport necessary for device operation.[86] Encapsulation was shown to increase the electroluminescence efficiency by 2 - 5×. Again device stability was not discussed.

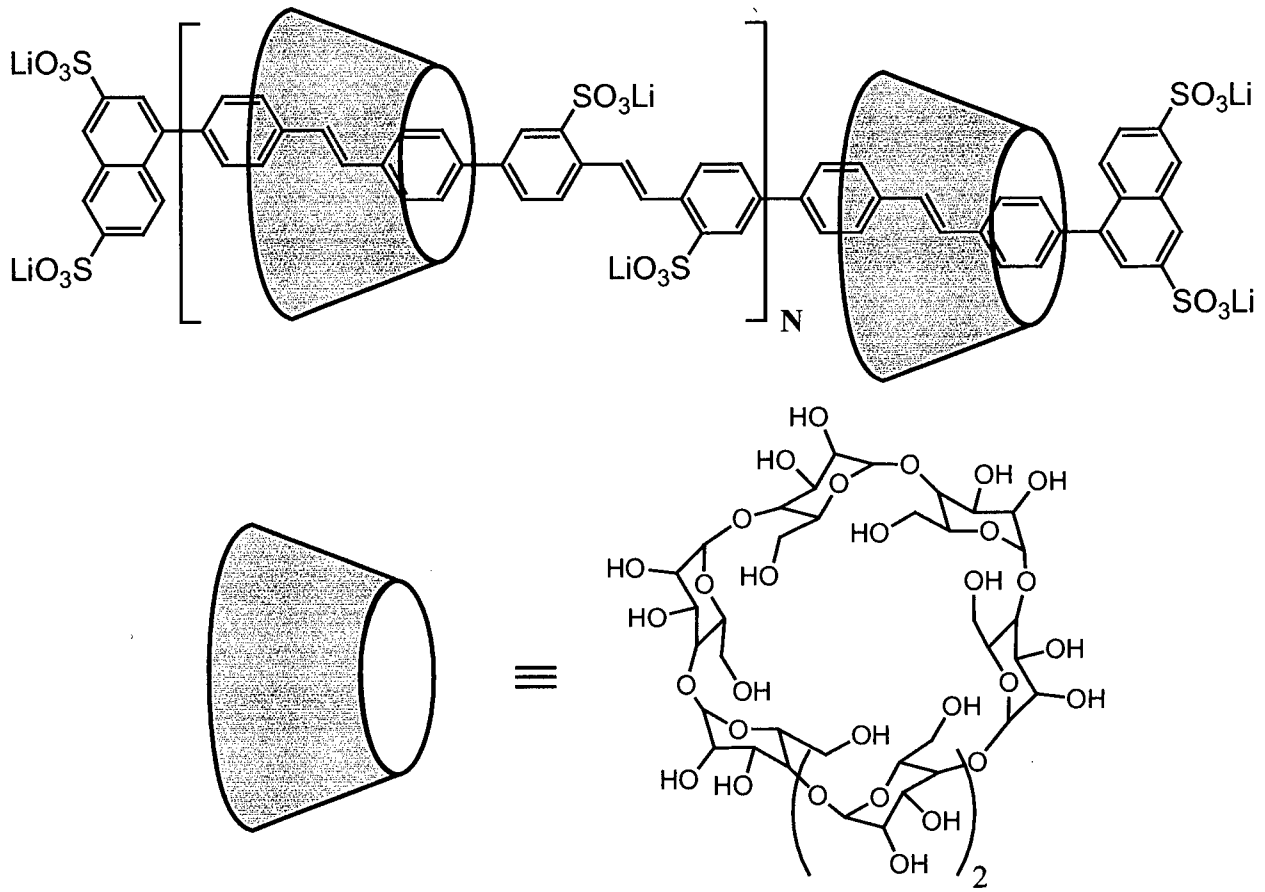

Figure 1.11 Encapsulation of conjugated polymer chain with β-cyclodextrin.[86]

This approach to encapsulation appears very promising and will hopefully be subject to further study. The current results clearly indicate that this approach is useful but have not yielded any further insight into the electroluminescence processes themselves. As noted in the literature, one limitation of this approach is the mobility of the macrocycle along the polymer chain, which can cause a non-uniform distribution of the encapsulant.[86]

Short, encapsulated oligomers prepared in this fashion could also be grafted to a conducting surface, and such a configuration would be ideal for electrical measurements on single polymer chains. This has not been reported to date.

1.4.7 Literature Summary

The work of Nguyen *et al.*[65] provided the clearest results on the properties on encapsulated conjugated polymers. The results on liquid crystal encapsulation[75] were important but further investigation of the encapsulated polymer would be needed to show the effect of chain isolation on electronic excitations.

The work on clay encapsulation[80,81] was interesting but did not provide much more understanding of the electronic processes in conjugated polymers. The work on β-cyclodextrin encapsulation[86] is important because a functional device was demonstrated, and further insight might be gained from photophysical studies.

These works illustrate collectively that encapsulated conjugated polymers exhibit novel behaviour, in particular enhanced luminescence efficiencies. However, the cause of this behaviour is difficult to identify without a detailed analysis of the nanostructure of the material – and incorrect conclusions might be drawn if such analysis is neglected. It is also clear that the ideal device structure, consisting of aligned and isolated conjugated polymer chains, remains to be reported.

1.5 Thesis Summary

This thesis describes the synthesis and characterization of conjugated polymer guests in mesoporous host materials. The principal motivation of the work was to create materials and device structures which would further the understanding of electronic processes within conjugated polymers. However, it was recognized early on that little understanding can be gained from materials which are not fully characterized. A change in material properties cannot be rationalized if the structure of the material is not known in detail, which is well illustrated by the work on MEH-PPV/clay composites discussed above. This realization guided this work

towards the application of high resolution characterization techniques to conjugated polymer composite materials. The unifying theme of the final work is then characterization of such composite materials on the nanometre scale.

In chapter 2, the main characterization techniques used for analysis of composite materials are reviewed, with an emphasis on electron microscopy techniques. The most important of these is electron energy-loss spectroscopy (EELS) and energy-filtered transmission electron microscopy (EFTEM). The application of EELS to the analysis of organic materials is reviewed.

A general introduction to ordered porous host materials is presented in chapter 3, and the literature on introduction of polymers into such hosts is reviewed. This is followed by a study of the incorporation of PPV into a mesoporous silica composite material. Chemical analysis of the composite material with nanometre resolution by EELS and EFTEM is used to show directly that the conjugated polymer is present inside the pores of the host.

Chapter 4 is devoted to the preparation of oriented porous thin films towards the goal of preparing an ideal electroluminescent device structure. Porous alumina membranes prepared at low temperatures are presented as very good candidates for preparing such a structure.

The initial analysis of conjugated polymer/porous alumina composite materials is described in chapter 5. The EELS and EFTEM measurements were carried out parallel to the pores of the host. The analysis was hindered by spectral features due to surface effects in EELS. Furthermore, the samples showed a further loss at a large distance from the sample surface that could not be associated with a surface plasmon.

Chapter 6 deals with this unexpected loss at large distance from the sample surface. The Cherenkov effect is identified as the source of this spectral feature. The experimental and theoretical results show that the spectroscopy of the samples on the local scale was affected by the large scale structure of the sample, due to the radiative nature of the Cherenkov effect.

Chapter 7 discusses further ways of preparing polymer/porous alumina film composites and their characterization. Initial work in the direction of preparing conjugated oligomers grafted to a silicon surface is described. The use of different driving forces for composite preparation is discussed, and the centrifugal force is investigated in detail. Thin sections of the samples are investigated by EELS and EFTEM. Low-energy losses in the alumina host at 200 kV are found to interfere with the polymer-specific losses.

Chapter 8 discusses some of the possible approaches towards ideal device fabrication. Although the overall goal of preparing an ideal device structure has not been realized, the elements for preparing such a device and the tools for its structural characterization have been developed.

References

1. Pope, M.; Swenberg, C. E. *Electronic Processes in Organic Crystals*; Clarendon Press: Oxford, 1982.

2. Higgins, S. J. *Chem. Soc. Rev.* **1997**, *26*, 247.

3. Goldenberg, L. M.; Bryce, M. R.; Petty, M. C. *J. Mater. Chem.* **1999**, *9*, 1957.

4. Horowitz, G. *Adv. Mater.* **1998**, *10*, 365.

5. Sirringhaus, H. T. N. F. R. H. *Science* **1998**, *280*, 1741.

6. Cacialli, F. *Philos. Trans. R. Soc. London, Ser. A* **2000**, *358*, 173.

7. Heeger, A. J. *Solid State Commun.* **1998**, *107*, 673.

8. Rees, I. D.; Robinson, K. L.; Holmes, A. B.; Towns, C. R. O.; Dell, R. *MRS Bull.* **2002**, *27*, 451.

9. Akcelrud, L. *Prog. Polym. Sci.* **2003**, *28*, 875.

10. Nunzi, J. M. *C.R. Phys.* **2002**, *3*, 523.

11. Kranzelbinder, G.; Leising, G. *Rep. Prog. Phys.* **2000**, *63*, 729.

12. Scherf, U.; Riechel, S.; Lemmer, U.; Mahrt, R. F. *Curr. Opin. Solid State Mater. Sci.* **2001**, *5*, 143.

13. Saxena, V.; Malhotra, B. D. *Current Applied Physics* **2003**, *3*, 293.

14. Tour, J. M. *Acc. Chem. Res.* **2000**, *33*, 791.

15. Tour, J. M. *Molecular electronics: commercial insights, chemistry, devices, architecture and programming.*; World Scientific: London, 2003.

16. Bumm, L. A.; Arnold, J. J.; Cygan, M. T.; Dunbar, T. D.; Burgin, T. P.; Jones, L.; Allara, D. L.; Tour, J. M.; Weiss, P. S. *Science* **1996**, *271*, 1705-1707.

17. Reed, M. A.; Zhou, C.; Muller, C. J.; Burgin, T. P.; Tour, J. M. *Science* **1997**, *278*, 252-254.

18. Shirakawa, H.; Louis, E. J.; MacDiarmid, A. G.; Chiang, C. K.; Heeger, A. J. *Chem. Commun.* **1977**, 578.

19. Greenham, N. C.; Friend, R. H. *Semiconductor device physics of conjugated polymers*; Solid State Physics; Academic Press: New York, 1995; Vol. 49, p. 1-149.

20. Burn, P. L.; Kraft, A.; Baigent, D. R.; Bradley, D. D. C.; Brown, A. R.; Friend, R. H.; Gymer, R. W.; Holmes, A. B.; Jackson, R. W. *J. Am. Chem. Soc.* **1993**, *115*, 10117-10124.

21. Cardin, D. J. *Adv. Mater.* **2002**, *14*, 553.

22. Nguyen, T. Q.; Doan, V.; Schwartz, B. J. *J. Chem. Phys.* **1999**, *110*, 4068.

23. Pekker, S.; Morin, A.; Berniere, F. *Polymer Communications* **1990**, *31*, 75.

24. Kobryanskii, V. M. *Polym. Degrad. Stab.* **1991**, *33*, 387.

25. Kalinowski, D. *J. Phys. D: Appl. Phys.* **1999**, *32*, R179.

26. Tang, C. W.; Van Slyke, S. A. *Appl. Phys. Lett.* **1987**, *51*, 913-915.

27. Burroughes, J. H.; Bradley, D. D. C.; Brown, A. R.; Marks, R. N.; Mackay, K.; Friend, R. H.; Burns, P. L.; Holmes, A. B. *Nature* **1990**, *347*, 539-41.

28. Papadimitrakopoulos, F.; Konstadinidis, K.; Miller, T. M.; Opila, R.; Chandross, E. A.; Galvin, M. E. *Chem. Mater.* **1994**, *6*, 1563-8.

29. Rothberg, L. J.; Yan, M.; Papadimitrakopoulos, F.; Galvin, M. E.; Kwock, E. W.; Miller, T. M. *Synth. Met.* **1996**, *80*, 41-58.

30. Scott, J. C.; Kaufman, J. H.; Brock, P. J.; DiPietro, R.; Salem, J.; Goitia, J. A. *J. Appl. Phys.* **1996**, *79*, 2745.

31. Kim, J. S.; Ho, P. K. H.; Murphy, C. E.; Baynes, N.; Friend, R. H. *Adv. Mater.* **2002**, *14*, 206.

32. He, G. F.; Chang, S. C.; Chen, F. C.; Li, Y. F.; Yang, Y. *Appl. Phys. Lett.* **2002**, *81*, 1509.

33. Baldo, M. A.; Thompson, M. E.; Forrest, S. R. *Nature* **2000**, *403*, 750.

34. Kan, S. D.; Zhang, J. Y.; Liu, X. D.; Shen, F. Z.; Ma, Y. G.; Shen, J. C. *Synth. Met.* **2003**, *135*, 253.

35. Welter, S.; Brunner, K.; Hofstraat, J. W.; De Cola, L. *Nature* **2003**, *421*, 54.

36. Samuel, I. D. W.; Rumbles, G.; Collison, C. J.; Friend, R. H.; Moratti, S. C.; Holmes, A. B. *Synth. Met.* **1997**, *84*, 497.

37. Becker, H.; Burns, S. E.; Friend, R. H. *Phys. Rev. B: Condens. Matter* **1997**, *56*, 1893-1905.

38. Dannetun, P.; Loegdlund, M.; Fahlman, M.; Boman, M.; Stafstroem, s.; Salaneck, W. R.; Lazzaroni, R.; Fredriksson, C.; Bredas, J. L.; et al. *Synth. Met.* **1993**, *55*, 212-17.

39. Cao, Y.; Parker, I. D.; Yu, G.; Zhang, C.; Heeger, A. J. *Nature* **1999**, *397*, 414.

40. Wilson, J. S.; Dhoot, A. S.; Seeley, A. J. A. B.; Khan, M. S.; Kohler, A.; Friend, R. H. *Nature* **2001**, *413*, 828.

41. Wohlgenannt, M.; Vardeny, Z. V. *J. Phys.: Condens. Matter* **2003**, *15*, R83.

42. Wohlgenannt, M.; Jiang, X. M.; Vardeny, Z. V. *Synth. Met.* **2003**, *137*, 1069.

43. Karabunarliev, S.; Bittner, E. R. *J. Chem. Phys.* **2003**, *119*, 3988.

44. Karabunarliev, S.; Bittner, E. R. *Phys. Rev. Lett.* **2003**, *90*, No. 057402.

45. Baigent, D. R.; Greenham, N. C.; Gruener, J.; Marks, R. N.; Friend, R. H.; Moratti, S. C.; Holmes, A. B. *Synth. Met.* **1994**, *67*, 3-10.

46. Brown, T. M.; Friend, R. H.; Millard, I. S.; Lacey, D. J.; Butler, T.; Burroughes, J. H.; Cacialli, F. *J. Appl. Phys.* **2003**, *93*, 6159-6172.

47. Ho, P. K. H.; Kim, J. S.; Burroughes, J. H.; Becker, H.; Li, S. F. Y.; Brown, T. M.; Cacialli, F.; Friend, R. H. *Nature* **2000**, *404*, 481.

48. Cygan, M. T.; Dunbar, T. D.; Arnold, J. J.; Bumm, L. A.; Shedlock, N. F.; Burgin, T. P.; Jones, L.; Allara, D. L.; Tour, J. M.; Weiss, P. S. *J. Am. Chem. Soc.* **1998**, *120*, 2721-2732.

49. Bein, T.; Enzel, P. *Angew. Chem. Int. Ed. Engl.* **1989**, *28*, 1962.

50. Heller, C. M.; Campbell, I. H.; Laurich, B. K.; Smith, D. L.; Bradley, D. D. C.; Burn, P. L.; Ferraris, J. P.; Mullen, K. *Phys. Rev. B: Condens. Matter* **1996**, *54*, 5516-5522.

51. Hagler, T. W.; Pakbaz, K.; Voss, K. F.; Heeger, A. J. *Phys. Rev. B: Condens. Matter* **1991**, *44*, 8652-66.

52. Hoofman, R. J. O. M.; De Haas, M. P.; Siebbeles, L. D. A.; Warman, J. M. *Nature* **1998**, *392*, 54-56.

53. Ozin, G. A.; Chomski, E.; Khushalani, D.; Maclachlan, M. J. *Curr. Opin. Colloid Interface Sci.* **1998**, *3*, 181-193.

54. Moller, K.; Bein, T. *Chem. Mater.* **1998**, *10*, 2950-2963.

55. Enzel, P.; Bein, T. *Chem. Commun.* **1989**, *18*, 1326.

56. Enzel, P.; Bein, T. *J. Phys. Chem.* **1989**, *93*, 6270.

57. Wu, C.-G.; Bein, T. *Science* **1994**, *264*, 1757-1759.

58. Wu, C.-G.; Bein, T. *Conducting polymer wires in mesopore hosts*; Studies in Surface Science and Catalysis; Elsevier: Amsterdam, 1994; Vol. 84, p. 2269-2276.

59. Wu, C.-G.; Bein, T. *Science* **1994**, *266*, 1013-1015.

60. Esnouf, S.; Beuneu, F.; Enzel, P.; Bein, T. *Phys. Rev. B: Condens. Matter* **1997**, *56*, 12899-12904.

61. Cai, Z. H.; Martin, C. R. *J. Am. Chem. Soc.* **1989**, *111*, 4138.

62. Martin, C. R.; Van Dyke, L. S.; Cai, Z. H.; Liang, W. B. *J. Am. Chem. Soc.* **1990**, *112*, 8976.

63. Martin, C. R. *Chem. Mater.* **1996**, *8*, 1739-1746.

64. Wu, J. J.; Gross, A. F.; Tolbert, S. H. *J. Phys. Chem. B* **1999**, *103*, 2374.

65. Nguyen, T. Q.; Wu, J. J.; Doan, V.; Schwartz, B. J.; Tolbert, S. H. *Science* **2000**, *288*, 652.

66. Tolbert, S. H.; Wu, J. J.; Gross, A. F.; Nguyen, T. Q.; Schwartz, B. J. *Microporous Mesoporous Mater.* **2001**, *44*, 445.

67. Schwartz, B. J.; Nguyen, T. Q.; Wu, J. J.; Tolbert, S. H. *Synth. Met.* **2001**, *116*, 35.

68. Nguyen, T. Q.; Wu, J. J.; Tolbert, S. H.; Schwartz, B. J. *Adv. Mater.* **2001**, *13*, 609.

69. Smith, R. C.; Fischer, W. M.; Gin, D. L. *J. Am. Chem. Soc.* **1997**, *119*, 4092-4093.

70. Gin, D. L.; Smith, R.; Deng, H.; Leising, G. *Synth. Met.* **1999**, *101*, 52.

71. Markart, P.; Zojer, E.; Tasch, S.; Smith, R.; Gin, D. L.; Leising, G. *Synth. Met.* **1999**, *102*, 1155.

72. Zojer, E.; Markart, P.; List, E. J. W.; Graupner, W.; Smith, R.; Leising, G.; Shinar, J.; Gin, D. L. *Synth. Met.* **1999**, *102*, 1270.

73. List, E. J. W.; Markart, P.; Graupner, W.; Leising, G.; Partee, J.; Shinar, J.; Smith, R.; Gin, D. L. *Opt. Mater.* **1999**, *12*, 369.

74. Gadermaier, C.; List, E. J. W.; Markart, P.; Graupner, W.; Partee, J.; Shinar, J.; Smith, R.; Gin, D.; Leising, G. *Synth. Met.* **2000**, *111*, 523.

75. Gin, D. L.; Yonezawa, K. *Synth. Met.* **2001**, *121*, 1291.

76. Firouzi, A.; Schaefer, D. J.; Tolbert, S. H.; Stucky, G. D.; Chmelka, B. F. *J. Am. Chem. Soc.* **1997**, *119*, 9466-9477.

77. Tolbert, S. H.; Firouzi, A.; Stucky, G. D.; Chmelka, B. F. *Science* **1997**, *278*, 264-268.

78. Greenham, N. C.; Samuel, I. D. W.; Hayes, G. R.; Phillips, R. T.; Kessener, Y. A. R. R.; Moratti, S. C.; Holmes, A. B.; Friend, R. H. *Chem. Phys. Lett.* **1995**, *241*, 89-96.

79. Wagaman, M. W.; Grubbs, R. H. *Macromolecules* **1997**, *30*, 3978.

80. Lee, T. W.; Park, O. O.; Kim, J. J.; Hong, J. M.; Kim, Y. C. *Chem. Mater.* **2001**, *13*, 2217.

81. Lee, T. W.; Park, O. O.; Yoon, J.; Kim, J. J. *Synth. Met.* **2001**, *121*, 1737.

82. Lee, H. C.; Lee, T. W.; Park, O. O. *Opt. Mater.* **2003**, *21*, 187.

83. Lee, H. C.; Lee, T. W.; Lim, Y. T.; Park, O. O. *Appl. Clay Sci.* **2002**, *21*, 287.

84. Taylor, P. N.; O'Connell, M. J.; McNeill, L. A.; Hall, M. J.; Aplin, R. T.; Anderson, H. L. *Angew. Chem. Int. Ed. Engl.* **2000**, *39*, 608.

85. Craig, M. R.; Hutchings, M. G.; Claridge, T. D. W.; Anderson, H. L. *Angew. Chem. Int. Ed. Engl.* **2002**, *41*, 1769-1772.

86. Cacialli, F.; Wilson, J. S.; Michels, J. J.; Daniel, C.; Silva, C.; Friend, R. H.; Severin, N.; Samori, P.; Rabe, J. P.; O'Connell, M. J.; Taylor, P. N.; Anderson, H. L. *Nature Mater.* **2002**, *1*, 160-164.

CHAPTER 2 Characterization of Nanocomposite Materials

The chemical analysis of aperiodic structures at high spatial resolution is proving to be a central challenge of nanoscience. As new methods are devised to assemble materials into structures on the nanometre scale, it is becoming more important to show by means as direct as possible that the desired physical and chemical structures are obtained. With the advent of field-emission electron microscopes, the atomic force microscope (AFM) and the scanning-tunnelling microscope (STM), topographical characterization at nanometre resolution has become a relatively routine experiment. However, chemical analysis at the nanometre scale is still far from reaching the same level of simplicity, and there are instrumental limits on the achievable resolution.[1]

The development of characterization techniques for composite materials based on porous inorganic hosts was an ongoing challenge within our research group. The central goal was to establish the polymer distribution within the composite material on the nanometre scale.

Optical techniques for characterization are pushed to their present-day limit by confocal fluorescence microscopy, which is a widely used tool for establishing the distribution of fluorescent materials with 0.1 μm resolution in 3-D. This can be readily used for many conjugated polymers in optically transparent hosts. A recently developed technique, near-field scanning optical microscopy,[2] can be used to map fluorescence in 2-D with even higher resolution. But for work at resolution better than 10 nm, electron microscopy is used for

topographical and chemical analysis. This is introduced below and is followed by a review of high resolution chemical analysis techniques.

Two forms of electron microscopy are most relevant to current research in materials science: scanning electron microscopy (SEM) and transmission electron microscopy (TEM). SEM is a more widely used technique due to its ever-improving simplicity, while TEM is often necessary when details in the nanometre range are important.

2.1 Scanning Electron Microscopy

The SEM is a very versatile instrument for the characterization of surface topography and material composition.[3] An energetic beam of electrons (typically 1 to 30 kV) is rastered across the surface of the specimen, and an image is constructed by detecting electrons emitted from the surface. If an electron interacts elastically with an atomic nucleus in the sample and is returned out, it is said to be backscattered. These electrons provide some sensitivity to the atomic number of the sample but are emitted in relatively low yield. A backscattered electron detector may be used to obtain some elemental contrast in a sample but with limited resolution.

If an electron undergoes a number of inelastic processes in the sample before being re-emitted out, it is called a secondary electron. These are emitted in a yield approaching unity and are largely independent of material composition. The intensity of secondary electron emission observed at each point is modulated by the local sample structure, as more electrons can escape from protrusions than from depressions. This allows a topographical image to be formed. The secondary electron detector normally used in SEM presents a surface image with a point resolution of ~1.5 nm at accelerating voltages from 10 to 20 kV (Hitachi S-4700 field-emission SEM, UBC Electron Microscopy Lab). Lower accelerating voltages may be used to reduce charging effects and to increase surface detail, at the expense of resolution.

For insulating samples, a conductive coating must be applied to prevent charge build-up on the surface, as low-voltage imaging does not provide sufficient resolution. This is usually accomplished by sputtering a thin coating of gold-palladium onto the sample. This coating is adequate for most SEM work but begins to show some structure at higher magnifications (above 100,000×), which was the usual operating regime for this work. Other coating materials (platinum, chromium) are smoother and are more suitable for high resolution work but were not readily available for use at UBC.

In the SEM, the contrast between an inorganic host material and an organic guest is not very large, especially with a conductive coating on the surface. Some inferences may be made from changes in the geometry (e.g., complete filling of pores).

2.2 Transmission Electron Microscopy

In the TEM, electrons are transmitted through a very thin sample.[4] The contrast is provided by the ability of the sample to scatter electrons, which is largely a product of thickness and atomic number. The accelerating voltage (beam energy) is typically set at 200 kV for materials science, in order to observe thicker specimens, with some loss of contrast over operating at 80 kV (as used for biological samples).

In general, a TEM is required to investigate structures with detail below 5 - 10 nm. Sub-nanometre resolution is readily achievable on standard TEM instruments. The achievable information limit on a modern field-emission TEM at 200 kV is 0.12 nm (Tecnai F20 TEM, Nano-Imaging Facility, SFU). A TEM can also be operated in scanning mode (STEM), where it functions similarly to an SEM, but with a higher resolution and the choice of detecting transmitted electrons (bright-field imaging for unscattered electrons, dark-field imaging for strongly scattered electrons) or secondary electrons.

The large electron-beam energy causes damage to the sample over time. Porous silica and alumina films tend to be fairly sensitive to beam damage in the TEM, as has been observed for the mesoporous material MCM-41.[5,6] Organic materials are similarly sensitive.

Organic materials scatter electrons in the TEM only weakly, due to the low atomic number of carbon. The simplest approach to improving the contrast of organic materials is heavy-metal staining, which is widely used for biological specimens. The vinylic carbons in poly(1,4-phenylene vinylene) (PPV) and its derivatives are readily stained by osmium tetroxide. The phenyl group may also be stained by ruthenium tetroxide.[7] This should provide better contrast in the TEM because of the increased electron scattering by the heavy nuclei. However, in situations where the amount of polymer is limited, this may still not provide sufficient analytical contrast, and the use of more specialized techniques for chemical analysis is required.

2.2.1 TEM Sample Preparation

The central drawback of the TEM is the need for electron-transparent samples. Small particles may be investigated directly, but bulk samples must be thinned or sectioned to be observed. The useful thickness range is a function of the accelerating voltage and composition; for work at 200 kV, a thickness below 200 nm is usually required. While sample preparation techniques are well established, they are generally time-consuming.

The observation of porous films in the plan geometry, that is looking down the channels, is straightforward and not sensitive to film thickness, provided free-standing films can be prepared. The film cross-sections are more difficult to image, as they must be prepared in the form of thin sections less than 200 nm thick in order to be electron-transparent.

The preparation of these thin sections is not entirely trivial for hard materials. The conventional technique for cross-section preparation of such materials is dimpling and ion-

milling. Many samples are glued to form a sandwich structure, which is then sawed into 1 mm slices. A 3 mm disk is cut from this slice, ground to 100 μm thickness, and then dimpled in the centre until the sample is ~25 μm thick at the centre. The sample is then ion-milled using an argon ion beam until a small hole is formed. The cross-sections are finally observed in the TEM along the edges of the milled hole. This process is evidently tedious and suffers from artifacts introduced by the ion-milling process (amorphisation, preferential removal of elements).

The state-of-the-art in thin-section preparation involves the focused ion-beam (FIB) technique. It is executed inside an SEM with a beam of gallium ions: the sample is milled away at a precisely known location until the desired section is obtained. This approach is also prone to producing damage artifacts. For the duration of most of this work, there was no ready access to the proper instrument - only one existed in Canada outside of industrial research laboratories. In late 2002, a new FIB instrument was installed at SFU.

As a simple alternative, the small-angle cleavage (SAC) technique was developed by McCaffrey for routine cross-section preparation of thin films for TEM.[8-10] There are two major requirements for successful execution of the technique: a substrate that cleaves readily and a thin film (< 300 nm) with good adhesion to the substrate. The sample is cleaved at a shallow angle (< 30°) to form a sharp wedge (Figure 2.2). The last micrometre of the wedge near the tip is then sufficiently thin for observation in cross-section by TEM. With practice, SAC samples can be produced within half a day, which is substantially faster than the dimpling technique. However, the technique is less useful for films that are not homogeneous in the plane of the substrate, as the gradual change in thickness of the wedge makes it difficult to visualize films with additional structure in the depth of the cross-section. For such films, ultramicrotomy and focused-ion beam milling are more suitable approaches to thin section preparation. Nevertheless, the SAC technique is very useful for viewing cross-sections without artifacts from the sectioning process.

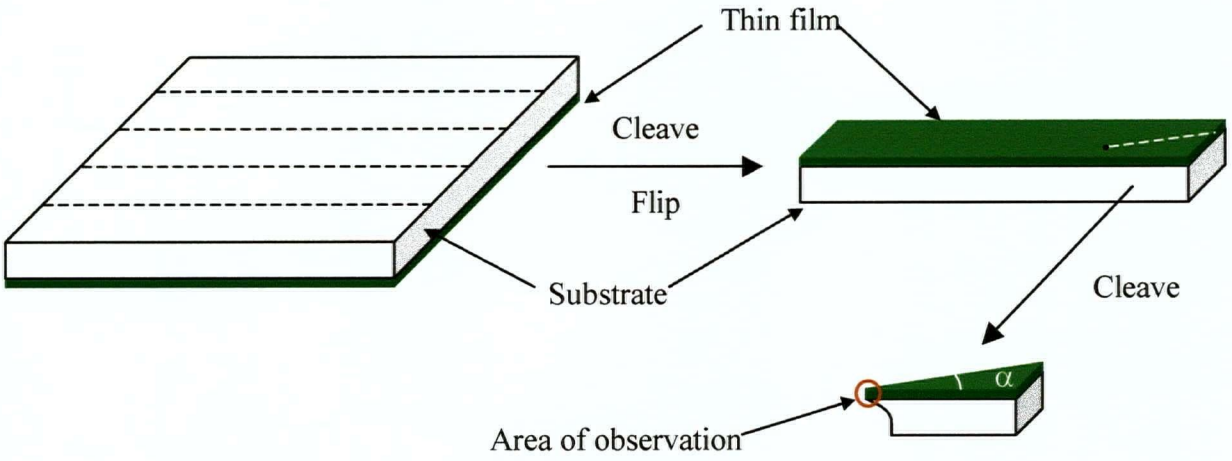

Figure 2.2 The small angle cleavage (SAC) technique applied to a thin film: the tip of the final specimen will often be thin enough over a sufficient length for TEM observation if $\alpha < 30°$.

Ultramicrotomy is commonly used to prepare cross-sections of biological specimens. The specimen is first embedded in epoxy resin, then trimmed with a razor blade or glass knife to form a truncated pyramid around the area of interest (Figure 2.1). After careful cleaning and washing to remove any small particles, the pyramid is sectioned from bottom to top using a

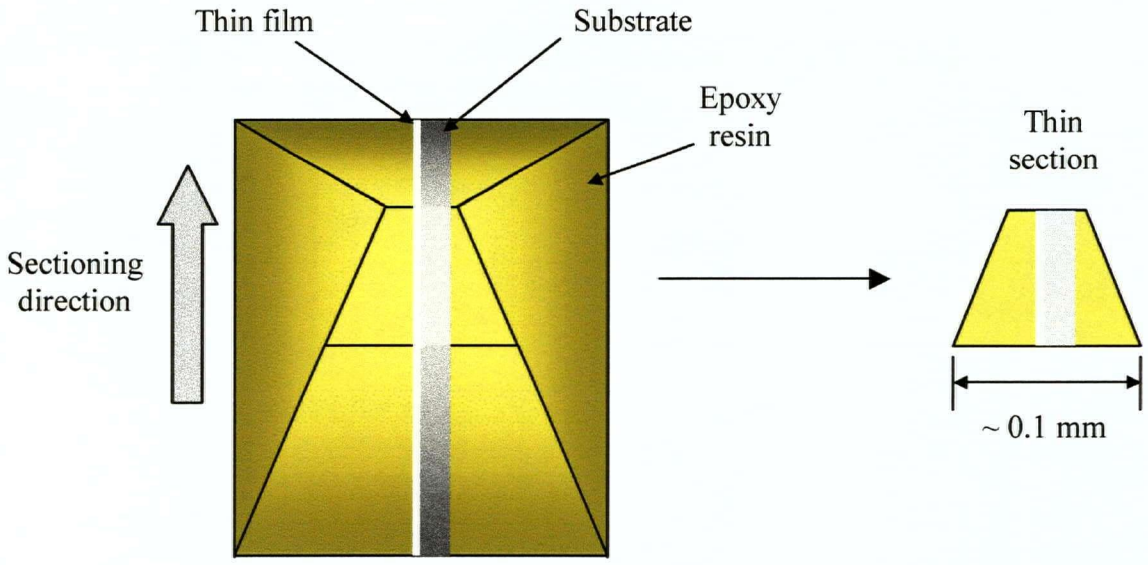

Figure 2.1 Truncated pyramid geometry of epoxy-embedded sample for sectioning by ultramicrotomy. The resulting sections float into a water bath where they are collected with TEM grids.

diamond knife; the resulting thin sections float into a water bath, where they may be collected using a TEM grid. The sections are typically 20 to 60 nm thick.

This technique is most readily applicable to soft materials, but in fact can be used to section even the hardest materials.[11,12] Cross-sections of self-assembled mesoporous silica films on mica and graphite were produced by ultramicrotomy.[13,14] Furneaux *et al.* successfully used ultramicrotomy to obtain thin sections of porous alumina films for TEM.[15]

2.3 High Resolution Chemical Analysis

The different approaches to spatially resolved chemical analysis are reviewed here, followed by a more detailed description of the technique that was used in this work, electron energy-loss spectroscopy (EELS) within the TEM. The STM, which can give chemical information at very high resolution, is not discussed here as it is not applicable to insulating materials. These and other emerging techniques, especially scanning probe techniques, are described in the proceedings of a recent workshop on nanoscale spectroscopy.[2]

Most of the techniques for chemical analysis rely on initially exciting inner-shell (core) electrons by an energetic beam of electrons or X-rays (Figure 2.3) and then detecting the results of the de-excitation process. The outer-shell electrons also provide less direct information for chemical analysis under certain circumstances. The spatial resolution is limited, in all cases, by the initial excitation volume. The resolution limits of the techniques discussed here are summarized in Table 2.1.

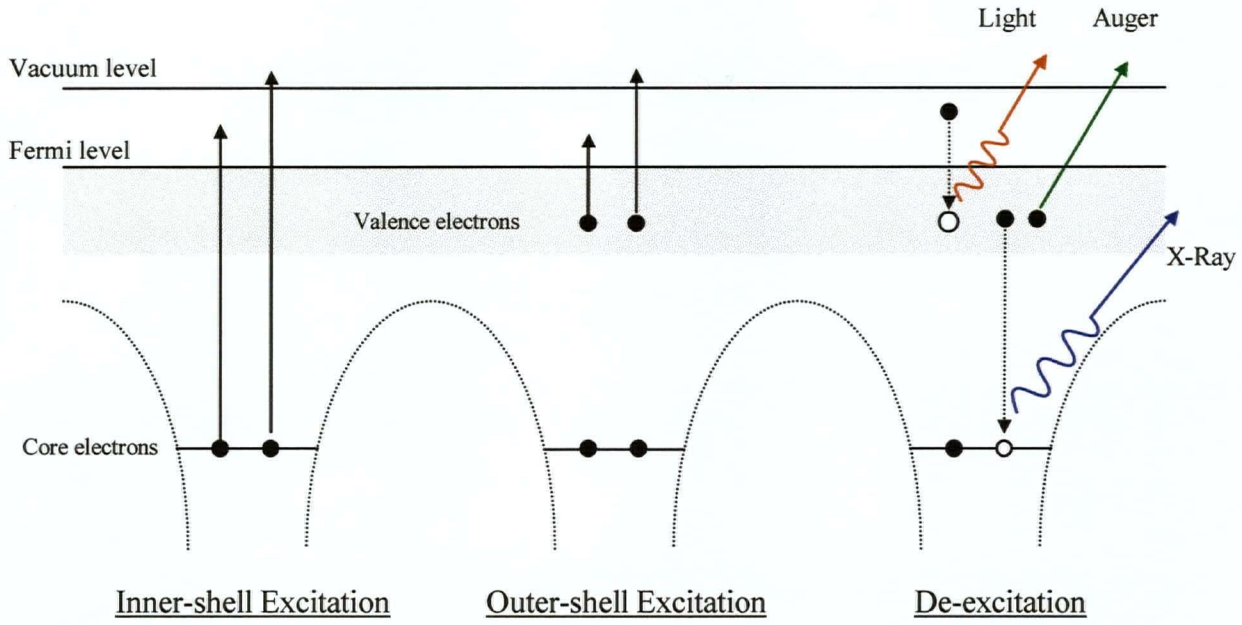

Figure 2.3 Electronic excitation and de-excitation mechanisms in a solid. (adapted from ref. 1)

Table 2.1 Current spatial resolution limits of chemical analysis techniques.

Technique	Sampling Depth (nm)	Lateral Resolution (nm)
X-ray photoelectron spectroscopy	~1.0	10^6 ($30^{\dagger}$)
Scanning Auger microscopy	~1.0	> 10
Energy-dispersive X-ray spectroscopy in SEM	1000	1000
Energy-dispersive X-ray spectroscopy in TEM	100	10
Electron energy-loss spectroscopy in TEM	100	1

† for a synchrotron X-ray source

2.3.1 X-Ray Photoelectron Spectroscopy

Monochromatic X-rays are used as the excitation source for X-ray photoelectron spectroscopy (XPS); these result in the emission of photoelectrons and Auger electrons from the sample. The kinetic energy of the ejected electrons is measured, yielding the core electron energies. The relative abundance of any element may be readily calculated, and some information on the chemical state of the element may also be obtained. Although the lateral resolution is limited by the beam diameter (~1 mm for conventional sources; ~30 nm for

synchrotron sources[16]), this technique is very surface-sensitive as a result of the limited mean free path of the generated photoelectron, which is on the order of 1 nm. However, the adsorption of atmospheric hydrocarbons on the surface can affect the analysis of carbon-containing samples. With the development of more refined X-ray optics, this technique may come to be very important for high resolution analysis, as it induces less sample damage than electron microscopy.[16]

2.3.2 Energy-Dispersive X-Ray Spectroscopy and Scanning Auger Microscopy

The electron beam within an SEM can be used as a highly focused source of excitation (down to ~1 nm diameter for a field emission source) for the generation of X-rays and Auger electrons. These are collected and analysed to form the basis for energy-dispersive X-ray (EDX) analysis and scanning Auger microscopy (SAM), respectively. In the case of bulk samples, the X-ray signal used for EDX originates from a relatively large domain surrounding the point excited by the electron beam, due to the penetration depth of the energetic electrons and the low absorption of X-rays. This large excitation volume effectively reduces the spatial resolution to 1 μm but also allows for a thin conductive film to be applied to the surface if the sample is insulating. On the other hand, only Auger electrons released near the surface can escape and be detected (as with photoelectrons), with the result of higher lateral resolution (~10 nm) than EDX but with the requirement that the sample be conductive (or very thin with a conductive backing) to avoid charging effects.

When coupled to a STEM, EDX may also be used to quantify the composition of thin film samples. Since the sample must be sufficiently thin to transmit electrons, the excitation volume for X-rays is greatly reduced and the lateral resolution is limited by scattering of the electron beam within the thin section, effectively reaching 10 nm. In practice, sufficient material

must also be present to obtain reasonable counting statistics, which limits the minimum sample thickness that may be used. Beam damage to the sample may also affect the results if a particular component is being removed at a higher rate.

2.3.3 Electron Energy-Loss Spectroscopy

Finally, the distribution of energy losses incurred by the transmitted electron beam in a TEM may also be measured to yield elemental composition. This approach belongs to a family of techniques described generally as electron energy-loss spectroscopy. Although it is limited to thin samples, it provides higher resolution (~1 nm) and sensitivity (as few as 1 to 10 atoms can be detected[1]) than all the techniques listed above (see Table 2.1). It is ideally suited for the analysis of nanocomposite materials and is described in more detail below.

2.4 General Principles of EELS

The standard reference for EELS in the TEM is the book by Egerton.[1] A more recent publication by Brydson[17] covers some new developments and focuses on the experimental aspects of EELS. In general, the interactions between a travelling electron and the components of a solid are termed scattering events (Figure 2.4). If the electron is scattered from an atomic nucleus, the process occurs without the electron losing any significant amount of energy. This elastic scattering can cause large deviations in the trajectory of the electron, to the extent where it may be backscattered out of the solid, or smaller deviations (e.g., diffraction for crystalline materials). Some electrons will also excite collective oscillations of the atoms in the solid (phonons); these occur at low energies in the meV range and are not distinguishable from the unscattered and elastically scattered electrons in the TEM (though they may be in other forms of

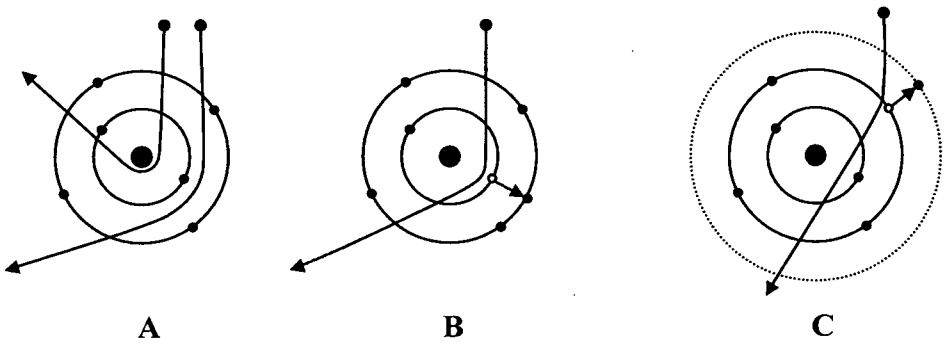

Figure 2.4 Geometry of (a) elastic, (b) inelastic, inner-shell and (c) inelastic, outer-shell scattering events involving an electron and a carbon atom. (adapted from ref. 1)

EELS with higher energy resolution). These electrons are detected by the spectrometer as the zero-loss peak, the width of which gives the energy resolution of the instrument. A typical loss spectrum is shown in Figure 2.5.

Inelastic scattering occurs when the electron interacts with either the inner-shell or outer-shell electrons of an atom (Figure 2.4). The scattering from inner-shell electrons produces an energy loss characteristic for each element, with a value typically between 50 and 2000 eV. In the loss spectrum, these appear as an ionization edge (e.g., at 284 eV for carbon 1s electrons) and are usually employed for elemental analysis. The fine structure of the ionization edge is also used to derive additional information about the chemical state of the element. There has been extensive work on modelling these edges,[1,18] but since they play no role in this work they are not discussed any further.

The excited state produced by inelastic scattering can also manifest itself as a collective excitation of the outer-shell electrons, generally referred to as a plasmon. On longer time scales, the energy of the plasmon is distributed over many electrons, but all the energy may be carried by a single electron on short time scales, which makes such excitations possible even in

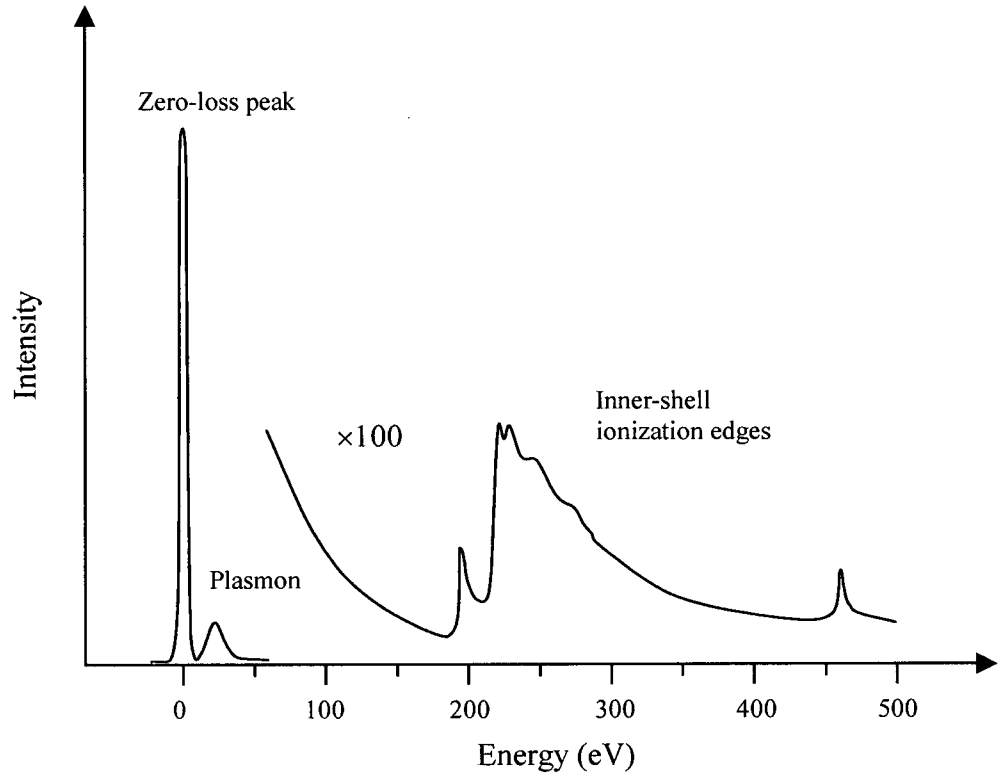

Figure 2.5 Principal features of an EEL spectrum. (adapted from ref. 17)

insulators.[1] Typically, plasmons involving both σ and π electrons appear between 5 and 50 eV for most materials. Aromatic organic materials also show a distinct π-π^* plasmon around 7 eV.

The outer-shell electrons that are excited in these bulk plasmons are difficult to model from first principles, especially in non-metals. They may be more readily treated by considering the response of the whole solid to the travelling electron, which is very similar to the response to a passing photon. The latter is given by the complex dielectric function $\varepsilon(\omega)$. If the sample thickness is known accurately, the low-loss spectrum may be used to calculate $\varepsilon(\omega)$ for the material and compare it to data from optical measurements.[19] The correlation between the two is sufficient to allow the use of either one to predict the other, and as such EELS complements and extends optical techniques for determining $\varepsilon(\omega)$.

The bulk plasmons occur within the bulk of the material and must be distinguished from excitations that appear at interfaces, which are termed surface plasmons. Geometries where the electron beam interacts extensively with the surface of the material can lead to important surface plasmon effects, typically below 20 eV in energy. Together, the bulk and surface plasmons dominate the low-loss spectrum (< 50 eV). Plasmons of both types can be excited from substantial distances from the sample: up to 8.0 nm for the bulk plasmon and over 12 nm for surface plasmons.[20] The fall-off is however exponential and reasonable counting statistics are obtained up to half these distances.

The intensity of the loss peaks relative to the total spectrum area is a function of sample thickness. Furthermore, both types of plasmons can lead to multiple scattering events per electron (plural scattering), leading to the appearance of multiple peaks in the loss spectrum with a Poisson distribution. In this case, the single scattering distribution can be recovered by deconvoluting the spectrum (see chapter 5).

The beam energies typically used in TEM lead to electrons with relativistic speeds, which may also lose energy through the Cherenkov effect. This loss mode proved to be very important for the samples that were investigated here and is discussed in more detail in chapter 6.

2.5 EELS Instrumentation

The schematic of a modern TEM with EELS capabilities is shown in Figure 2.6. The type of electron source determines the brightness, energy spread and STEM probe size; a field-emission source is usually employed for materials science work. The beam is accelerated to the desired energy (usually 200 kV for materials science), and magnetic lenses are used to form the probe. In TEM mode, the probe is diffuse and illuminates a large part of the sample; the convergence semi-angle α is also small, which is equivalent to nearly parallel illumination. The

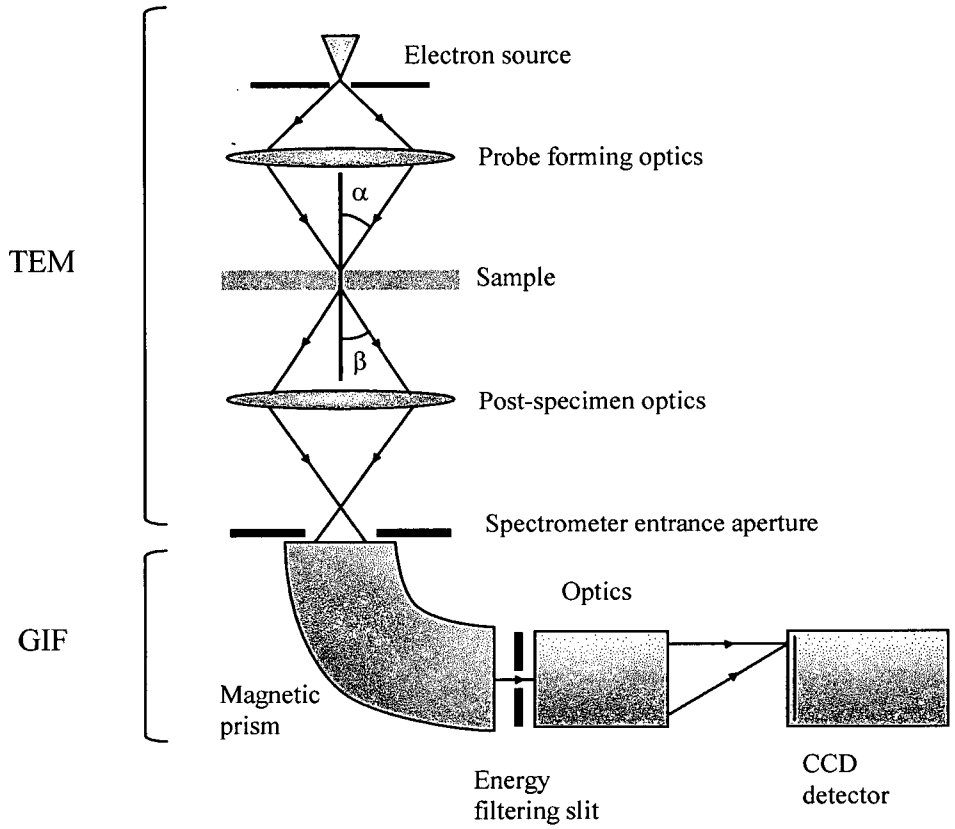

Figure 2.6 Schematic of post-column Gatan Imaging Filter on a TEM.

transmitted electrons are transferred by further magnetic lenses to the Gatan imaging filter (GIF).[21] The GIF consists of a magnetic prism spectrometer coupled to a charge-coupled device (CCD) detector by multipole magnetic lenses. In imaging mode, the TEM image is formed on the CCD; if energy filtering is required, a slit is inserted after the spectrometer to select electrons with the desired energy loss. In spectroscopy mode, the loss spectrum is projected on the CCD.

In STEM mode, the probe is focused to a spot that can be as small as 0.2 nm in diameter. This strong focusing entails a larger α (>10 mrad). The image is recorded using a dark-field detector (which detects electrons that are strongly scattered by the sample), thereby allowing the main electron beam to continue into the GIF where the loss spectrum is measured. Thus it is straightforward to perform EELS experiments with the microscope in STEM mode: the electron

probe is scanned across the sample to produce the image; the probe may then be reliably positioned in the location of interest on the sample to record a loss spectrum.

2.6 Approaches to EELS Data Acquisition

The optimal approach to chemical analysis by EELS depends on the complexity of the loss spectrum. In TEM mode, the energy of the image-forming electron beam may be filtered using a slit of set width (energy-filtered TEM, EFTEM). Elemental distributions may be imaged directly by filtering on the appropriate spectral feature (Figure 2.7). This approach is generally useful when a limited number of well-understood components need to be mapped over a large area. The energy resolution is set by the slit width and is usually 1 eV or greater. The spatial resolution is essentially the same as the TEM, but the magnification is limited by the presence of the slit to ~100,000×.

In STEM mode, loss spectra may be acquired at specific points, lines or areas (Figure 2.7). This allows detailed examination of specific areas on the sample. The spatial resolution is limited to ~1 nm by the electron probe size and scattering within the sample; the effect of the latter may be limited by restricting the collection angle. The energy resolution in STEM mode is determined by the energy spread of the electron beam. With a field-emission electron source, this spread is about 0.6 to 0.9 eV, depending on the current output of the electron source.

The process of acquiring a complete loss spectrum for each point in an area of interest is called spectrum imaging. This allows detailed processing of the spectra over the whole image and is useful in cases where it is not possible to separate the requisite spectral information by EFTEM. However, this process can be fairly time-consuming.

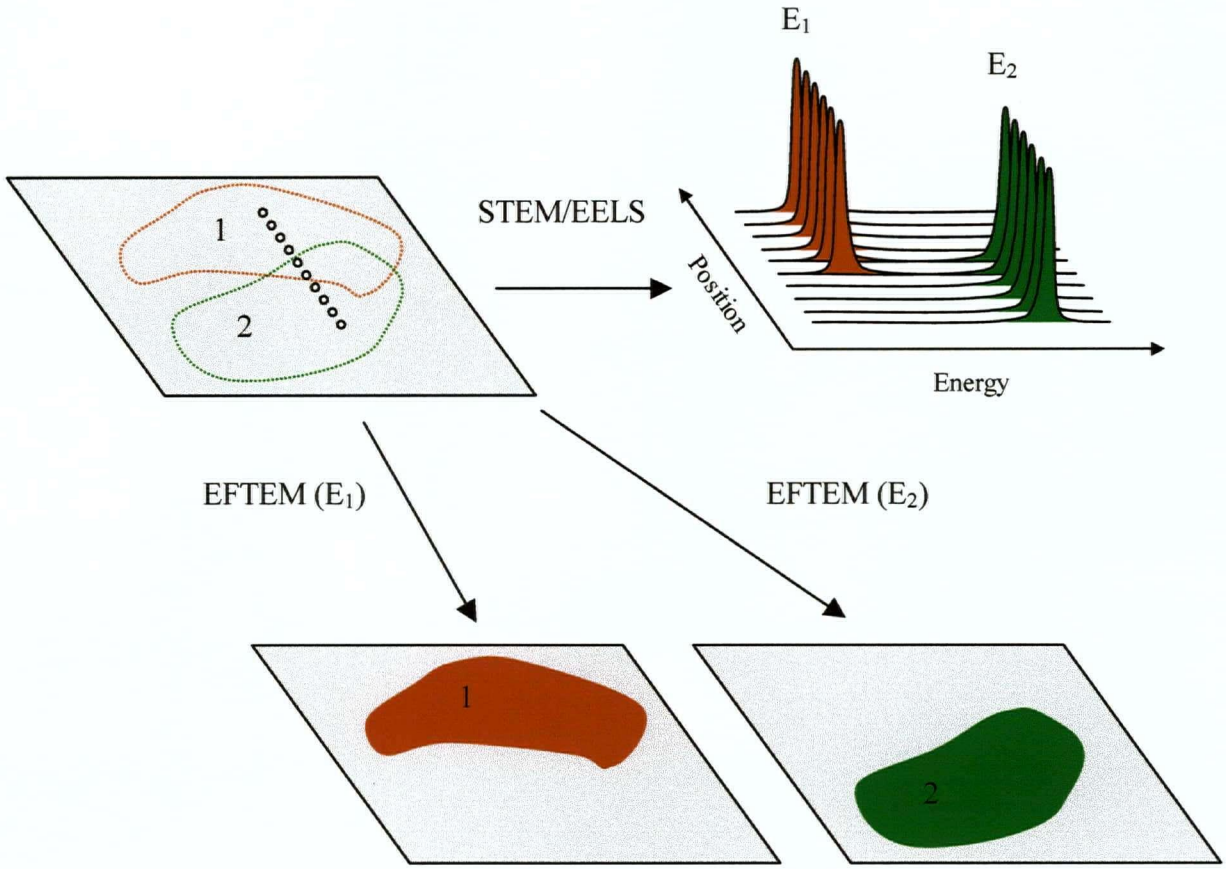

Figure 2.7 Illustration of chemical analysis of a two-component sample by STEM/EELS over a set of points and EFTEM over the whole image.

2.7 Quantitative Analysis of EELS Spectra

EELS and EFTEM are most commonly used to provide qualitative analysis of material composition. Quantification of the elemental or phase composition is less straightforward. An accurate thickness map must be first generated, to correct for the thickness dependence of the losses. Plural scattering effects must be also be eliminated. The scattering cross-section of each component, at a specific ionization edge or plasmon, must be determined through calculation or reference samples. A complete discussion of the quantification process is provided by Egerton.[1]

The focus of this work was on the qualitative level and no attempts were made to quantify material composition by these techniques.

2.8 Application of EELS to Organic Materials

Both EELS and EFTEM have been used to investigate many organic materials. In many cases, special precautions are taken to limit the radiation damage to the samples, e.g., by using a diffuse beam, collecting over many different areas, and keeping the sample at cryogenic temperatures. There is also still debate over whether a diffuse beam (i.e., EFTEM) or a focused probe (i.e., STEM) causes the least amount of damage to organic materials.[22] It has become evident that each material must be studied separately to understand its beam stability.

The first important study of organic materials by EELS, by Isaacson, investigated thin films of the nucleic acid bases.[23] The complex dielectric function $\varepsilon(\omega)$ was obtained with a resolution of ~0.25 eV. The derived absorption coefficient showed very good agreement with UV absorption data, provided that the electron dose was carefully limited to minimize damage. More recently, biological cell-staining chromophores have also been mapped at high resolution by filtering on the low-loss peaks of the chromophores.[24] The resolution limit of this technique was estimated to be 1.6 nm, based on the edge sharpness of larger structures.[25]

Carbon nanotubes have been extensively studied by EELS,[26-28] as they are fairly stable to the beam. The low-loss spectra show the expected π plasmon around 4 to 6 eV and the bulk plasmon near 23 eV.

EFTEM has proved to be a very useful tool for the study of polymer blends.[7,29] The ionization edges of minor component elements (nitrogen for polyamides, oxygen for poly(methyl methacrylate), sulfur for poly(phenylene sulfide)) may be used with some effectiveness to determine polymer distributions.[30,31] But certain phases can show trace oxygen contamination (e.g., polybutadiene) that complicates the identification process. Polymers with aromatic groups, such as polystyrene, can be readily identified in a blend due to the distinctive π-π^* plasmon at 7 eV.[32] The polymers may also be stained in various ways to increase contrast; this comes with the

advantage of phase stabilization by the cross-linking of chains and the disadvantage of altered chemical states and possible shrinkage.[32]

These reports clearly indicate that conjugated polymers can be readily distinguished with EELS and EFTEM by the distinctive π plasmon of aromatic rings; analysis using the carbon K-edge is also possible when there is sufficient material present. The analysis of the low-loss spectrum requires accurate removal of the zero-loss peak; this is discussed in more detail in chapter 5.

2.9 Conclusion

EELS and EFTEM are both highly suited for high resolution characterization of nanostructured conjugated polymers. This application is successfully demonstrated in chapter 3 on a conjugated polymer/mesoporous silica composite, and less successfully in chapters 5 and 7 on a conjugated polymer/porous alumina composite. These latter results showed how the sample geometry and relativistic effects can play a large role in the low-loss spectrum, making chemical analysis less straightforward.

References

1. Egerton, R. F. *Electron energy-loss spectroscopy in the electron microscope*; 2nd ed.; Plenum Press: New York, 1996.

2. Watanabe, Y.; Heun, S.; Salviati, G.; Yamamoto, N., Eds. *Nanoscale spectroscopy and its applications to semiconductor research;* Springer: Berlin, 2000

3. Goldstein, J. I. *Scanning electron microscopy and X-ray microanalysis*; 3rd ed.; Kluwer Academic/Plenum Publishers: New York, 2003.

4. Fultz, B. *Transmission electron microscopy and diffractometry of materials*; Springer: New York, 2001.

5. Ozkaya, D.; Thomas, J. M.; Shephard, D. S.; Maschmeyer, T.; Johnson, B. F. G.; Sankar, G.; Oldroyd, R. *Inst. Phys. Conf. Ser.* **1997**, *153*, 403.

6. Blanford, C. F.; Carter, C. B. *Microsc. Microanal.* **2003**, *9*, 245.

7. Correa, C. A.; Hage, E. *Polymer* **1999**, *40*, 2171.

8. McCaffrey, J. P. *Ultramicroscopy* **1991**, *38*, 149.

9. Walck, S. D.; McCaffrey, J. P. *Thin Solid Films* **1997**, *308*, 399.

10. Suder, S.; Faunce, C. A.; Donnelly, S. E. *Thin Solid Films* **1997**, *304*, 157.

11. Malis, T. F.; Steele, D. *Ultramicrotomy for materials science*; Specimen preparation for Transmission Electron Microscopy of Materials II; Materials Research Society: Pittsburgh, PA, U.S.A., 1990, p. 3.

12. Quintana, C. *Micron* **1997**, *28*, 217.

13. Yang, H.; Kuperman, A.; Coombs, N.; Mamicheafara, S.; Ozin, G. A. *Nature* **1996**, *379*, 703.

14. Yang, H.; Coombs, N.; Sokolov, I.; Ozin, G. A. *J. Mater. Chem.* **1997**, *7*, 1285.

15. Furneaux, R. C.; Thompson, G. E.; Wood, G. C. *Corros. Sci.* **1978**, *18*, 853.

16. Spence, J. C. H.; Howells, M. R. *Ultramicroscopy* **2002**, *93*, 213.

17. Brydson, R. *Electron Energy Loss Spectroscopy*; BIOS, in association with the Royal Microscopy Society: Oxford, 2001; Vol. 48.

18. Egerton, R. F.; Malac, M. *Ultramicroscopy* **2002**, *92*, 47.

19. Daniels, J.; Festenberg, C. v.; Raether, H.; Zeppenfeld, K. *Springer Tracts Mod. Phys.* **1970**, *54*, 78.

20. Muller, D. A.; Silcox, J. *Ultramicroscopy* **1995**, *59*, 195.

21. Gatan; Pleasanton, CA, U.S.A. (www.gatan.com).

22. Varlot, K.; Martin, J. M.; Quet, C. *Micron* **2001**, *32*, 371.

23. Isaacson, M. *J. Chem. Phys.* **1972**, *56*, 1803.

24. Ottensmeyer, F. P.; Davis, J. A.; Heng, Y. M.; Barfels, M. M. G. *Microbeam Analysis 2000;* Institute of Physics Conference Series; Institute of Physics Publishing; Bristol; no. Number; p. 181.

25. Barfels, M. M. G.; Jiang, X. G.; Heng, Y. M.; Arsenault, A. L.; Ottensmeyer, F. P. *Micron* **1998**, *29*, 97.

26. Kuzuo, R.; Terauchi, M.; Tanaka, M. *Jpn. J. Appl. Phys.* **1992**, *31*, L1484.

27. Bursill, L. A.; Stadelmann, P. A.; Peng, J. l.; S., P. *Phys. Rev. B* **1994**, *49*, 2882.

28. Stephan, O.; Kociak, M.; Henrard, L.; Suenaga, K.; Gloter, A.; Tence, M.; Sandre, E.; Colliex, C. *J. Electron. Spectrosc. Relat. Phenom.* **2001**, *114*, 209.

29. Du Chesne, A. *Macromol. Chem. Phys.* **1999**, *200*, 1813.

30. Horiuchi, S.; Yase, K.; Kitano, T.; Higashida, N.; Ougizawa, T. *Polym. J.* **1997**, *29*, 380.

31. Horiuchi, S.; Ishii, Y. *Polym. J.* **2000**, *32*, 339.

32. Varlot, K.; Martin, J. M.; Quet, C. *Polymer* **2000**, *41*, 4599.

CHAPTER 3 A PPV/MCM-41 Composite Material

Many of the host properties desired for optimal conjugated polymer encapsulation can be found in self-assembled porous inorganic materials. These materials have been of longstanding scientific and industrial interest, due to their large internal surface area, large sorption capacity, thermal stability and catalytic activity towards small molecules.[1] More recently, as instruments for structural and chemical analysis on the nanometre scale have become commonplace, porous materials have been investigated as templates for novel nanostructured materials. A brief overview of the properties and applications of self-assembled inorganic porous materials is given here, with an emphasis on the mesoporous material MCM-41.

MCM-41, in its pure silica form, possesses many of the properties of an ideal host for conjugated polymers: it has narrow and aligned channels, with optically transparent and electrically insulating walls. This made it attractive to us for an initial study on polymer/host composite material synthesis and characterization. The literature already contained important work on the synthesis of polymer/MCM-41 composite materials, in particular with non-luminescent conjugated polymers. The preparation and characterization of a new composite material involving MCM-41 as a host for the luminescent conjugated polymer poly(1,4-phenylene vinylene) (PPV, Figure 3.1) is described in this chapter.

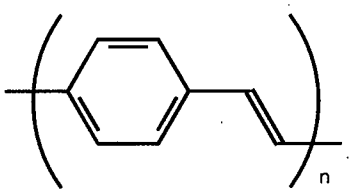

Figure 3.1 Chemical structure of poly(1,4-phenylene vinylene) (PPV).

3.1 Ordered Porous Host Materials

Porous materials are categorized according to their pore size into three classes: microporous, mesoporous and macroporous (Table 3.1). For the purpose of polymer encapsulation and orientation, the materials of interest would have an ordered pore structure with a pore diameter being near the boundary between the microporous and mesoporous classes (~2 nm).

Table 3.1 IUPAC classification of porous materials by pore size.[1]

Pore Diameter	Designation
< 2 nm	microporous
2 – 50 nm	mesoporous
> 50 nm	macroporous

3.1.1 Zeolites

The major class of ordered microporous materials is the zeolite family.[1] Zeolites are crystalline aluminosilicates possessing a wide variety of pore structures, including one, two and three dimensional pore networks (Figure 3.2).[2] A number of naturally occurring zeolites are known but a large number of synthetic zeolites have been discovered since the 1940's. The synthesis usually consists of hydrothermal crystallization of a reactive gel at elevated temperature in a sealed vessel.[3] The inorganic zeolite framework condenses into a structure determined by the templating (or structure-directing) agents, which can include water molecules,

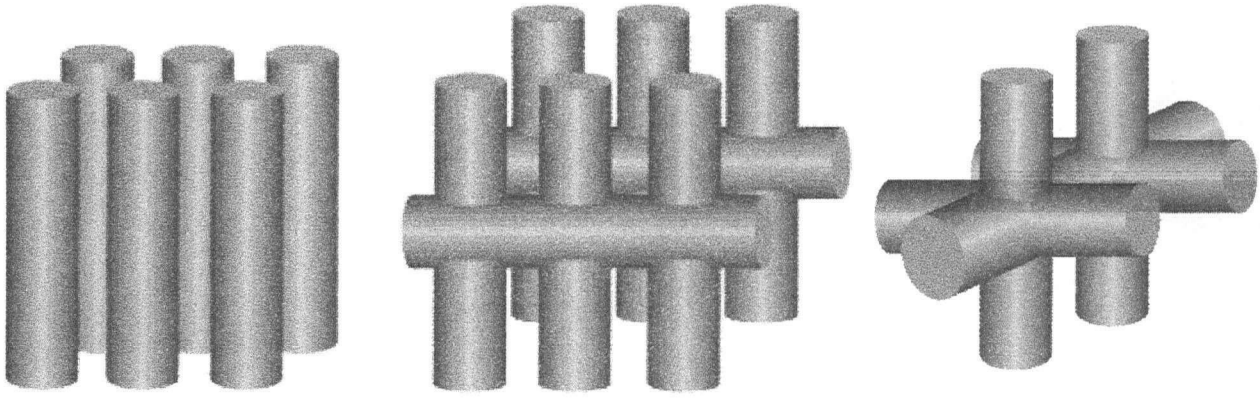

Figure 3.2 Examples of pore topologies with (a) 1-D, (b) 2-D and (c) 3-D connectivity.

organic cations and salts. Following the synthesis, the trapped templating agent can be removed by calcination or ion-exchange to expose the pore structure. The crystalline nature of zeolites allows very precise structural characterization using X-ray diffraction and solid-state nuclear magnetic resonance. The well-defined structure also leads to high selectivity in catalytic reactions.

The largest pore size reported to date in zeolites is on the order of 1.2 nm in diameter.[4] These zeolites can accommodate smaller polymers (e.g. polystyrene[5]) but not larger polymers (in particular conjugated polymers with solubilizing side-chains). A further complication arises from the small crystallite size exhibited by zeolites: the preparation of continuous thin films is not readily possible, although recent results in this area appear promising.[6] For these reasons, mesoporous materials are more useful as general hosts for conjugated polymers.

3.1.2 Mesoporous Materials

Mesoporous host materials are desirable for many applications, but were not available with well-defined pore structures until 1992, when Beck *et al.* reported the discovery of the M41S family of mesoporous aluminosilicate materials.[7,8] Whereas zeolites are templated by

small organic molecules, M41S materials were shown to be templated by liquid crystalline phases formed by straight-chain surfactants (Figure 3.3). Of particular interest in this family was the siliceous material MCM-41, which shows uniform 1-D channels packed in a 2-D hexagonal array (Figure 3.4). This simultaneously endows the material with a large surface area (1000 m^2 g^{-1}, almost all internal) and a large pore volume (0.8 cm^3 g^{-1}). The straight channels are ideal for polymer guest accommodation, though 180° defects in channel direction are possible. The pore walls usually consist of silica but other oxides can be readily incorporated into the framework This general approach to templating has since been applied to the synthesis of many new porous materials.[9]

The synthesis of MCM-41 proceeds from a mixture of water, surfactant, silica source and an acid or base catalyst; this forms a gel that is then heated in a sealed container. The spacing of the hexagonal phase can be readily altered by the choice of surfactant chain length and the addition of organic swelling agents.[8] Variations on the silica source,[11] pH of the mixture,[12], counter-ions[8,13] and reaction temperature[14] also affect the final structure. Thus pore diameters from 1.5 to 10 nm may be obtained; recent developments with polymeric templating agents have

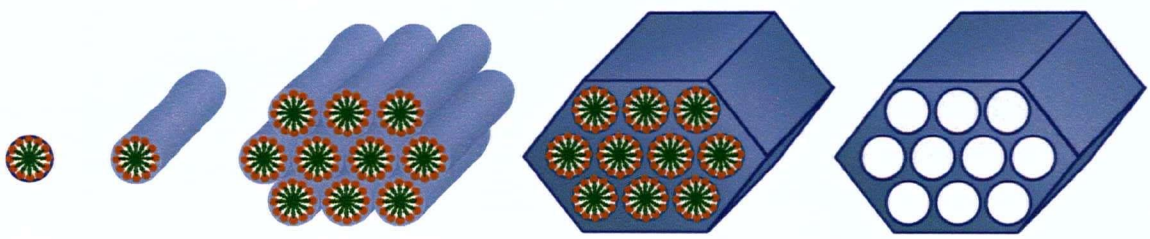

Figure 3.3 Stages in the formation of MCM-41: (a) surfactant micelle with the hydrophobic chains in the center and the polar head groups lining the outside, (b) cylindrical surfactant micelle, (c) hexagonal array formed cooperatively by surfactant micelles and silicate species, (d) condensed material (as-made MCM-41), (e) calcined material. (adapted from ref. [10])

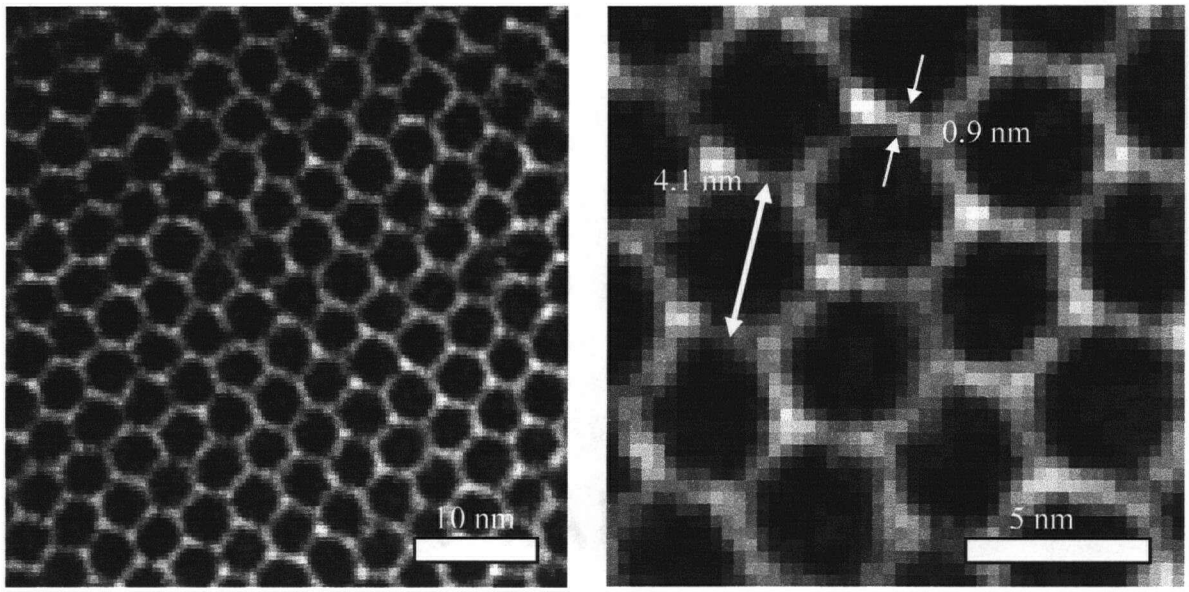

Figure 3.4 Transmission electron micrograph of MCM-41 material obtained using $C_{16}H_{33}(CH_3)_3NCl$ surfactant, showing hexagonal lattice spacing and wall thickness. (courtesy of G. Botton, CANMET/Natural Resources Canada)

extended this range to 50 nm.[15,16]

At the completion of the synthesis, the organic templating agent is normally removed by calcination, a process that also induces further condensation of the silica framework through dehydration. Solvent extraction[17] and supercritical fluid extraction[18] have also been shown to be effective in removing the templating agents. The final form of the material is then a powder with a typical particle size of 1 μm. The formation of MCM-41 thin films has also been extensively investigated; it is discussed in chapter 4.

The high degree of order in the M41S family of materials derives from the cooperative arrangement of the cylindrical surfactant micelles and the silicate ions in the liquid crystalline phase. This long-range order in the packing of the channels can be observed by X-ray diffraction. However, the silica framework itself is amorphous and microporous, and its inner surface has many slightly different chemical sites. Thus MCM-41 is referred as a zeolitic material to reflect that is an aluminosilicate material with only long-range ordering. The loss of

crystallinity, when compared to the zeolites, makes characterisation more difficult; this is offset, in the context of guest incorporation, by the benefits of tunable pore diameters.

Mesoporous silica-based materials may be readily modified since there are many accessible surface hydroxy groups: it has been found that 26-30% of all Si atoms in MCM-41 bear a surface hydroxy group.[19] The surface derivatization can proceed by well-developed silane chemistry.[8,20] Additional functionality can be achieved by substituting other elements into the framework,[21] and using organically-modified framework sources.[22]

This flexibility and the large internal surface area make MCM-41 an attractive host material, and the creation of composite materials based on MCM-41 has been reviewed recently.[22,23] In many studies, it has not always been evident that MCM-41 provides any substantial advantage over disordered porous materials, except possibly in its somewhat larger specific surface area. However, the well-defined channels are evidently necessary for the role of template for nanometre-scale wires and ordered encapsulation.

3.2 Characterization of MCM-41 Materials

The characterization techniques described in chapter 2 are directly applicable to MCM-41, especially high resolution transmission electron microscopy (TEM), electron energy-loss spectroscopy (EELS) and energy-filtered transmission electron microscopy (EFTEM), which allow local chemical characterization. A number of other techniques are used to measure material-averaged properties.

While there is general agreement on the formation mechanism for MCM-41, there is widespread disagreement on its exact structure. This seems to be due to the fact that the mesoporous 2-D hexagonal phase can be readily made under a variety of different conditions using different starting materials, and the exact characterization of the wall structure is difficult.

3.2.1 Diffraction Techniques

Diffraction is used to identify the presence of an ordered phase. The interplanar spacing d_{hkl} associated with a plane identified by the Miller indices *hkl* must satisfy the Bragg condition:

$$2d_{hkl}\sin\theta = n\lambda,\ n = 1,2,3,\ldots \qquad \text{(Eq. 3.1)}$$

For a hexagonal system, diffraction cannot be observed between planes when l is odd, or $(h + 2k) = 3n$, where n is an integer. However, $l = 0$ for a 2-D system, so peaks are expected for all the planes (100), (110), (200), (210), etc. The 2-D interplanar spacing d_{hk0} is related to the lattice constant as:

$$d_{hk0} = \frac{a}{\sqrt{\frac{4}{3}(h^2 + hk + k^2)}} \qquad \text{(Eq. 3.2)}$$

Powder X-ray diffraction is routinely used to characterize MCM-41 materials. Neutron scattering has also been used to investigate the pore structure in more detail.[24,25] While X-ray powder diffraction data is usually plotted against diffraction angle (2θ), neutron scattering data is presented as a function of the magnitude of the scattering vector, Q:

$$Q = \frac{4\pi\sin\theta}{\lambda} \qquad \text{(Eq. 3.3)}$$

Diffraction techniques may be used to investigate the presence of molecular guests within the channels of MCM-41 if there is contrast matching between the guest and the host. In the case of X-ray diffraction, sufficient electron density to match the pore walls is obtained for halogenated organic compounds.[26] For neutron scattering, contrast matching has been reported for 59% deuterated benzene in MCM-41.[27] Therefore, not all guests can be readily detected using diffraction techniques.

3.2.2 Physisorption

Physisorption is widely used to characterize the surface and pore structure of mesporous materials.[28] Adsorbates of different size and chemical functionality are used to probe the structure and reactivity of the material surface. Microporosity is generally probed using argon while mesoporosity is investigated with nitrogen. The nitrogen adsorption isotherm can be separated into three regimes: (1) micropore filling and monolayer formation, (2) multilayer formation, and (3) capillary condensation and further superficial adsorption (Figure 3.5). Regime (2) yields the total surface area of the sample, which is usually determined using the Brunauer-

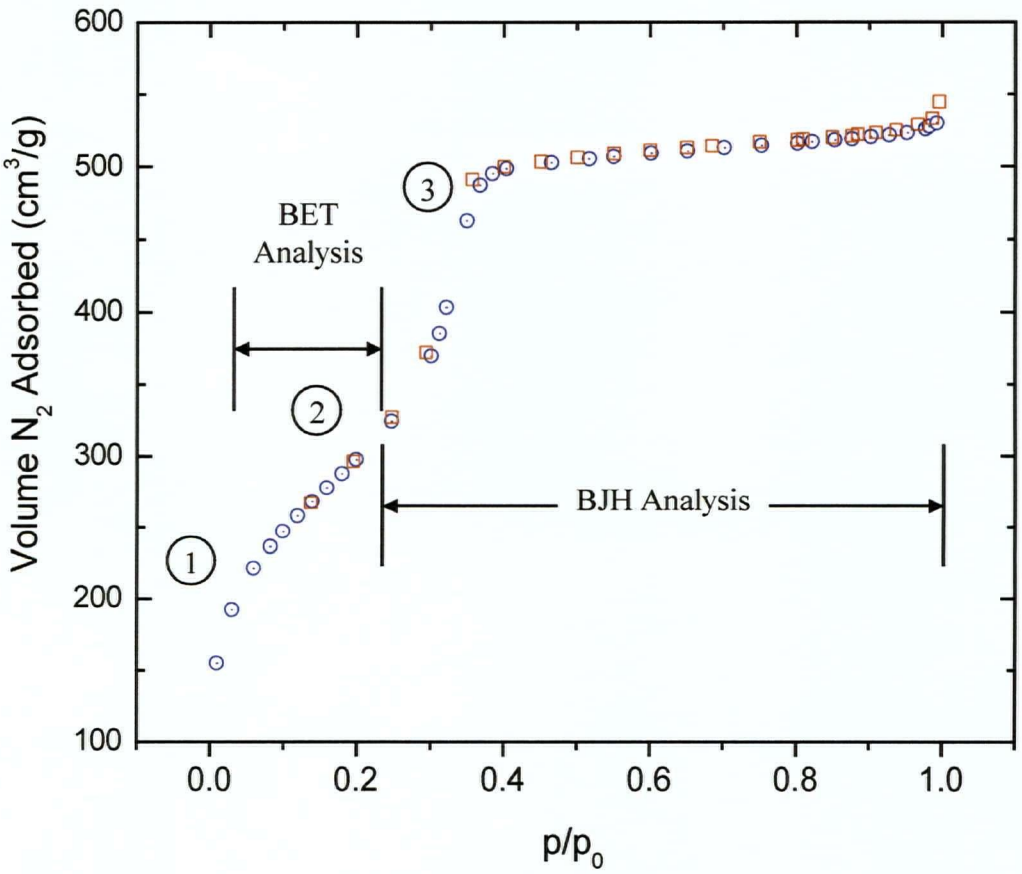

Figure 3.5 Nitrogen (○) adsorption and (□) desorption isotherms for MCM-41. The lack of hysteresis is characteristic of MCM-41 materials. The points used for total surface area (BET) and pore size distribution (BJH) analysis are indicated.

Emmett-Teller (BET) approach.[29] Regime (3) is usually analysed to determine the pore size distribution, which is the most important and also most debated property of mesoporous materials.

The classic determination of pore size distributions from adsorption isotherms is that of Barrett, Joyner and Halenda (BJH analysis);[30] recently more sophisticated approaches have been shown to yield better absolute agreement with other techniques for determining size distributions.[31,32] In the BJH approach, the thickness of the adsorbed nitrogen layer for a given relative pressure is given by the Harkins-Jura equation[33] with the following empirical parameters calibrated for MCM-41 materials: [34]

$$t\left(\frac{p}{p_0}\right) = 0.1\left[\frac{60.65}{0.03071 - \log\frac{p}{p_0}}\right]^{0.3968} + 0.3\,nm \qquad \text{(Eq. 3.4)}$$

However, there is no single unambiguous technique for measuring this distribution for mesoporous materials. The variations in the structure of MCM-41 due to differing synthesis conditions make it difficult to compare results between different studies in the literature, and lead to contradictory conclusions about the pore structure.[16,24,35,36] Nevertheless, MCM-41 behaves as an ideal adsorbent and can be used as a reference material.[34] In this work, BJH analysis is used to quantify the shift in the capillary condensation point in the nitrogen adsorption isotherm.

3.2.3 Other Techniques

Thermogravimetric analysis (TGA) is used to reveal the organic content of composite materials based on MCM-41. The host itself shows no mass loss up to 1000 °C. The thermal degradation processes for an organic material occur at specific temperatures and this may be

used to determine the mass content of specific organic components in the composite. The derivative of the TGA data is used to emphasize the presence of different degradation processes, and these can be fitted satisfactorily by Gaussian functions. This allows the mass content of each process to be determined more accurately.

Fourier-transform infrared spectroscopy (FT-IR) can be used to identify the organic components through their characteristic molecular vibrations, as the silica matrix is mostly transparent to infrared radiation.

3.3 Polymerization within MCM-41

Reports on polymer inclusion in MCM-41 appeared in the mid 1990's, involving both conjugated and insulating polymers. *In situ* polymerization within the channels of MCM-41 was reported initially by Wu and Bein.[37] Oxidative polymerization of aniline was achieved by first condensing the monomer from the vapour phase into the host channels. The loaded host was then soaked in an aqueous solution of oxidant, which produced encapsulated polymer chains. Acrylonitrile was polymerized similarly, using instead a solution of radical initiator.[38] Unger *et al.* prepared other free-radical initiated polymers in MCM-41: polystyrene, poly(methyl methacrylate) and polyvinylacetate.[39] The monomers were loaded into MCM-41 through vapour exchange, and the gas-phase radical initiator was subsequently diffused into the loaded MCM-41.

3.3.1 PPV in MCM-41

The introduction of PPV into MCM-41 must also proceed through *in situ* synthesis because of the insoluble and infusible nature of the polymer. The polymerization of PPV can be

carried out by numerous routes,[40] the simplest being a base-initiated condensation known as the Gilch route[41] (Figure 3.6). However, this route was not exploitable within the MCM-41 host: while the monomer could be readily loaded into MCM-41 through sublimation, the subsequent introduction of a base of sufficient strength was not possible. Aqueous bases attacked and dissolved the host, and non-aqueous bases solubilized the monomer and extracted it from the pores before polymerization could occur. Other polymerization routes were investigated and an elegant solution to this problem was found through the work of Kumar *et al.*,[42] who had prepared PPV within the pores of Vycor, a disordered porous glass. This approach used a more reactive monomer, xylylene bis(tetrahydrothiophenium chloride), which could be polymerized by deprotonated surface hydroxy groups.

In similar fashion, MCM-41 was converted to a basic form by deprotonating its surface hydroxy groups with a non-aqueous base (tetrabutylammonium hydroxide (TBAOH) in methanol) and isolated. This activated form of MCM-41 thus contained the initiating base within its channels. Polymer confinement occured through the rapid polymerization of the monomers within the host channels (Figure 3.7).

The key evidence to each step in this process is based on FT-IR spectroscopy, TGA, nitrogen physisorption, EELS and EFTEM. X-ray and neutron diffraction experiments provided no additional information on the composite materials.

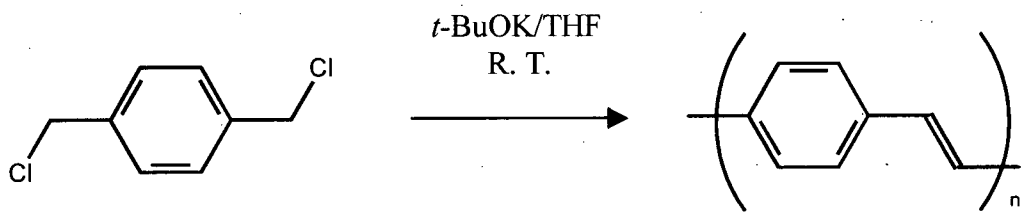

Figure 3.6 The Gilch route to PPV starting from dichloro-*p*-xylene.

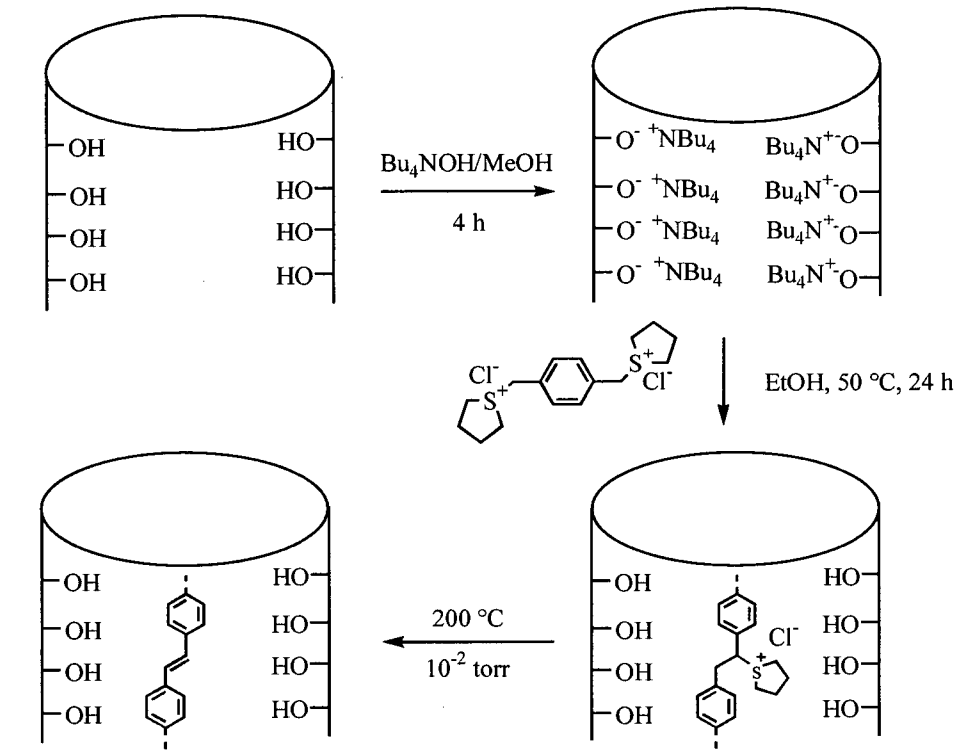

Figure 3.7 Synthetic scheme for the preparation of PPV/MCM-41 hybrid material. Only one chain is shown in the pore for clarity.

3.4 Experimental Results

The pure silica MCM-41 host was synthesized following a literature procedure.[43] Characterization with X-ray diffraction and nitrogen physisorption indicated substantial variations from batch to batch in the lattice constant (4.3 to 4.5 nm) and BJH pore diameter (3.1 to 3.6 nm). Thus comparisons were only made with materials prepared in the same batch. The BET surface area was $(1.0 \pm 0.1) \times 10^3$ m^2 g^{-1}, and the total pore volume was 0.8 cm^3 g^{-1}. The FT-IR spectrum of the empty host showed absorption bands for the surface hydroxy groups from 3700 to 3000 cm^{-1}, the silica framework from 1100 to 600 cm^{-1}, and adsorbed water at 1700 cm^{-1}.

Following TBAOH treatment of MCM-41, TGA showed 10% water content and a 38% mass loss between 100 and 300°C; this was ascribed to the decomposition of the TBA counter-ion (Figure 3.8(a)). The mass content of TBA suggests that 15% of all Si atoms in MCM-41 had an associated with a TBA counter-ion. The presence of the counter-ion reduced the BJH pore diameter by 1.2 nm (Figure 3.8(b)). The polymerization step then yielded a bright green powder. Excess monomer and possible side-products could be easily separated from the powder by washing during filtration. Thermal conversion of the polymer under vacuum led to a fluorescent yellow powder.

X-ray diffraction of the resulting PPV/MCM-41 composite indicated that the sample order remained (Figure 3.9(b)). The result of neutron scattering experiments carried out by L. Fan, Z. Tun and J. Young on MCM-41 and two polymer-containing samples is shown in Figure 3.9(b). The strong scattering peak at $Q \approx 0.16$ is in agreement with the X-ray data. The presence of polymer in the sample did not seem to alter this peak substantially.

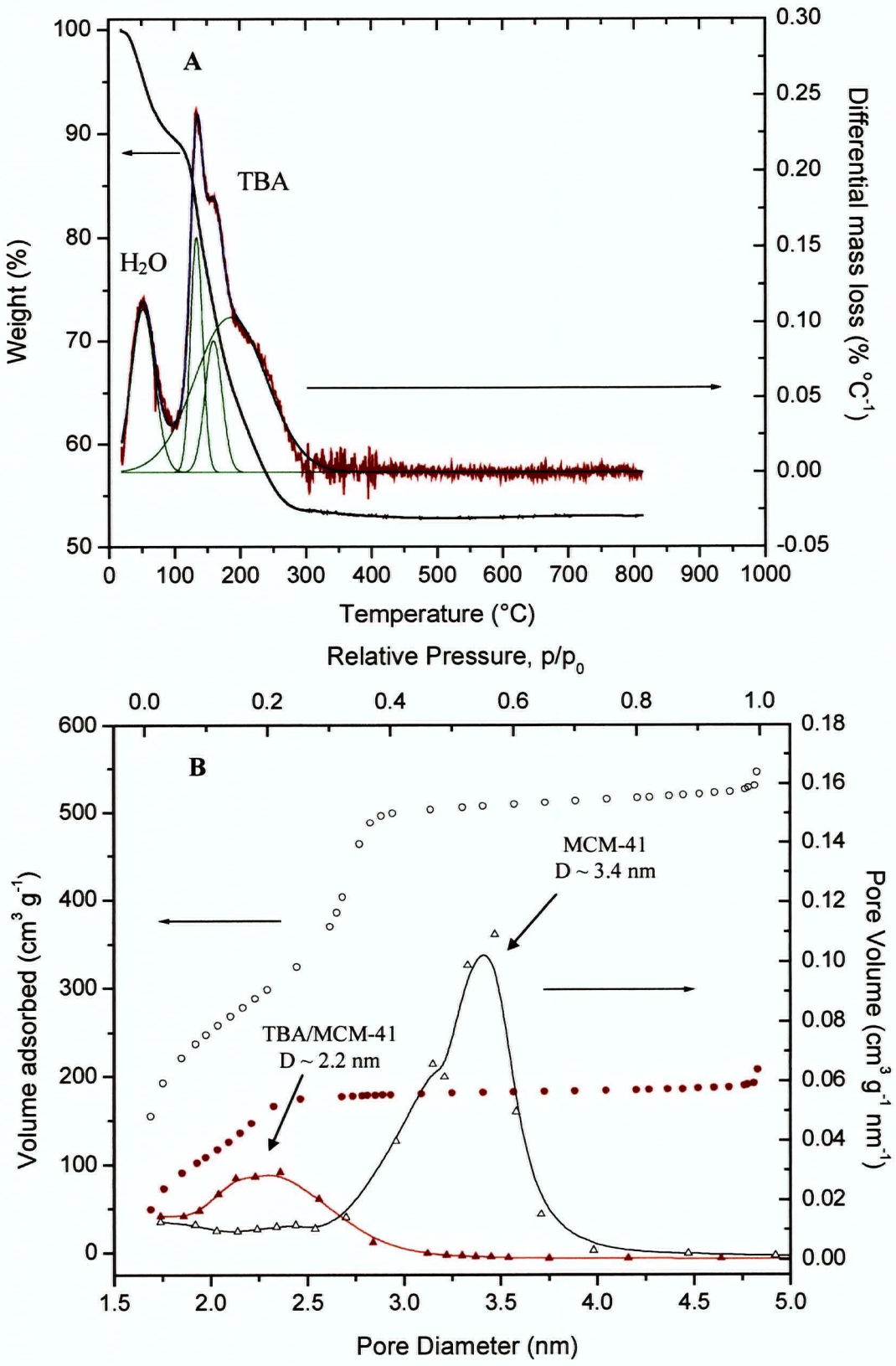

Figure 3.8 (a) Thermogravimetric analysis of TBAOH-treated MCM-41, (b) (○), (●) nitrogen adsorption isotherm and (Δ), (▲) BJH pore size distribution for empty and TBAOH-treated MCM-41, respectively.

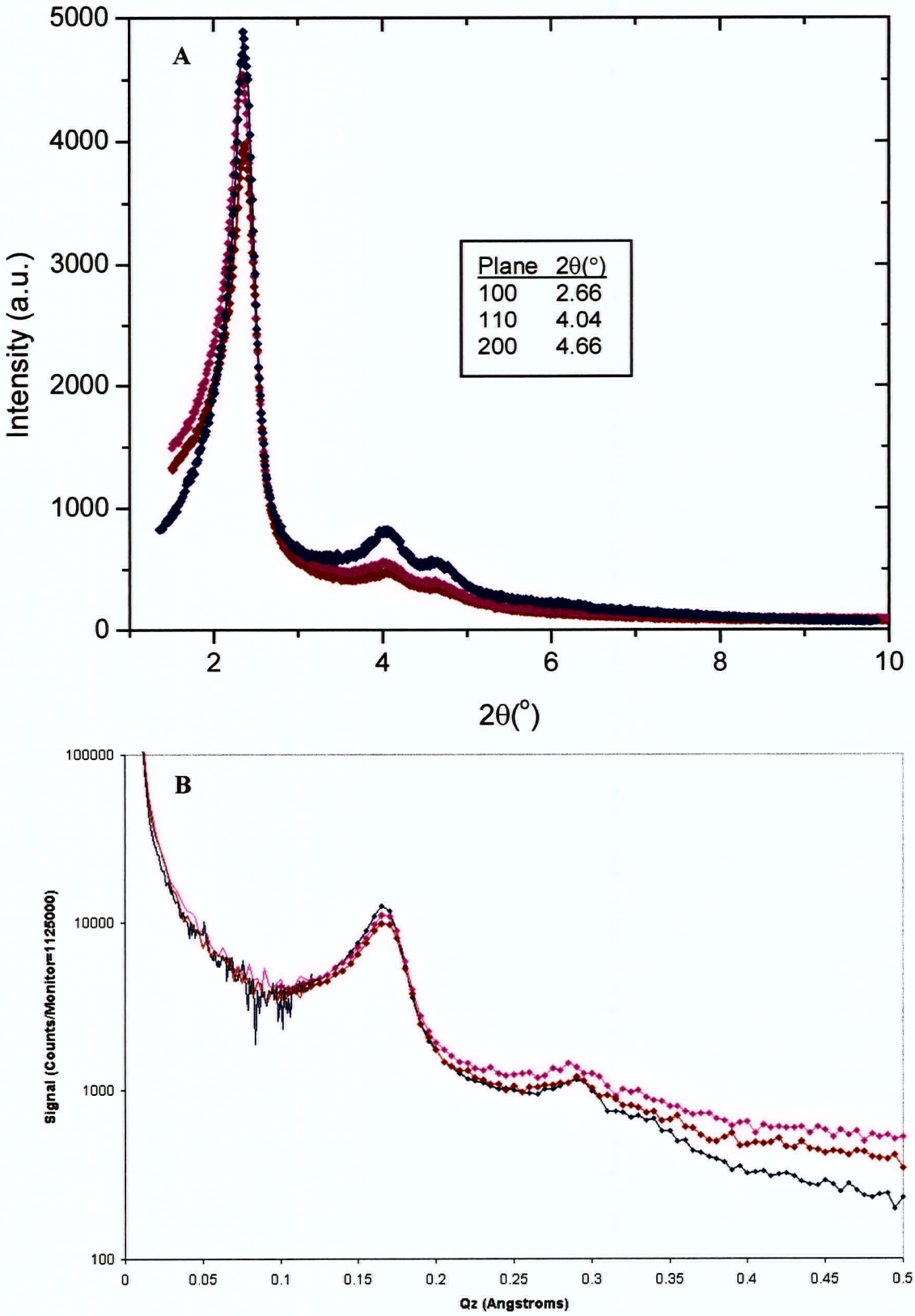

Figure 3.9 (a) Powder X-ray diffraction pattern and (b) neutron scattering data for (♦) MCM-41, PPV/MCM-41 (♦) sample 1 and (♦) sample 2.

TGA of the composite material (Figure 3.10(a)) showed an initial water desorption at 40°C, followed by a 1% weight loss at 250°C, which is most likely due to residual TBA in the material that did not decompose during the thermal conversion process. The polymer degradation began at 350°C and showed at least two different decomposition processes, at 525°C and 730°C. Samples consistently showed a polymer content of 8 ± 2 wt. %. Analysis of the nitrogen adsorption isotherm (not shown) indicated a reduced BET surface area (8.5×10^2 m^2g^{-1}) and pore volume (0.51 ± 0.04 cm^3g^{-1}). The BJH pore diameter was observed to decrease by 0.3 ± 0.1 nm (Figure 3.10(b)).

The FT-IR spectrum (Figure 3.11(a)) showed new bands characteristic of PPV. The band at 3025 cm^{-1} is associated with the C-H stretch in *trans*-vinylene, while the bands at 1517 and 1422 cm^{-1} are due to 1,4-phenylene ring stretching modes.[44] The distribution of polymer was investigated by EELS and EFTEM. The low loss spectra of the empty and polymer-filled MCM-41 are compared in Figure 3.11(b). The zero-loss peak has been removed by careful subtraction of a reference peak, revealing that only PPV/MCM-41 has losses below 8 eV. EFTEM images acquired at 0, 6 and 12 eV with a 2 eV window were used to image the distribution of the losses (Figure 3.12).

The UV/Vis absorbance spectrum of the composite showed an onset at 500 nm and a peak at 420 nm, while the photoluminescence (PL) spectrum showed peaks at 517, 547 and 590 nm (Figure 3.13(a)). The temperature-dependent PL spectra of encapsulated PPV were measured in collaboration with M. McCutcheon and J. Young, using an excitation wavelength of 386 nm (Figure 3.13(b)).

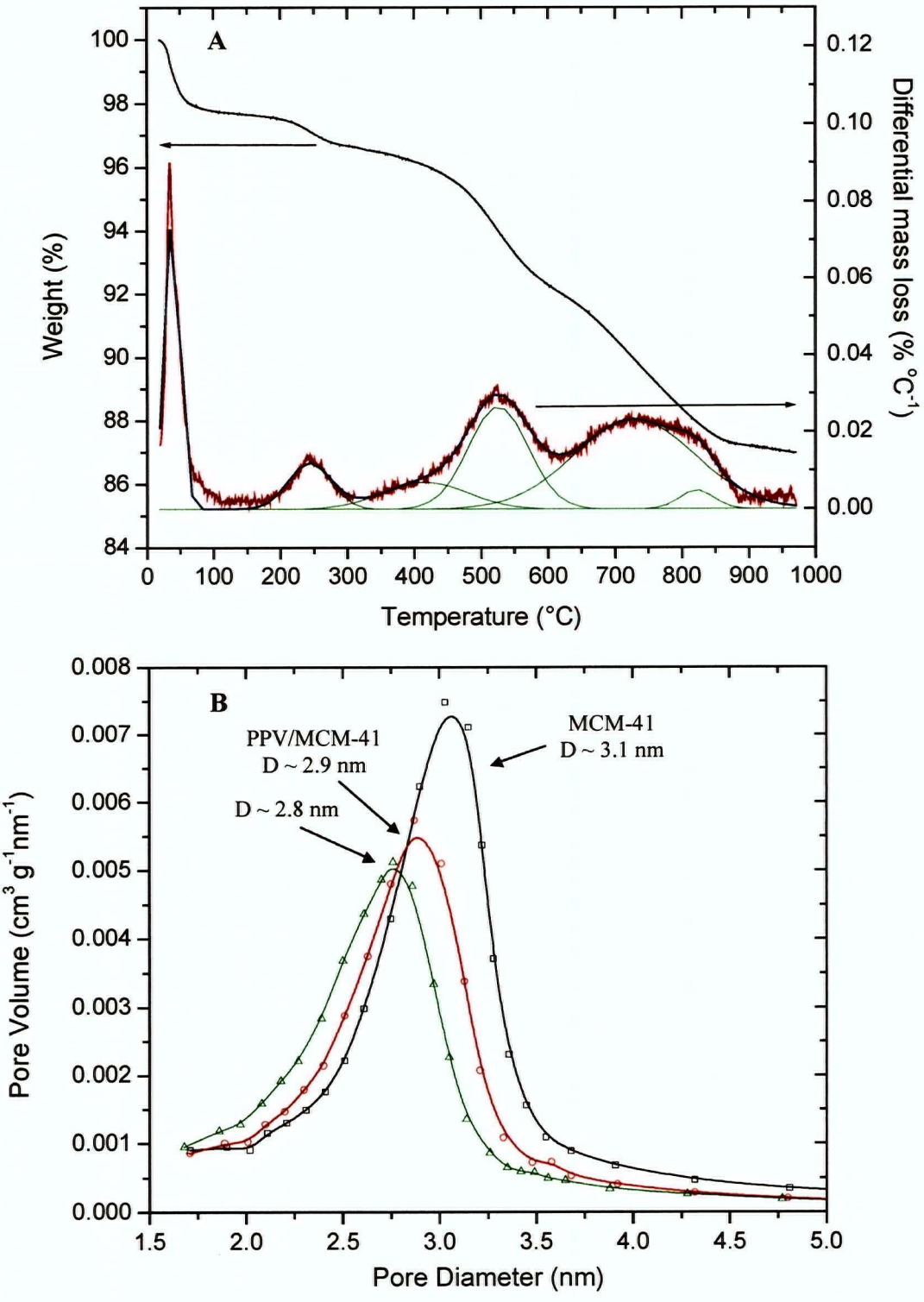

Figure 3.10 (a) Thermogravimetric analysis of PPV/MCM-41, and (b) BJH pore size distribution of (□) empty MCM-41, PPV/MCM-41 (Δ) sample 1 and (○) sample 2.

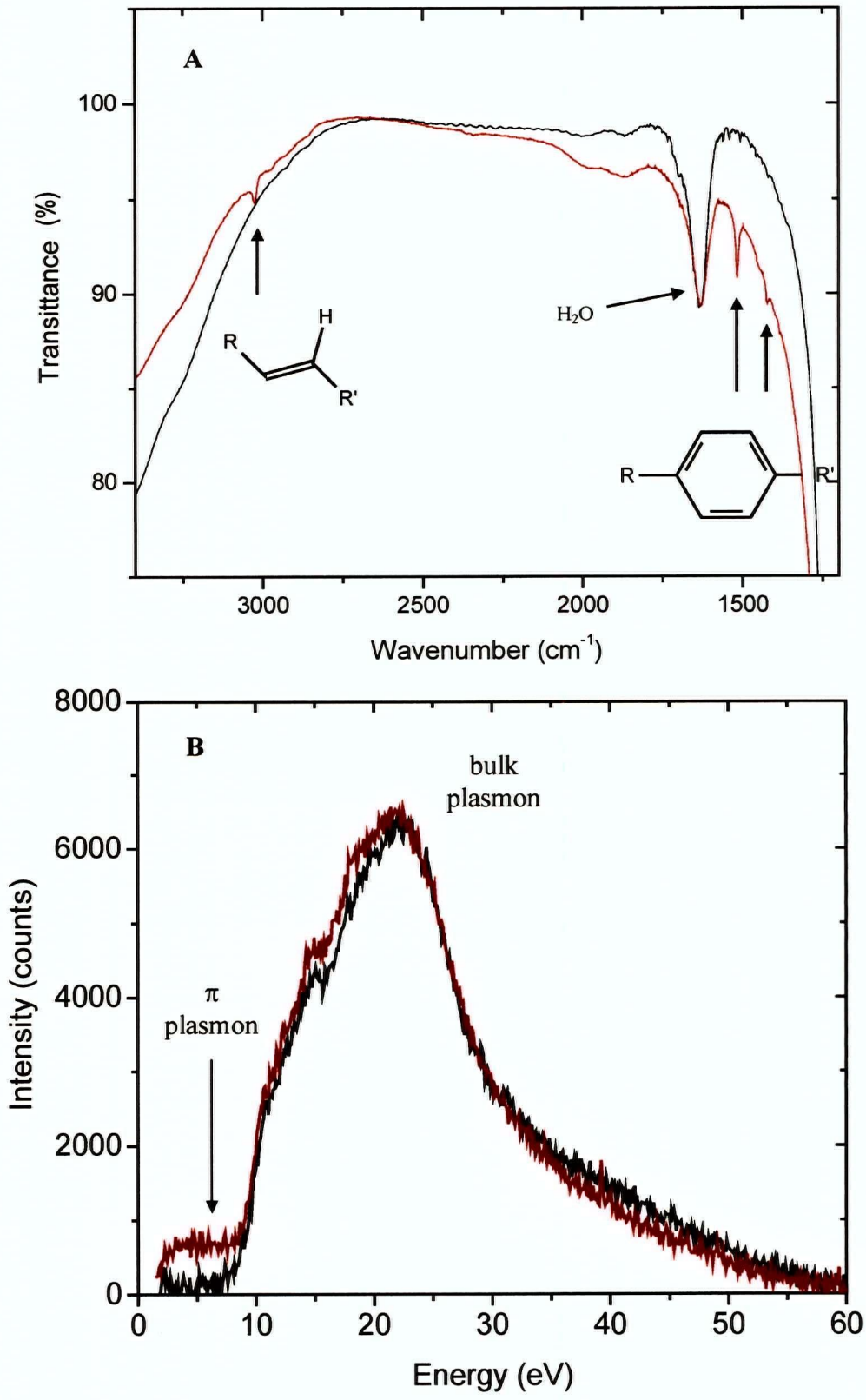

Figure 3.11 Spectral signature of (—) PPV/MCM-41 and (—) MCM-41, using (a) FT-IR and (b) EELS.

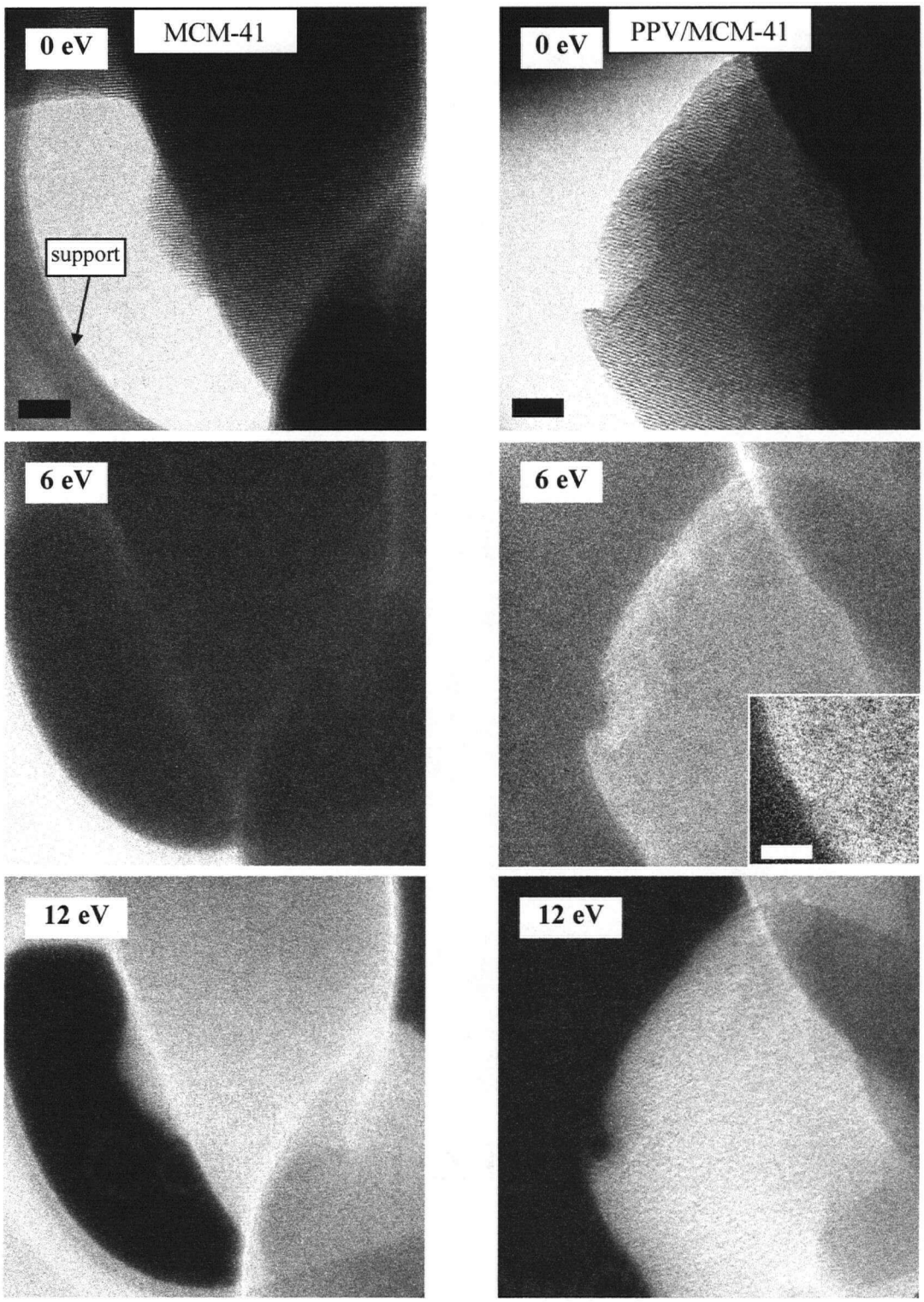

Figure 3.12 EFTEM images for (a) MCM-41 and (b) PPV/MCM-41, filtered with a 2 eV window centered on the given energies. The 6 eV image reveals the polymer distribution in the composite material; the contrast has been enhanced on the inset. Note the presence of the lacey carbon support in (a), which also shows a strong π-π^* plasmon. The main scale bar is 50 nm and the inset scale bar is 20 nm.

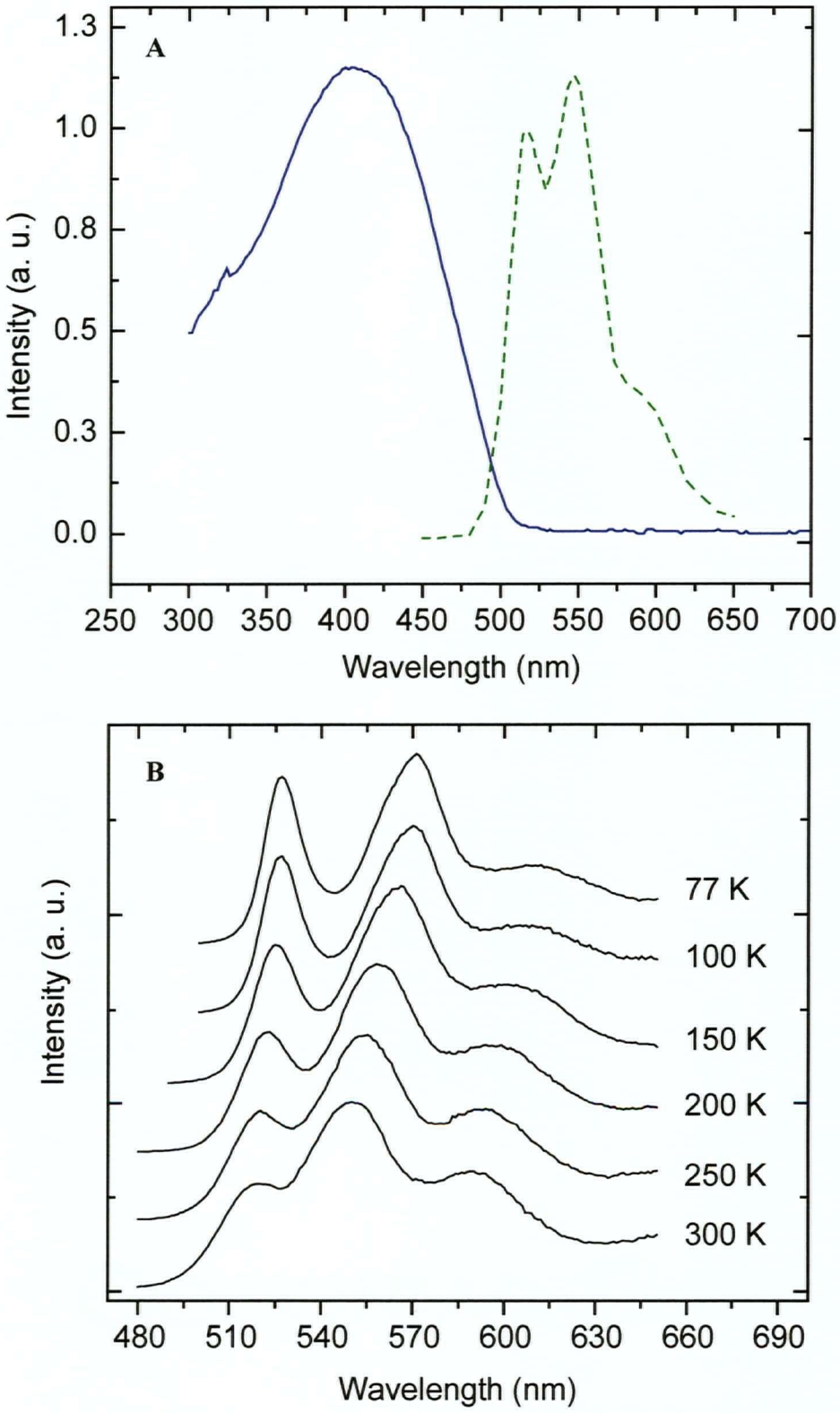

Figure 3.13 (a) Room temperature (—) UV/Vis absorbance and (- - -) photoluminescence of PPV/MCM-41 composite, (b) temperature-dependent photoluminescence spectra of PPV/MCM-41.

3.5 Discussion

The presence of PPV is clearly indicated by the UV/Vis absorbance, fluorescence and FT-IR spectrum of the composite sample. The central issue in the characterization of this material is whether the polymer chains actually reside in the channels of MCM-41, or possibly form a thin coat on the outside of the host particles.

3.5.1 Thermogravimetric Analysis

The TGA data for PPV/MCM-41 (Figure 3.10(a)) clearly indicate that the thermal behaviour of the polymer is altered from its unencapsulated form, which shows only one degradation process at 540°C.[45] The higher temperature degradation process at 730°C has also been observed for PPV encapsulated in montmorillonite.[46] This strongly suggests the presence of some encapsulated polymer. The lower degradation process might be associated with unencapsulated polymer.

A simple model for the composite material can be used to determine the approximate polymer mass content for a given number of polymer chains per channel in MCM-41. With the assumptions that (1) the polymer chains have no conformational defects, (2) they are oriented parallel to the channels, (3) the effect of end-groups can be ignored, and (4) the polymer on the external surface is minimal, the mass fraction F of polymer in MCM-41 for a given number of chains N per pore can be calculated, using parameters given in Table 3.2:

$$F = \frac{N \cdot 2.57 \times 10^{-22}}{1.90 \times 10^{-20} + N \cdot 2.57 \times 10^{-22}} \qquad \text{(Eq. 3.5)}$$

Table 3.2 Parameters for calculation of PPV mass fraction in MCM-41

Property	Value	Source
PPV repeat length	0.66 nm	Ref. 47
PPV repeat unit mass	102.1 g mol^{-1}	
MCM-41 wall density	2.2 g cm^{-3}	amorphous SiO_2
MCM-41 lattice constant	4.3 nm	X-ray diffraction
MCM-41 pore diameter	3.1 nm	N_2 physisorption

Values of F for small values of N are given in Table 3.3. This clearly shows that even one polymer chain per pore would represent a substantial mass loading of the sample. The experimental mass content of 8% suggests that the pores of MCM-41 contain 6 polymer chains each on average. If assumption (4) is invalid, and some of the polymer (~50%) is externally located as suggested by the TGA, each channel contains 3 polymer chains on average.

Table 3.3 Polymer mass fraction F for N polymer chains per pore in MCM-41, using Eq. 3.5.

N	1	2	4	6	8	10
F (%) ± 1%	1	3	5	8	10	12

3.5.2 Physisorption Data

The reduction of the BJH pore diameter of the composite material, albeit small, was observed reproducibly and is significant. The BJH method assumes a cylindrical geometry for the pores and does not provide any information about the arrangement of the polymer chains within the pores; one possible interpretation is that the polymer is present as a thin layer on the walls of the pores. As the PPV backbone is planar, a polymer chain can lie flat against the pore wall and produce a relatively small change in the BJH pore diameter. The observed differences in pore diameter reduction could suggest differences in polymer conformation within the pores, leading to a different effect on the isotherm. The small amount of residual TBA ions observed by

TGA (1 wt. %) would be expected to reduced the BJH pore diameter by 0.03 nm, based on the effect of 38 wt. % TBA content.

If polymerization occurred strictly in solution, due to proton transfer from the solvent or trace water and consequent migration of the basic species into the bulk solution, the polymer might be present strictly as a layer coating the outside of the MCM-41 particles. The effect on the nitrogen adsorption isotherm would then be very different: if the pores were fully blocked, clearly no substantial adsorption would occur, which is not the case. Partial blockage of the pores by a superficial layer would not alter the observed capillary condensation point, but would introduce hysteresis into the isotherm, which was also not observed. An external layer that did not impede the adsorption process would not reduce the observed pore diameter, but simply reduce the specific surface area and pore volume due to the presence of additional, non-porous mass in the sample. The relative decrease in the specific surface area (15%) and pore volume (36%) is greater than the additional mass (8%) and also in agreement with the relative decrease expected for a cylindrical geometry ($dV/V = 2\ dA/A$).

3.5.3 X-ray and Neutron Diffraction

The X-ray diffraction data indicated that the polymerized sample retained the overall order of the host material, with no substantial shift in the diffraction peak positions. No attempt was made to interpret the changes in the peak intensities.

The neutron scattering results showed only small differences between the empty MCM-41 and the PPV/MCM-41 composite. Modelling of MCM-41 coated with a 0.1 nm-thick coating of material contrast-matched to the pore walls has been shown to decrease the amplitude of the main scattering peak and shift the relative position of the smaller peak.[48] The small difference observed in the main peak ($Q \approx 0.16$) between the two PPV/MCM-41 samples does

not correlate with the BJH pore diameters, and the smaller peak ($Q \approx 0.28$) is not sufficiently resolved on all samples to determine any shift relative to the main peak. The difference in scattering cross-section between PPV and MCM-41 cannot be determined without further modelling and it is not possible to state what the effect of a small amount of PPV in the pores would have on the diffraction pattern. As they stand, these results are not in disagreement with the hypothesis of a small number of chains present in the pores.

3.5.4 EELS and EFTEM

Normal TEM investigation of the MCM-41 and PPV/MCM-41 particles revealed no readily visible differences. A substantial surface layer of polymer would have been visible as an amorphous (structure-free) layer at the particle edges. For 1 μm particles, an external polymer mass content of 4% would give rise to a uniform external layer of ~7 nm (assuming a polymer density of 1 g cm^{-3}) Also, no bulk polymer particles were observed.

The electron energy-loss spectrum of PPV/MCM-41 particles clearly showed the loss attributable to the π-π^* plasmon at 6-7 eV, which was absent from the empty MCM-41 sample. Losses below 5 eV were due to the optical absorption of PPV, which has an onset at 2.5 eV and a peak near 3 eV.[49] At energies above 8 eV, the spectra are dominated by the broad bulk plasmon of the silica matrix centered at 22 eV, in agreement with the value observed for a form of mesoporous silica.[50] The polymer bulk plasmon would be expected to appear at a similar energy[51] and could not be distinguished. The shoulders visible between 10 and 20 eV are most likely due to weak surface plasmons. The stability of the material seemed very good under a diffuse beam without any special measures to limit beam damage.

Energy filtering on the π-π^* plasmon is experimentally most practical as the tail of the zero-loss peak is substantial below 5 eV. The 6 eV energy-filtered images of MCM-41 and

PPV/MCM-41 may be compared to determine the polymer distribution in the composite. Empty MCM-41 does not show any substantial losses at 6 eV, and the filtered image is correspondingly dark. PPV/MCM-41, on the other hand, shows 6 eV losses distributed throughout the particle. Intensity variations are seen, and these are due to thickness variations of the sample, as seen in the 0 eV image. There is no indication of edge brightness, which would have suggested the presence of a thin polymer coating on the outside of the particles. The periodicity of the host material is also visible in the 6 eV image of PPV/MCM-41. While this structure is not fully resolved, it strongly suggests that the polymer is confined in the channels.

These results corroborate the physisorption and TGA data in suggesting that the polymer chains are incorporated into the channels of MCM-41. While the presence of some external polymer may be indicated by the TGA data, the EFTEM results indicate that this can only be in the form of a very thin layer (< 2 nm), corresponding to < 1 wt. % external polymer. The measurements were carried out on the same samples that were used for neutron scattering, further indicating that neutron scattering was not particularly suited for investigating these samples without resorting to deuteration to match the scattering cross-section of the host and guest.

This demonstrates the ability of EFTEM to reveal directly the presence of conjugated polymer at very high resolution. The previous estimate of the resolution limit for mapping small conjugated molecules was based on the edge sharpness of a molecular crystal,[52] whereas these results show directly that such high resolution is achievable.

Furthermore, EFTEM was used to image directly the presence of an organic guest in the channels of MCM-41 for the first time. The low number of polymer chains per pore also suggests that it may be possible to image a single isolated conjugated polymer chain (perhaps dispersed in a non-conjugated polymeric matrix) by this technique.

3.5.5 UV/Vis Absorbance and Photoluminescence

The UV/Vis absorbance spectrum of the composite is very similar to that of PPV, indicating a substantial degree of polymerization. However, it did not show any of the structure observed in the absorbance spectrum of stretch-ordered PPV.[53] The PL spectrum at room temperature is in close agreement with literature reports. The structure observed in the spectrum is similar to that of unencapsulated PPV. The peaks are red-shifted with decreasing temperature; this effect has been attributed in bulk PPV to the reduction of torsional modes in the polymer chain that affect the effective conjugation length.[53]

The optical measurements did not reveal any substantially new behaviour in the composite material. Initial attempts at measuring PL dynamics were unsuccessful, as the sample rapidly bleached under laser excitation at 386 nm.

3.6 Conclusion

The experimental evidence showed that a PPV/MCM-41 composite was successfully synthesized. Chemical analysis by EELS and EFTEM allowed the presence of PPV inside the channels to be established unambiguously. The polymer mass content suggested that 3 to 6 polymer chains resided in each pore.

However, this material is less than ideal for property comparisons for a number of reasons. The *in situ* synthesis leads to a polymer that cannot be fully characterized due to its insolubility. Comparison of the PL dynamics with normal PPV would be difficult, due to the simultaneous change in structure and environment, which has also been an issue in the work of Gin *et al.* on PPV in a lyotropic liquid crystal host.[54] There is most likely some polymer coating the outside of the MCM-41 particles, which would further complicate the analysis. This was also found in the work of Tolbert *et al.* on MEH-PPV in an oriented mesoporous silica host, and the

energy migration between polymer outside and inside the channels was studied.[55] Such studies are not possible on the composite prepared here because of the lack of macroscopic orientation.

These complications can be eliminated if the host is prepared in the form of an oriented thin film, and if a soluble form of PPV is used instead. This allows a fully characterized polymer to be used and more meaningful comparisons to be made. Therefore further efforts were directed towards the creation of an appropriate thin film host.

Experimental Details

MCM-41 was synthesized according to a literature procedure using hexadecyltrimethylammonium chloride as the surfactant.[43] The synthesis was carried out at 80 °C for 2 days in a Teflon-lined stainless steel bomb for most samples. One large batch was synthesized in a polypropylene bottle to provide enough sample for neutron scattering. After washing with methanol and water, the collected powder was calcined under air with a heating rate of 1°C min^{-1} to 540°C and held at that temperature for 6 hours. Nitrogen adsorption analysis was performed on a Micromeritics ASAP 2010 instrument.

Thermogravimetric analysis was carried out using a TA Instruments TGA 51 under N_2 flow and a heating rate of 10 °C min^{-1}. Infrared spectra were obtained from KBr pellets using a BOMEM MB155S FT-IR spectrometer. Powder X-ray patterns were collected on a Rigaku Rotaflex rotating-anode diffractometer.

Chemicals were obtained from Aldrich Inc. Xylylene bis(tetrahydrothiophenium chloride) was purified by recrystallization from water. Ethanol was dried over 4A molecular sieves.

Adapting the work of Kumar et al.,[42] the calcined MCM-41 was dried under vacuum at 100 °C and then treated with 1 M tetrabutylammonium hydroxide in methanol under dry conditions. This mixture was left to stand for 4 h at room temperature, after which the basic MCM-41 was filtered off and dried under vacuum. The resulting solid was placed in a 10-20% w/w solution of xylylene bis(tetrahydrothiophenium chloride) in dry ethanol at 50 °C for 24 h, and then washed with ethanol and water to remove excess monomer and base. The bright yellow-green powder was dried under vacuum at room temperature; subsequent heating to 200°C under vacuum (10^{-2} Torr) for 6 h resulted in the powder turning bright yellow in color.

For TEM analysis, samples were deposited on lacey carbon-coated Cu grids (Ted Pella, Inc.) from a suspension in methanol. Electron energy-loss spectroscopy and energy-filtered transmission electron microscopy were carried out on a Tecnai F20 TEM equipped with a Gatan Imaging Filter. The accelerating voltage was 197 kV (200 kV nominally, offset by 3 kV by the GIF). Loss spectra were recorded in TEM mode by placing the particle of interest above the GIF entrance aperture (diameter 2.0 mm). The zero-loss peak was recorded separately for subtraction by moving to an empty area on the grid. The system energy resolution, given by the FWHM of the zero-loss peak, was 0.9 eV. The energy dispersion of the spectrometer was 0.10 eV/pixel, which was calibrated using a 50 eV wobble on the drift tube. EFTEM images were acquired with a 2 eV slit.

The UV/Vis absorbance spectrum was measured for PPV/MCM-41 as a nujol mull, using a Unicam UV-2 spectrometer. Low-temperature PL spectra were obtained by pressing the samples between quartz plates in a cryostat and using the frequency-doubled output of a Ti:Sapphire laser (386 nm) to excite the sample. The luminescence was passed through a Czerny-Turner scanning monochromator (Digikröm 242 from CVI Laser Corporation, using only one 600 grooves mm^{-1} grating) and collected with a Hamamatsu R2257 photomultiplier tube. The spectra were corrected for the response of the grating and the photomultiplier tube by measuring the spectrum of a quartz tungsten halogen lamp (Oriel 77501 Illuminator) of known output.

References

1. van Bekkum, H.; Flanigen, E. M.; Jacobs, P. A.; Jansen, J. C., Eds. *Introduction to Zeolite Science and Practice;* Elsevier: Amsterdam, 2001

2. McCusker, L. B. *Structural Aspects of Molecular Sieves*; Comprehensive Supramolecular Chemistry; Elsevier Science: New York, 1996; Vol. 7, p. 393.

3. Kessler, H. *Synthesis of Molecular Sieves*; Comprehensive Supramolecular Chemistry; Elsevier Science: New York, 1996; Vol. 7, p. 425.

4. Flanigen, E. M. *Zeolites and Molecular Sieves: A Historical Perspective*; Studies in surface science and catalysis; Elsevier: Amsterdam, 2001; Vol. 137, p. 11.

5. Frisch, H. L.; Xue, Y. P.; Maaref, S.; Beaucage, G.; Pu, Z. C.; Mark, J. E. *Macromolecular Symposia* **1996**, *106*, 147.

6. Lai, Z. P.; Bonilla, G.; Diaz, I.; Nery, J. G.; Sujaoti, K.; Amat, M. A.; Kokkoli, E.; Terasaki, O.; Thompson, R. W.; Tsapatsis, M.; Vlachos, D. G. *Science* **2003**, *300*, 456.

7. Kresge, C. T.; Leonowicz, M. E.; Roth, W. J.; Vartuli, J.; Beck, J. S. *Nature* **1992**, *359*, 710.

8. Beck, J. S.; Vartuli, J. C.; Roth, W. J.; Leonowicz, M. E.; Kresge, C. T.; Schmitt, K. D.; Wu, C. T.-W.; Olson, D. H.; Sheppard, E. W.; McCullen, S. B.; Higgins, J. B.; Schlenker, J. L. *J. Am. Chem. Soc.* **1992**, *114*, 10834.

9. Linssen, T.; Cassiers, K.; Cool, P.; Vansant, E. F. *Adv. Colloid Interface Sci.* **2003**, *103*, 121.

10. Beck, J. S.; Vartuli, J. C. *Curr. Opin. Solid State Mater. Sci.* **1996**, *1*, 76.

11. Anderson, M. T.; Martin, J. E.; Odinek, J. G.; Newcomer, P. P. *Chem. Mater.* **1998**, *10*, 1490.

12. Edler, K. J.; White, J. W. *Chem. Mater.* **1997**, *9*, 1226.

13. Cheng, C. F.; Park, D. H.; Klinowski, J. *J. Chem. Soc., Faraday Trans.* **1997**, *93*, 193.

14. Cheng, C. F.; Zhou, W. Z.; Park, D. H.; Klinowski, J.; Hargreaves, M.; Gladden, L. F. *J. Chem. Soc., Faraday Trans.* **1997**, *93*, 359.

15. Zhao, D.; Feng, J.; Huo, Q.; Melosh, W.; Frerickson, G. H.; Chmelka, B. F.; Dtucky, G. D. *Science* **1998**.

16. Schuth, F. *Curr. Opin. Colloid Interface Sci.* **1998**, *3*, 174.

17. Zhang, Z. R.; Suo, J. S.; Zhang, X. M.; Li, S. B. *Acta Phys.-Chim. Sinica* **1999**, *15*, 333.

18. Kawi, S.; Lai, M. W. *Chem. Commun.* **1998**, 1407.

19. Landmesser, H.; Kosslick, H.; Storek, W.; Fricke, R. *Solid State Ionics* **1997**, *101*, 271.

20. Jaroniec, C. P.; Kruk, M.; Jaroniec, M.; Sayari, A. *J. Phys. Chem. B* **1998**, *102*, 5503.

21. Sayari, A.; Liu, P. *Microporous Mater.* **1997**, *12*, 149.

22. Ozin, G. A.; Chomski, E.; Khushalani, D.; Maclachlan, M. J. *Curr. Opin. Colloid Interface Sci.* **1998**, *3*, 181.

23. Moller, K.; Bein, T. *Chem. Mater.* **1998**, *10*, 2950.

24. Edler, K. J.; Reynolds, P. A.; White, J. W. *J. Phys. Chem. B* **1998**, *102*, 3676.

25. Ramsay, J. D. F. *Adv. Colloid Interface Sci.* **1998**, *77*, 13.

26. Marler, B.; Oberhagemann, U.; Vortmann, S.; Gies, H. *Microporous Mater.* **1996**, *6*, 375.

27. Ramsay, J. D. F.; Hoinkis, E. *Physica B* **1998**, *248*, 322.

28. Sing, K. S. W. *Adv. Colloid Interface Sci.* **1998**, *77*, 3.

29. Brunauer, S.; Emmett, P. H.; Teller, E. *J. Am. Chem. Soc.* **1938**, *60*, 309.

30. Barrett, E. P.; Joyner, L. G.; Halenda, P. P. *J. Am. Chem. Soc.* **1951**, *73*, 373.

31. Ravikovitch, P. I.; Haller, G. L.; Neimark, A. V. *Adv. Colloid Interface Sci.* **1998**, *77*, 203.

32. Choma, J.; Jaroniec, M.; Burakiewicz-Mortka, W.; Kloske, M. *Appl. Surf. Sci.* **2002**, *196*, 216.

33. Harkins, W. D.; Jura, G. *J. Am. Chem. Soc.* **1944**, *66*, 1362.

34. Kruk, M.; Jaroniec, M.; Sayari, A. *Langmuir* **1997**, *13*, 6267.

35. Albouy, P. A.; Ayral, A. *Chem. Mater.* **2002**, *14*, 3391.

36. Schacht, S.; Janicke, M.; Schuth, F. *Microporous Mesoporous Mater.* **1998**, *22*, 485.

37. Wu, C.-G.; Bein, T. *Science* **1994**, *264*, 1757.

38. Wu, C.-G.; Bein, T. *Science* **1994**, *266*, 1013.

39. Llewellyn, P. L.; Ciesla, U.; Decher, H.; Stadler, R.; Schüth, F.; Unger, K. K. *Zeolites and related microporous materials: State of the art 1994;*; Elsevier; no. Number; p. 2013.

40. Hsieh, B. R. *Poly(p-phenylene vinylene)s: Methods of preparation and properties*; Polymeric Materials Encyclopedia; CRC Press: Boca Raton, Fl, 1996; Vol. 9, p. 6537.

41. Gilch, H. G.; Wheelwright, W. L. *J. Polym. Sci., Part A: Polym. Chem.* **1966**, *4*, 1337.

42. Kumar, D. N.; Bhawalkar, J. D.; Prasad, P. N. *Appl. Opt.* **1998**, *37*, 510.

43. Khushalani, D.; Kuperman, A.; Coombs, N.; Ozin, G. A. *Chem. Mater.* **1996**, *8*, 2188.

44. Papadimitrakopoulos, F.; Konstadinidis, K.; Miller, T. M.; Opila, R.; Chandross, E. A.; Galvin, M. E. *Chem. Mater.* **1994**, *6*, 1563.

45. Gagnon, D. R.; Capistran, J. D.; Karasz, F. E.; Lenz, R. W.; Antoun, S. *Polymer* **1987**, *28*, 567.

46. Oriakhi, C. O.; Zhang, X. R.; Lerner, M. M. *Applied Clay Science* **1999**, *15*, 109.

47. Martens, J. H. F.; Bradley, D. D. C.; Burn, P. L.; Friend, R. H.; Holmes, A. B.; Marseglia, E. A. *Synth. Met.* **1991**, *41*, 301.

48. Tun, Z.; Mason, P. C. *Acta Crystallogr., Sect. A: Found. Crystallogr.* **2000**, *56*, 536.

49. Samuel, I. D. W.; Crystall, B.; Rumbles, G.; Burn, P. L.; Holmes, A. B.; Friend, R. H. *Synth. Met.* **1993**, *54*, 281.

50. Yin, J. S.; Wang, Z. L. *Appl. Phys. Lett.* **1999**, *74*, 2629.

51. Egerton, R. F. *Electron energy-loss spectroscopy in the electron microscope*; 2nd ed.; Plenum Press: New York, 1996.

52. Barfels, M. M. G.; Jiang, X. G.; Heng, Y. M.; Arsenault, A. L.; Ottensmeyer, F. P. *Micron* **1998**, *29*, 97.

53. Pichler, K.; Halliday, D. A.; Bradley, D. D. C.; Burn, P. L.; Friend, R. H.; Holmes, A. B. *J. Phys.: Condens. Matter* **1993**, *5*, 7155.

54. Gin, D. L.; Yonezawa, K. *Synth. Met.* **2001**, *121*, 1291.

55. Tolbert, S. H.; Wu, J. J.; Gross, A. F.; Nguyen, T. Q.; Schwartz, B. J. *Microporous Mesoporous Mater.* **2001**, *44*, 445.

CHAPTER 4 Preparation of Mesoporous Thin Film Host

Microporous and mesoporous materials often have anisotropic pore structures. A good example is the mesoporous material MCM-41, discussed in the previous chapter: it has straight 1-D channels arranged in a 2-D hexagonal lattice. This anisotropy can only be exploited, however, if the macroscopic orientation of the material can be controlled either during or after synthesis. Such control over the orientation is necessary for a number of applications, including photonic materials, membranes and sensors. It is also key to fabricating the ideal device where only intrachain processes can occur: proper channel orientation will allow good charge transport along the conjugated polymer chains in the device, and a narrow pore diameter will favour the isolation of the polymer chains (Figure 1.5; Table 1.2). The development of a porous thin film host with oriented 1-D channels was thus of central importance to this research effort.

Notwithstanding all the requirements expressed in Table 1.2, the central challenge is the fabrication of porous thin films with 1-D channels aligned in the direction of the substrate normal. The synthesis of films and membranes with such oriented porous structures has been the subject of continuous scientific pursuit.[1-5] Impressive progress has been made in many areas but the goal of fabricating uniform defect-free membranes with very small pores remains elusive. Membranes with pores down to 10 nm diameter are readily available, but the size regime below that is not well developed. As the membranes of interest for this work lie in this uncharted territory, it was clear at the outset that substantial effort would be required to develop the desired thin film host. However, a number of promising first reports were present in the literature, which

suggested that the goal was within reach. These reports are reviewed here and the investigations into the more promising routes discussed.

Many of the characterization techniques applicable to analysing bulk mesoporous samples can also be applied to thin films. X-ray diffraction can be used to evaluate the orientation of the film.[6] Physisorption measurements are not straightforward, due to the limited total surface area of the films. The most important techniques are based on electron microscopy: scanning electron microscopy (SEM) and transmission electron microscopy (TEM) allow high resolution inspection of the film structure on the local level, as reviewed in chapter 2.

4.1 Alignment of Porous Thin Films

Self-assembly is an attractive route for materials synthesis because of the inherent order of the resulting materials. Once the appropriate conditions for self-assembly are known, the synthesis is usually straightforward. Thus a lot of effort has been devoted to the pursuit of systems which self-assemble into porous thin films and membranes with various geometries.

For self-assembled mesoporous materials, the methods used to achieve alignment fall into two general categories: interface-induced alignment and field-induced alignment (including electric, magnetic and flow fields). These various methods are reviewed here, and it will become obvious that no ideal approach to the fabrication of the desired membrane via self-assembly exists as of yet. Some very recent work on solvent evaporation-induced alignment does appear very promising in creating mesoporous thin films with channels normal to the substrate.[7]

4.1.1 Interface-Induced Alignment

Surfactant-templated materials, including the members of the M41S family (MCM-41, MCM-48), have been found to align themselves in specific ways on a number of interfaces. It is thought that the arrangement of the initial layer of surfactant micelles on the interface largely determines the alignment of the growing film. Mica and graphite induce a parallel alignment of cylindrical micelles (Figure 4.1) through fairly weak electrostatic and van der Waals interactions respectively.[8,9] The resulting films still have substantial in-plane disorder (direction of channels, 180° defects), which limits their usefulness. The air-water interface has also been shown to favour a similar type of ordering.[10] Films grown on Si (100) and (111) show no preferential ordering, but Si (110) does induce alignment parallel to the [001] direction,[6] indicating that proper registry of the templating mesophases with the interface is necessary to achieve ordering. However, a straightforward approach to predicting which surfaces will produce proper registry has not been found yet.

It is also possible to modify a surface to induce alignment in a preferred direction, as shown by the rubbing method,[11] which is commonly used to align liquid crystalline materials for display applications. A thin polyimide film is coated on the substrate and then rubbed in a particular direction, which aligns the channels of the mesoporous material parallel to the rubbing

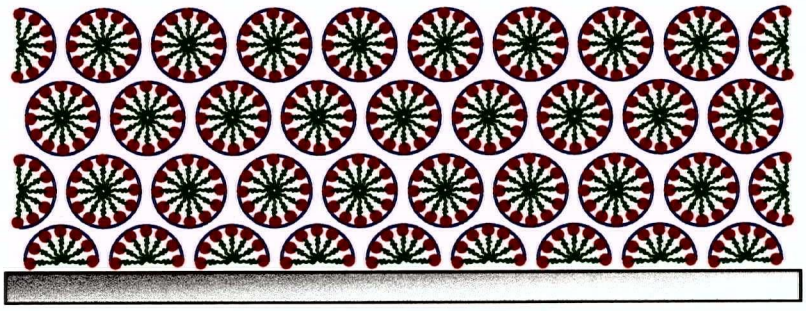

Figure 4.1 2-D hexagonal packing of surfactant micelles in aqueous solution onto a graphite surface, after ref. 8.

direction. In-plane X-ray diffraction shows that the distribution of channel directions has a FWHM of 29°.

The orientation of the initial template layer on the surface can also be controlled by modifying the chemical structure of the templating agent (Figure 4.2). This has been shown through the use of a two-headed quarternary ammonium salt to form a structure designated SBA-2.[12] The initial reports on the structure of SBA-2 films, based on TEM studies, suggested that there was a continuous channel normal to the interface. A later study using high-resolution TEM showed that the initial structure assignment was erroneous and that there was a higher degree of connectivity in the porous structure than originally identified.[13]

It is therefore still difficult to self-assemble a film with oriented channels normal to the interface. One plausible approach around this problem is the use of a substrate that presents vertically-oriented interfaces, i.e., by using a larger porous support to nucleate the film. Porous alumina[14-17] (see below) and capillaries[18] have been used as substrates for the growth of zeolites and mesoporous silicates. These oriented supports present interfaces oriented parallel to the substrate normal (Figure 4.3). This has been recently used to prepare membranes of MCM-48,

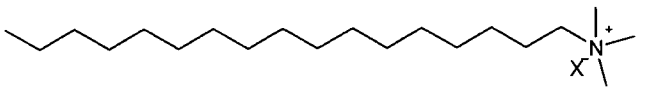

A

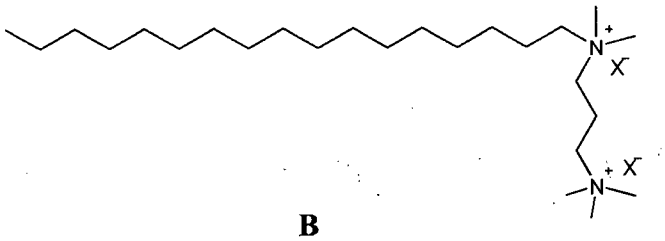

B

Figure 4.2 Surfactant templates for (a) MCM-41 and MCM-48 structures ($C_{16}H_{33}N(CH_3)_3X$) and (b) SBA-2 structure ($C_{16}H_{33}N(CH_3)_2(CH_2)_3N(CH_3)_3X_2$), where X = Br or Cl.

which has an isotropic cubic structure, and therefore cannot show a preferred orientation. A supported MCM-41 structure has not been reported to date, perhaps because the desired orientation is not achieved. Nevertheless, one would expect that the surface curvature of the porous support (i.e., the inverse of the channel radius) would have a significant effect in favouring alignment of the channels in the axial direction over the circumferential direction.

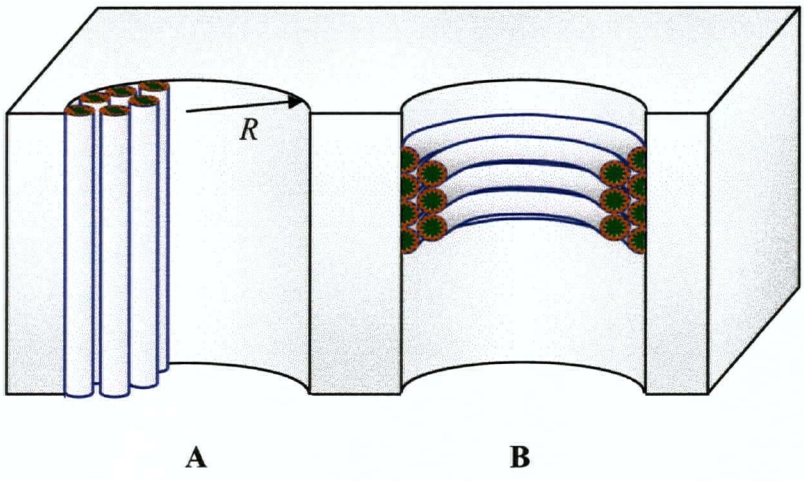

Figure 4.3 The two extreme possibilities for surfactant micelle alignment in a porous support: (a) in the axial direction and (b) in the circumferential direction. A smaller radius of curvature R would be expected to favour the axial orientation.

4.1.2 Field-Induced Alignment

Externally applied fields offer an attractive approach to obtaining the desired channel alignment in porous materials. In many cases, the product material is only partially aligned with the applied field, as only an average alignment is achieved, with substantial deviations presumably due to thermal disorder of the templates.

It has been shown that the application of a large magnetic field (~12 T) can be used to align the channels in a mesoporous material.[19] This results from anisotropy in the diamagnetic

susceptibilities of the templating agents. Once the template micelles reach equilibrium with the magnetic field (with 60% of the domains aligned with the magnetic field, as seen by solid-state NMR), condensation of the silica framework is achieved by allowing gaseous HCl to diffuse in. The resulting material was characterized by X-ray diffraction, which suggested that 78% of the pores were aligned in the desired direction.[20]

Hillhouse *et al.* have used a flow field to induce preferential alignment of a mesoporous silica film grown in a capillary tube.[21] The channels were found to be oriented in the direction of the external flow for thin films (< 200 nm), based on observation of the macroscopic morphology of the film by SEM. Thicker films tended to lose this preferred alignment and became similar to films grown under static conditions. More work in this direction was carried out by Kim and Yang.[22]

The flow field provided by laser-induced ablation has also been used to generate aligned structures.[23,24] The laser was used to create a seed film of material oriented by the ablation of a guest molecule, ferrocene. Further treatment with the synthesis mixture then formed a continuous film with an orientation derived from the seed film.

The use of both an interface and an applied electric field to fully control alignment has also been demonstrated.[25] An elastomeric mold was used to create micron-scale channels on a substrate between two electrodes (Figure 4.4). The electric field creates an electro-osmotic flow between the two electrodes, which is further guided by the channels. Thus both the flow and the presence of the interfaces contribute to aligning the template micelles, leading to a very high degree of alignment parallel to the flow direction. Localized Joule heating then induces condensation of the silica framework. While this approach created high quality alignment of the channels (X-ray diffraction indicated that the directional spread was 1.7°, substantially better than other methods for aligning the micelles), it would not be straightforward to fabricate thin

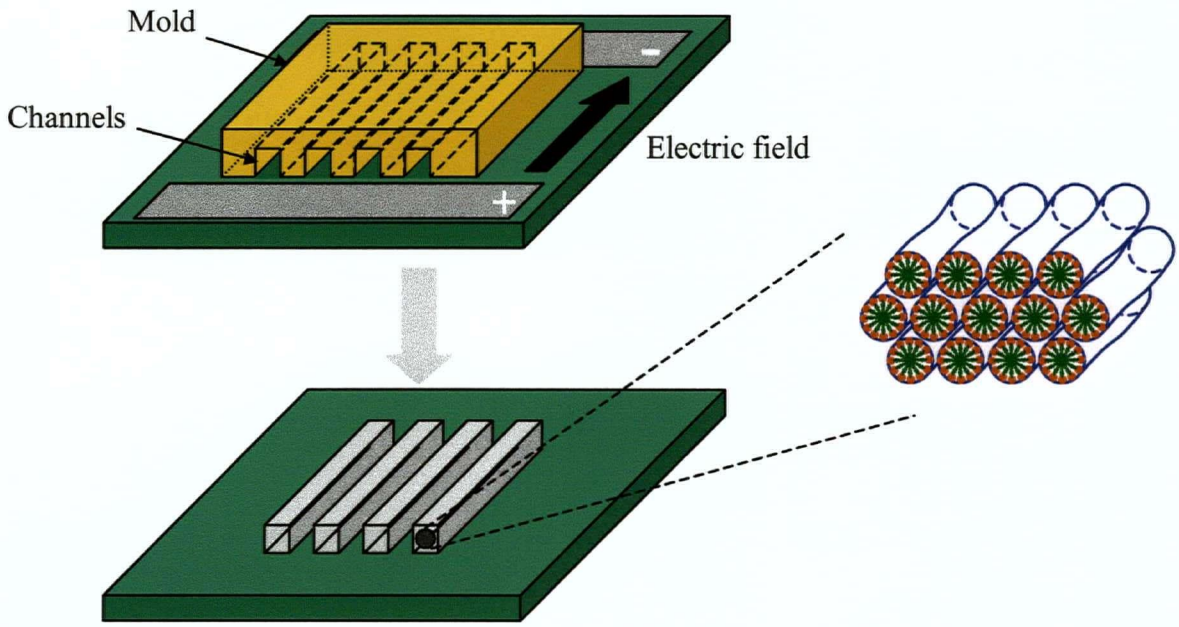

Figure 4.4 Orientation of mesoporous channels by electro-osmotic flow, after ref. 25.

films (i.e., with channel lengths from 100 to 200 nm) using this technique. One possibility may be to combine it with a porous support of the type discussed above.

4.1.3 Oriented Porous Thin Films by Other Approaches

Track-etch membranes[26] are prepared by exposing a polycarbonate or polyester film to a beam of energetic heavy ions in a linear accelerator. The ions leave damage tracks that are roughly normal to the film surface, and which are then etched chemically to the desired diameter. The obtainable diameters range from 10 nm to several microns. These are available commercially from Whatman, Inc. under the Nucleopore trademark. While the technology behind these membranes is fairly well developed, it is unclear if they can be prepared in the form of thin films, or obtained with smaller pore diameters.

Kondoh *et al.* reported an almost ideal porous film structure, attained by oxidizing $FeO:SiO_2$ thin films with a specific stoichiometry at 600 °C.[27] The alignment was thought to be induced by the direction of oxygen flow, as the oxidized Fe precipitated out (as Fe_2O_3) in columns perpendicular to the film surface. The Fe_2O_3 columns could be conveniently etched out, leaving behind a porous silica matrix. The resulting film had an average pore size of 4 nm, as determined by nitrogen physisorption and supported by TEM studies.

Porous alumina (anodic aluminum oxide) is also commercially important, especially for microfiltration.[28] It is produced by anodizing aluminum samples in aqueous electrolytes. Under the appropriate conditions, the resulting oxide has vertical pores running through it, and the pore spacing can be controlled by the applied potential. The exact cause of the alignment of the channels is still unclear but appears to be related to both the applied potential and the strain created by the expansion of the lattice from aluminum to aluminum oxide. The alignment of the channels is almost perfect after extended growth and published reports indicated that the diameter may be adjusted from 20 to 500 nm. Thick membranes are commercially available from Whatman, Inc. under the Anopore trademark.

It may be possible to prepare similar structures by electron-beam lithography and chemical etching of an appropriate substrate. At the early stages of this thesis, the feature size for this technique was on the order of 50 nm, and thus too large for the purpose of this project. Direct electron-beam drilling of alumina or silica films using a field-emission TEM in scanning mode is a very promising approach for creating a small number of very small diameter holes.[29]

Porous thin films based on the self-assembled SBA-2 structure, the FeO/SiO_2 system and porous alumina were initially judged to be promising thin film hosts. Their synthesis and characterization was undertaken to investigate further their suitability as oriented thin film hosts for conjugated polymers.

4.2 Further Investigation of SBA-2 Mesoporous Silica Films

Self-assembled films are attractive candidates for study as they are often highly ordered and uniform. Assuming that the chemistry to yield the correct geometry can be found, these films would be ideal host materials for conjugated polymers. As stated above (section 4.1), the geometry of a film nucleated on an interface is thought to depend on the arrangement of the very first layer of templating agent on the interface. As such, control of the template-interface interactions should in principle allow the preparation of films with the desired pore orientation. Most of the work reported in the literature has focused on thin films related to the MCM-41 structure and based on straight-chain alkyl ammonium surfactants. These adopt the well-established parallel alignment with the interface in a hexagonal structure. A different orientation can only be expected from films with substantially different structures.

The structure type is controlled by the choice of surfactant and pH. A small number of geometrical parameters have been found to govern the type of structure produced by a given surfactant. The hydrophobic tail length, hydrophilic head size and charge can all be adjusted to yield fairly predictable structures.[30] Tolbert *et al.* found that the use of a two-headed surfactant (Figure 4.2(b)), which templates the 3-D hexagonal SBA-2 structure, allowed the synthesis of thin films with a possible channel normal to the interface. In this case the initial layer on the surface was found to consist of packed hemispheres, representing the higher symmetry of SBA-2. The proposed structure consisted of large cages, the connectivity of which would determine the form of the channels through the material.

As such, the material appeared promising and was investigated in more depth. The reported SBA-2 structure was synthesized on freshly-cleaved mica substrates. The presence of the SBA-2 phase was confirmed by X-ray diffraction (Figure 4.5). The (002) peak appears strongly, indicating that the film is aligned with the *c* axis perpendicular to the film. The (112) and (004) peaks appear weakly. The calcined sample showed a shift in the (002) peak to higher angle, indicating that the framework size had decreased during calcination.

In order to investigate the microstructure of SBA-2 films, the samples grown on mica were embedded in epoxy resin and sectioned using a diamond knife. However, the film did not survive the sectioning process and thus no further information on the pore structure was obtained

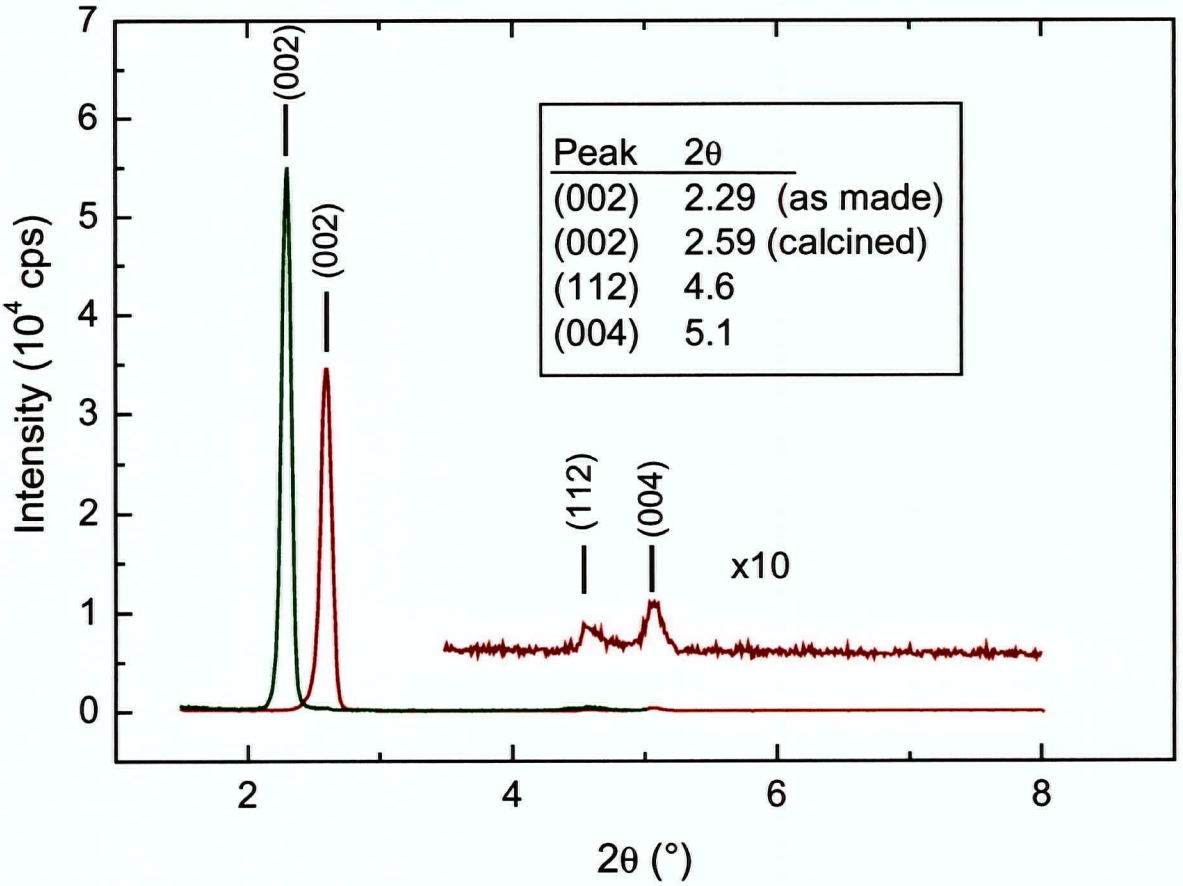

Figure 4.5 X-ray diffraction pattern of SBA-2 film grown on mica (—) before and (—) after calcination.

in this fashion. A report appearing at this time indicated that SBA-2 did not have the desired connectivity, based on high resolution TEM imaging.[13] This study of bulk SBA-2 indicated that the structure grown as a film would have straight 1-D channels parallel to the interface and zigzag channels running perpendicularly to the interface, a geometry not conducive to conjugated polymer inclusion. In view of this information, and promising developments with porous alumina films, no further characterization was attempted.

4.3 Further Investigation of the FeO/SiO_2 System

The FeO/SiO_2 system is the subject of one report in the literature.[27] The inspiration for this approach reportedly comes from the observation of elongated Fe_2O_3 structures in natural samples. In this material, the ordering is determined by the direction of oxygen diffusion as FeO is oxidized to Fe_2O_3 within the SiO_2 matrix. The morphology of the resultant materials depends strongly on the relative concentration of FeO and SiO_2. At compositions between 70:30 and 60:40 $FeO:SiO_2$, it is reported that columns of Fe_2O_3 grow perpendicularly to the substrate within the SiO_2 matrix (Figure 4.6). These columns can then be etched out by aqueous HCl, leaving behind the SiO_2 matrix. The resulting 1-D channels in SiO_2 have a diameter of 4 nm, as determined by a Barrett-Joyner-Halenda (BJH) analysis of the nitrogen physisorption isotherm.

When the $FeO:SiO_2$ ratio is lower than 60:40, the resulting Fe_2O_3 particles are trapped in the SiO_2 matrix and cannot be etched out. Higher FeO levels lead to an oxidized film with larger, disordered Fe_2O_3 structures. Use of the correct $FeO:SiO_2$ ratio should produce a thin film host with nearly ideal characteristics: porous SiO_2 films with vertical 4 nm channels with easily controlled thickness. The slight drawback of this process is the rather high processing temperature (600°C).

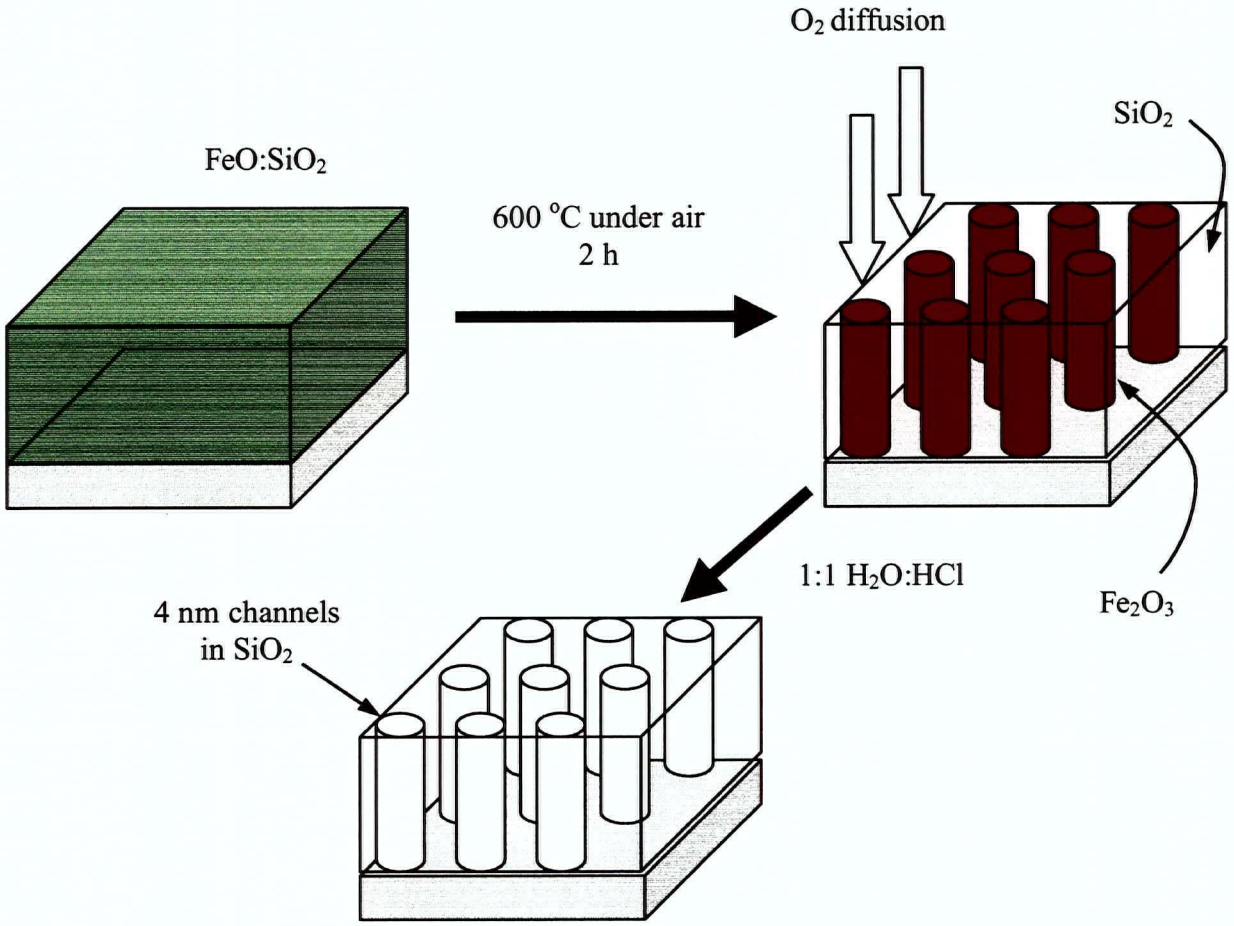

Figure 4.6 Preparation of thin film with oriented channels from a $FeO:SiO_2$ film.

The duplication of these published results was attempted. Using a 65:35 $FeO:SiO_2$ target, thin films were sputtered unto glass and silicon substrates using radio-frequency (RF) sputtering. Freshly-sputtered films were initially transparent with a deep green colour. Following oxidation at 600 °C, the films turned red in appearance, indicating the formation of Fe_2O_3. This colour disappeared completely upon etching with 1:1 $HCl:H_2O$, suggesting that most of the Fe_2O_3 had been removed from the thin film. These observations were in agreement with the chemistry suggested by the initial reference.

The microstructure of the films at different stages of processing was investigated by TEM. Cross-sections of the thin films were readily obtainable by the small-angle cleavage (SAC) technique.

The cross-section of the oxidized, unetched film is shown in Figure 4.7 (a). Very little structure is apparent, in contrast with the published micrographs, where columnar structures were visible. The energy-dispersive X-ray (EDX) analysis of the thin film with a STEM (Figure 4.8(a)) yielded a Fe:Si atomic ratio of 2.1 ± 0.2, which was within the range deemed optimal (1.9 – 2.3). XPS analysis, on the other hand, yielded a Fe:Si ratio of 0.9, suggesting the surface FeO content was well below the desired level. The etched film is shown in Figure 4.7 (b), and there is insufficient contrast to observe the pore structure. The EDX spectrum showed that the Fe_2O_3 had been fully removed (Figure 4.8(b)), indicating that there were no isolated Fe_2O_3 particles. This suggested that the Fe:Si ratio was near or above optimal. The XPS results, which reflect the composition at the surface, may indicate that the film had a lower concentration of Fe near the surface.

Heavy-element staining of the pore surface was attempted to improve the contrast between

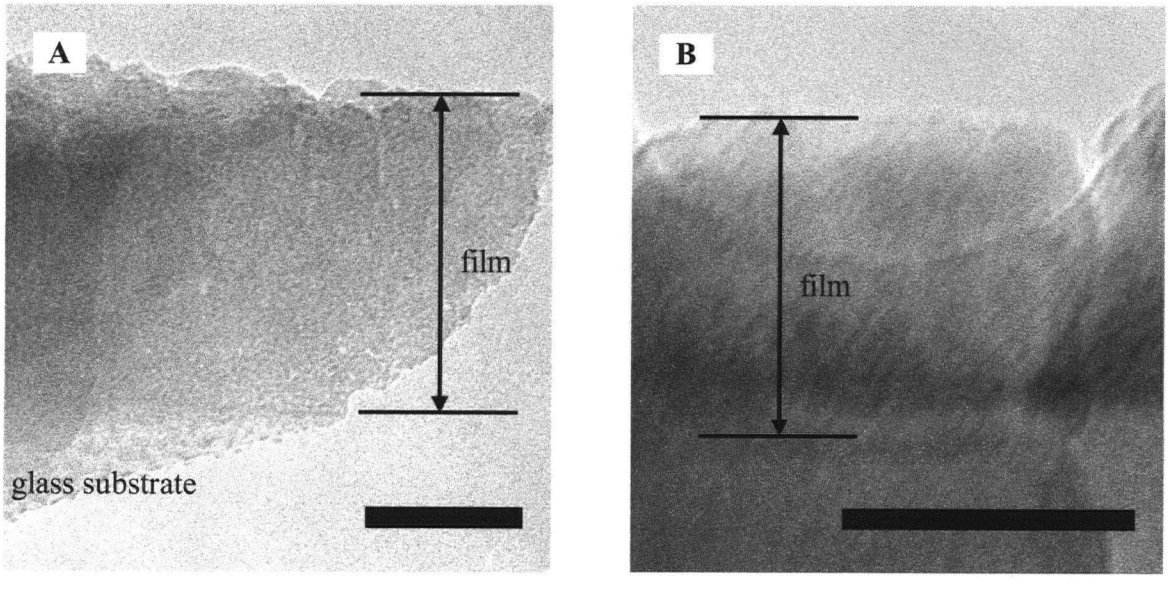

Figure 4.7 TEM image of cross-section of $FeO:SiO_2$ film on glass (a) after oxidation, before etching, (b) after etching and Pb-staining. The cross-section was prepared by the SAC technique. The scale bars are 50 nm long.

the pores and the surrounding matrix. Lead acetate is known to bind to surface hydroxy groups, but it did not improve the contrast of the pores, despite clear indication of the presence of Pb by the EDX spectrum (Figure 4.8(c)).

The nitrogen adsorption isotherm on a 200-nm thick sample (anticipated total surface area ~0.5 m^2) did not show a clear condensation step, suggesting a wide distribution of pore sizes. The measurements were also limited in accuracy by instrumental drift. This stood in contrast with the reported adsorption isotherm, which showed a clear capillary condensation step corresponding to a 4 nm BJH diameter. While the thin films were porous, as evidenced by the complete removal of the Fe_2O_3 by etching, no well-defined channels could be detected by electron microscopy or nitrogen physisorption. Attempts to contact the authors to discuss possible processing issues were unsuccessful. Further efforts to reproduce this work were abandoned since porous alumina showed more promise.

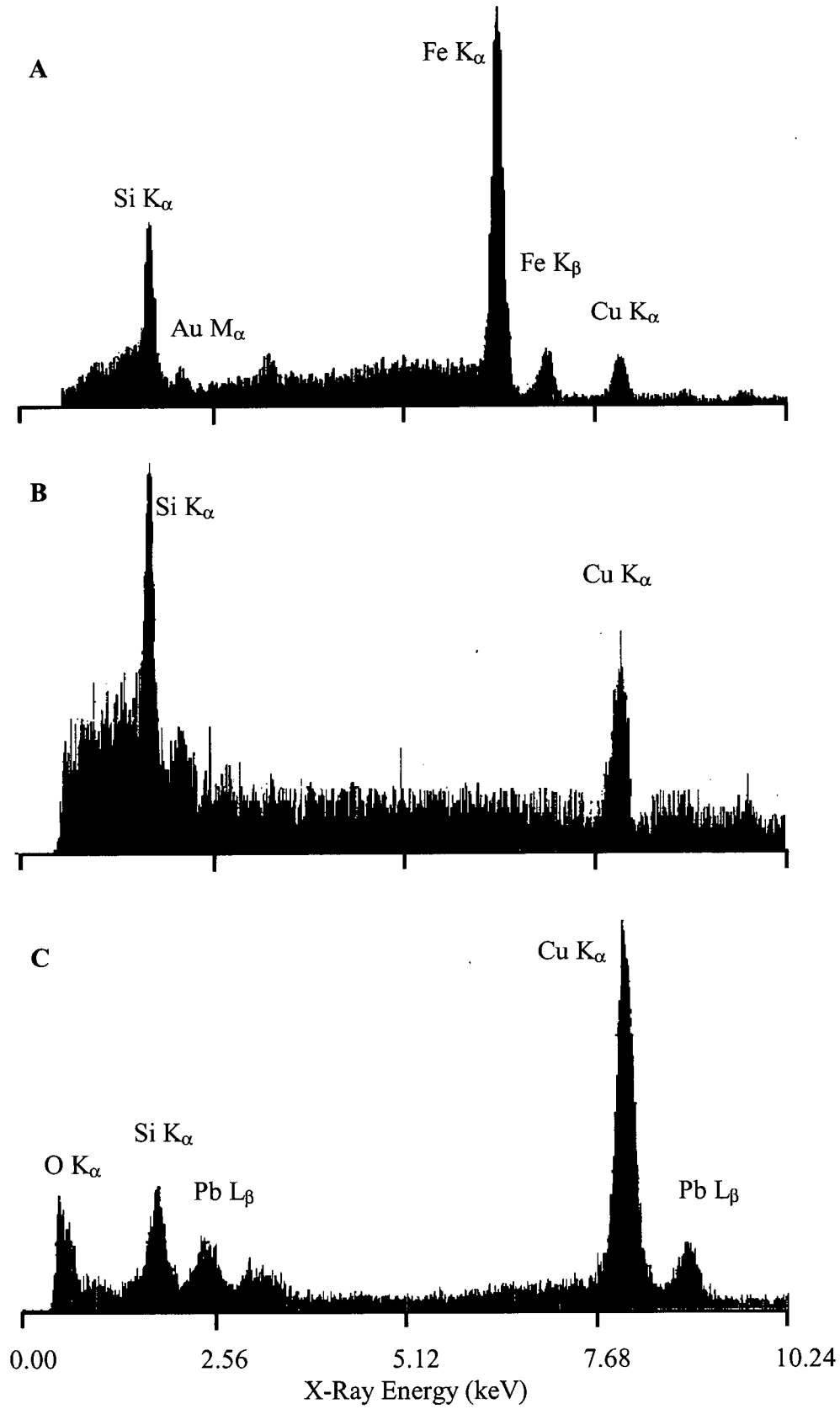

Figure 4.8 EDX spectrum obtained from cross-sections of FeO:SiO2 films: (a) oxidized (some Au contamination is apparent), (b) etched to remove Fe_2O_3, (c) Pb-stained.

4.4 Porous Alumina Films (Anodic Aluminum Oxide)

Anodic films on aluminum have a long history of industrial application as cosmetic and protective layers. The choice of anodization conditions (electrolyte, temperature, potential) has a dramatic effect on the structure of the resulting alumina film. The porous films obtained under the appropriate conditions were found to exhibit a structure which fitted the requirements expressed in Table 1.2 very closely.

The porous nature of some of these films has been reviewed in depth by Thompson and Wood.[31] Due to their industrial importance, these films have been extensively studied since the 1930's. Many characteristics of the films were well understood by the 1980's, and it was recognized that very ordered films could be produced under certain conditions. The self-ordering phenomenon was not fully exploited until the 1990's: in 1993, Masuda *et al.* reported a simple technique for the production of porous anodic alumina with highly ordered pores and a

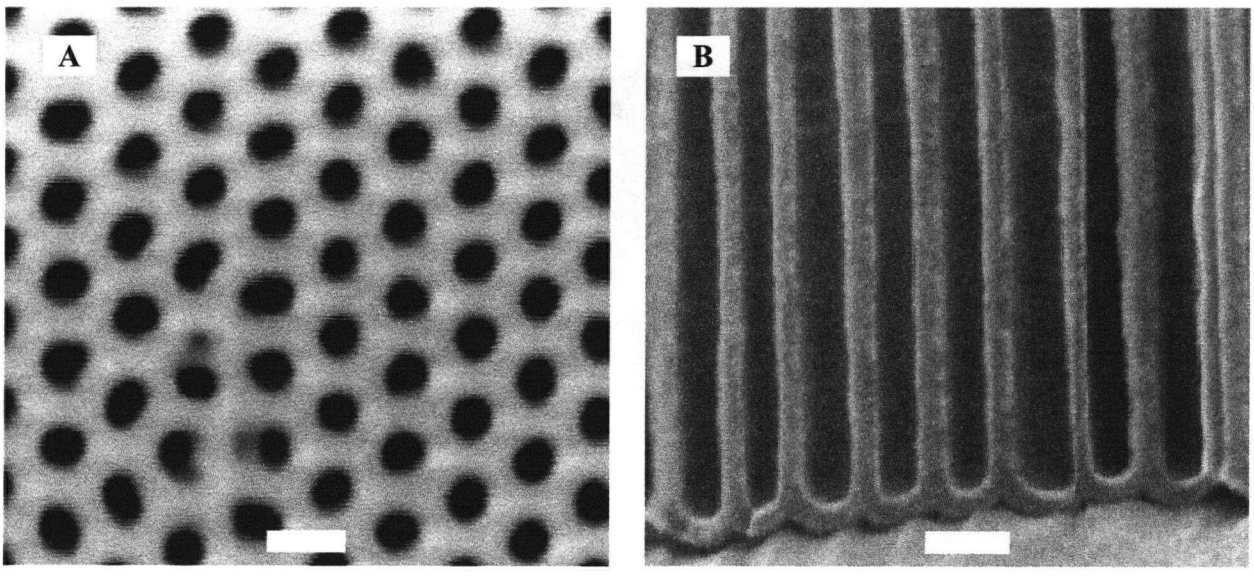

Figure 4.9 SEM images of porous alumina film produced at 40 V in 0.3 M oxalic acid, using Masuda's two-step approach: (a) top view, (b) cross-section. The scale bars are 100 nm long. Images courtesy of Dr. K. Rademacher.

corresponding narrow pore size distribution (Figure 4.9).[32] This development led to the widespread application of porous alumina membranes both as hosts for other materials[33-36] and as templates[37] for the synthesis of tubules[38] and wires[39,40] with uniform diameters in the 30 to 100 nm regime. The development of well-ordered large pore samples allowed the fabrication of photonic crystals either directly using patterned porous alumina films[41,42] or by transferring the pattern to another substrate by dry chemical etching.[43-46] The anodization of other materials, most notably silicon, also produces very useful porous structures.[47]

Porous alumina is prepared by anodizing aluminum in an acidic electrolyte, typically phosphoric, sulfuric or oxalic acid. The anode is attached to the aluminum substrate, while the cathode usually consists of a platinum mesh electrode (Figure 4.10). Under the appropriate conditions, the pores are straight and hexagonally packed,[48,49] as shown in Figure 4.9. The structural parameters are shown in Figure 4.11: the pore diameter is *D* and the lattice spacing is

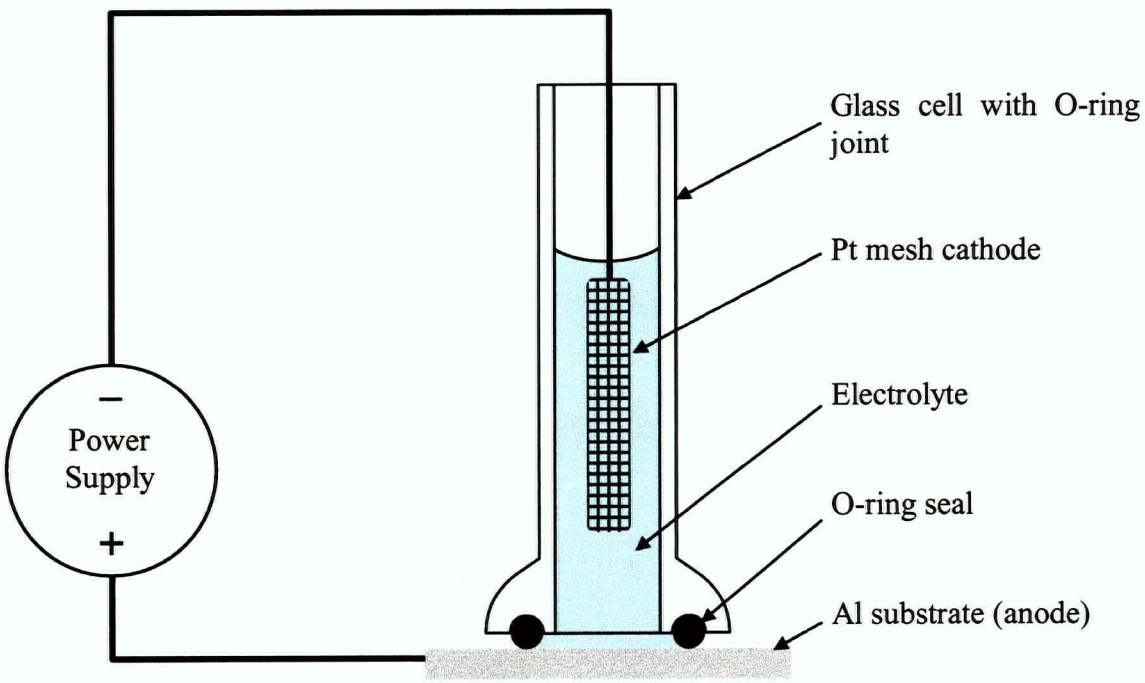

Figure 4.10 A simple electrochemical cell for anodization of aluminum substrates.

L. The oxide growth process leaves a barrier layer at the bottom of the pores with a thickness on the order of *L*/2.

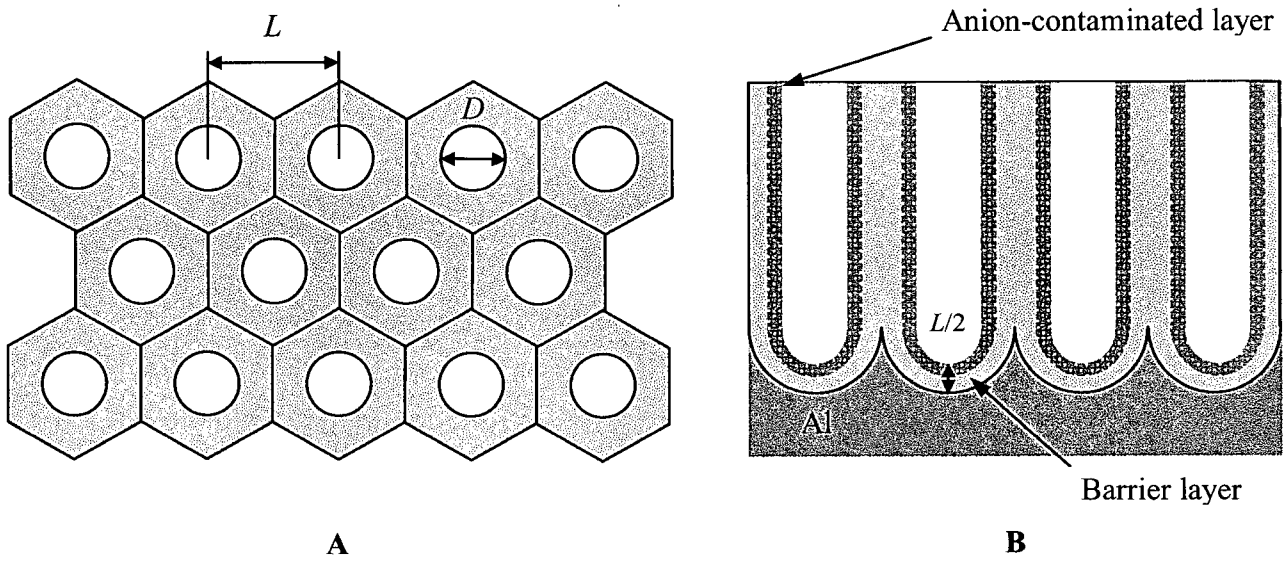

Figure 4.11 Structure of porous alumina films grown on aluminum: (a) geometry of pore packing, (b) cross-section showing barrier layer of thickness ~*L*/2 at bottom of pores.

4.4.1 Pore Wall Structure

The nature of the pore walls has been studied extensively. The results of many early studies have been reviewed by Thomson and Wood.[31] The pore walls consist of a relatively thick, amorphous, anion-contaminated surface layer over a more dense core of pure alumina. The two different zones of alumina can be readily distinguished in TEM micrographs of the material.[31,49,50] There exists considerable variation in anion incorporation among the different films prepared using sulfuric, oxalic, and phosphoric acids.[51] Using TEM and EDX,[50] the anion distribution has been shown to be uniform through the less dense layer. After washing, the distribution of anions in the cell wall is lowest in the pure alumina core, reaches a maximum within the less dense layer and falls off near the pore surface. This distribution can be the result of an initially uniform anion contamination, which is altered during the post-synthesis water

rinse by preferential removal of anions near the pore surface.[52,53] The nature of the anion contamination may be very important for electric device applications of porous alumina, as the anions may become mobile under high electric fields, causing electrical short-circuits or affecting the electrical properties of the polymer host. These anions may be removed completely by thermal treatment of the free-standing membrane.[54-59] Membranes prepared using oxalic acid as the electrolyte show the removal of oxalate ion over 200-400°C, with crystallization of the pore walls occurring at 820-840°C. When sulfuric acid is used as electrolyte, the contaminating anions are removed at 970°C.

4.4.2 Pore Growth Processes

A number of empirical relationships have been established for porous alumina growth:

(1) the spacing of the pores is proportional to the applied potential (2.5 to 2.8 nm V^{-1})[49];

(2) the pores form an ordered lattice at certain potentials for each electrolyte;

(3) the pore depth (film thickness) is proportional to the total charge passed (proportional to time under galvanostatic anodization).

While these empirical relationships have been thoroughly investigated, the processes which govern the growth of the pores are not fully understood. A qualitative analysis has been presented by Thompson and Wood.[31] In acidic electrolytes, pore formation must be the result of the concurrent oxidation of the aluminum to alumina and dissolution of the alumina by the electrolyte, along with a higher alumina dissolution rate in depressions. This suggests that field-assisted dissolution is a key driving force behind pore growth. A localized temperature increase at the metal-oxide interface due to Joule heating may also play a role in the process. The larger effect of electrolyte temperature on the film parameters indicates that local temperature variations do not have a dominating role in the process.

The pore structure may be further altered by etching with phosphoric acid, which attacks the alumina much faster than sulfuric acid or oxalic acid. The anion-contaminated layer is also attacked faster than the the more dense cell boundary. Typically, the pore walls are etched in 5 wt. % phosphoric acid at a rate of 8 nm h^{-1} at room temperature.[60]

4.4.3 Pore Lattice Formation

For a given electrolyte, self-ordering may be obtained over a range of applied potentials. Published values are shown in Table 4.1. Under these conditions, the pore lattice becomes ordered with a domain size between 1 and 4 μm. Below this range of potentials, there is considerable pore branching during the growth process. Thus not all pore sizes are readily accessible if an ordered pore lattice is desired.

The method for obtaining fully ordered structures consists of a two-step anodization process.[32,48,61] An initial long anodization period is carried out, until the pores are growing in the ideal arrangement at the metal/oxide interface. The oxide is then stripped using a phosphoric acid/chromic acid solution, where the chromic acid protects the aluminum substrate from dissolution once the oxide is removed (Figure 4.12). This leaves a scalloped surface that is

Table 4.1 Published parameters for self-ordered porous alumina growth.

Electrolyte	Concentration	Potential (V)	Temperature (°C)	Spacing (nm)	Reference
Oxalic acid	0.3 M	40	1	105	49,61
Sulfuric acid	20 wt %	18.7	1	50	62
Sulfuric acid	0.3 M	25	not reported	66.3	49
Sulfuric acid	20 wt %	15-25	1	41 – 68	63
Phosphoric acid	1 wt %	195	not reported	501	49

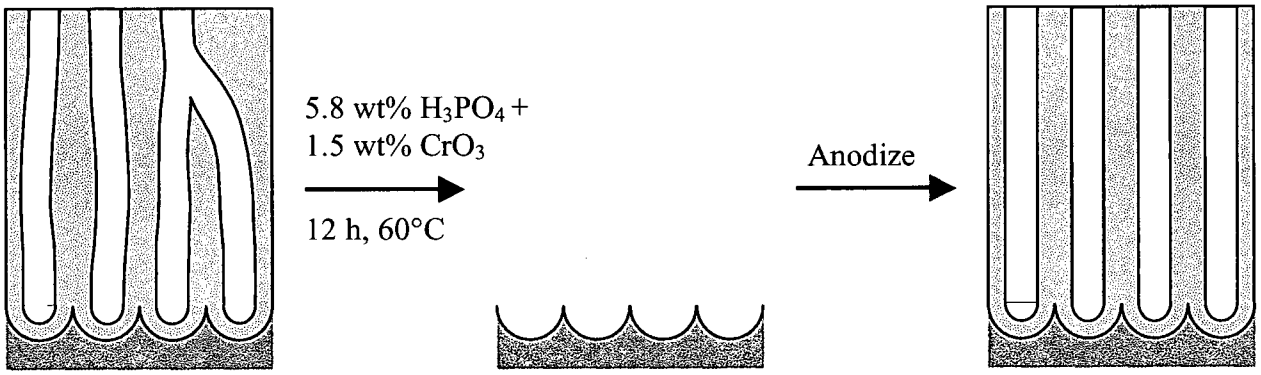

Figure 4.12 Preparation of fully-ordered porous alumina film by a two-step anodization process.The initial oxide layer is stripped, followed by further anodization of the substrate.

anodized in a second step for the desired duration, yielding a fully ordered film of the appropriate thickness. Masuda has elegantly shown that ordered pore growth is initiated by the scalloped surface by preparing similar nanoindentations on aluminum surfaces with a patterned SiC wafer[61] and with an atomic force microscope.[64] This nanoidentation technique allowed the fabrication of defect-free lattices on the mm scale. Masuda also reported that electrolyte concentration and temperature have no significant effect on the formation of the lattice.

The self-ordering of the pore lattice has also been the subject of several investigations but still remains to be understood.[47,49,62,65] It has been shown through computer simulation that ordered lattices can arise from initial pore formation on isolated defects,[51] given a fixed interpore spacing. However, the origin of the fixed lattice spacing remains unclear. The mechanical stress of expansion from aluminum to alumina has been suggested as a source of repulsive interaction between growing pores.[62] Nielsch *et al.* pointed out that all ordered porous alumina films have a 10% porosity (ratio of pore area to unit cell area) independent of the electrolyte and potential.[49] These points are discussed further below.

4.4.4 Preparation of Optimal Host from Porous Alumina

Porous alumina is evidently a very versatile material, as the pore size and spacing can be easily adjusted over a wide range and the thickness of the porous film is simple to control. Thin films may be prepared on various substrates by anodizing evaporated aluminum films of the correct thickness.[60] This also allows cross-sections for SEM to be prepared in a convenient manner.

The smallest pore size reported in the literature is 20 nm, obtained using 20 wt % sulfuric acid at 15 V.[63] There is a recent report of a membrane with 5 nm pore size[66] but it was simply obtained at a low potential without any ordering, and characterized indirectly by gas diffusion measurements. The conditions for the preparation of films with an ordered lattice of pores with diameters below 20 nm are not established in the literature. However, Moskovits reported unpublished results at a conference showing that the pore diameter could be very effectively reduced through manipulation of the electrolyte temperature.[67] In order to reach temperatures well below 0 °C, a mixture of methanol and water was used as the solvent.[68] Using 1.2 M sulfuric acid in a 3:1 mixture of methanol and water, pore sizes down to 4 nm could be reached at anodization temperatures of -40 °C.

In our hands, this approach was also successful. It was found that a 1:1 methanol:water mixture was effective as the solvent down to -50 °C. While keeping the anodization potential and electrolyte concentration constant, films were anodized at 20°C, -8°C and -40°C (Figure 4.13). The films anodized at 20°C and -8°C were observed by SEM, whereas the film obtained at -40 °C required a TEM to distinguish the pores. It can be seen that while the ordering is not perfect, the pore spacing does not vary significantly from 40 nm - the spacing is clearly fixed by the applied potential. The pore diameter, on the other hand, changes dramatically with temperature: from 21 nm at 20 °C to 4 nm at -40 °C (Figure 4.14).

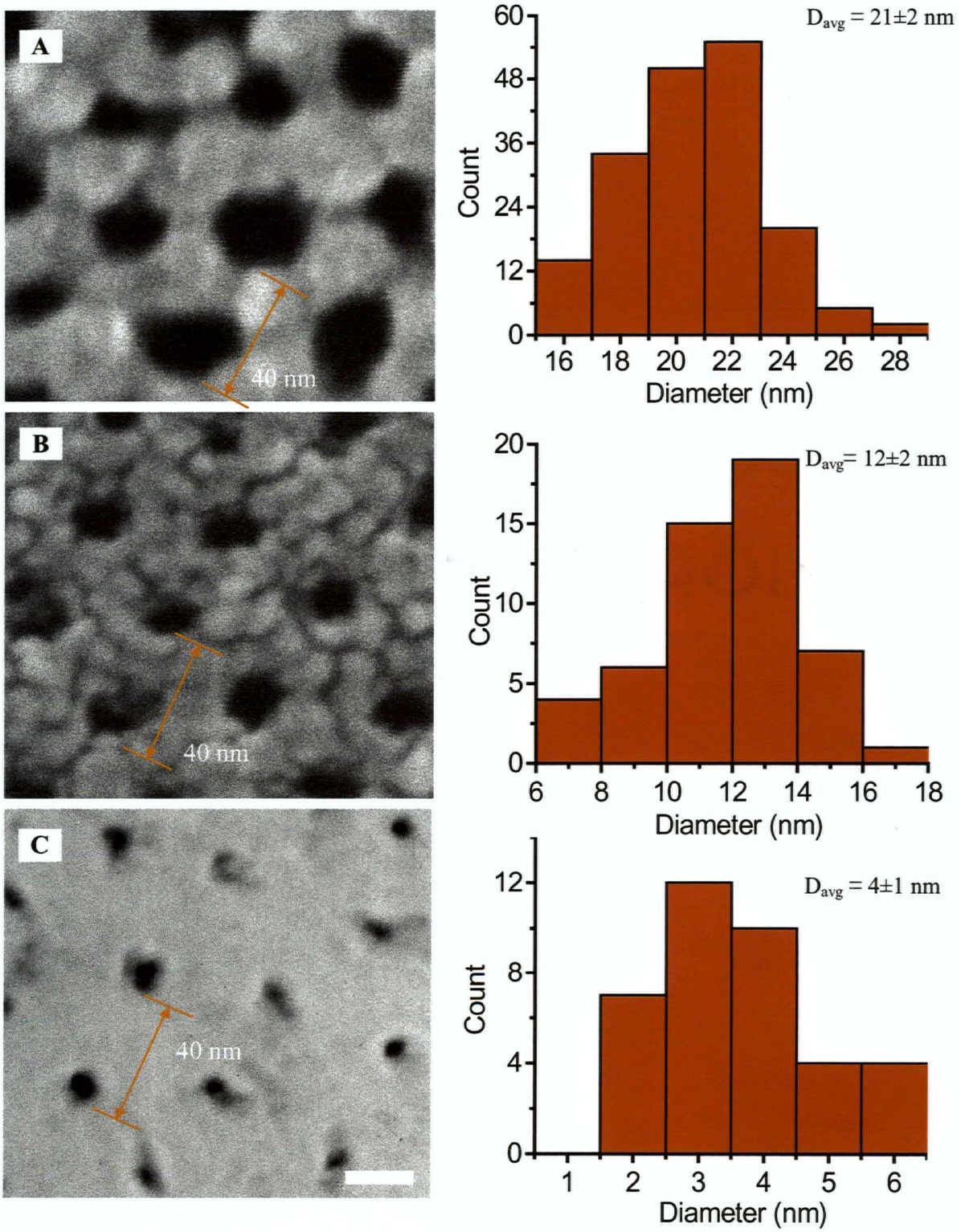

Figure 4.13 Porous alumina samples anodized at (a) 20 °C, (b) -8 °C and (c) -40 °C at 15.0 V in 1.2 M H_2SO_4 (1:1 H_2O:MeOH), with resulting pore size distributions. The scale bar is 20 nm.

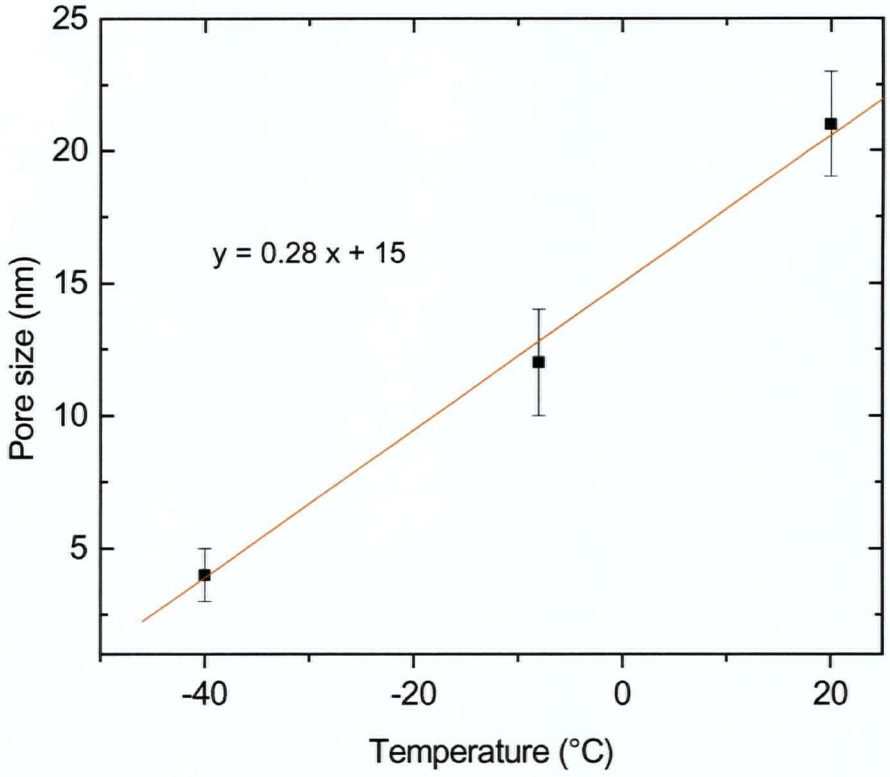

Figure 4.14 Effect of temperature on pore diameter for samples anodized at 15.0 V in 1.2 M sulfuric acid.

The effect of electrolyte concentration was also investigated by raising the concentration of sulfuric acid to 5.0 M. However, there was no effect on the pore size at fixed potential and temperature. This stands in contrast with the results of Patermarakis *et al.*, who reported that the square of the pore base diameter is inversely proportional to the proton activity at the base of the pore, based on room temperature data obtained galvanostatically with different concentrations of sulfuric acid.[53]

The samples anodized at -40°C clearly show some ordering. This fact allows some comment to be made on the proposal that the ordering of the pore lattice is driven by mechanical stress in the aluminum to alumina transformation. Their coefficients of thermal expansion are 23.1×10^{-6} K^{-1} and 8.4×10^{-6} K^{-1}, respectively.[69] This difference in expansion coefficients would suggest that any effects due to the stress of expansion would be very different at lower

temperatures, and any process dependent on this stress would be altered. The fact that the lattice spacing remains the same despite the change in temperature would argue against any dominating role for mechanical stress in the ordering process. Further experiments would be required to validate this hypothesis fully.

The drawback of anodizing at lower temperatures is that the anodization rate is reduced drastically. The current density declines to 10 $\mu A\ cm^{-2}$ at -40 °C and the oxide growth rate becomes ~200 nm/24 h. While this is much slower than normal anodization, it is not unreasonable for obtaining a film with a pore size that is otherwise difficult to fabricate. Moreover, since the spacing of the pores is the same at room temperature, the initial anodization of the two-step process for preparing highly-ordered films can be carried out at room temperature.

4.4.5 Barrier Layer Thinning

The barrier layer created during the anodization process (Figure 4.9) must be removed to allow electrical contact to the conjugated polymer guest. The aluminum substrate for the porous alumina film may itself be used as the cathode material. The requirement then is for a method to remove, or at least to thin significantly, the barrier layer present between the pores and the aluminum.

Phosphoric acid etching is the simplest approach to barrier layer removal, provided the aluminum substrate is removed and the film etched from the bottom.[32] Otherwise, ion milling with an argon-ion beam may be employed.[70] The practical limitation of this method is the diameter of the beam in the ion mill, which is on the order of 1 mm on the instrument available at UBC (VCR ion mill, Metals and Materials Engineering). This restricted the sample area which could be processed easily, making it impractical for device fabrication.

Reactive ion etching (RIE) may be used attack the alumina selectively and directionally, and this approach was investigated by Dr. K. Rademacher in our research group. In this approach, a boron trichloride/argon plasma is used to etch away the alumina. A carbon tetrafluoride/oxygen mixture can also be used to etch alumina,[71] but these gases were not readily available on the etcher at UBC. Applied from the bottom of the sample (with the aluminum removed by saturated $HgCl_2$), this method was found to open some pores. However, the conditions for opening the pores from the top of the sample were not found.

Barrier layer thinning may also be achieved by reducing the potential at the end of the anodization step. This can be executed either stepwise or gradually. If this is carried out stepwise,[72] pore-branching occurs as smaller pores nucleate at the bottom of the original pores; the branching leads to an inverted tree structure at the bottom of the anodized layer. This is used in the commercially-available Anodisc membranes to obtain 20 nm pore sizes. Better control of the rate of potential reduction leads to a small hole at the bottom of each pore.[73] It should be noted that extended anodization at very low potential (< 1 V) eventually leads to the separation of the alumina membrane from the aluminum substrate.

4.5 Conclusion

It was shown that a porous alumina host for conjugated polymers can be readily prepared with the desired properties. The formation of small diameter films was achieved using the low-temperature anodization method reported by Moskovits. The resulting films show aligned 1-D channels with a diameter of 4 ± 1 nm, and the barrier layer could be effectively thinned by a simple potential reduction method. However, many aspects of porous alumina film formation are still poorly understood, and it may be possible to improve the low temperature film growth rate by further exploring different combinations of electrolyte, temperature and anodization potential.

Experimental Details

1. SBA-2 Films[8,12]

The 16-3-1 gemini surfactant was synthesized according to the literature procedure[74]. Thin films with the SBA-2 structure were then grown on mica substrates. The reaction mixture was of the following molar composition: 1.0 H_2O: 0.076 HCl: 9.5×10^{-4} 16-3-1: 1.8×10^{-3} tetraethylorthosilicate. After 5 minutes of stirring, this mixture was transferred to a Teflon-lined stainless steel bomb. A freshly cleaved mica substrate was then floated upside down on the solution, and the sealed bomb was placed in an oven at 80°C for 16 h. After cooling to room temperature, the mica substrate was retrieved and rinsed with distilled water and dried in air. The surfactant was removed by calcination in air: the temperature was slowly raised to 540 °C over 18 h to avoid cracking the film, and held at 540°C for 6 h.

X-ray diffraction patterns were obtained on a Rigaku 6 kW powder diffractometer. Nitrogen physisorption measurements were carried out on a Micromeritics ASAP 2010 instrument at 77 K. Samples were embedded in EPON resin for ultramicrotomy with a diamond knife (Microstar).

2. FeO:SiO_2 System

A 3" sputtering target with a composition of 65:35 FeO:SiO_2 by powder mixing volume (Pure Tech) was used to prepare thin films on glass and silicon substrates by RF sputtering. This process produces a plasma in the working gas (argon), which then strips material from the target and deposits it on the substrate. It is an efficient way to deposit dielectric materials. The RF power was set to literature value, 200 W, while the argon pressure was 10 mTorr, the highest obtainable on the sputtering system being used. A sputtering time of 4 h yielded 200 nm-thick

films. The films were dark green in colour. The oxidation of the films was carried out at 600°C in air, resulting in a change of colour to red. Etching with 1:1 HCl:H_2O overnight produced a clear film. When cross-sections were required, 0.1 mm-thick coverslips (#0, E.M. Sciences) were used as the substrate. The cross-sections prepared by SAC were observed with a Hitachi H-800 TEM equipped with an X-ray detector for EDX analysis. The analysis area for EDX was selected by using the microscope in STEM mode and scanning over the area of interest only. Quantitative analysis of the EDX spectra was carried out using the ZAPTEM program, yielding a composition of 25% Fe, 12% Si and 63% O.

XPS analysis was performed on a Leybold MAX200 system using monochromated Al K_α radiation as the excitation source. The peaks were fitted using the XPSPEAK computer program (R. W. M. Kwok, Chinese University of Hong Kong). The Fe 2p, Si 2p and O 1s peaks were used to calculate atomic percentages: 12 % Fe, 13 % Si, 74 % O.

Nitrogen physisorption measurements were carried out on a Micromeritics ASAP 2010 instrument at 77 K. A 200 nm film was deposited onto coverslips with a total projected area of 60 cm^2. The approximate total surface area was 0.5 m^2, using an estimated porosity of 25% and the reported specific surface area of 800 $m^2\ g^{-1}$.

3. Porous alumina

Aluminum foil (99.99+%, Aldrich) was degreased in acetone, then rinsed with distilled water. No electropolishing was done. Aluminum thin films were prepared on n-type silicon substrates by electron-beam evaporation (with a base pressure of 2×10^{-6} Torr) from aluminum slugs (99.999%, Alfa Aesar) in a graphite crucible or RF sputtering (3" target, 99.99% purity, 300 W with 6 mTorr argon).

Anodization was carried out under the conditions given in the text. Most samples were anodized without any stirring of the electrolyte, although stirring will improve the ordering of the pore lattice. For the two-step process, the initially grown oxide layer was stripped by immersing the substrate in 5.8 wt. % H_3PO_4 + 1.5 wt. % CrO_3 at 50 to 60 °C overnight. Anodization was then continued at the initial conditions. Pore-widening was effected by 5% H_3PO_4 at 20 °C for the given periods. Low temperature anodization was carried out in a FTS Systems (Stone Ridge, N.Y.) Multi-Cool chiller.

Samples were coated with a thin layer of Au/Pd for SEM (Hitachi S-4700), typically with an accelerating voltage between 10 and 20 kV and a 6 mm working distance. Free-standing films and ultramicrotomed cross-sections were observed by TEM (Hitachi H-800 at 200 kV, Hitachi H-7600 at 80 kV). Pore size distributions were determined using the Scion Image computer program (Scion Corp., MD, www.scioncorp.com) or the equivalent ImageJ program (National Institute of Health, www.nih.gov). The pore diameters were calculated for a circle of area equivalent to the imaged pores.

Ar ion milling was done using a VCR Ion mill with 5 kV ion energy, 40 μA beam current and 90° angle of incidence. Reactive ion etching was done with a PlasmaQuest ECR etcher. To open a majority of pores from the bottom of the sample, the RF power was 150 W, the microwave power 300 W, and the substrate temperature was 48 °C. The gas flow rates for $Ar/BCl_3/Cl_2$ were 20.5/20.1/2.8 sccm, respectively. The etching time was 480 s.

References

1. Brinker, C. J. *Curr. Opin. Colloid Interface Sci.* **1998**, *3*, 166.

2. Edler, K. J.; Roser, S. J. *Int. Rev. Phys. Chem.* **2001**, *20*, 387.

3. Schuth, F. *Curr. Opin. Colloid Interface Sci.* **1998**, *3*, 174.

4. Tsapatsis, M.; Gavalas, G. R. *MRS Bull.* **1999**, *24*, 30.

5. Chiang, A. S. T.; Chao, K. J. *J. Phys. Chem. Solids* **2001**, *62*, 1899.

6. Miyata, H.; Kuroda, K. *J. Am. Chem. Soc.* **1999**, *121*, 7618.

7. Ryan, K. M.; Erts, D.; Olin, H.; Morris, M. A.; Holmes, J. D. *J. Am. Chem. Soc.* **2003**, *125*, 6284.

8. Yang, H.; Kuperman, A.; Coombs, N.; Mamicheafara, S.; Ozin, G. A. *Nature* **1996**, *379*, 703.

9. Yang, H.; Coombs, N.; Sokolov, I.; Ozin, G. A. *J. Mater. Chem.* **1997**, *7*, 1285.

10. Yang, H.; Coombs, N.; Dag, O.; Sokolov, I.; Ozin, G. A. *J. Mater. Chem.* **1997**, *7*, 1755.

11. Miyata, H.; Kuroda, K. *Chem. Mater.* **1999**, *11*, 1609.

12. Tolbert, S. H.; Schaffer, T. E.; Feng, J. L.; Hansma, P. K.; Stucky, G. D. *Chem. Mater.* **1997**, *9*, 1962.

13. Zhou, W. Z.; Hunter, H. M. A.; Wright, P. A.; Ge, Q. F.; Thomas, J. M. *J. Phys. Chem. B* **1998**, *102*, 6933.

14. Tsai, T. G.; Shih, H. C.; Liao, S. J.; Chao, K. J. *Microporous Mesoporous Mater.* **1998**, *22*, 333.

15. Chu, L.; Anderson, M. A. *J. Membr. Sci.* **1996**, *110*, 141.

16. Nishiyama, N.; Ueyama, K.; Matsukata, M. *Microporous Mater.* **1996**, *7*, 299.

17. Nishiyama, N.; Park, D. H.; Koide, A.; Egashira, Y.; Ueyama, K. *J. Membr. Sci.* **2001**, *182*, 235.

18. Raimondi, M. E.; Maschmeyer, T.; Templer, R. H.; Seddon, J. M. *Chem. Commun.* **1997**, 1843.

19. Firouzi, A.; Schaefer, D. J.; Tolbert, S. H.; Stucky, G. D.; Chmelka, B. F. *J. Am. Chem. Soc.* **1997**, *119*, 9466.

20. Tolbert, S. H.; Firouzi, A.; Stucky, G. D.; Chmelka, B. F. *Science* **1997**, *278*, 264.

21. Hillhouse, H. W.; Okubo, T.; van Egmond, J. W.; Tsapatsis, M. *Chem. Mater.* **1997**, *9*, 1505.

22. Kim, W. J.; Yang, S. M. *Chem. Mater.* **2000**, *12*, 3227.

23. Munoz, T.; Balkus, K. J. *J. Am. Chem. Soc.* **1999**, *121*, 139.

24. Balkus, K. J.; Scott, A. S.; Gimon-Kinsel, M. E.; Blanco, J. H. *Microporous Mesoporous Mater.* **2000**, *38*, 97.

25. Trau, M.; Yao, N.; Kim, E.; Xia, Y.; Whitesides, G. M.; Aksay, I. A. *Nature* **1997**, *390*, 674.

26. Kros, A.; Nolte, R. J. M.; Sommerdijk, N. A. J. M. *Adv. Mater.* **2002**, *14*, 1779.

27. Kondoh, S.; Iwamoto, Y.; Kikuta, K.; Hirano, S. *J. Am. Ceram. Soc.* **1999**, *82*, 209.

28. Thompson, G. E. *Thin Solid Films* **1997**, *297*, 192.

29. Berger, S. D.; Salisbury, I. G.; Milne, R. H.; Imeson, D.; Humphreys, C. J. *Philos. Mag. B* **1987**, *55*, 341.

30. Huo, Q. S.; Margolese, D. I.; Stucky, G. D. *Chem. Mater.* **1996**, *8*, 1147.

31. Thompson, G. E.; Wood, G. C. *Anodic films on aluminum*; Treatise on Materials Science and Technology; Academic Press: New York, 1983; Vol. 23, p. 205.

32. Masuda, H.; Nishio, K.; Baba, N. *Thin Solid Films* **1993**, *223*, 1.

33. Xu, C. X.; Xue, Q. H.; Zhong, Y.; Cui, Y. P.; Ba, L.; Zhao, B.; Gu, N. *Nanotechnology* **2002**, *13*, 47.

34. Gao, T.; Meng, G. W.; Tian, Y. T.; Sun, S. H.; Liu, X. O.; Zhang, L. D. *J. Phys.: Condens. Matter* **2002**, *14*, 12651.

35. Yang, Y.; Li, H. Y.; Chen, H. L.; Bao, X. M. *Chem. J. Chin. Uni.* **2002**, *23*, 768.

36. Hornyak, G.; Kroll, M.; Pugin, R.; Sawitowski, T.; Schmid, G.; Bovin, J. O.; Karsson, G.; Hofmeister, H.; Hopfe, S. *Chem. Eur. J.* **1997**, *3*, 1951.

37. Hoyer, P. *Curr. Opin. Colloid Interface Sci.* **1998**, *3*, 160.

38. Shelimov, K. B.; Davydov, D. N.; Moskovits, M. *Appl. Phys. Lett.* **2000**, *77*, 1722.

39. Routkevitch, D.; Bigioni, T.; Moskovits, M.; Xu, J. M. *J. Phys. Chem.* **1996**, *100*, 14037.

40. Yang, Y.; Chen, H. L.; Mei, Y. F.; Chen, J. B.; Wu, X. L.; Bao, X. M. *Solid State Commun.* **2002**, *123*, 279.

41. Masuda, H.; Ohya, M.; Asoh, H.; Nakao, M.; Nohtomi, M.; Tamamura, T. *Jpn. J. Appl. Phys., Part 2* **1999**, *38*, L1403.

42. Yokoo, A.; Notomi, M.; Suzuki, H.; Nakao, M.; Tamamura, T.; Masuda, H. *IEEE J. Quantum Elec.* **2002**, *38*, 938.

43. Li, A. P.; Muller, F.; Birner, A.; Nielsch, K.; Gosele, U. *Adv. Mater.* **1999**, *11*, 483.

44. Masuda, H.; Watanabe, M.; Yasui, K.; Tryk, D.; Rao, T.; Fujishima, A. *Adv. Mater.* **2000**, *12*, 444.

45. Nakao, M.; Oku, S.; Tanaka, H.; Shibata, Y.; Yokoo, A.; Tamamura, T.; Masuda, H. *Opt. Quantum Mater.* **2002**, *34*, 183.

46. Mikulskas, I.; Juodkazis, S.; Tomasiunas, R.; Dumas, J. G. *Adv. Mater.* **2001**, *13*, 1574.

47. Li, F. Y.; Zhang, L.; Metzger, R. M. *Chem. Mater.* **1998**, *10*, 2470.

48. Masuda, H.; Hasegwa, F.; Ono, S. *J. Electrochem. Soc.* **1997**, *144*, L 127.

49. Nielsch, K.; Choi, J.; Schwirn, K.; Wehrspohn, R. B.; Gosele, U. *Nano Lett.* **2002**, *2*, 677.

50. Ono, S.; Masuko, N. *Corros. Sci.* **1992**, *33*, 503.

51. Randon, J.; Mardilovich, P. P.; Govyadinov, A. N.; Paterson, R. *J. Colloid Interface Sci.* **1995**, *169*, 335.

52. Patermarakis, G.; Moussoutzanis, K.; Nikolopoulos, N. *J. Solid State Electrochem.* **1999**, *3*, 193.

53. Patermarakis, G.; Moussoutzanis, K.; Chandrinos, J. *J. Solid State Electrochem.* **2001**, *6*, 39.

54. Mardilovich, P. P.; Govyadinov, A. N.; Mazurenko, N. I.; Paterson, R. *J. Membr. Sci.* **1995**, *98*, 143.

55. Mardilovich, P. P.; Govyadinov, A. N.; Mukhurov, N. I.; Rzehvskii, A. M.; Paterson, R. *J. Membr. Sci.* **1995**, *98*, 131.

56. Ozao, R.; Ochiai, M.; Yoshida, H.; Ichimura, Y.; Inada, T. *J. Therm. Anal. Calorim.* **2001**, *64*, 923.

57. Ozao, R.; Ochiai, M.; Ichimura, N.; Takahashi, H.; Inada, T. *Thermochim. Acta* **2000**, *352*, 91.

58. Ozao, R.; Yoshida, H.; Ichimura, Y.; Inada, T.; Ochiai, M. *J. Therm. Anal. Calorim.* **2001**, *64*, 915.

59. Ozao, R.; Yoshida, H.; Inada, T. *J. Therm. Anal. Calorim.* **2002**, *69*, 925.

60. Crouse, D.; Lo, Y. H.; Miller, A. E.; Crouse, M. *Appl. Phys. Lett.* **2000**, *76*, 49.

61. Masuda, H.; Yamada, H.; Satoh, M.; Asoh, H.; Nakao, M.; Tamamura, T. *Appl. Phys. Lett.* **1997**, *71*, 2770.

62. Jessensky, O.; Müller, F.; U., G. *Appl. Phys. Lett.* **1998**, *72*, 1173.

63. Sulka, G. D.; Stroobants, S.; Moshchalkov, V.; Borghs, G.; Celis, J. P. *J. Electrochem. Soc.* **2002**, *149*, D97.

64. Masuda, H.; Kanezawa, K.; Nishio, K. *Chem. Lett.* **2002**, 1218.

65. Li, A. P.; Muller, F.; Birner, A.; Nielsch, K.; Gosele, U. *J. Appl. Phys.* **1998**, *84*, 6023.

66. Lira, H. D. L.; Paterson, R. *J. Membr. Sci.* **2002**, *206*, 375.

67. Moskovits, M., Canadian Society for Chemistry Conference, May 2000, Calgary, AB.

68. Ott, J. B.; Goates, J. R.; Waite, B. A. *J. Chem. Thermodyn.* **1979**, *11*, 739.

69. Lide, D. R., Ed. ***CRC Handbook of Chemistry and Physics;*** CRC Press: Boca Raton, 2000

70. Almawlawi, D.; Bosnick, K. A.; Osika, A.; Moskovits, M. *Adv. Mater.* **2000**, *12*, 1252.

71. Liang, J. Y.; Chik, H.; Yin, A. J.; Xu, J. *J. Appl. Phys.* **2002**, *91*, 2544.

72. Furneaux, R. C.; Rigby, W. R.; Davidson, A. P. *Nature* **1989**, *337*, 147.

73. Kukhta, A. V.; Gorokh, G. G.; Kolesnik, E. E.; Mitkovets, A. I.; Taoubi, M. I.; Koshin, Y. A.; Mozalev, A. M. *Surf. Sci.* **2002**, *507*, 593.

74. Zana, R.; Benrraou, M.; Rueff, R. *Langmuir* **1991**, *7*, 1072.

CHAPTER 5 Characterization of a Porous Alumina/MEH-PPV Composite Material

Composite materials based on porous alumina and conjugated polymers have been extensively investigated in our research group. A full characterization of these materials was important for understanding their properties, and the central goal was to establish the polymer distribution within the composite material on the nanometre scale. The initial experiments were aimed at investigating samples prepared by adsorbing the conjugated polymer poly[2-methoxy,5-(2′-ethylhexyloxy)1,4-phenylene vinylene) (MEH-PPV) from solution onto porous alumina (Figure 5.1).

This straightforward procedure yielded samples in which the presence of polymer was evidenced by the colour and fluorescent emission of the porous alumina layer (Figure 5.2). Confocal fluorescence microscopy was used to establish that MEH-PPV was distributed throughout the thickness of the porous alumina host with 0.1 μm resolution. However, the conjugated polymer could not be located with higher spatial resolution by either scanning electron microscopy (SEM) or transmission electron microscopy (TEM), owing to the poor beam contrast of the polymer guest. The vinylic carbons in MEH-PPV were readily stained by osmium tetroxide, as evidenced by the disappearance of the red-orange colour of the sample, but this did not improve the contrast in TEM or SEM, most likely due to the limited amount of polymer on the porous alumina surface.

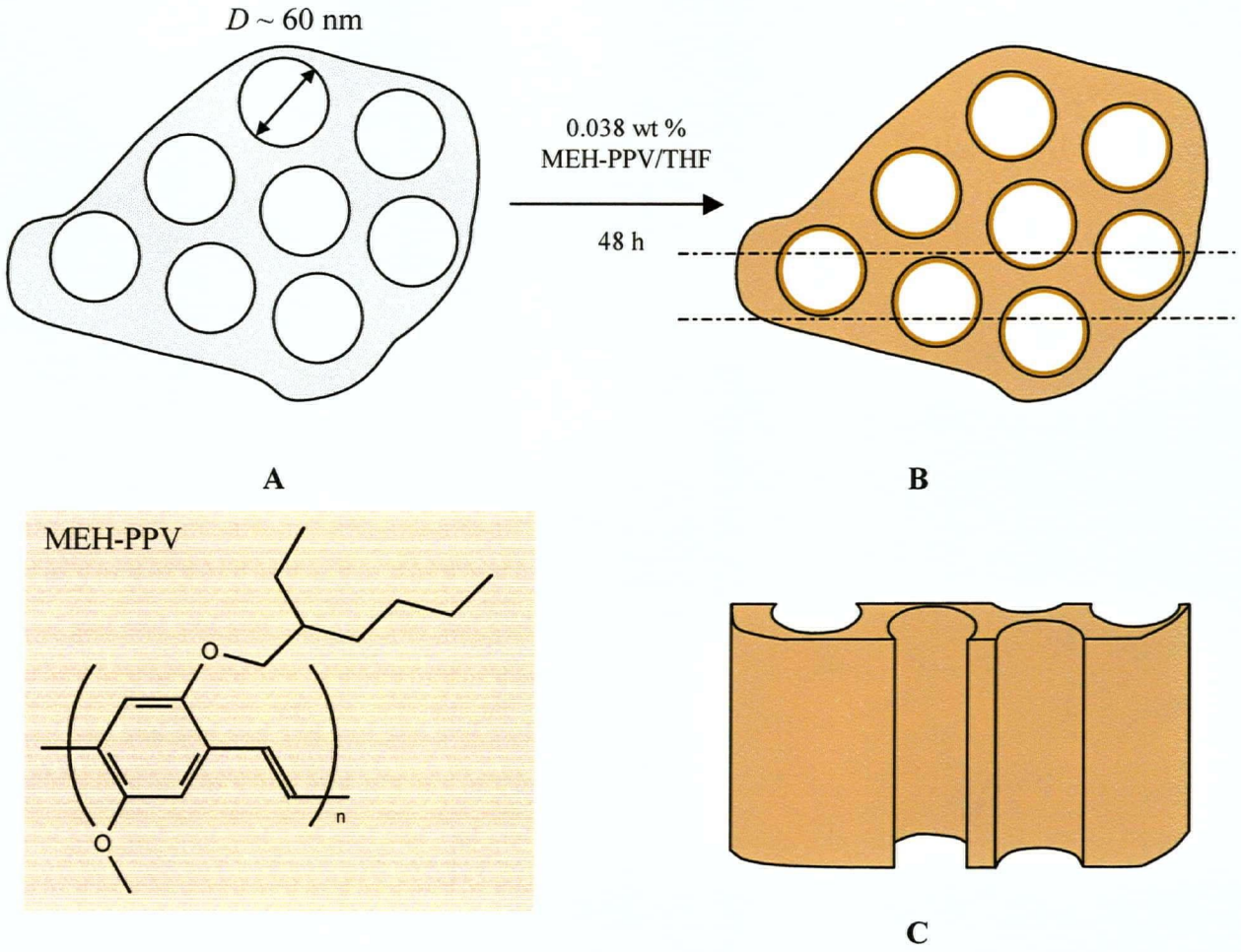

Figure 5.1 Adsorption of thin layer of MEH-PPV onto porous alumina host, showing (a) empty host, and polymer-coated host in (b) plan view and (c) as thin section for TEM.

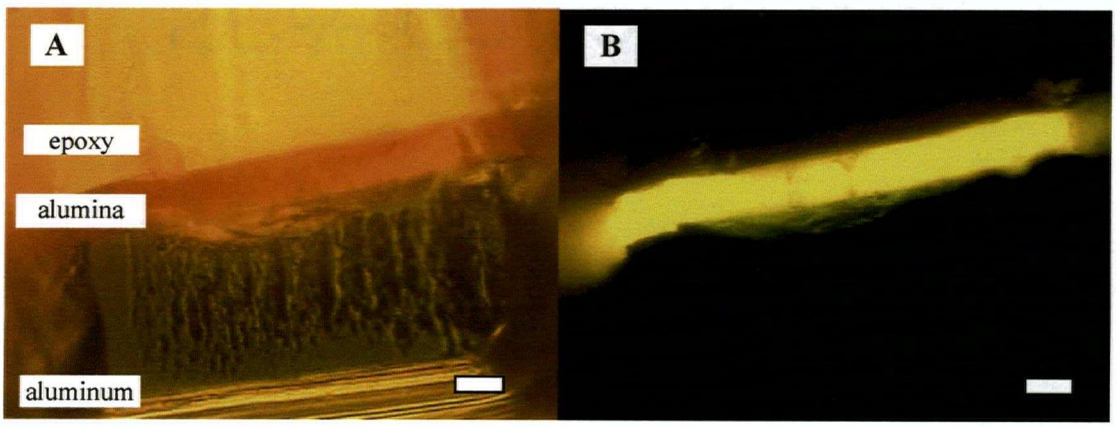

Figure 5.2 Porous alumina film after soaking in MEH-PPV solution, seen in cross-section, as shown by (a) light microscopy (b) fluorescence microscopy. The scale bar is 10 μm. Samples and images prepared by Dr. K. Rademacher.

There were no previously published studies of porous alumina films by EELS at the outset of this work; subsequently, a very relevant study of epoxy infiltration into porous alumina appeared in the literature.[1] In that work, the distribution of carbon, aluminum and oxygen was mapped by STEM/EELS using the corresponding ionization edges. The samples were also held at -134 °C using a cryogenic holder to minimize beam damage to the sample.

In principle, the porous alumina/MEH-PPV sample could have been mapped in the same manner as PPV/MCM-41 (chapter 3) through the use of the 7 eV π plasmon. The carbon K-edge could also have been used. Neither of these methods was successful but the experiments did produce some interesting results for further investigation.

5.1 EELS Samples

Two geometries are possible for investigating the porous alumina/MEH-PPV composite materials by EELS: the plan geometry (Figure 5.1(b)) and the cross-section (Figure 5.1(c)). The cross-sections may be prepared by ultramicrotomy, yielding thin sections (~30 nm thick) of the material. As the samples were known to contain very little polymer – possibly as little as a monolayer on the surface of the pores – this geometry would present a very small amount of polymer to the electron beam. In chapter 7, this geometry is investigated for samples with larger amounts of polymer.

It was deemed advantageous to investigate these particular samples in the plan geometry initially, such that the electron beam would pass down the pores and interact with all the polymer distributed along the length of the pores.

A number of samples were prepared for EELS measurements. In order to obtain the clean loss spectrum of MEH-PPV, thin film samples were prepared by casting from THF over water

and collecting the resulting film with a lacey carbon grid. The empty host material consisted of porous alumina membranes (0.2 and 1.4 μm thick), and the composite material investigated was a 1.4 μm porous alumina membrane which had been soaked in MEH-PPV.

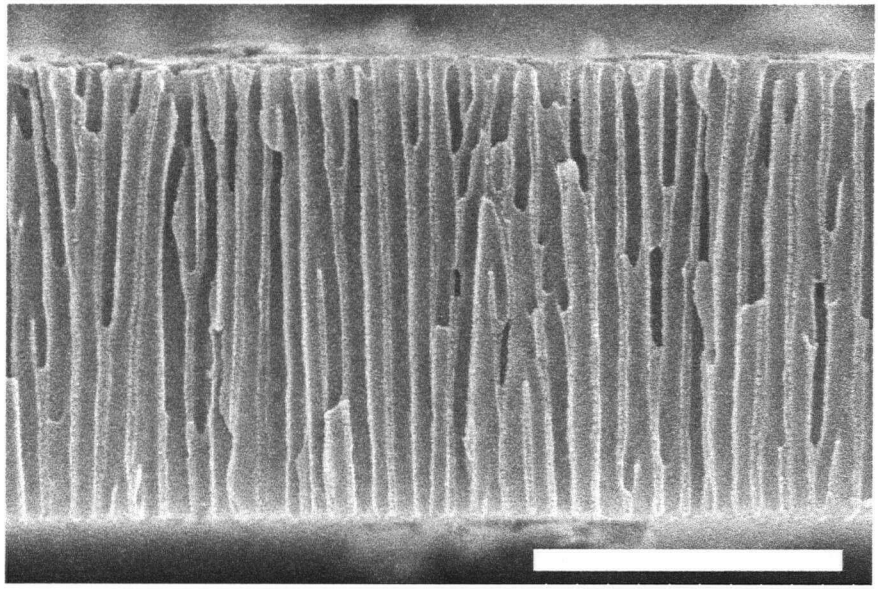

Figure 5.3 SEM image of cross-section of sample for EELS experiments. The scale bar is 1.0 μm.

5.2 MEH-PPV Low-Loss Spectra and Zero-Loss Peak Removal

The initial investigation of MEH-PPV focused on the low-loss spectrum and the distinctive π-π^* plasmon of conjugated organic materials. The bright field TEM image of the MEH-PPV film is shown in Figure 5.4, and the collected loss spectrum is in Figure 5.5. The π-π^* plasmon was seen clearly at 6.4 eV, whereas the bulk plasmon appeared at 22 eV, as anticipated for an aromatic material. However, there were no initially discernible features associated with the onset of optical absorption of the polymer chain at ~3 eV, largely due to the tail of the zero-loss peak. For these experiments, a clean zero-loss peak was not recorded immediately, and later acquisition yielded a peak with a significantly different shape. Hence a number of different

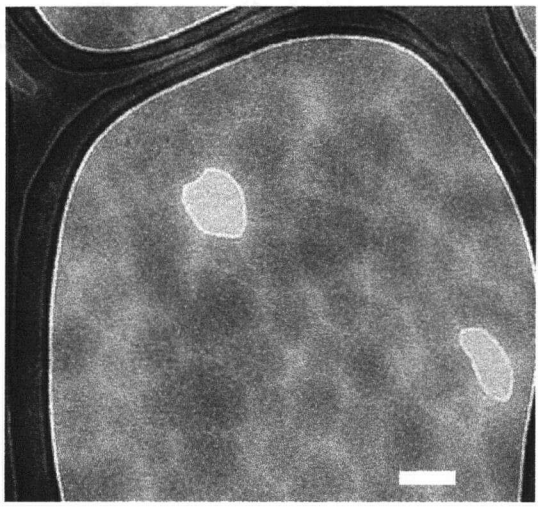

Figure 5.4 TEM image of MEH-PPV film supported by a lacey carbon grid. The scale bar is 100 nm.

approaches to removing the zero-loss peak from the spectrum were evaluated, as the tail of the zero-loss peak affects most of the features below 10 eV. The possible approaches include Fourier-log deconvolution,[2] matrix deconvolution,[3] extrapolation of the tail by a power-law fit and direct subtraction of the zero-loss peak.[4] These procedures were implemented as Visual Basic for Excel[5] scripts. Fourier-log and matrix deconvolution were based on FORTRAN programs presented by Egerton,[2] while the power-law fit was a simple linear least-squares regression procedure.

Fourier-log deconvolution was found to remove the effect of plural scattering very well, but it did introduce some artefacts near 4 eV, where the routine chooses the separation point between the zero-loss peak and the remainder of the spectrum. The algorithm was not designed to deal with spectra showing substantial losses on the tail of the zero-loss peak. This could have also been avoided by acquiring a clean zero-loss spectrum separately.

Matrix deconvolution did not remove the zero-loss peak very effectively but did remove the plural scattering smearing out the bulk plasmon peak. As such it was not very useful for examination of the spectrum over the 2 to 5 eV range.

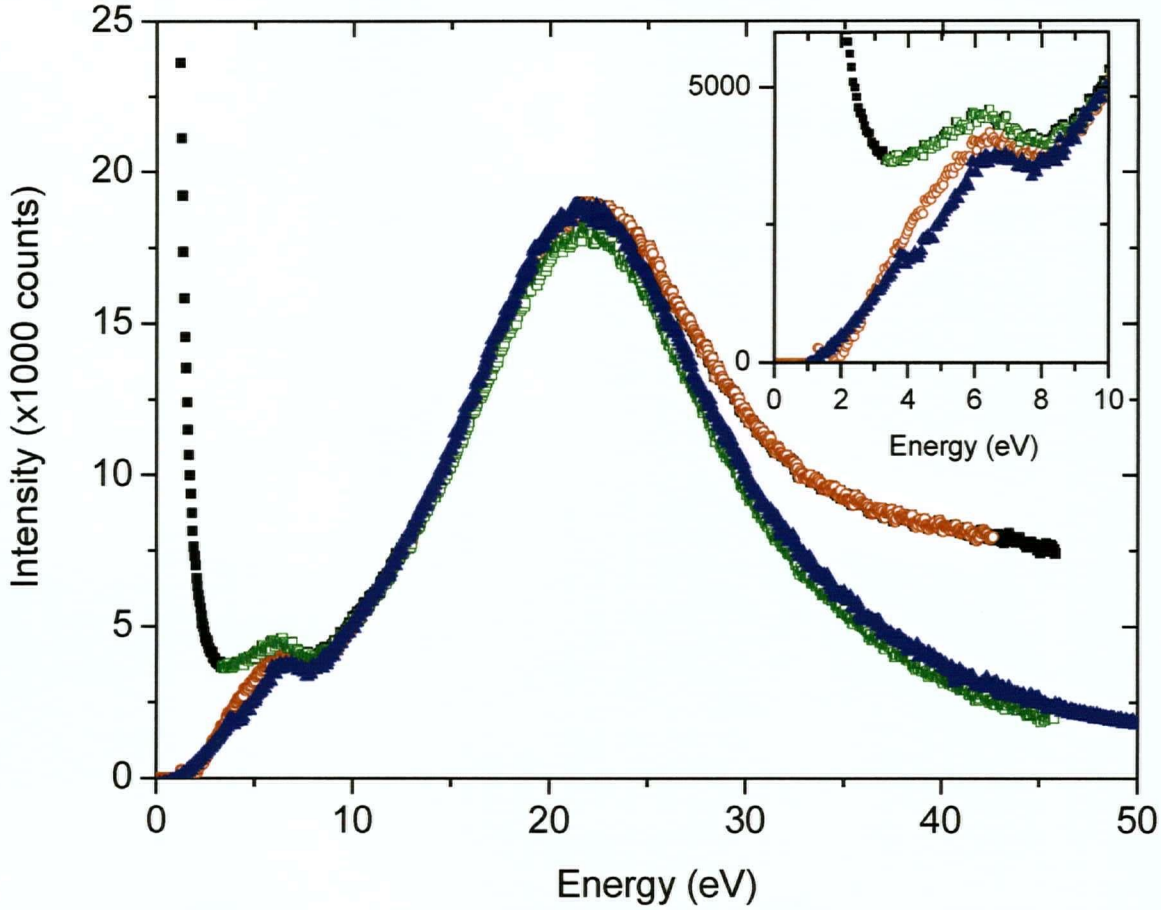

Figure 5.5 Low-loss spectrum of MEH-PPV thin film, also showing various approaches to removing the zero-loss peak: (■) raw data, (□) matrix deconvolution, (▲) Fourier-log deconvolution, (○) power law fit over 1.3 - 2.0 eV. The inset shows the detail over 0 - 10 eV.

Direct subtraction of the zero-loss peak can be applied in a very accurate way by the use of spline interpolation and curve-fitting techniques, as has been reported recently.[4] This method seemed to be the most reliable for revealing weak spectral features in the 2 to 5 eV range. However, it again required an accurate spectrum of the clean zero-loss peak; the lack of this information made it impossible to apply to the data presented here.

Finally, the power-law fit does not address plural scattering but does remove the tail of the zero-loss peak fairly smoothly, with minimal artefacts in the 2-5 eV range. The possibility of a weak shoulder feature being fitted out by this procedure cannot be ruled out, however (later

experiments showed that such a shoulder was present in some of the spectra – see section 6.5). Nevertheless, this approach seemed the most reliable one and as such, the power-law fit was used to process all the spectra, using least-squares linear regression to calculate the curve parameters. The implementation as a script allowed large numbers of spectra to be processed easily.

5.3 Porous Alumina Low-Loss Spectra

The low-loss spectrum of porous alumina (Figure 5.6) showed a bulk plasmon at 23 eV, which is in agreement with the literature value for amorphous alumina.[6] Crystalline alumina presents a plasmon at a slightly higher energy (26 eV).[2] This confirmed the amorphous nature of the pore walls, as reported in the literature from TEM observations.[7,8] Additional loss modes appear below the bulk plasmon: one or two below 10 eV, and one at 13 eV. The nature of these additional modes has not been fully established in the literature; it has been suggested that they are due to an aluminum(0) surface plasmon which would arise from a deviation from the ideal alumina stoichiometry,[6] but this is very unlikely for porous alumina. Reduction of alumina to aluminum by the electron beam is not observed in amorphous alumina, as aluminum atoms are removed preferentially over oxygen atoms.[9]

The presence of these additional loss modes, especially the ones below 10 eV, presents a difficulty as they would possibly mask the conjugated polymer π-π^* plasmon near 6 eV. Under these circumstances, it was necessary to study these additional loss modes in more detail.

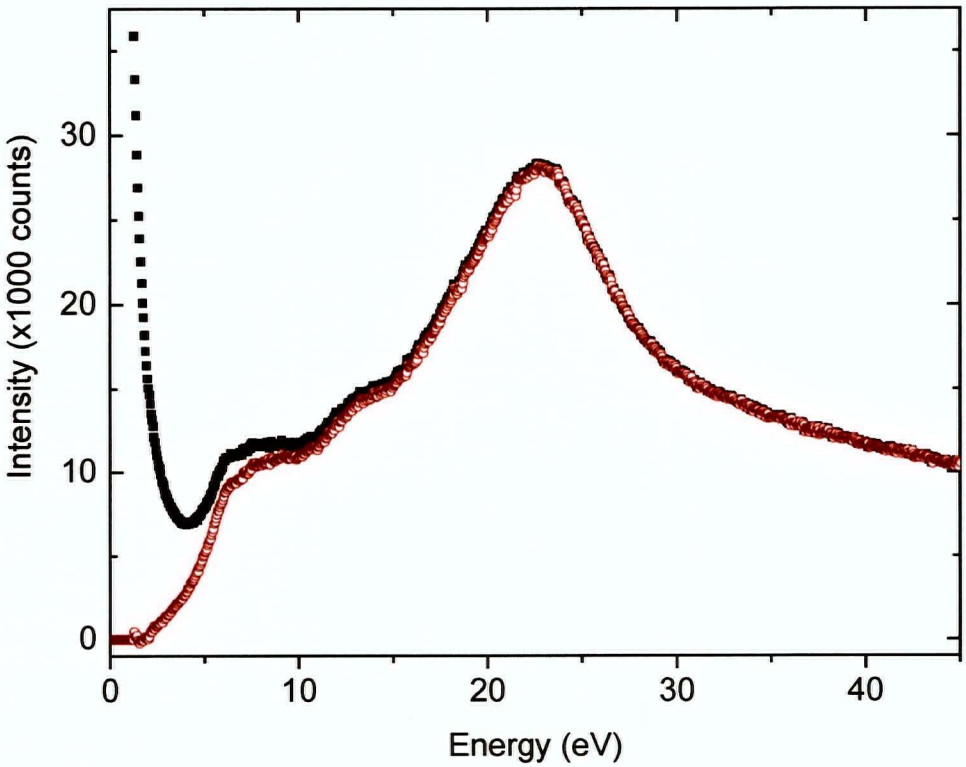

Figure 5.6 Low-loss spectrum of pore in porous alumina film, showing (■) collected data and (○) data with zero-loss peak removed by a power law fit over 1.3 to 2.0 eV.

The distribution of all the loss modes in a pore was determined by acquiring loss spectra at regular intervals over a line crossing a pore in STEM mode (Figure 5.7). This revealed a strong loss mode near the pore wall, some additional loss modes at intermediate distances from the wall, and one loss mode which extended at nearly constant level throughout the pore. Typical spectra for these three regimes are shown in Figure 5.8:

(a) at the wall, the alumina bulk plasmon is seen at ~22 eV, with a strong tail due to plural scattering;

(b) at ~7 nm from the wall, three surface plasmons at 8, 13 and 18 eV appear, with an additional shoulder at 7 eV; the shoulder at 3 eV is probably an artifact due to zero-loss peak subtraction;

(c) at ~ 23 nm from the wall, a strong peak at 7 eV is seen, and the surface plasmons are still seen as weaker shoulders.

These peak positions are most likely only accurate to about 1 eV, due to the presence of overlapping peaks and a substantial background due to plural scattering.

The distribution of these low-loss modes can also be visualized by EFTEM, as shown in Figure 5.9 for a thinner (0.2 μm) porous alumina film. The filtered images confirm that the 7 eV mode is weaker but evenly distributed throughout the hole. The losses at 13 eV are seen to be confined to the neighbourhood of the surface, and the bulk plasmon can be seen throughout the film and just outside the surface. The distribution of the 22 eV losses also shows the areas of lower and higher wall density: the material mostly consists of low density alumina with a higher density core forming a lattice between the pores.[8]

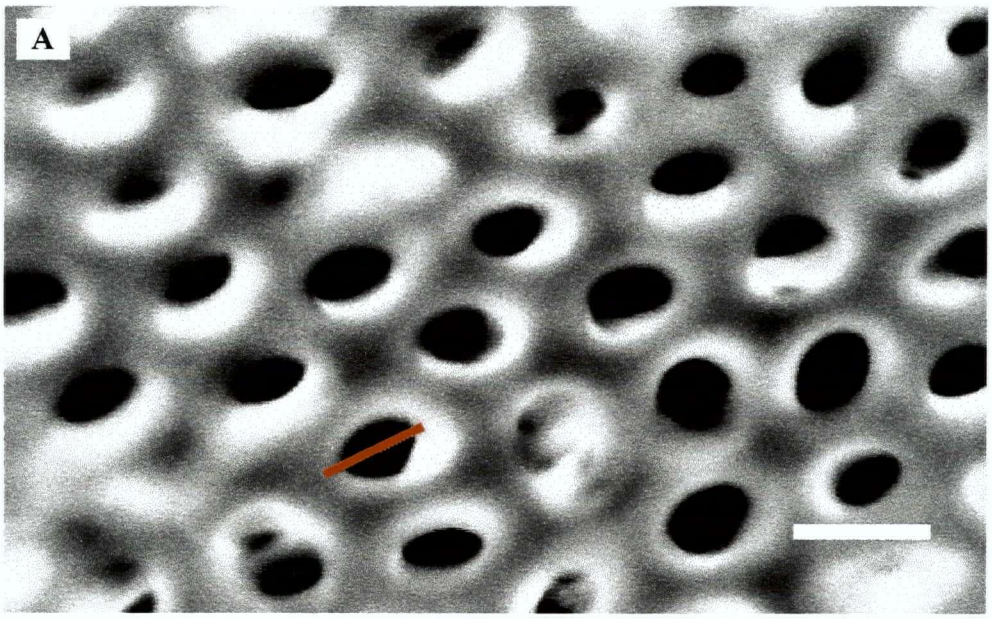

Figure 5.7 (a) STEM dark-field image of 1.4 μm thick porous alumina film, showing the location of line along which loss spectra were acquired at 2 nm intervals. The scale bar is 100 nm.

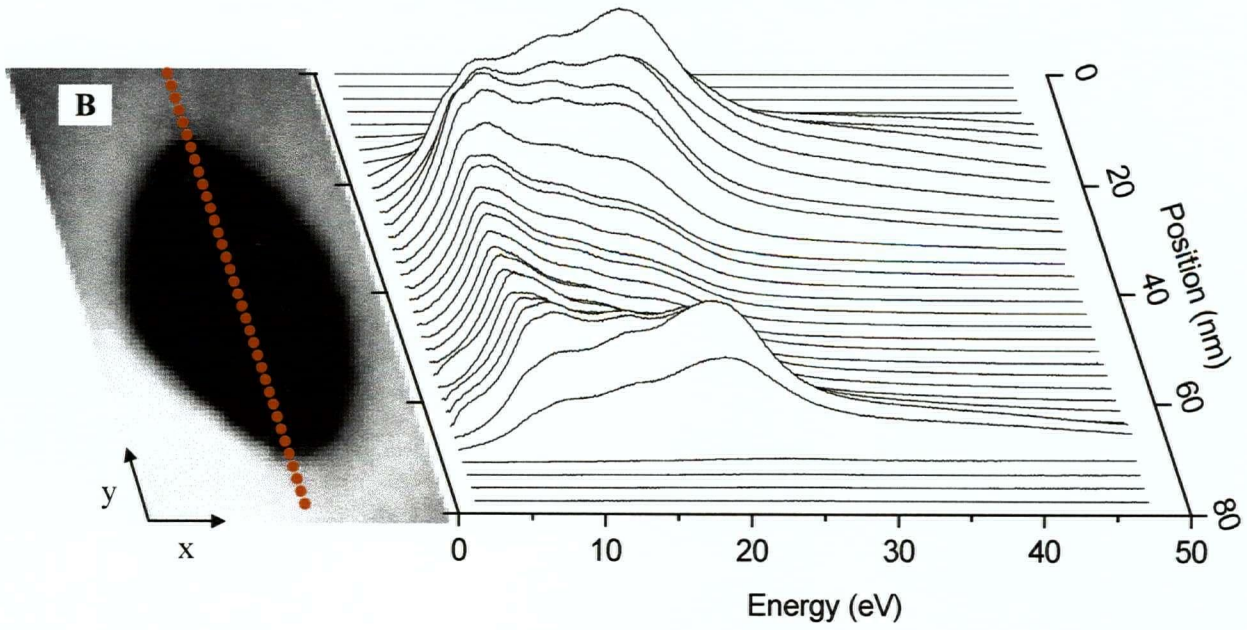

Figure 5.7 (b) Detail of analysis line and spatially-resolved low-loss spectra of porous alumina film. The zero-loss peak was removed by a power-law fit.

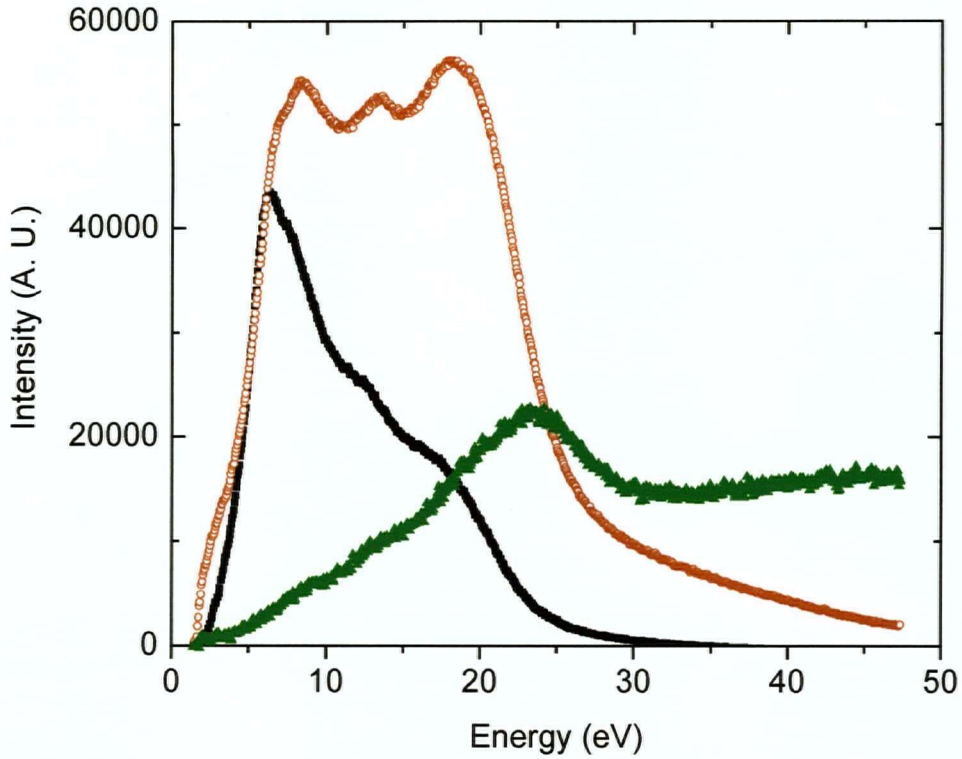

Figure 5.8 Representative low-loss spectra for porous alumina film: (■) near pore centre, (○)~7 nm from pore wall, and (▲) at wall.

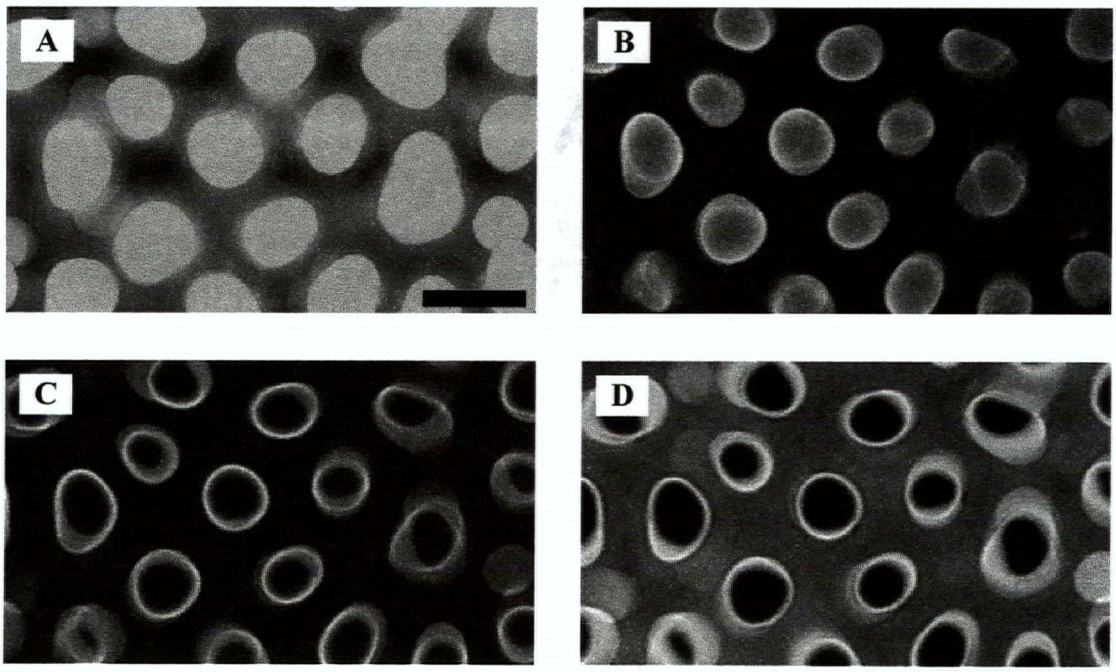

Figure 5.9 Energy-filtered images of 0.2 μm porous alumina film, using a 2 eV window: (a) 0 eV, (b) 6 eV, (c) 13 eV, (d) 22 eV. The scale bar is 100 nm.

5.4 Porous Alumina/MEH-PPV Composite Spectra

The spatial distribution of the low-loss spectra in a porous alumina/MEH-PPV composite material was obtained in the same manner, as shown in Figure 5.10. The distribution of loss modes was very similar to that of empty porous alumina host. The same strong peak at 7 eV was observed over the centre of the pore, but with no shoulder peaks at higher energies. At intermediate distances, the surface plasmons were identical to those of the empty porous alumina. The small differences observed in these modes may reflect the presence of polymer; detailed modelling of these effects would however require knowing the dielectric function of MEH-PPV to at least 10 eV, and at present it is only known to 5 eV.[10] In principle, this could be determined from a carefully measured MEH-PPV loss spectrum; however that was deemed beyond the scope of this thesis.

The near-wall spectra are shown in more detail in Figure 5.12. The low signal-to-noise level does not allow any significant conclusions to be made about the presence of the polymer through the π plasmon.

Some attempts were made to find the carbon K-edge loss near 280 eV but without any success. This approach has been shown to be successful for mapping epoxy penetration into porous alumina;[1] therefore the absence of the signal near 280 eV can be ascribed to the low amount or rapid degradation of the polymer in the samples investigated.

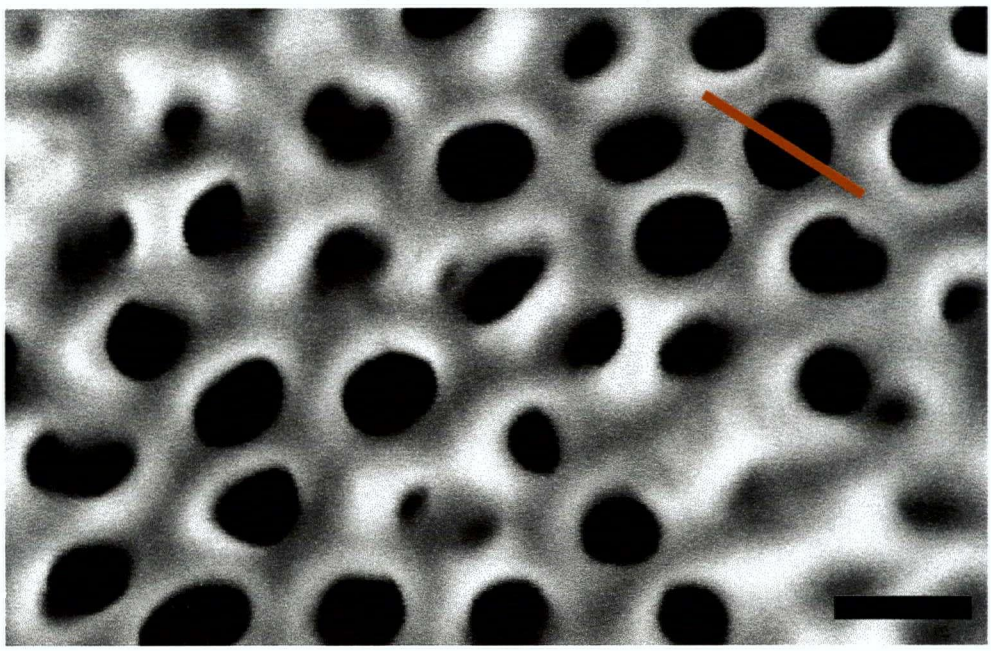

Figure 5.10 (a) STEM dark-field image of porous alumina/MEH-PPV composite, showing the line along which EEL spectra were acquired. The scale bar is 100 nm.

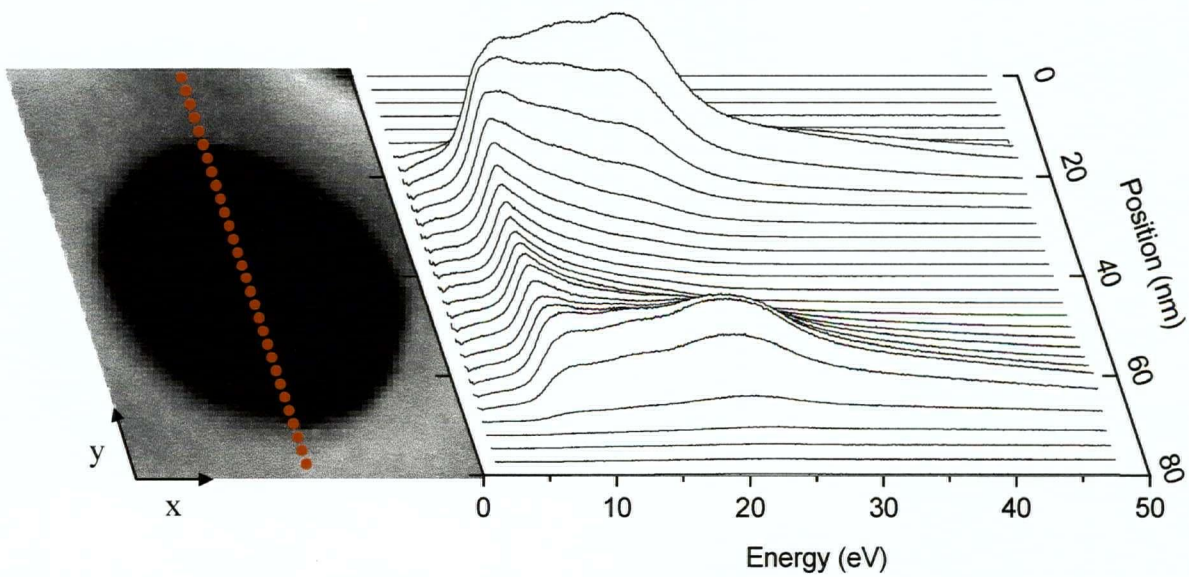

Figure 5.10 (b) Detail of analysis line and spatially-resolved low-loss spectra of porous alumina/MEH-PPV composite film. The zero-loss peak was removed by a power-law fit from 1.3 to 2.0 eV.

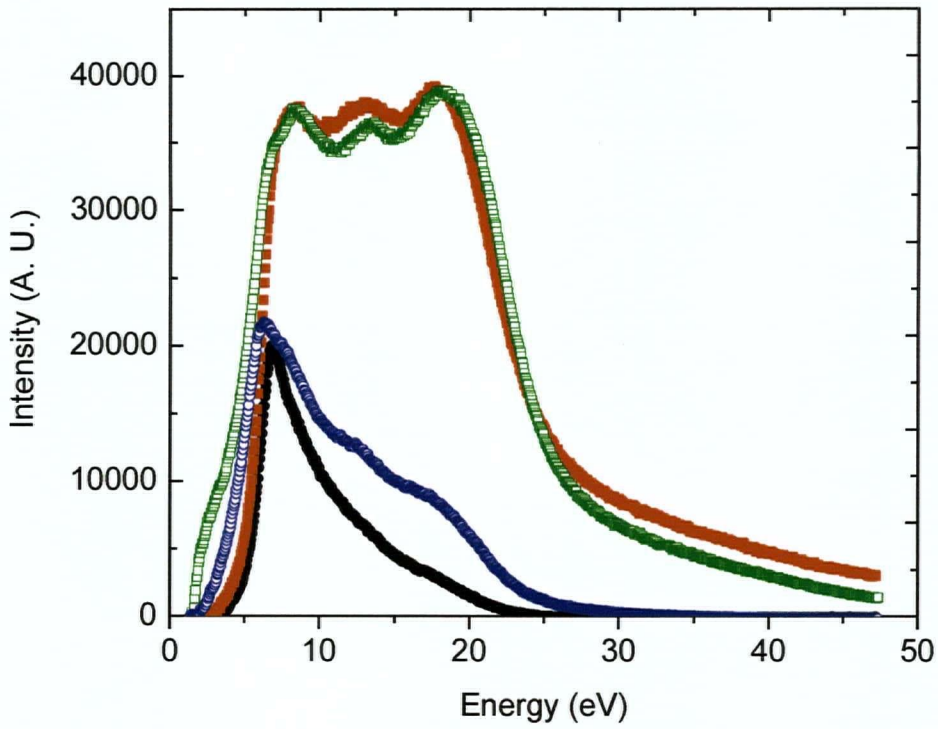

Figure 5.11 Comparison of low-loss spectra (○,●) near pore axis and (□,■) at ~7 nm from the pore wall, for porous alumina and porous alumina/MEH-PPV composite, respectively.

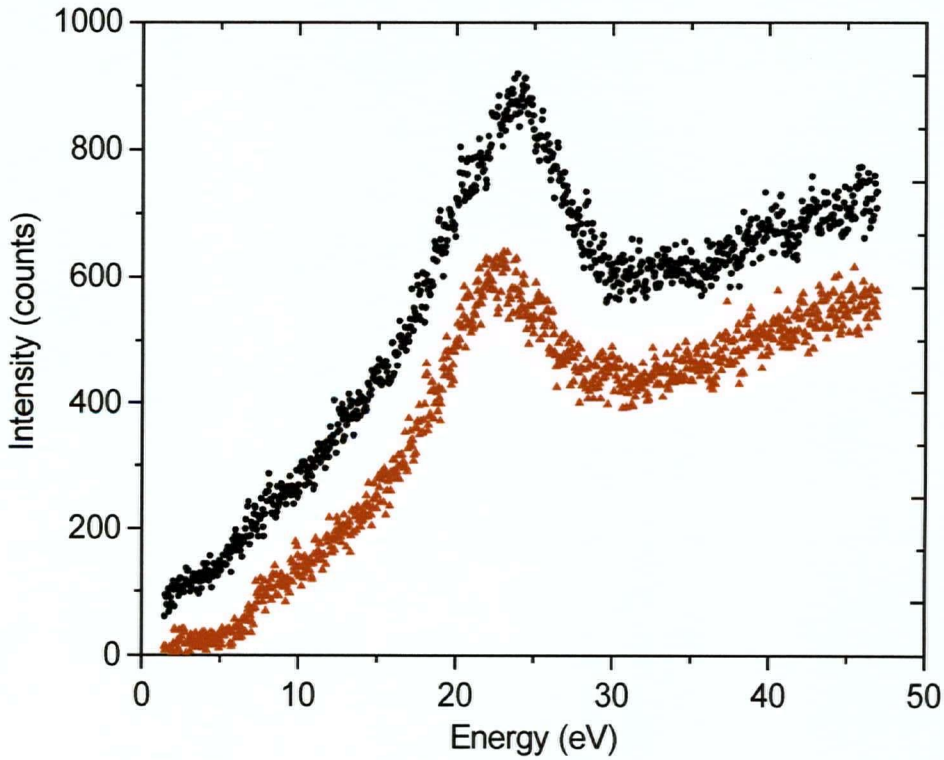

Figure 5.12 Comparison of low-loss spectra of empty (•) and MEH-PPV-treated (▲) porous alumina, nearest to pore wall.

5.5 Conclusion

Although the use of the π-π^* plasmon to identify conjugated organic molecules by EELS and EFTEM is well established, its application to the porous alumina/MEH-PPV composite in the plan geometry was not successful. Low-energy surface plasmons and an unexpected long-range interaction at 7 eV effectively masked the region of interest; the difficulty was compounded by the small amount of polymer present in the composite.

The effect of surface plasmons would have been minimized by employing a cross-sectional geometry instead. A larger polymer content in the composite would have also provided a stronger plasmon loss peak. Such samples are investigated by the same methods in chapter 7.

However, the most interesting feature arising from these results is indeed the loss peak at 7 eV. The nature of this interaction was studied in more detail and is the subject of the following chapter.

Experimental Details

Porous alumina thin films were prepared by anodizing 0.2 and 1.0 μm thick aluminum films evaporated onto *n*-type silicon(111) wafers by e-beam evaporation.[11] The anodization was carried out in 0.3 M oxalic acid at 20 °C with an applied potential of 40.0 V, using a glass cell with an O-ring seal to the sample. Upon completion of the anodization, the porous alumina film (1.4 μm thick) had detached from the substrate, but was still attached to the surrounding aluminium film. The barrier layer was removed by etching in 5 wt. % phosphoric acid for 40 min. The film was rinsed with distilled water, followed by ethanol and then dried. Some films were soaked in a solution of MEH-PPV (0.038 wt. % in THF) for 48 h. A diamond scribe was used to cut the porous alumina film to fit a 3mm Cu TEM grid, to which it was fixed using a

small amount of epoxy glue. MEH-PPV films were cast over water from a 0.05 wt % solution in THF and collected with a holey carbon grid (Ted Pella Inc.).

Osmium tetroxide staining was carried out before embedding the samples epoxy for ultramicrotomy. Samples were exposed to osmium tetroxide vapour by placing them next to a drop of 4% aqueous solution in a covered dish for 30 min. Direct immersion in this solution was also used.

Thin sections were obtained by ultramicrotomy. The samples were first sputter-coated with Au/Pd to prevent epoxy penetration into the porous alumina. The embedding medium was either EPON epoxy (various suppliers) or 302-3M epoxy (Epotek, Inc.). Sectioning was then carried out using a diamond knife with a 45° edge set with a 4 to 6° clearance angle, using water as the section collecting liquid.

Electron energy-loss spectroscopy was carried out on a Philips CM 20 TEM at CANMET/Natural Resources Canada equipped with a Schottky field-emission electron gun operated nominally at 200 kV, but lowered to 197 kV for spectroscopy. Measurements were made with a Gatan Imaging Filter using a dispersion of 0.05 eV/channel on a 1024-channel detector, covering -5 to 45 eV losses. Spatially-resolved spectra were collected at regular intervals with an estimated probe size of < 1 nm and an energy resolution of 1.0 eV (FWHM of zero-loss peak).

References

1. Arayasantiparb, D.; McKnight, S.; Libera, M. *J. Adhes.* **2001**, *76*, 353.

2. Egerton, R. F. *Electron energy-loss spectroscopy in the electron microscope*; 2nd ed.; Plenum Press: New York, 1996.

3. Su, D. S.; Schattschneider, P. *J. Microsc.* **1992**, *167*, 63.

4. Reed, B. W.; Sarikaya, M. *Ultramicroscopy* **2002**, *93*, 25.

5. Microsoft; Redmond, WA.

6. Kapsa, R.; Stara, I.; Zeze, D.; Gruzza, B.; Matolin, V. *Thin Solid Films* **1998**, *317*, 77.

7. Thompson, G. E.; Wood, G. C. *Anodic films on aluminum*; Treatise on Materials Science and Technology; Academic Press: New York, 1983; Vol. 23, p. 205.

8. Nielsch, K.; Choi, J.; Schwirn, K.; Wehrspohn, R. B.; Gosele, U. *Nano Lett.* **2002**, *2*, 677.

9. Berger, S. D. *Philos. Mag. B* **1987**, *55*, 341.

10. Tammer, M.; Monkman, A. P. *Adv. Mater.* **2002**, *14*, 210.

11. Crouse, D.; Lo, Y. H.; Miller, A. E.; Crouse, M. *Appl. Phys. Lett.* **2000**, *76*, 49.

CHAPTER 6 Aloof Cherenkov Effect in Porous Alumina

The unexpected low-loss spectral feature observed by electron energy-loss spectroscopy (EELS) in the centre of the pores of porous alumina films, as described in chapter 5, warranted further investigation. Several aspects of this feature were unusual: the lack of plural scattering, the rather large distances – up to 30 nm – from the pore wall at which it was still present without very much decay in intensity, and the fact that it appeared in the spectral region usually dominated by the optical properties of the material undergoing analysis. These characteristics suggested that the observed feature was not a surface plasmon. Preliminary discussions with theoreticians experienced with modelling EELS suggested that the most plausible hypothesis for its origin was rooted in the Cherenkov effect. A collaborative effort was then undertaken to validate this hypothesis. This chapter describes the further experimental and theoretical results that were used to show that the Cherenkov effect is responsible for these losses.

In this chapter, the energy of the electron beam in the transmission electron microscope (TEM) is given in units of keV, which is preferred from the theoretical standpoint. This is equivalent to the experimental accelerating voltage in the TEM.

6.1 The Cherenkov Effect

The Cherenkov effect is described as the emission of radiation when a charged particle moves through a medium at a speed greater than the speed of light in that particular medium.[1]

The effect was observed by Cherenkov in 1934,[2] in the form of a glow in fluids exposed to a radioactive source. The addition of quenching agents did not alter the luminescence, suggesting that the radiation was extraordinary in nature, and a full explanation of the effect was provided by Tamm and Frank in 1937.[3]

The complex dielectric function $\varepsilon(\omega) = \varepsilon_1(\omega) + i\varepsilon_2(\omega)$ defines the interactions between a medium and electromagnetic radiation. The real part alters the wavelength of the propagating radiation, thus reducing the speed of propagation of the radiation at an energy ω to $c/\sqrt{\varepsilon_1(\omega)}$, where c is the speed of light in vacuum. The imaginary part of the dielectric function describes the attenuation at a given energy ω.

Thus the Cherenkov condition is satisfied for electron velocities v when $\varepsilon_1(\omega) > c^2/v^2$, which results in the emission of radiation with frequency ω in a hollow cone with half-angle given by $\cos\theta_c = c/v\sqrt{\varepsilon_1(\omega)}$ (Figure 6.1). This radiation is analogous to the shockwave produced by objects travelling faster than the speed of sound in air. For 200 keV electrons, the Cherenkov condition is $\varepsilon_1(\omega) > 2.1$, which is amply satisfied for energies up to 12 eV for alumina (Figure 6.2). The thresholds for other electron energies commonly used in TEM are shown in Table 6.1.

Cherenkov radiation can be produced by electrons travelling in vacuum but passing near a material, provided the Cherenkov condition is satisfied within the material. The radiation is then produced by the induced polarization in the material and it is expected to be important up to electron-surface separations of the order of the range of the evanescent field of the electron in vacuum. For a given frequency component ω, the decay constant is $\sim v/\omega = \lambda v/2\pi c$, where λ is the wavelength of the Cherenkov radiation.[4] For 7 eV radiation, this is approximately 20 nm. It

will be shown below that the Cherenkov losses are actually sensitive to the sample structure up to much larger distances, due to the radiative nature of the Cherenkov effect.

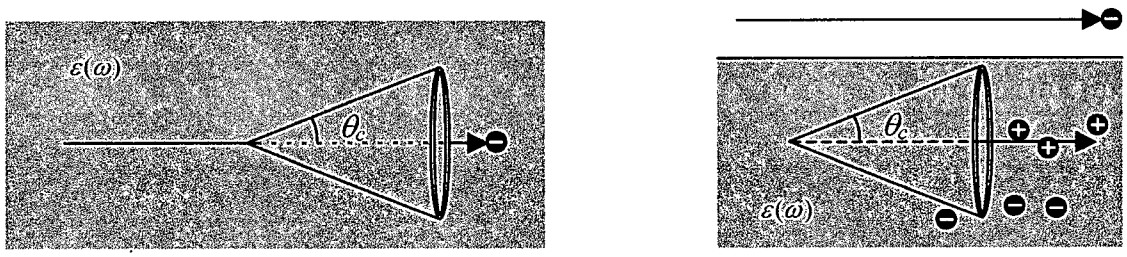

Figure 6.1 Geometry of Cherenkov radiation due to an electron travelling (a) through a medium and (b) near a medium with dielectric function $\varepsilon(\omega)$: light is emitted in the forward direction in a hollow cone.

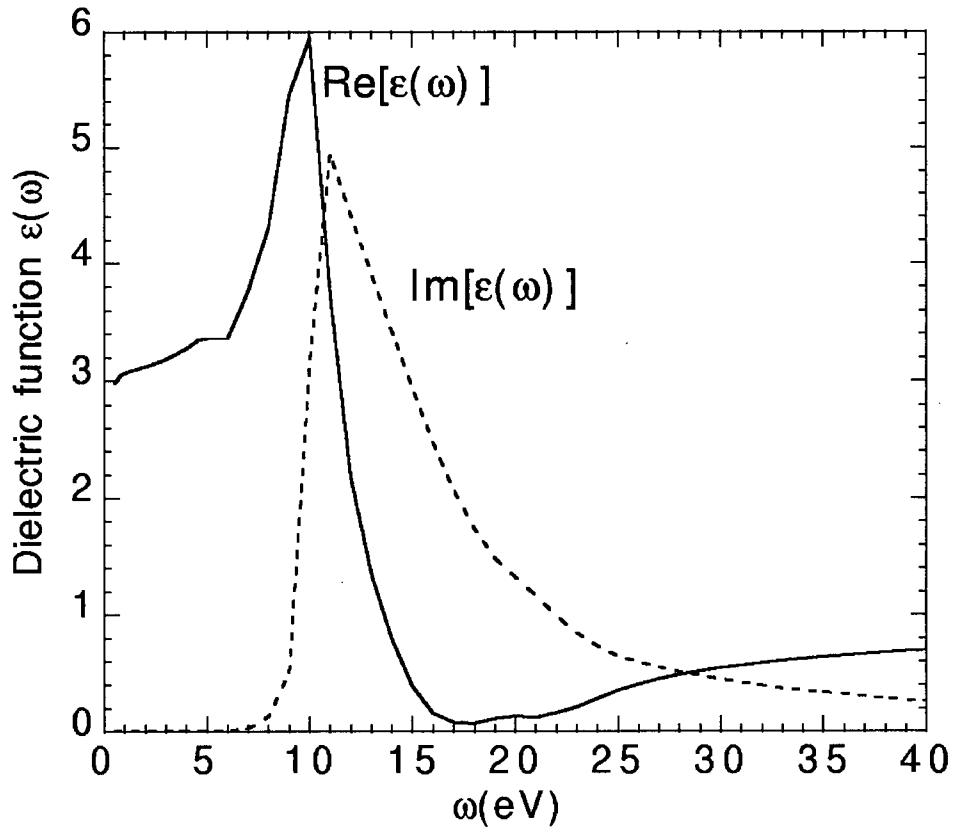

Figure 6.2 Dielectric function of alumina, after data from ref. 5. The Cherenkov condition is satisfied up to 12 eV for 200 keV electrons. Figure courtesy of A. Rivacoba.

Table 6.1 Cherenkov condition for common TEM beam energies.

Beam Energy (keV)	β (v/c)	Minimum $\varepsilon_1(\omega)$
80	0.50	4.0
100	0.55	3.3
120	0.59	2.9
200	0.70	2.1

Using EELS, losses due to the Cherenkov effect have been observed in dielectrics[6] and semiconductors[6,7] with the electron beam passing through the material, and the accompanying optical emissions have been recently measured.[8] It is only recently that the "aloof", or "near-field" Cherenkov effect has been considered, in a report on the loss spectra of alumina nanoparticles.[9] These results showed loss features below 10 eV for non-penetrating trajectories which could not be simulated with a non-relativistic model, but a relativistic model was not presented. Porous silicon also shows unusual spectral features at large beam-surface separations which may be due to the Cherenkov effect.[10] As such, the aloof Cherenkov effect had not been fully validated in the literature and merited further experimental and theoretical investigation.

As a point of interest, the microscopic nature of Cherenkov radiation is still the subject of debate. The long-standing viewpoint has been that the radiation is not emitted by the charged particle itself, rather by oscillations in the medium.[11,12] However, it has been recently suggested that the radiation is in fact better described as originating from the travelling charge.[13] This debate may be purely academic, as certainly both the medium and the travelling charge are required for the phenomenon. In the theoretical models presented below, the Cherenkov emission clearly arises from the response of the medium to the passing external electron.

6.2 Further Measurements

A number of variables could affect the 7 eV peak: pore diameter, lattice spacing, sample thickness, and primary electron beam energy. The primary beam energy was chosen as being the most indicative factor for the Cherenkov effect, as it would alter the Cherenkov condition, thus inducing a change in any loss features associated with Cherenkov radiation. It also addresses the concern that the observed peak is due to a finite pore length effect in the sample or an unexpected surface plasmon. The effect of varying the pore diameter with a fixed lattice spacing was also investigated.

6.3 Effect of Primary Beam Energy

The effect of primary beam energy was investigated by recording loss spectra with a lower primary beam energy. Measurements at 50 keV would have been the most revealing, since the Cherenkov condition would no longer have been satisfied and any associated losses would have disappeared altogether. This was not possible due to instrumental limitations, as the available Gatan Imaging Filter (GIF) was set up for operation at 117 and 197 keV. The measurements were carried out on the sample used earlier (chapter 4), a 1.4 μm porous alumina membrane. The microscope camera length and GIF entrance aperture were varied to investigate the effect of the spectrometer collection angle (β) on the collected spectra.

The new measurements at 197 keV confirmed the reproducibility of the peak at 7 eV in a 60 nm pore (Figure 6.3). The results of the measurements at 117 keV on the 1.4 μm film are shown in Figure 6.4: the general form of the loss spectra was very similar to those taken at 197 keV, but certain subtle differences were apparent when the spectra were compared (Figure 6.5). There is a small blue-shift of the loss peaks to higher energies (from 7 to 8 eV), both at the centre of the pore and at intermediate distances. The surface plasmon peaks are seen to be at the

same energies, indicating that the shift is not due to calibration error or to a change in geometry. Near the pore wall, the bulk plasmons are also seen to be in agreement at the two beam energies, again confirming that the shift observed in the axial loss peak is real and caused by the change in beam energy.

The collection angle was varied from 0.34 mrad to 6.0 mrad, which had very little effect on the form of the spectrum. This is in agreement with the small scattering angles for electrons interacting with surface plasmons. The scattering angle of the Cherenkov effect is also very small.[14]

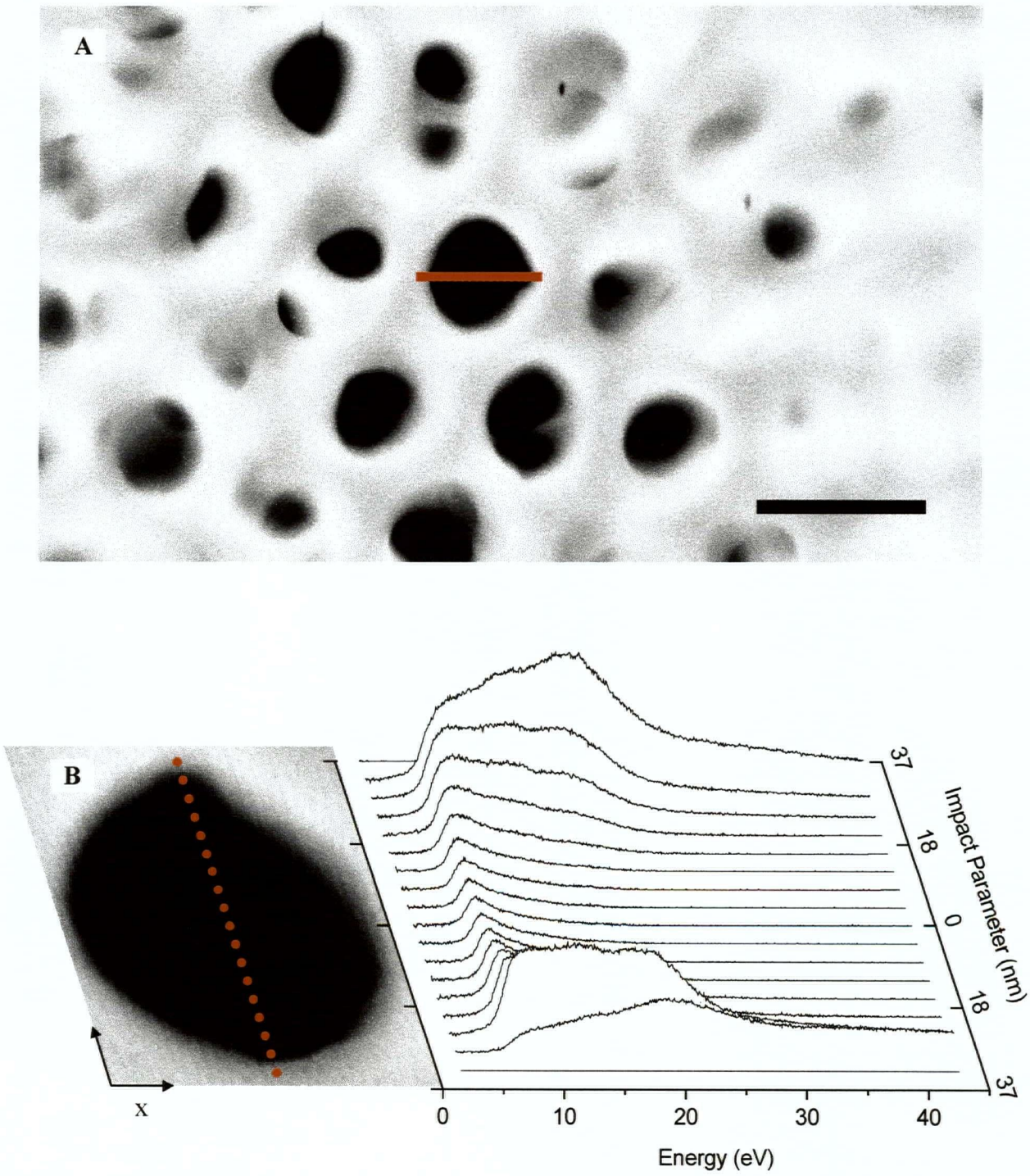

Figure 6.3 (a) STEM dark-field image, showing pore used for EELS analysis at 197 keV (scale bar is 100 nm). (b) EELS spectra acquired over the pore diameter with $\beta = 0.34$ mrad. The zero-loss peak has been removed using a power law fit over 1.3 - 2.0 eV.

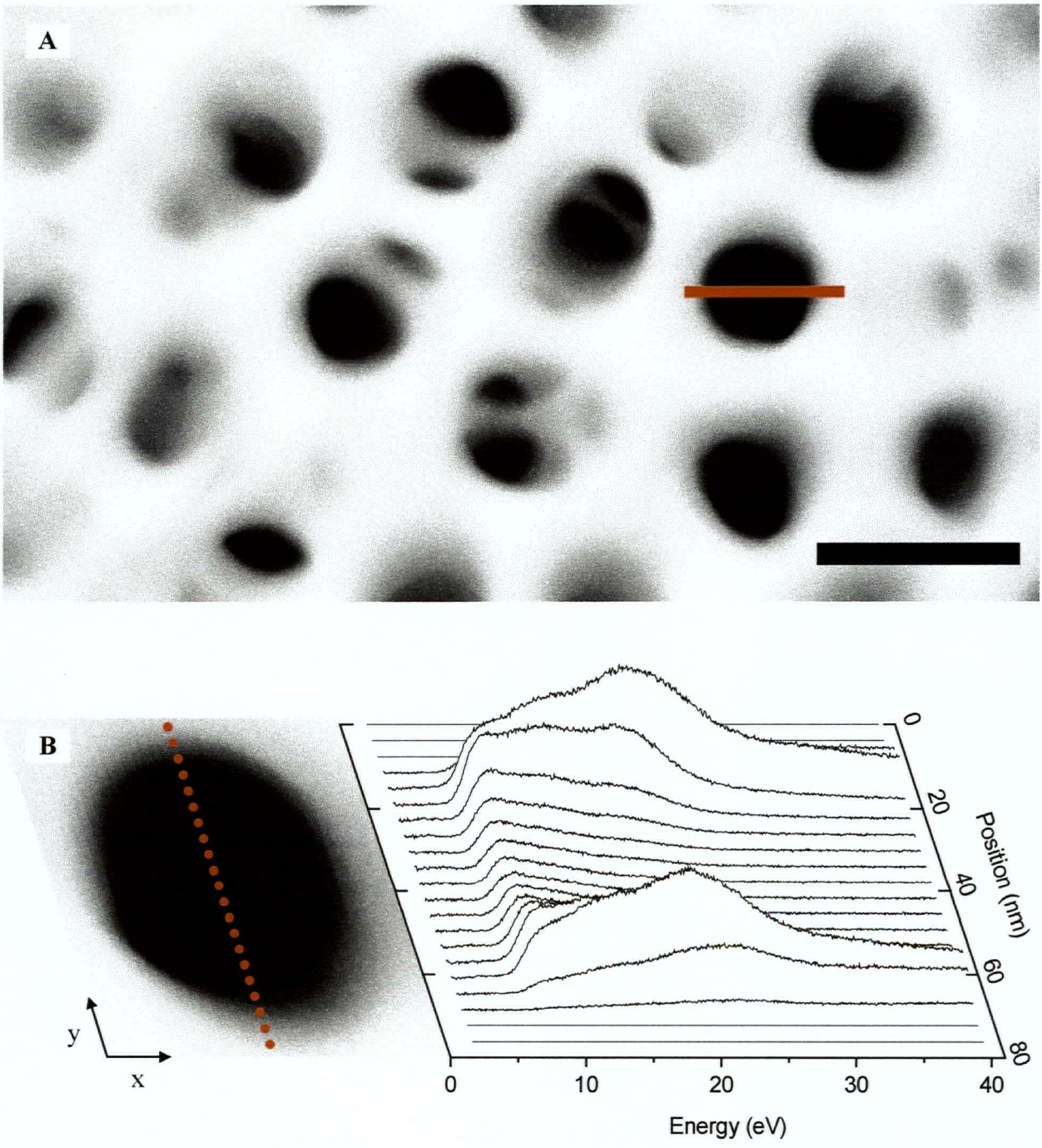

Figure 6.4 (a) STEM dark-field image, showing pore used for EELS analysis at 117 keV (scale bar is 100 nm). (b) EELS spectra acquired over the pore diameter with $\beta = 1.5$ mrad. The zero-loss peak has been removed using a power law fit over 1.3 - 2.0 eV.

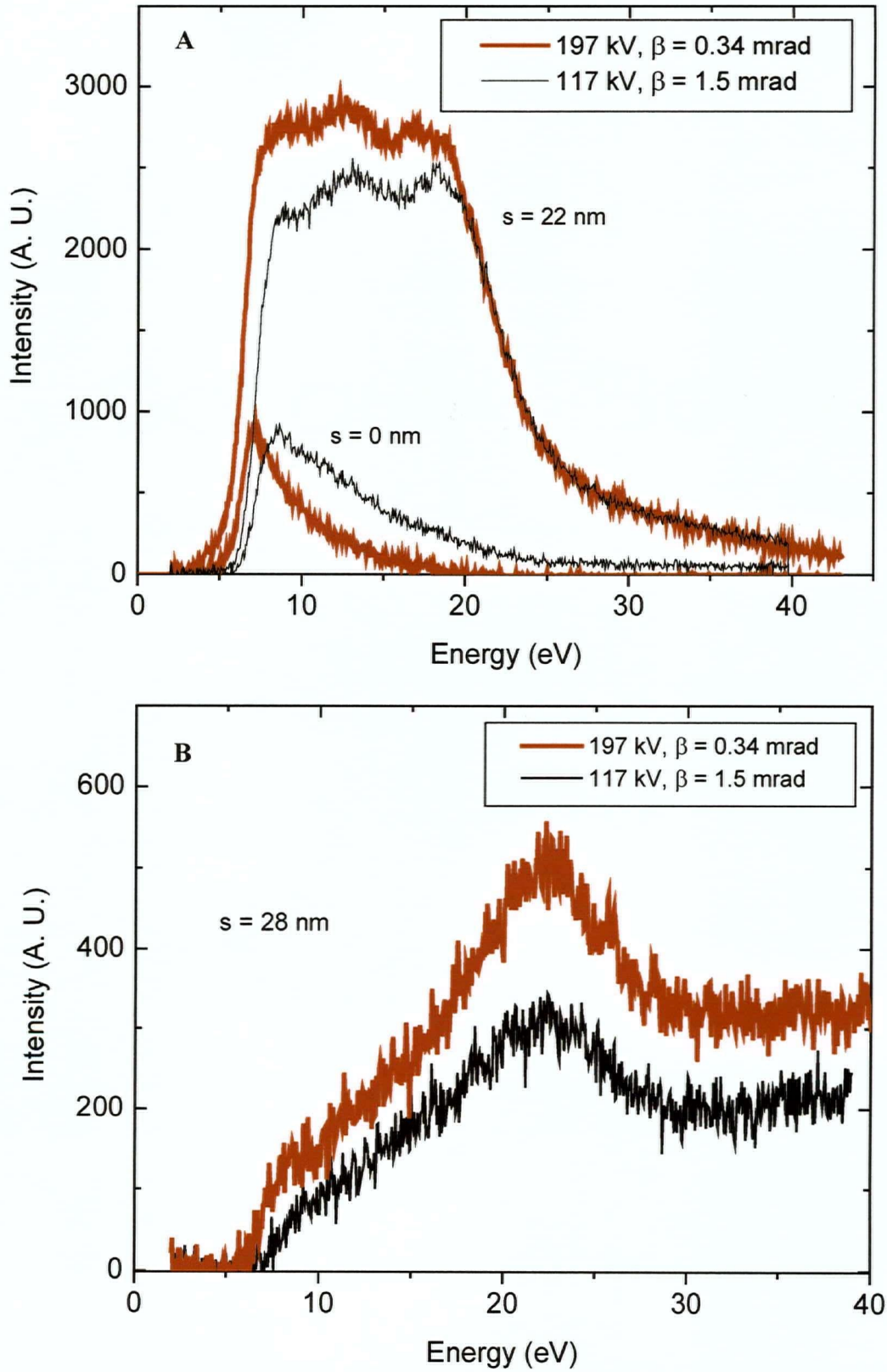

Figure 6.5 Comparison of low-loss spectra at 197 and 117 keV primary beam energies: (a) axial (s = 0 nm) and intermediate (s = 22 nm) spectra, and (b) wall-grazing (s = 28 nm) spectra.

6.4 Modelling of the Aloof Cherenkov Effect

The energy loss spectra were modelled by N. Zabala, A. Rivacoba and F. J. Garcia de Abajo at the Basque Country University in Spain. The details of the mathematical models are not presented here but they can be found in the literature.[15,16]

As mentioned in chapter 2, the low energy (< 50 eV) interactions between an electron beam and a material can be described by dielectric theory, where the dielectric function $\varepsilon(\omega)$ defines the response of the material to the electric field of the travelling electrons. The electrons experience energy losses due to the potential induced on the medium: the electric field of the electron beam polarizes the medium, and this induced polarization creates an electric field which acts to slow the electron beam. The losses are first calculated in the form of the distribution of energy loss probabilities per unit length, dP(ω)/dz. This would represent the form of the loss spectrum with perfect energy resolution and without any plural scattering, allowing the expected losses to be seen in detail.

The finite energy distribution of the electron beam (i.e., the shape of the zero-loss peak) is then taken into account through a convolution process, along with the effect of multiple scattering, to yield a direct comparison with the experimental spectrum. The finite size of the electron beam is not taken into account, and only trajectories parallel to the pore axis are considered.

The spatial dependence of the energy losses is described in terms of the impact parameter *s*, which is the distance between the electron beam and the centre of the pore (Figure 6.6). The effect of finite beam convergence angle in STEM mode leads to a substantial spread of the beam when thick membranes are considered – a typical value of α = 10 mrad leads to a total spread of 20 nm over 1 μm.

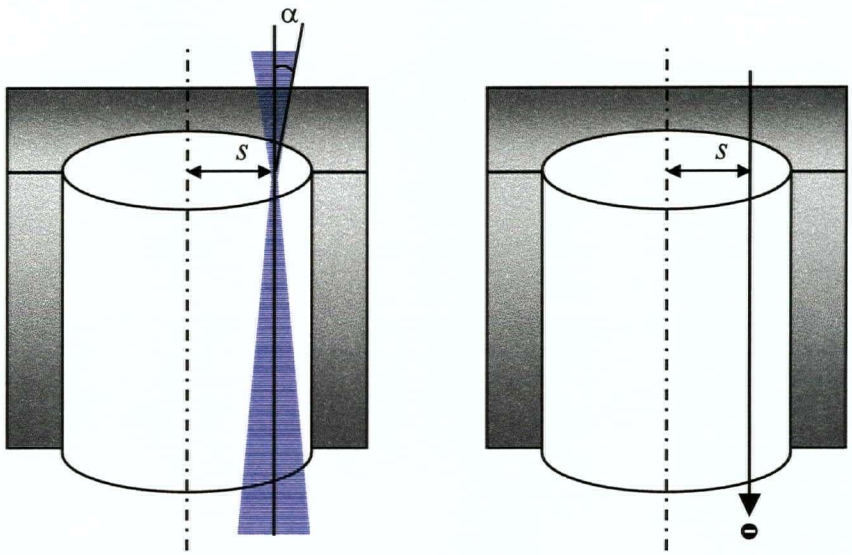

Figure 6.6 Comparison of (a) experimental electron beam with convergence angle α and (b) theoretical model.

6.4.1 Modelling of 197 keV Data

The energy loss probability distribution for relativistic electrons travelling paraxially to an infinite cylindrical hole in a dielectric medium was first described by Zabala *et al.*[17] This model allows the calculation of the losses associated with a single hole (radius a = 29 nm) in bulk alumina (Figure 6.7, Model A). Near the pore wall (s = 27 nm), surface plasmons between 10 and 25 eV dominate the loss function. This is in reasonable agreement with the experimentally observed spectrum. Near the pore centre (s = 0 nm), the loss probability is a monotonically decaying curve, falling to zero at 30 eV. This represents losses due to the Cherenkov effect, as no surface plasmons are excited at this distance. This simple model thus fails to describe the experimental spectrum near the pore centre: the asymmetrical peak at 7 eV observed for porous alumina differs substantially from the monotonically decaying curve.

The observed difference suggests that the Cherenkov losses are cut off at 7 eV. This discrepancy was assumed to arise from the effect of neighbouring pores, which alters the

dielectric function on a local level. Although these pores lie beyond the range of the evanescent field of the electron beam, they alter the medium through which the Cherenkov radiation propagates and directly affect the loss spectrum.

The effect of the neighbouring pores can be modelled in a number of ways. The simplest approach is to consider cylindrical shells of alumina with different outer radii, as shown in Figure 6.7 (Model B). This model for the porous alumina introduces two peaks into the distribution in the region of interest. Changes in the shell thickness shift the position of the dominant loss peak. This gives an indication of why the Cherenkov losses are cut off at 7 eV: only the Cherenkov radiation which can be transmitted by the membrane gives rise to associated electron energy losses. The Cherenkov radiation is confined within the cylindrical shell, due to total internal reflection at the vacuum interfaces (the condition for total internal reflection is guaranteed by the Cherenkov condition).[16] The cylindrical shell geometry leads to a quantization rule for the transmitted radiation, cutting out much of the low-energy Cherenkov radiation and the losses which would have been associated with it.[16] The basic physics behind the observed loss peak is therefore fairly clearly represented by this simple shell model.

More refined representations of the dielectric properties of porous alumina were also investigated, by modelling the nearest neighbouring pores directly, either with six or twelve cylindrical nearest neighbours (1+6 or 1+12 pores). The resulting loss distributions for electrons with axial paths (s = 0 nm) and near wall paths (s = 20 nm) are shown in Figure 6.8. The model with 1+6 pores clearly provides a peak at 7 eV. The 1+12 model, which would be expected to be more accurate than the 1+6 model, deviates substantially by presenting a second peak at ~8 eV. However, the subtle differences between these models would not be discernible experimentally, due to the limited energy resolution (~0.9 eV) of EELS in a TEM. Losses below 7 eV are also present in these models and this is discussed further below.

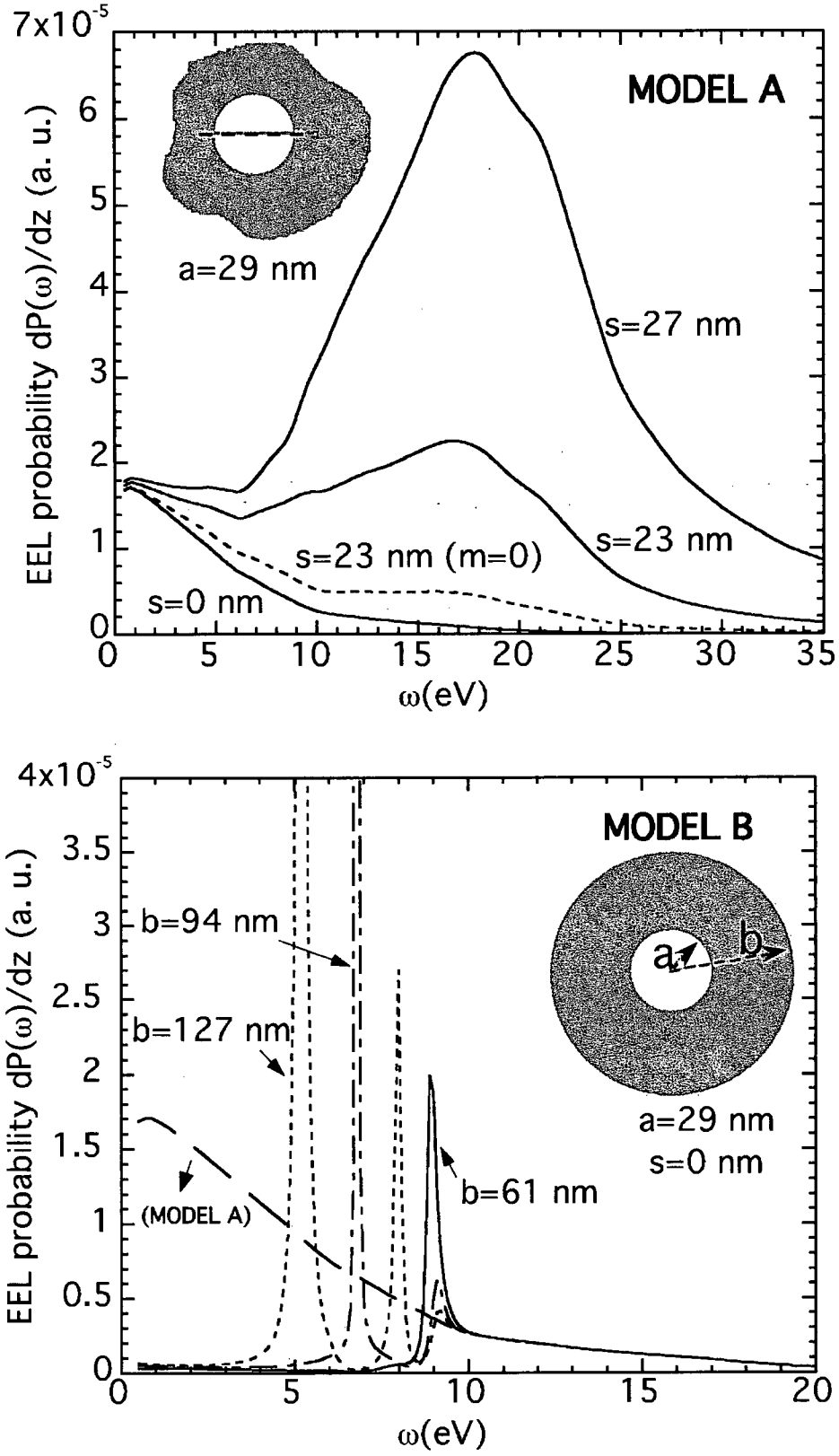

Figure 6.7 Theoretical loss distribution for 200 keV electrons travelling (Model A) down a single pore in alumina, and (Model B) down a cylindrical pore of outer radii 61, 94 and 127 nm. The inner pore radius is 29 nm. Figures courtesy of N. Zabala, F. J. García de Abajo and A. Rivacoba.

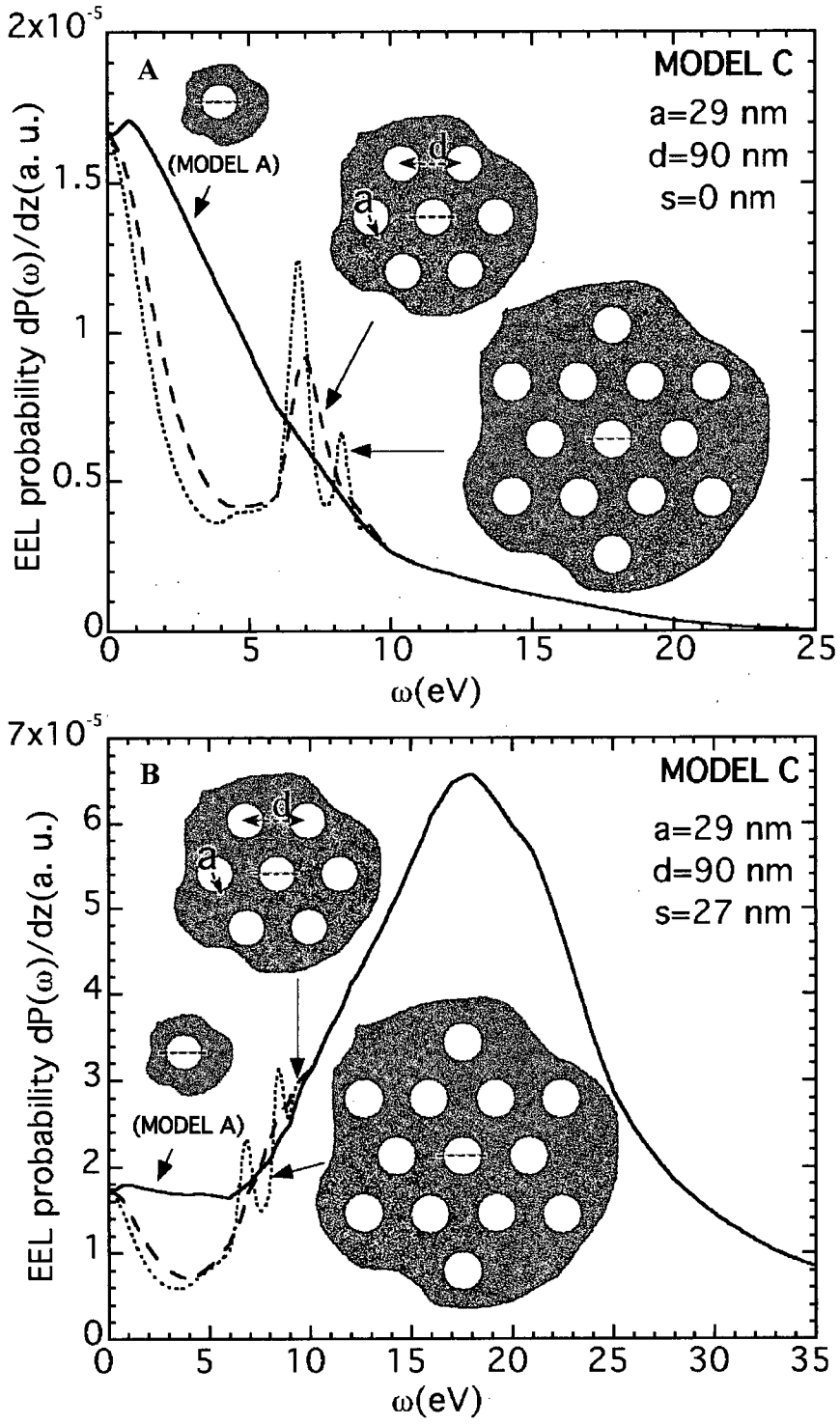

Figure 6.8 Theoretical loss distribution for 200 keV electrons travelling down a cylindrical hole with 0, 6 and 12 neighbouring pores (Model C), showing the loss probability for (a) axial (s = 0 nm) and (b) near-wall (s = 27 nm) trajectories. The pore radius is 29 nm and the spacing is 90 nm. Figures courtesy of N. Zabala, F. J. García de Abajo and A. Rivacoba.

6.4.2 Modelling of 117 keV Data

At the lower primary beam energy, the electron velocity has decreased to $v/c \approx 0.6$. The Cherenkov condition is thus $\varepsilon_1(\omega) > 2.8$, which is also satisfied up to ~11 eV for alumina (Figure 6.2). The energy loss probability does depend directly on v/c, and the theoretical spectra reflect this (Figure 6.9). At $s = 0$ nm, the loss peak shifts to higher energy by ~1.5 eV, in qualitative agreement with the experimental result.

6.4.3 Comparison with Experiment

The loss probability of the 1+6 cylinder model was convoluted with the experimental zero-loss peak to yield a direct comparison with experiment at three representative impact parameters. (Figure 6.10). The quantitative agreement at $s = 22$ nm and $s = 28$ nm is quite good. At $s = 0$ nm, the magnitude of the Cherenkov peak is overestimated by a factor of 2 at 200 keV; at 120 keV the agreement is improved. This indicates that some effects may still not be fully understood, either experimentally or theoretically. One possibility is the effect of finite beam convergence angle in STEM mode, which leads to a substantial spread of the beam when thick membranes are considered. However, a comparison of the spatial distribution of losses as revealed by EFTEM (α small) and STEM/EELS indicates that the difference is not very pronounced. Overall, the agreement between theory and experiment is satisfactory, and shows that the origin of the loss peaks is well represented by the models presented here.

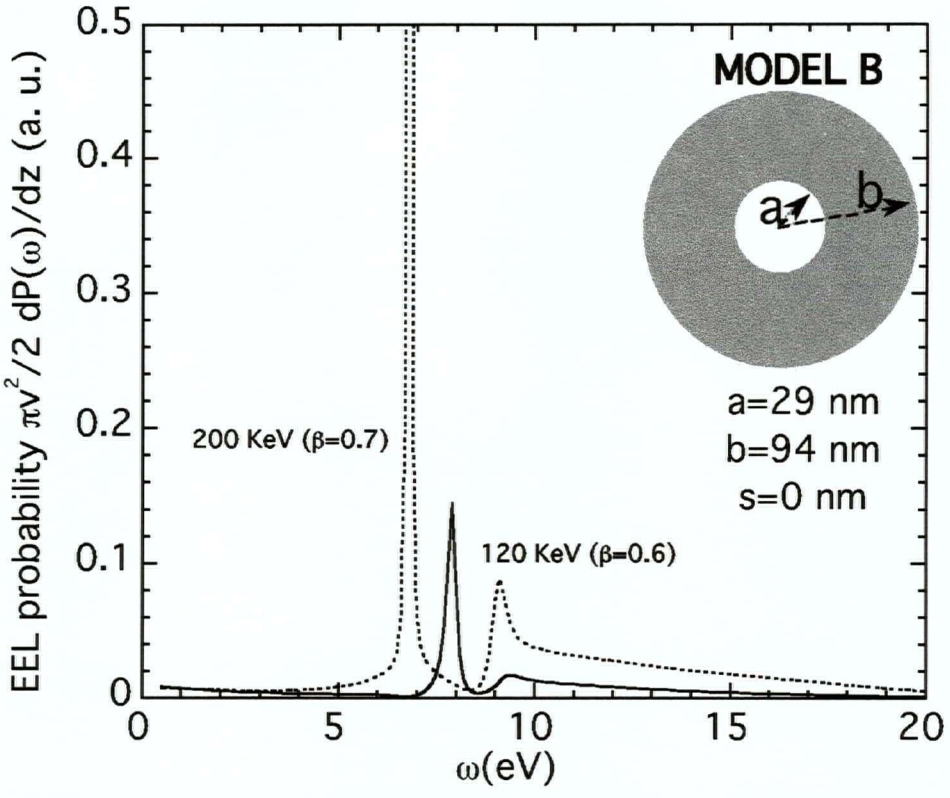

Figure 6.9 Effect of electron velocity on the loss probability function illustrated using Model B. ($\beta = v/c$ in this context). Figure courtesy of N. Zabala, F. J. García de Abajo and A. Rivacoba.

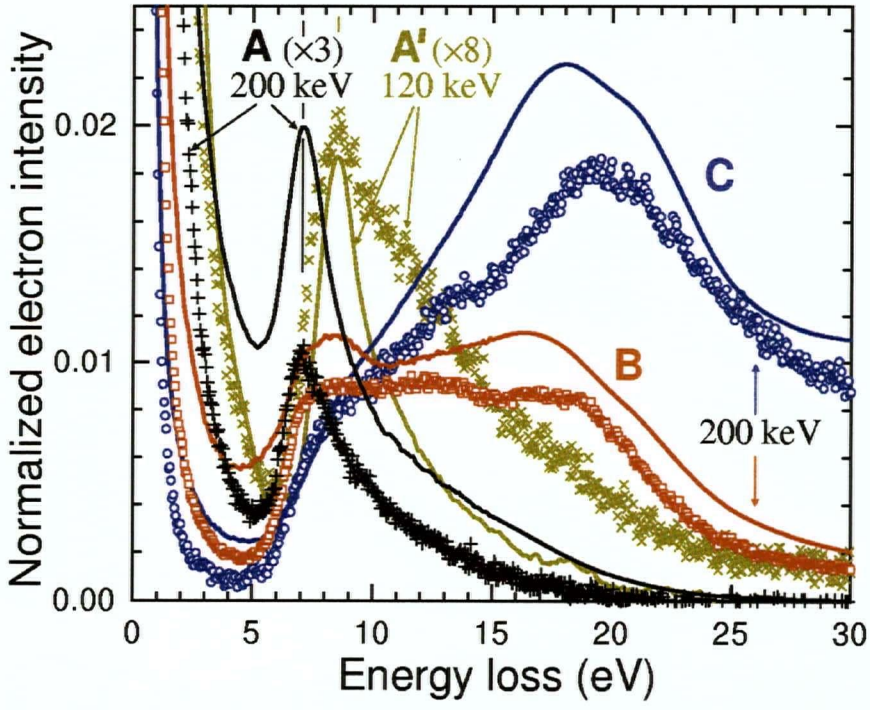

Figure 6.10 Comparison between theoretical and experimental spectra at different impact parameters *s*: (a) 0 nm, (b) 22 nm, (c) 28 nm, using the 1+6 cylinder model (radius 29 nm, spacing 90 nm). Figure courtesy of F. J. García de Abajo.

6.5 Effect of Pore Diameter on the Cherenkov Peak

The cylindrical shell model indicated that the Cherenkov loss peak shifts with the thickness of the shell, which is equivalent to changing the pore diameter while keeping a fixed pore spacing. This effect was investigated in more detail by preparing ordered porous alumina membranes through a two-step anodization process (chapter 4). The lattice spacing was fixed by the anodization potential (105 nm at 40 V), while the pore diameter was altered by etching the samples with phosphoric acid. In this manner, well-ordered domains of about 800 nm diameter were obtained, with average pore diameters of 62, 74 and 82 nm (Figure 6.11). The SEM image of the cross-section showed that the pores were straight (Figure 6.12). The channel diameters did not appear to be uniform throughout the thickness of the membrane. This may have been an artifact due to a slight tilt in the cleavage plane or it may a consequence of the fabrication process (see the experimental details), which might have been avoided through further optimization. The sample would still be expected to show the loss spectrum of the smaller pore diameter with less intensity.

The loss peak was recorded at the centre of the pore for each ordered membrane (Figure 6.13(a)). The loss peak is shifted to higher energy as the pore diameter is increased, from 6.7 eV at 62 nm to 7.9 eV at 82 nm. This is in qualitative agreement with the prediction that a thicker alumina shell will lead to a lower energy cutoff, as more of the Cherenkov radiation is able to propagate in the membrane. Changing the primary beam energy to 117 keV again shifted the loss peak to higher energies. The intensity of the loss peak diminishes with pore diameter due to the larger distance to the pore wall, resulting in a smaller interaction between the electron beam and the membrane (the membrane thickness difference also has an effect, but not as substantial, see Table 6.2). The loss intensity may also decrease due to the reduced wall thickness (Figure 6.7).

Table 6.2 Cherenkov loss peak parameters for ordered samples.

Pore Diameter (nm)	Membrane Thickness (μm)	Peak Position (eV)	
62	2.1 ± 0.3	6.7	(197 keV)
59	2.1 ± 0.3	7.8	(117 keV)
74	2.1 ± 0.3	7.5	
82	0.85 ± 0.05	7.9	

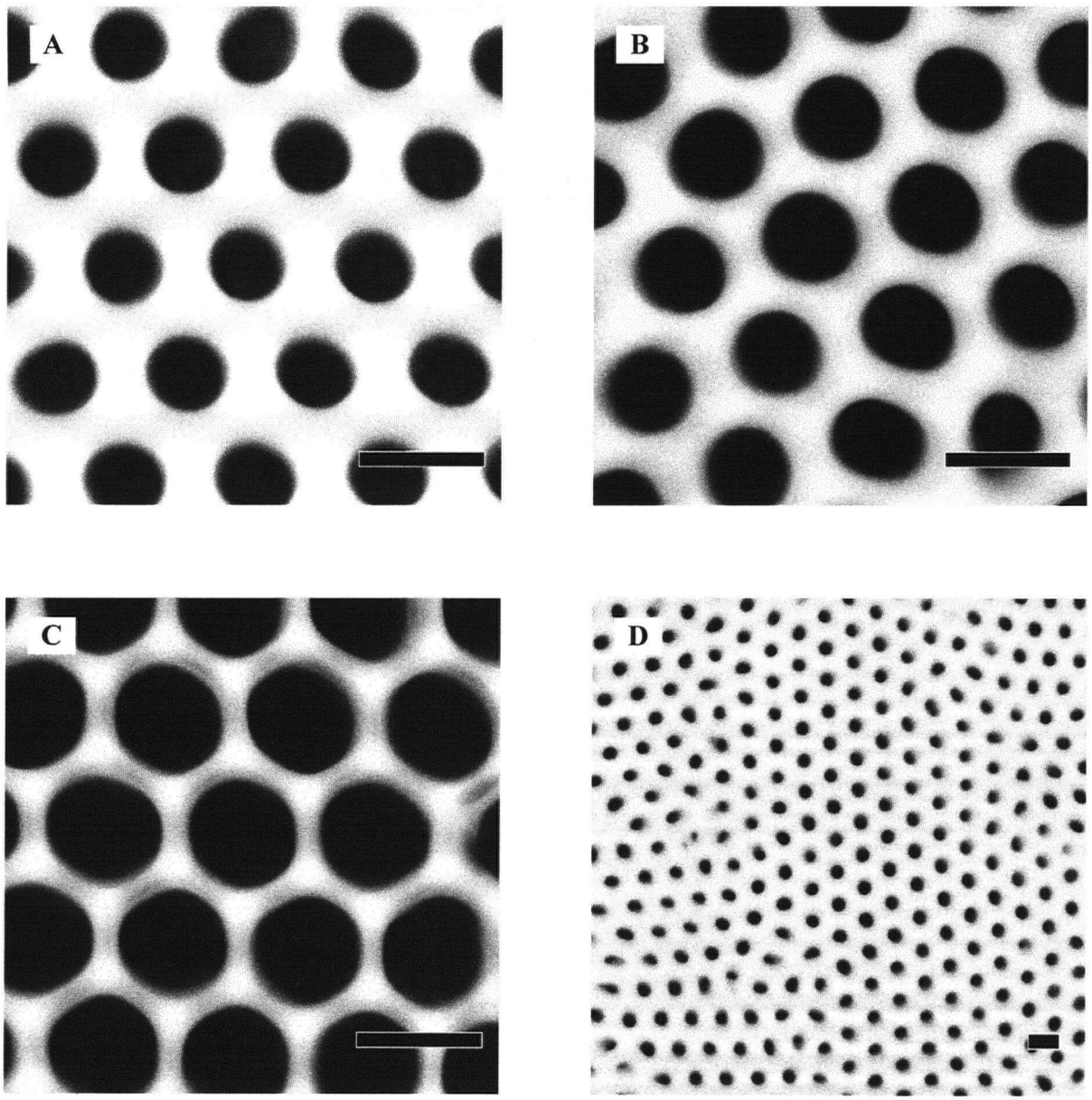

Figure 6.11 STEM dark field images showing geometry of ordered porous alumina membranes produced by a two-step anodization at 40 V in 0.3 M oxalic acid: (a) 62 nm, (b) 74 nm, (c) 84 nm diameters; (d) lower magnification image showing size of ordered domains. The scale bars are 100 nm.

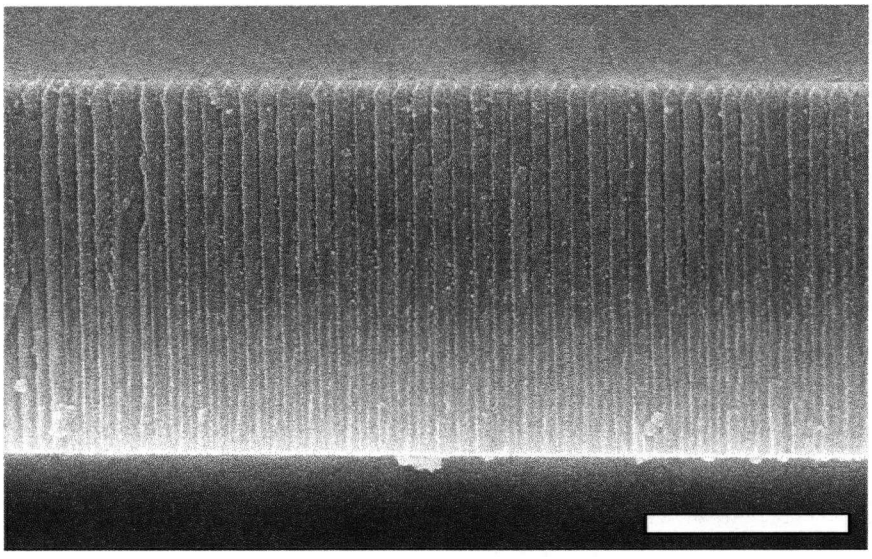

Figure 6.12 Cross-section of ordered porous alumina membrane. Note the pore diameters appear larger at the bottom. The scale bar is 1 μm.

More careful measurement of the zero-loss peak also allowed the examination of losses down to 2 eV. This revealed that there was no sharp cut-off at the low energy side of the Cherenkov loss peak (Figure 6.13(b)). Instead, the losses extend at least to 2 eV at a roughly constant value. The zero-loss peak subtraction was not sufficiently good between -2 and 2 eV to extract any further information. The precision of the result is affected by noise in the spectra. The uncertainty in the calculated spectrum may be determined from the counting statistics: the CCD detector is susceptible to shot noise, which is a Poisson process with an uncertainty of $\sqrt{N}$ for N counts.[18] The uncertainty in the dark current, which is subtracted from each collected spectrum, may be estimated from the noise in the spectrum of the zero-loss peak, well away from the peak itself. These calculations suggested a noise level of ~200 counts at 1 eV and ~1000 counts at 0 eV, which would not account for the large fluctuations observed in the calculated spectrum. Changes in experimental conditions (e.g., stray fields) may then be the cause of the

imperfect subtraction of the zero-loss peak, and the range of validity of the subtraction can only be estimated from the quality of fit at the left-hand side of the zero-loss peak.

Overall, the observed beam energy and pore radius dependence agrees with the predictions of the shell model. It does not clarify the extent of the long range interaction with the pore lattice, for which further measurements at different energies and on different samples would be necessary. As this pore lattice effectively forms a 2-D photonic crystal, these results introduce the possibility that EELS could be used to extract useful information from 2-D photonic nanostructures through the Cherenkov effect.[19] The possibility of observing novel Cherenkov radiation effects in photonic crystals has also been the subject of theoretical discussion.[20]

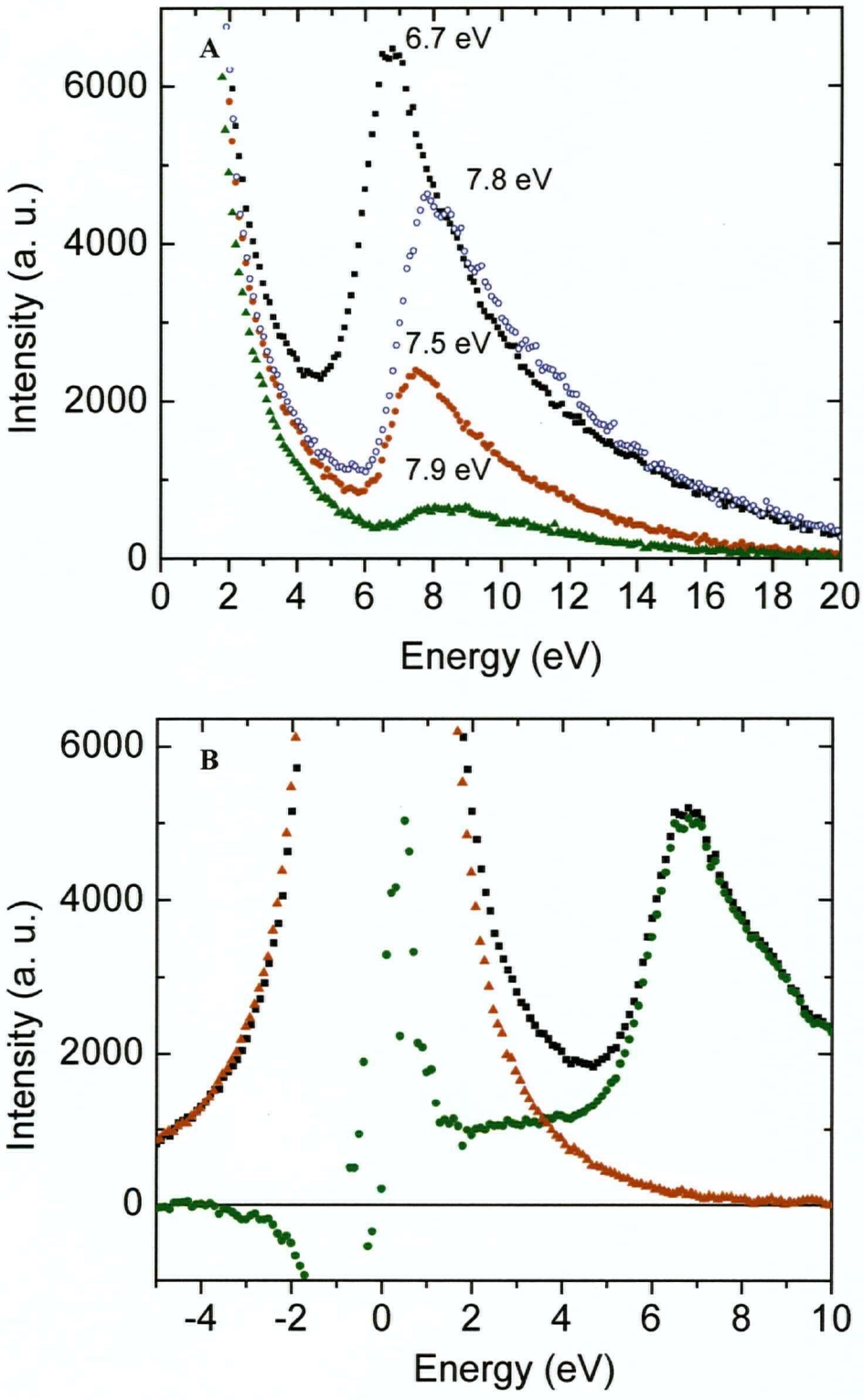

Figure 6.13 (a) Cherenkov peak shift for a fixed lattice spacing (105 nm) with different diameters: (■) 62 nm, (●) 74 nm, and (▲) 82 nm at 197 keV and (○) 62 nm at 117 keV; (b) (●) losses down to 2 eV revealed by subtraction of the (▲) zero-loss peak (diameter 62 nm, 197 keV). The losses between –2 and 2 eV are not meaningful.

6.6 Conclusion

The 7 eV loss peak observed by EELS in the centre of the pores of porous alumina films was found to be most likely due to the Cherenkov effect. The clearest evidence is the shift in the loss peak to higher energy with decreasing accelerating voltage. A number of models were investigated, and it was found that the local loss spectrum is affected by the sample structure on a much larger scale, due to the radiative nature of the Cherenkov losses. The theoretical model of the loss peak at different primary beam energies matched the experimental data reasonably well. Certain aspects of the material and geometry were not modelled, and could account for the small discrepancies observed: the anion contamination of the porous alumina, and the exact geometry of the pores neighbouring the pore being investigated.

More direct evidence for the Cherenkov effect could be obtained by detecting the generated radiation[8] but the systems in existence today detect luminescence below 6 eV only. The nature of these losses could be further studied by fabricating and studying single pores, pore clusters and pore lattices with exactly defined geometries, such that a closer match to the theoretical models could be obtained. However, the aspect ratios seen in porous alumina are not readily achieved using other fabrication approaches. Further measurements on an instrument equipped with an electron monochromator (zero-loss peak FWHM ~0.1 eV) would be needed to establish the experimental loss spectrum with sufficient detail to choose the correct theoretical representation of the pore lattice.

Finally, it should be pointed out that the identification of this phenomenon was mostly due to several serendipitous choices of experimental factors: the measurement geometry, which in truth was not really useful for chemical analysis, a thick membrane which maximized the loss probability, and a pore diameter which was sufficiently large to avoid surface plasmon losses near the centre.

Experimental Details

Porous alumina thin films were prepared by anodizing 0.2 and 1.0 μm thick Al films evaporated onto *n*-type silicon wafers by e-beam evaporation[21]. The anodization was carried out in 0.3 M oxalic acid at 20°C with an applied potential of 40.0 V, using a glass cell with an O-ring seal to the sample. Upon completion of the anodization, the porous alumina film had detached from the substrate, but was still attached to the surrounding aluminium film. The barrier layer was removed by etching in 5 wt. % phosphoric acid for 40 min. The film was rinsed with distilled water, followed by ethanol and then dried.

Using the same samples (chapter 5), electron energy-loss spectroscopy was carried out on a Tecnai F20 (Medical Imaging Facility, University of Calgary) TEM with a Schottky field emission electron gun operated at nominally at 120 and 200 kV. The primary beam energy used for spectroscopy was 117 and 197 keV. Measurements were made with a Gatan Imaging Filter (GIF) using a dispersion of 0.05 eV/channel on a 1024-channel detector, covering -5 to 45 eV losses. The collection semi-angle was between 0.34 and 6.0 mrad; the convergence angle was not determined. The probe size was estimated to be < 1 nm while the energy resolution was 0.9 eV (FWHM of zero-loss peak).

Measurements on ordered samples were carried out on Tecnai F20 (Nano-imaging Facility, Simon Fraser University) equipped with a GIF. The dispersion was set to 0.10 eV/channel. The FWHM of the electron probe was measured to be 0.6 nm. The energy resolution was 0.90 eV at 197 keV and 0.87 eV at 117 keV.

Ordered samples were prepared by anodizing 99.99+% aluminum foil (Aldrich) for 2-3 hours at 40 V in 0.3 M oxalic acid for the first step, with stirring. The anodized layer was stripped overnight by immersing in 5.8 wt. % H_3PO_4 + 1.5 wt. % CrO_3 at 50 to 60°C overnight. A second anodization step was carried out for 10-20 min under the same conditions. The

resulting film was washed with water and dried, then glued to a glass slide (membrane down) with CrystalBond, a thermopolymer adhesive. The aluminum susbtrate was removed by etching with a saturated $HgCl_2$ solution, leaving the alumina membrane attached to the glass slide with the barrier layer facing up. This layer was etched for 120 min in 5% H_3PO_4 with stirring. After washing with water and drying, the adhesive was removed by soaking in acetone, and the membrane inspected by TEM. The pore walls could be further etched to increase the diameter as desired. Film thicknesses were determined by SEM; in some cases there was substantial variation over the whole film, leading to some uncertainty in the thickness.

References

1. Jackson, J. D. *Classical Electrodynamics*; Wiley: New York, 1999.

2. Cherenkov, P. A. *Dokl. Akad. Nauk SSSR* **1934**, *2*, 451-453.

3. Tamm, I. E.; Frank, I. M. *Dokl. Akad. Nauk SSSR* **1937**, *14*, 107.

4. Garcia de Abajo, F. J.; Blanco, L. A. *Phys. Rev. B* **2003**, *67*, No. 125108.

5. Palik, E. D. *Handbook of Optical Constants of Solids*; Palik, E. D., Ed.; Academic Press: Orlando, 1985.

6. Daniels, J.; Festenberg, C. v.; Raether, H.; Zeppenfeld, K. *Springer Tracts Mod. Phys.* **1970**, *54*, 78-135.

7. Chen, C. H.; Silcox, J.; Vincent, R. *Phys. Rev. B.* **1975**, *12*, 64-71.

8. Yamamoto, N.; Araya, K.; Toda, A.; Sugiyama, H. *Surf. Interface Anal.* **2001**, *31*, 79.

9. Abe, H.; Kurata, H.; Hojou, K. *J. Phys. Soc. Jpn.* **2000**, *69*, 1553.

10. Williams, P.; Levy-Clement, C.; Albu-Yaron, A.; Brun, N.; Colliex, C. *J. Porous Mater.* **2000**, *7*, 159.

11. Tyapkin, A. A. *Physics of Particles and Nuclei* **2001**, *32*, 506.

12. Ginzburg, V. L. *Physics-Uspekhi* **2002**, *45*, 341.

13. Platonov, K. Y.; Fleishman, G. D. *Physics-Uspekhi* **2002**, *45*, 235.

14. Egerton, R. F. *Electron energy-loss spectroscopy in the electron microscope*; 2nd ed.; Plenum Press: New York, 1996.

15. Zabala, N.; Rivacoba, A.; Garcia de Abajo, F. J.; Pattantyus, A. *Surf. Sci.* **2003**, *532-535*, 461-467.

16. Zabala, N.; Pattantyus-Abraham, A. G.; Garcia de Abajo, F. J.; Rivacoba, A.; Wolf, M. O. *Phys. Rev. B* , in press.

17. Zabala, N.; Rivacoba, A.; Echenique, P. M. *Surf. Sci.* **1989**, *209*, 465.

18. Reed, B. W.; Sarikaya, M. *Ultramicroscopy* **2002**, *93*, 25.

19. Garcia de Abajo, F. J.; Pattantyus-Abraham, A. G.; Zabala, N.; Rivacoba, A.; Wolf, M. O.; Echenique, P. M. *Phys. Rev. Lett.* **2003**, *91*, No. 143902.

20. Luo, C.; Ibanescu, M.; Johnson, S. G.; Joannopolous, J. D. *Science* **2003**, *299*, 368.

21. Crouse, D.; Lo, Y. H.; Miller, A. E.; Crouse, M. *Appl. Phys. Lett.* **2000**, *76*, 49-51.

CHAPTER 7 Polymer Guest Incorporation

Porous alumina films were shown to be a very close approximation to an ideal host material in chapter 4: they have 4 nm pores running perpendicular to the film normal, and the film thickness can be easily controlled. The introduction of the conjugated polymer guest into the porous alumina host must be considered within the constraints imposed by the desired light-emitting device structure and the properties of the polymer guest.

The introduction of the polymer guest into the porous thin film host can be accomplished first through *in situ* synthesis. In this direction, some initial work on the surface-graft polymerization of poly(1,4-phenylene vinylene) (PPV) on a silicon surface is presented in this chapter. Secondly, bulk-synthesized polymer may be introduced into the host through a variety of methods. A novel approach, centrifugal loading, is investigated and used to prepare samples for in-depth characterization, in particular high-resolution chemical analysis by electron energy-loss spectroscopy (EELS) and energy-filtered transmission electron microscopy (EFTEM).

7.1 Internal Polymer Synthesis

In situ synthesis of the polymer guest is attractive due to the relatively rapid diffusion of monomers into the host material. Many conjugated polymers, such as PPV, polythiophene and polyacetylene, can only be introduced into the host in this manner, due to their insoluble and infusible nature. The groups of Martin and Bein separately carried out pioneering work on

conjugated polymer synthesis in porous alumina[1] and mesoporous silica,[2] respectively. This approach was also exploited in the creation of the PPV/MCM-41 composite discussed in chapter 3. Recent reports describe the formation of poly(1,4-phenylene)[3] and poly(2,5-diethoxyphenylene)[4] by oxidative coupling in porous alumina membranes. Chemical vapour deposition of a polymer precursor has been shown to introduce PPV into porous alumina as well.[5]

The two difficulties that face this approach is control over the degree of polymerization and confinement of the polymerization to the pore volume. The degree of *in situ* polymerization may differ significantly from the bulk-synthesized polymer. This may be especially relevant in pores which approach molecular dimensions (< 2 nm). This difference can make meaningful property comparisons more difficult. Nevertheless, materials prepared in this manner may have useful applications in devices. Polymerization confinement may be achieved by first loading one of the reactants into the porous host. This is exemplified in the synthesis of confined polyaniline, where aniline is first diffused into the pores.[2] The synthesis of PPV/MCM-41 discussed in chapter 3 relied on the ability of the MCM-41 surface to act as an initiating base when monomer was subsequently introduced. However, if the pre-loaded species can diffuse out of the pores, bulk polymerization cannot be prevented entirely. A better approach is to initiate the polymerization from a substrate supporting the porous film on one side, which is known as surface-graft polymerization. This last approach appears very promising and some preliminary work has been carried out in this direction.

7.1.1 Surface-Graft Polymerization of Conjugated Polymers

Surface-graft polymerization is a route to polymer confinement by virtue of polymer growth being localized to the end of chains initiated from the surface. The use of a suitable

surface-bound initiator is key to this route. If the initiator is bound to a material suitable for use as an electrode, it can be guaranteed that each polymer chain is attached to the electrode interface in a chemically well-defined manner. The presence of a porous host on top of this electrode would then yield a device with surface-grafted polymer chains separated by the walls of host. In this manner, only continuous polymer chains would exist in each channel of the host. The problem of bulk polymerization is eliminated entirely.

Living polymerization is the method of choice for preparing surface-grafted polymers. This usually involves an anionic or radical polymerization mechanism. There are two established living polymerization routes to conjugated polymers: ring-opening metathesis polymerization (ROMP)[6,7] and electropolymerization.[8] ROMP may be used to prepare very well defined polymers, and it has been demonstrated to create surface-grafted polymers from a surface initiator.[9,10] However, the preparation of the required monomer, catalyst and surface initiator were beyond the scope of the present work. The use of electropolymerization to prepare surface-grafted conjugated polymers has been demonstrated for polyaniline[11,12] and polythiophene.[13] In practice, electropolymerization has the disadvantage of producing chains with many chemical defects and was not explored further for this reason. One further possibility is the Gilch route: it has been reported that it proceeds by an anionic mechanism[14] and could therefore also be initiated from a surface (Figure 7.1). Preliminary efforts in this direction did not yield any grafted polymer, presumably because the surface initiation group was not in sufficient concentration to compete with the bulk polymerization process. It is also possible that the surface initiator group reacts with neighbouring initiators to deactivate the surface.

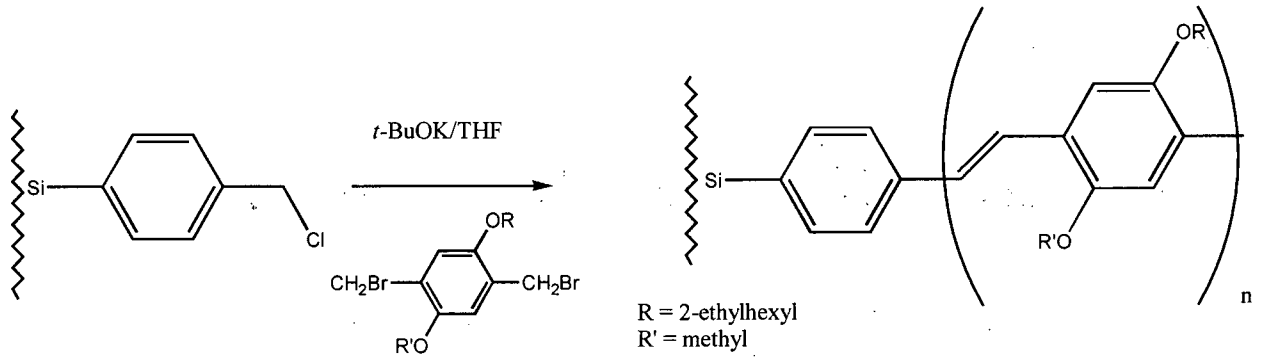

Figure 7.1 Surface-initiated anionic polymerization of MEH-PPV.

Step (or condensation) polymerization was explored as an alternative route to the preparation of surface-grafted polymers. Condensation reactions have been used to make well-defined conjugated oligo(phenylene vinylene)s in high yield.[8] Poly(phenylene ethynylene) derivatives of substantial length have been prepared in this manner through repeated coupling of oligomers.[15]

This approach was conceived to be applicable to the preparation of PPV chains bound to a conductive substrate. An example of a synthetic route is shown in Figure 7.2, based on the Wadsworth-Horner-Emmons (WHE) synthesis of aromatic olefins from aldehydes and phosphonate esters. This reaction is known to produce *trans* conjugated olefins in high yield and has been applied to the synthesis of PPV derivatives.[16-19] It has also been demonstrated on a solid support.[20-22]

The hydrogen-terminated silicon surface is a convenient substrate for evaluating this route due to its well known chemistry.[23,24] Porous silicon substrates[25] are particularly useful as their high surface area allows the use of transmission FT-IR for characterization. The most relevant reactions on this surface have been developed by the groups of Sailor[26-28], Buriak[29-32] and Wayner.[33-35] Among these, cathodic electrografting has been used to graft functionalized alkynes and alkenes to the silicon surface (Figure 7.3).[30] Of particular interest was the grafting

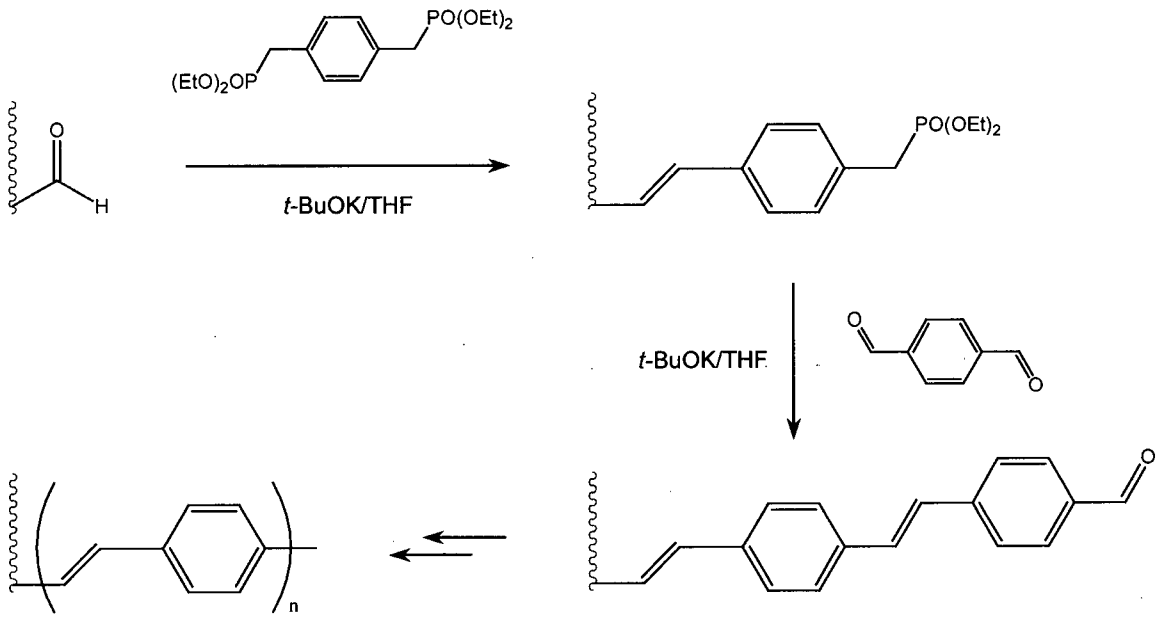

Figure 7.2 Step polymerization of surface-grafted PPV by the WHE reaction.

of phenylacetylene and 4-bromophenylacetylene through the acetylene carbon, which suggested that a fully conjugated bond to the silicon surface could be formed. Most importantly, the presence of the aromatic halogen allows the use of well known chemistry to further derivatize the surface: the brominated phenyl ring could be used to form grafted oligo(phenylene) chains through the Suzuki coupling.[8] As PPV derivatives were of interest in this work, a grafted aromatic aldehyde was pursued to create surface-bound oligo(1,4-phenylene vinylene) chains through the WHE reaction discussed above.

The actual encapsulation of polymer by such surface chemistry would be accomplished by

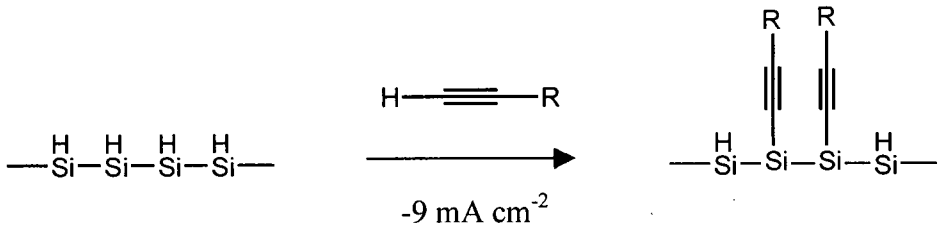

Figure 7.3 Porous silicon derivatization by cathodic electrografting (R = phenyl, 4-bromophenyl, etc.).[30]

the preparation of porous alumina films on a silicon substrate.[36] The key step in the process would be the successful preparation of the hydrogen-terminated silicon surface, which requires removal of the native silicon dioxide film. This is usually accomplished with aqueous hydrogen fluoride or ammonium fluoride. Initial tests indicated that porous alumina was stable to the latter solution. Reactive ion etching, commonly used in the semiconductor industry, can also be used to remove the native oxide layer in the presence of porous alumina[36] but this may not work well with all pore sizes.

7.1.2 Derivatization of Porous Silicon Surfaces

The functionalization of porous silicon substrates by cathodic electrografting was studied. 4-ethynylbenzaldehyde has the two desired functional groups: an alkyne for binding to silicon and an aldehyde for further chemistry by the WHE reaction. As the grafting process is reductive at the silicon surface, the aldehyde group was protected by conversion to the cyclic acetal (Figure 7.4).

A porous silicon substrate was then derivatized by cathodic electrografting of this protected aldehyde (Figure 7.5), using tetrabutylammonium hexafluorophosphate in methylene chloride as the electrolyte. The chemical changes were followed by FT-IR spectroscopy. New C-H stretches and aromatic bands appeared after electrografting (Figure 7.6(a)); the cyclic acetal

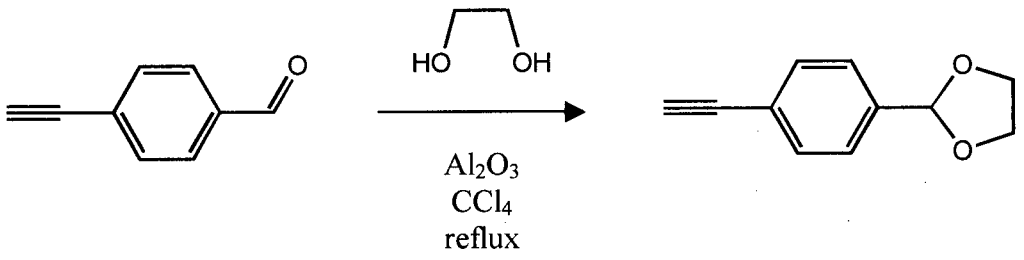

Figure 7.4 Protection of aldehyde in 4-ethynylbenzaldehyde.

band at 943 cm^{-1} could also be distinguished. The alkyne stretch was expected to appear near 2100 cm^{-1} but could not be confirmed due to the overlapping H-Si stretches. The strong Si-O framework stretch at 1100 cm^{-1} indicated the presence of substantial surface oxide.

Following deprotection of the aldehyde, a strong C=O stretch peak appeared at 1700 cm^{-1} along with a weaker H-C=O peak at 2733 cm^{-1} (Figure 7.6(b)). The aromatic bands were also enhanced, while the cyclic acetal band disappeared. The aliphatic C-H stretches remaining at 2969 and 2930 cm^{-1} may be due to chemi- or physisorbed electrolyte.[30] Although the structure of the surface-grafted species could not be fully established, it was clear that a surface-bound aldehyde was present.

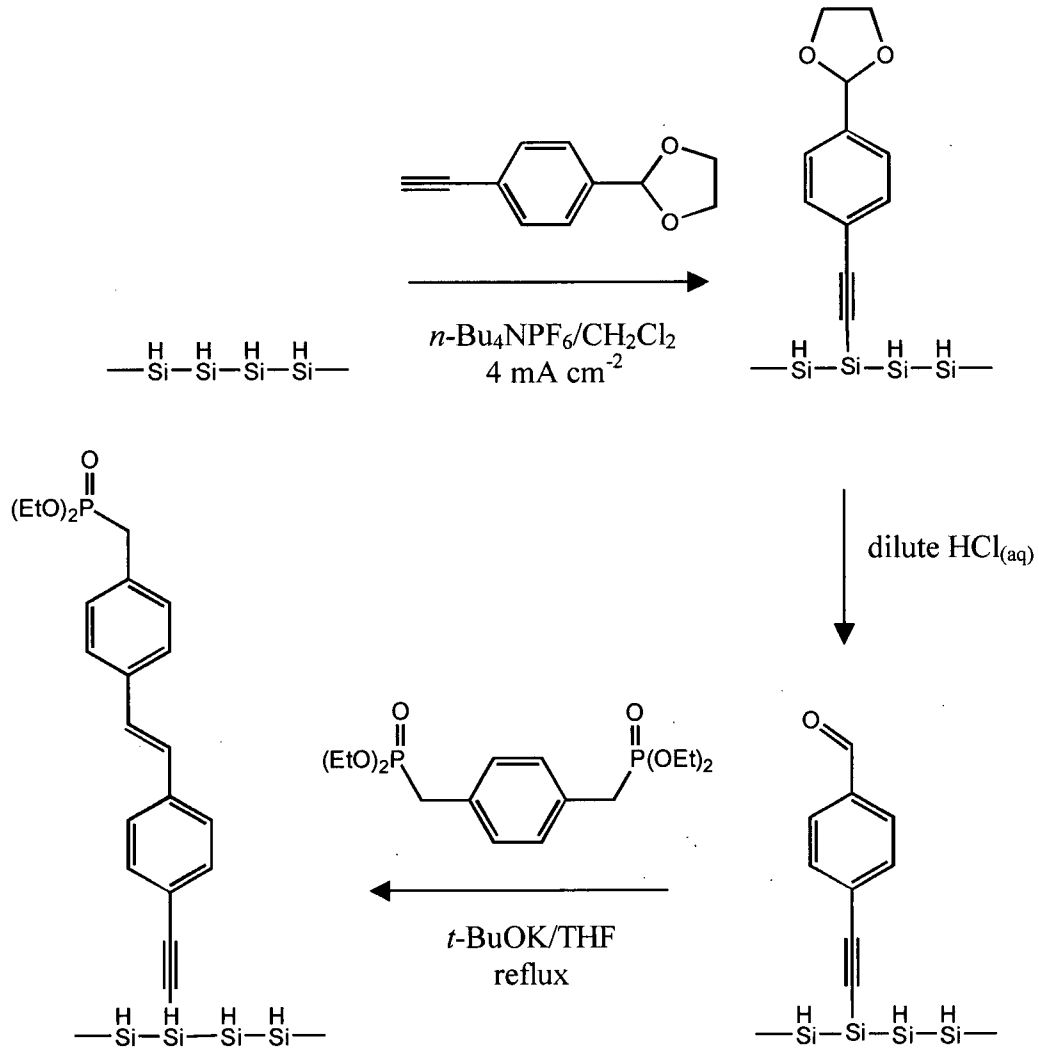

Figure 7.5 Synthetic route to conjugated dimer on porous silicon surface.

7.1.3 Wadsworth-Horner-Emmons Reaction on Silicon Surface

The terminal aldehyde on the silicon surface was reacted with 1,4-xylylenebis(diethylphosphonate). The FT-IR spectrum of the resulting surface (Figure 7.6(c)) showed that the C=O stretch at 1700 cm^{-1} was completely removed and a new shoulder assigned to a P=O stretch had appeared at 1260 cm^{-1}. The aliphatic C-H stretches around 2969 and 2933 cm^{-1} were in agreement with the C-H stretches observed in the phosponate ester, although they may still be due to the electrolyte. This surface also exhibited blue photoluminescence, as shown in Figure 7.7. The emission maximum was observed at 400 nm. The excitation spectrum, detected at 400 nm, had a maximum at 322 nm. This is in agreement with the literature value of 4-ethynylstilbene[37] and would suggest that the interaction of the π electron system with the silicon substrate is weak.

These initial results strongly suggest that the desired surface-grafted species was obtained. However, more detailed analysis with model compounds would be required to fully confirm this.

While this chemistry was carried out on porous silicon substrates, it should be readily applicable to hydrogen-terminated silicon wafers as well. Short oligomers grafted to silicon would then represent a very well defined junction between an organic and an inorganic semiconductor. The rate of polymer growth can be increased by synthesizing appropriate dimers or trimers in bulk, then using them to grow the surface-grafted polymer.[15]

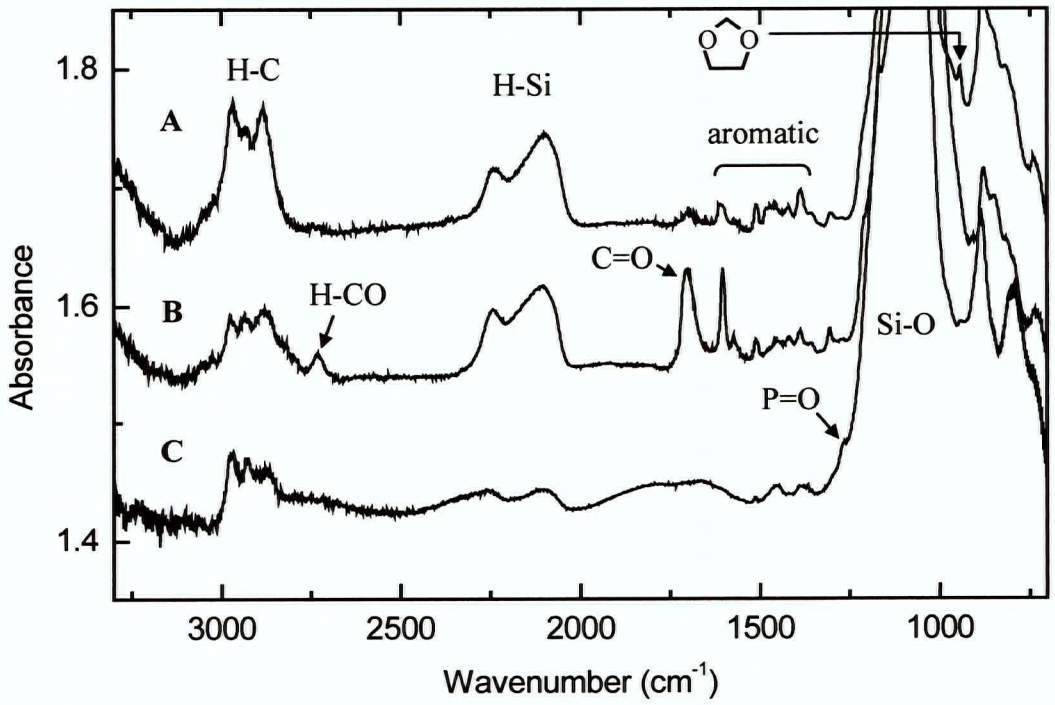

Figure 7.6 FT-IR spectra after (a) cathodic electrografting, (b) deprotection of aldehyde and (c) WHE reaction on porous silicon substrate.

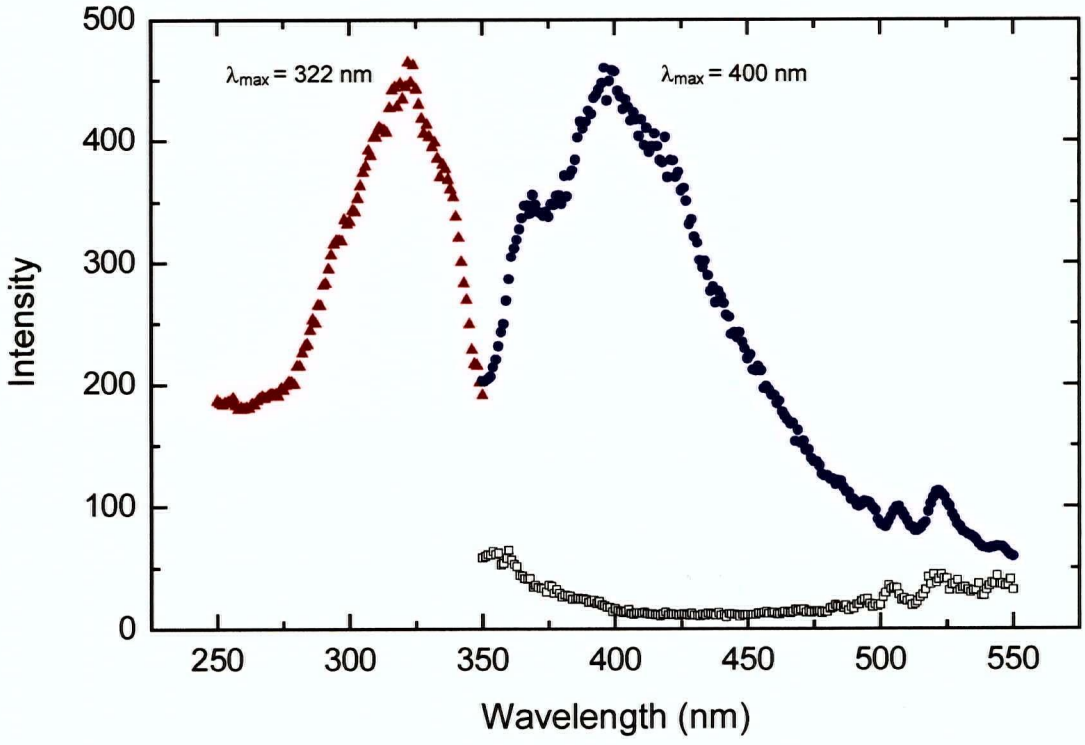

Figure 7.7 Photoluminescence of derivatized porous silicon: (▲) excitation spectrum (detected at 400 nm) and (●) emission spectrum (excited at 300 nm) of WHE reaction product; (□) emission of deprotected aldehyde.

7.2 External Polymer Synthesis

Soluble conjugated polymers and precursor polymers are readily prepared through bulk synthesis. Such polymers may then be inserted into the pores of the host material in a number of ways. This process allows the use of known bulk synthetic routes to control the properties of the polymer, and direct characterization of the polymer properties before encapsulation. Purification could then remove possible undesirable by-products. This is also the best approach for definite comparisons between the encapsulated and bulk polymer, as ambiguity relating to differences in the chemical structure is eliminated.

The central challenge lies in finding a suitable driving force for polymer insertion into the host material. One key example in the literature in the work of Tolbert *et al.*, where the MEH-PPV polymer (Figure 7.8) was shown to insert itself into a derivatized mesoporous silica material through diffusion and adsorption.[38] A second example is the use of a pressure difference (vacuum or filtration loading).[39,40] A third novel example, to date unexplored in the literature, is the use of centrifugal forces to drive the polymer into the host membrane. These latter two approaches are more useful when the host pore size is larger than a few nm.

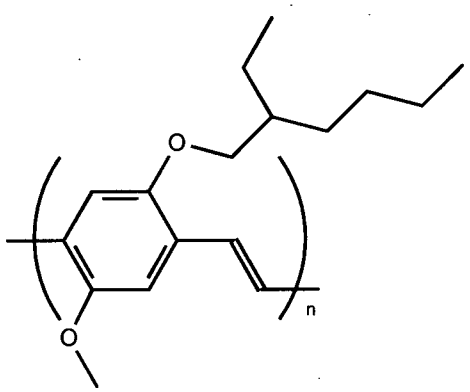

Figure 7.8 Chemical structure of poly[2-methoxy,5-(2′-ethylhexyloxy)-1,4-phenylene vinylene) (MEH-PPV).

7.2.1 Polymer Adsorption Loading

Direct adsorption is a very simple method for incorporating polymer into mesoporous hosts. The MEH-PPV/porous alumina composite studied in chapter 5 was prepared by this approach.

The process is driven by the favourable interactions between the polymer and the pore surface. In the case of alumina, both the electron-rich phenyl rings and the pendant ether oxygens can interact with surface hydroxy groups.[41,42] However, it is not clear if such an approach can be used to introduce more than a monolayer of polymer. It is most likely that this process can only achieve high loading of the host when the ratio of pore surface area to pore volume is high, i.e., when the pore diameter is small. The pore density must be high as well. These conditions are met by mesoporous silica materials; on the other hand, porous alumina can be made with small pore diameters only with a low pore density, due to the fixed pore spacing at the anodization potential for ordered pore growth (see chapter 4).

Since high polymer loading was desired for evaluation of the high resolution characterization techniques, polymer loading by adsorption was not investigated further.

7.2.2 Vacuum (Filtration) Loading

This approach is very useful for introducing material into porous membranes, as has been reported recently for gold nanoparticles.[39,40] The polymer solution is drawn through the porous membrane, and rapid solvent evaporation deposits polymer into the pores. Due to the large pressure difference exerted on the membrane, it must either be very thick or supported in some form. It was found that polymer could be readily introduced into thick porous alumina membranes (60 μm thick Anopore commercial membranes with 200 nm pore size) by simply filtering a polymer solution (Figure 7.9(a)). The substantial polymer loading afforded by this

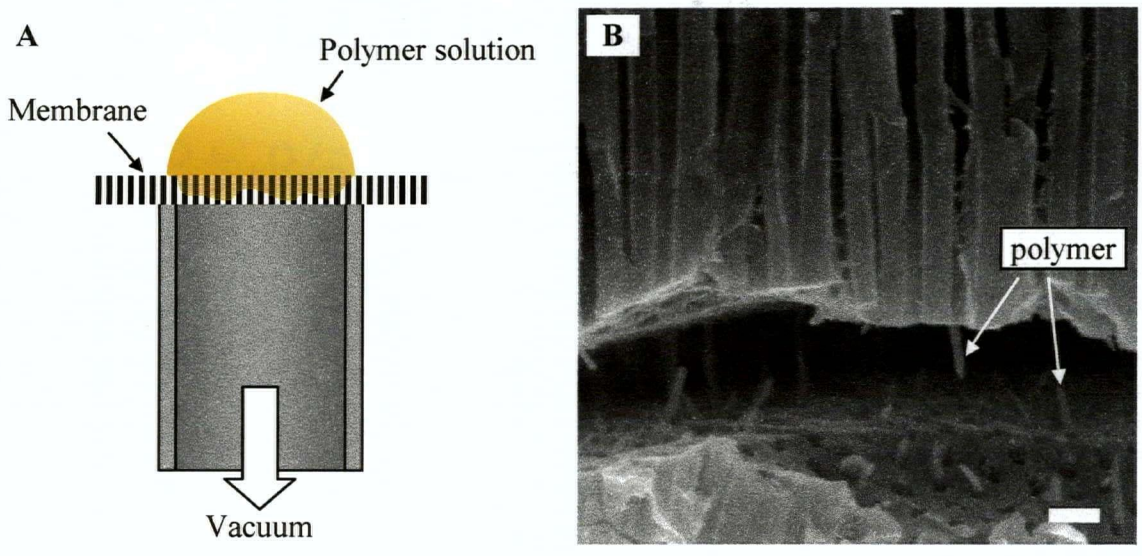

Figure 7.9 (a) Vacuum-driven polymer infiltration into a porous membrane, (b) SEM image of polymer in 200 nm pores of Anopore membrane. The scale bar is 500 nm.

approach allowed the polymer to be seen directly in the pores of the membrane by SEM (Figure 7.9(b)). These thicker membranes could also be used as a support for vacuum loading polymer into thinner membranes. Nevertheless, this approach was not pursued further owing to its requirement of a free-standing membrane and the relative fragility of such membranes.

7.2.3 Centrifugal Loading

The centrifugal force may be used to drive polymer into the pores of the alumina host. Centrifugation is generally used as a separation technique for small particles in solution, but can also be used to create density gradients in polymer solutions.[43] Two loading processes may be possible, depending on the speed of the centrifuge. Direct sedimentation of the polymer may be achieved at very high speeds (150 000 RPM), where the forces are on the order of 9×10^6 N.[43] Such centrifuges were available for use but could not be readily modified to incorporate a vertically oriented substrate. Preliminary experiments were carried out on a typical chemistry

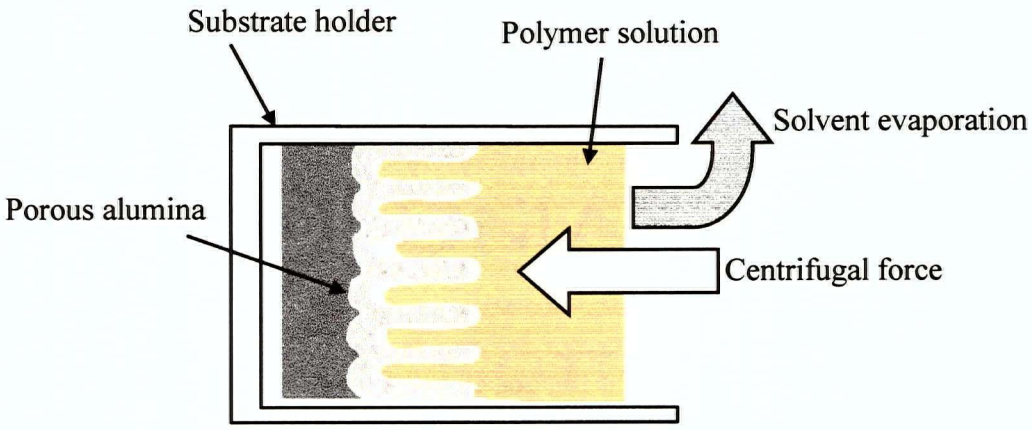

Figure 7.10 Centrifugal polymer loading into a porous alumina film.

laboratory centrifuge, in which the speeds are on the order of a few thousand RPM. It was realized that this speed may be sufficient if the centrifugal force is applied while allowing solvent evaporation, as depicted in Figure 7.10. This second approach was investigated initially, using MEH-PPV dissolved in tetrahydrofuran (THF), and was found to be effective.

7.3 Preparation of Centrifuged Samples

The experimental setup for polymer loading is shown in Figure 7.11: a simple laboratory centrifuge has been modified with a holder for flat substrates. The holder consisted of a threaded stainless steel barrel which could be sealed to the vertically oriented substrate. The seal between the barrel of the holder and the substrate was chosen to be a Viton O-ring, as rubber O-rings are sensitive to many common solvents and Teflon O-rings were found not to provide reproducible seals. The solvent evaporation rate could be controlled to some extent by capping the end of the barrel with a rubber septum.

Although porous alumina membranes with 4 nm pore diameter were available for study, membranes with larger pore sizes (typically ~20 nm) were used. These were more easily fabricated in large numbers for different studies, and the larger amount of polymer which could

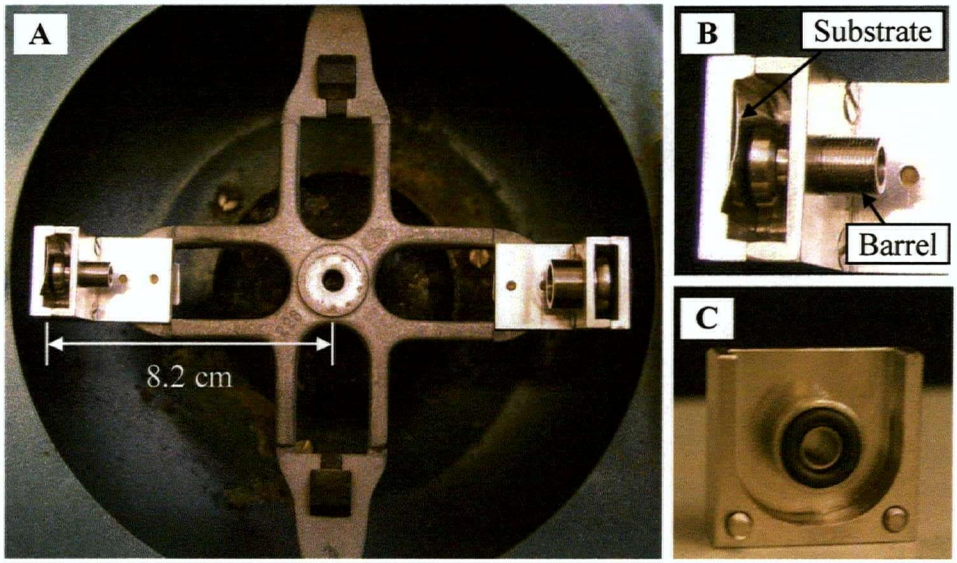

Figure 7.11 (a) Centrifuge rotor assembly with two substrate holders, (b) detail of substrate holder from above and (c) from inside, showing O-ring seal.

be introduced into these pores was important for the development of the characterization techniques for composite samples in general.

The pore volume in a porous alumina film can be calculated from the exposed substrate area (0.28 cm^2) and the approximate porosity (30%). For a 1 μm-thick film, this amounts to ~8 nL. Complete pore filling would then require a polymer mass in the tens of μg. For a polymer solution of 0.038 wt % MEH-PPV in THF, the corresponding volume is on the order of tens of μL.

Consistent results were obtained by using three consecutive centrifuging steps:

(1) MEH-PPV solution, without capping the barrel, ~2 min

(2) additional solvent only, with a capped barrel, ~15 min

(3) barrel cap removed, ~5 min

The first step deposits a small amount of polymer onto the substrate, and the second step serves to drive it further into the pores and distribute it uniformly. The last step, with the cap removed, ensures that the solvent is fully evaporated.

7.4 Characterization of Centrifuged Samples

The MEH-PPV distribution in the centrifuged samples was investigated using a number of different techniques. Visually, the samples showed a thicker ring of polymer deposited at the edge of the exposed area; in some cases, small polymer particles were visible on the surface. The polymer distribution in the centre of the sample was usually even.

7.4.1 Scanning Electron Microscopy

With larger pore samples, the SEM may be used to determine the polymer distribution. The backscattered electron detector was not useful at the magnifications of interest (> 50 000×) and the scattering difference between the carbon-based polymer and the alumina host is not sufficient for useful contrast. The secondary-electron detector, which provides topographical information at high resolution, was used for this study.

When cross-sections of the host material are observed by SEM, a partially filled pore may not stand out evidently. A completely filled pore would eliminate most of the visible structure in the porous film. In many cases, a superficial polymer layer could be readily distinguished (Figure 7.12). Part of this polymer layer could also be seen penetrating into the pores, which indicated some pore filling.

In the case of substantial pore filling, the polymer acts as a replica of the pore space. This can be visualized by etching away the aluminum substrate and the alumina host, as shown in Figure 7.13. The result of this process is shown in Figure 7.14: elongated polymer tubules are visible, indicating substantial penetration of the polymer into the porous alumina host. When thicker polymer-loaded samples were investigated in this fashion, the polymer tubules were observed to have collapsed into bundles (Figure 7.14(b)).

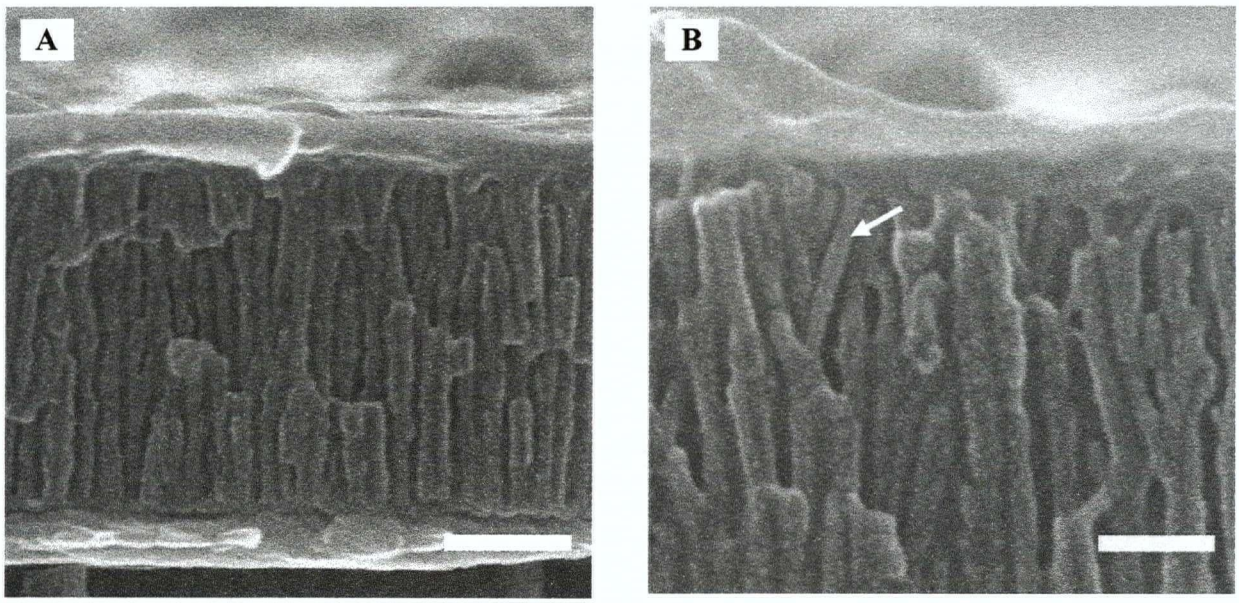

Figure 7.12 SEM image of cross-sections of centrifuged samples, showing (a) polymer overlayer and (b) some polymer penetration into pores. The scale bars are 200 and 100 nm.

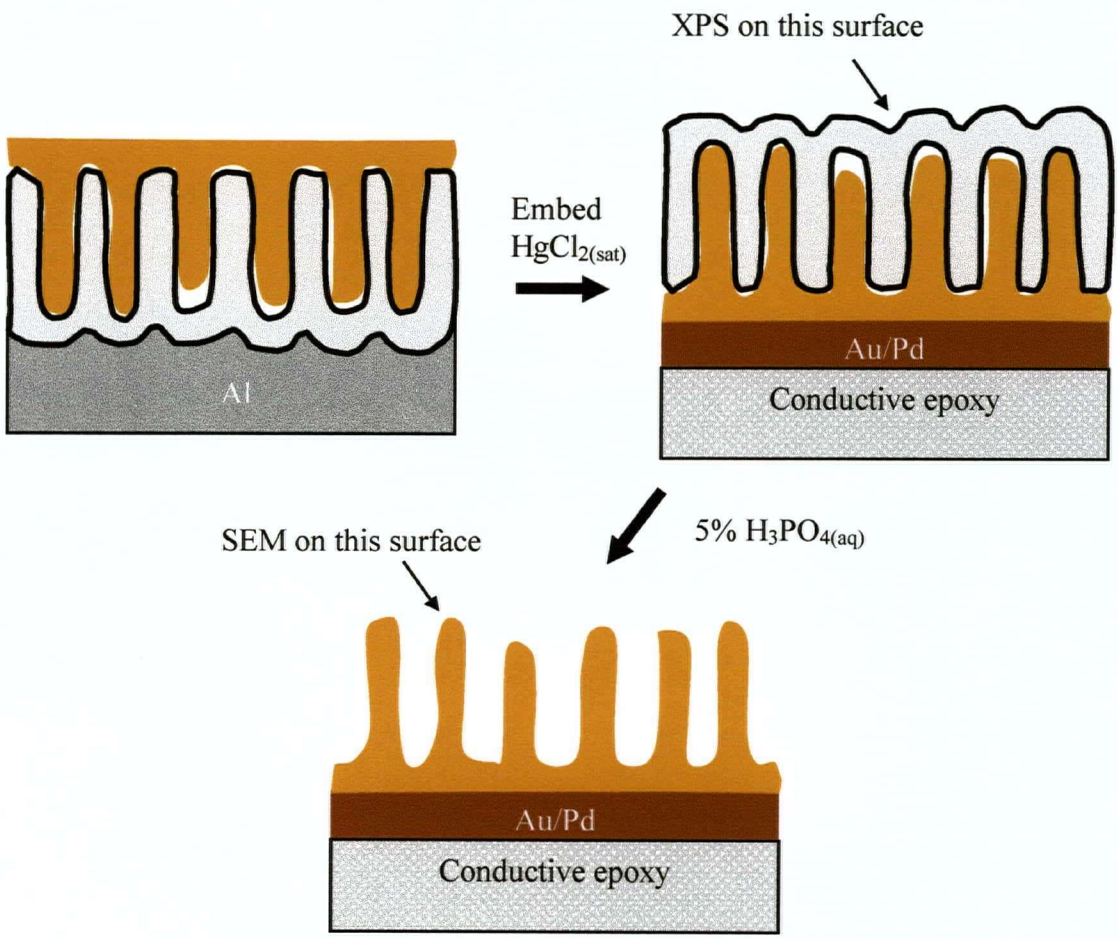

Figure 7.13 Analysis of polymer penetration into porous alumina by XPS and SEM.

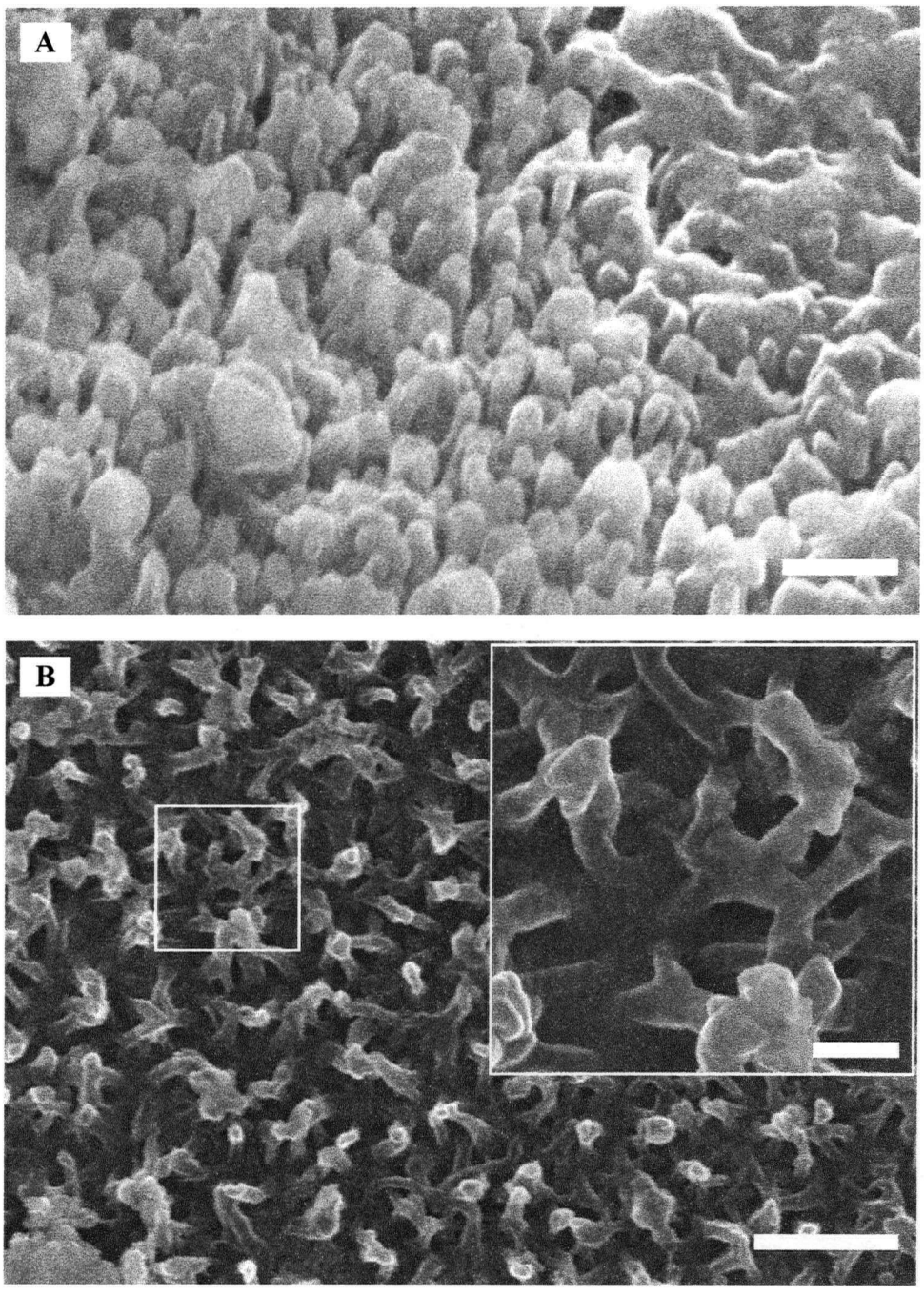

Figure 7.14 SEM images of centrifuged samples, observed from bottom with the host etched away. The scale bars are (a) 200 nm and (b) 1.0 μm (200 nm in the inset).

7.4.2 X-ray Photoelectron Spectroscopy

For the purpose of device preparation, it is necessary to create composite films in which the polymer penetrates the depth of the membrane. Otherwise, electrical contact to the polymer is not possible. This cannot be determined reliably from the SEM images, but may be obtained by X-ray photoelectron spectroscopy (XPS). This is a very surface-sensitive technique, because of the limited mean free path of the generated photoelectrons. The sampling depth is effectively on the order of 1 nm. By analysing the bottom interface of the composite, it may be used to establish whether polymer has penetrated to the bottom of the pores (Figure 7.13). The presence of a carbon signal on this surface, after argon-ion sputtering to remove any adsorbed atmospheric hydrocarbons, would indicate complete polymer penetration to the bottoms of pores. The argon sputtering also served to thin the barrier layer at the bottom of the pores.

The result of this experiment is shown in Figure 7.15. The aluminum 2p (74.7 eV) and oxygen 1s (532 eV) signals are present in both the empty and centrifuged samples. Their

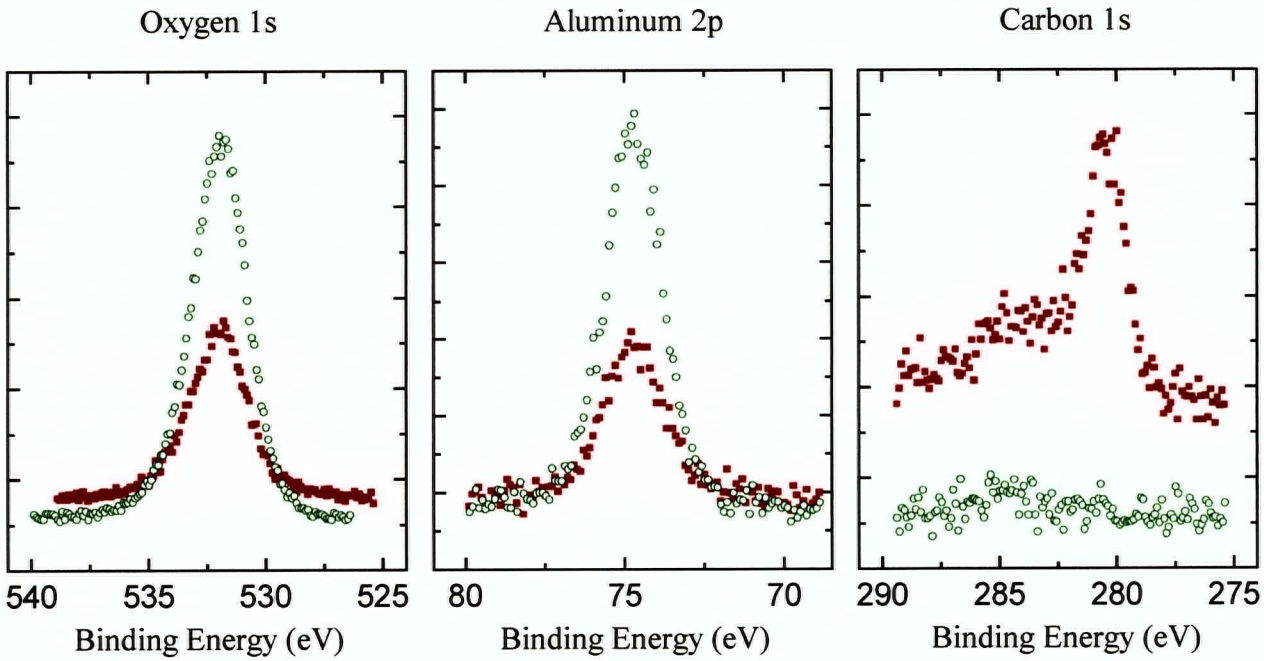

Figure 7.15 XPS results from bottom of (○) empty porous alumina and (■) centrifuged sample.

positions are very close to the expected energies for aluminum oxide (74.3 and 531.1 eV, respectively)[44,45] However, the carbon 1s signal is only present in the centrifuged sample. The main carbon peak, at 280.4 eV, was substantially below the normal range (from 288 eV for oxides to 281 eV for carbides) and this was assigned to sputtering damage.[46] Quantification of the amount of polymer present at the bottom of the pore was not attempted. The results clearly indicate that this loading approach is effective at producing fully penetrated composite materials.

7.4.3 Transmission Electron Microscopy

Thin sections for TEM investigation were prepared by ultramicrotomy of epoxy-embedded samples. Prior to embedding, a thin layer of Au/Pd was deposited by DC sputtering on top of the samples. For the empty host, this prevented epoxy infusion into the pores. For the centrifuged samples, this layer prevented dissolution of MEH-PPV into the epoxy. The thickness of the Au/Pd layer was between 20 and 50 nm.

Sections were cut to thicknesses between 20 and 80 nm. As the pore spacing is 40 nm for porous alumina prepared at 15 V, section thicknesses on that same order will contain not more than one pore. Substantially thinner sections were more difficult to prepare without inducing substantial deformation to the porous alumina film. Nevertheless, good quality sections as thin as 20 nm were obtained for some samples.

Beam damage to the porous alumina host was evident in the appearance of circular defects in the alumina. The stability could be improved substantially by the use of a diffuse electron beam. Under such conditions, the sensitivity of a charge-coupled device (CCD) detector was necessary to capture images within a reasonable amount of time (< 10 s) to avoid any sample drift.

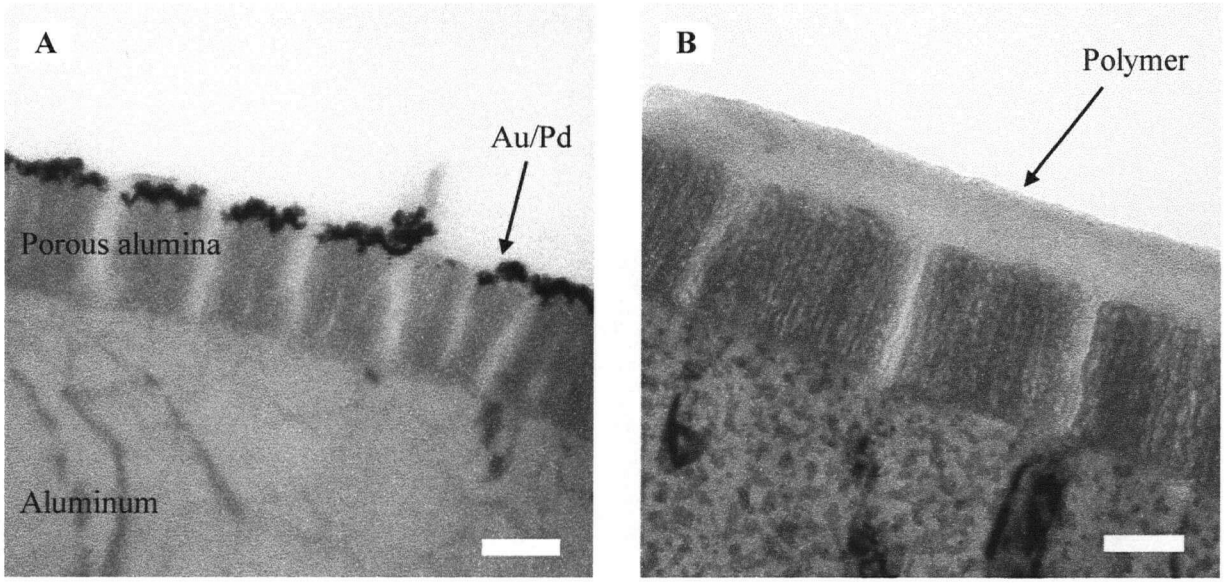

Figure 7.16 TEM images of thin sections of (a) empty porous alumina host and (b) centrifuged sample (beam damage to the host is apparent). The scale bars are 100 nm, and the accelerating voltage was 80 kV.

The cross-section of the empty porous alumina host is shown in Figure 7.16(a). The Au/Pd layer is clearly visible. TEM images of a centrifuged samples are shown in Figure 7.16(b). In this case a polymer overlayer was visible, and the Au/Pd layer was attached to the embedding epoxy, which usually separated away during the sectioning process.

In order to establish the polymer distribution, pores that could be distinguished clearly in the sections were examined. In the empty film, a thin alumina film was associated with many pores, corresponding simply to a section which cut through part of the pore wall. As such, in the centrifuged sample, the presence of polymer could not be distinguished from a pore with a partially sectioned wall. Although in many cases the polymer overlayer seemed to be connected continuously with the material filling the pore, the MEH-PPV distribution could not be established unambiguously by simple examination of the TEM images. The samples were investigated further by EELS and EFTEM.

7.4.4 Energy-filtered Transmission Electron Microscopy

The approach demonstrated in chapter 3 on PPV/MCM-41 samples was applied to the analysis of the centrifuged MEH-PPV/porous alumina composite. It was again anticipated that the aromatic π-π^* plasmon in the low-loss spectrum would reveal the polymer distribution in the composite material. Due to time constraints, only one sample was investigated at an accelerating voltage of 200 kV.

A 2 μm-thick porous alumina film was used to prepare a centrifuged sample. Both the empty host and the centrifuged sample were ultramicrotomed to produce sections ~50 nm thick. The TEM image of an empty host section is shown in Figure 7.17(a); low-loss spectra acquired on the host and on the aluminum substrate are shown in Figure 7.17(b). The alumina bulk plasmon loss had a maximum at 23 eV, in agreement with a previously reported value for amorphous alumina.[47] The aluminum substrate showed a surface plasmon loss at 7 eV and bulk

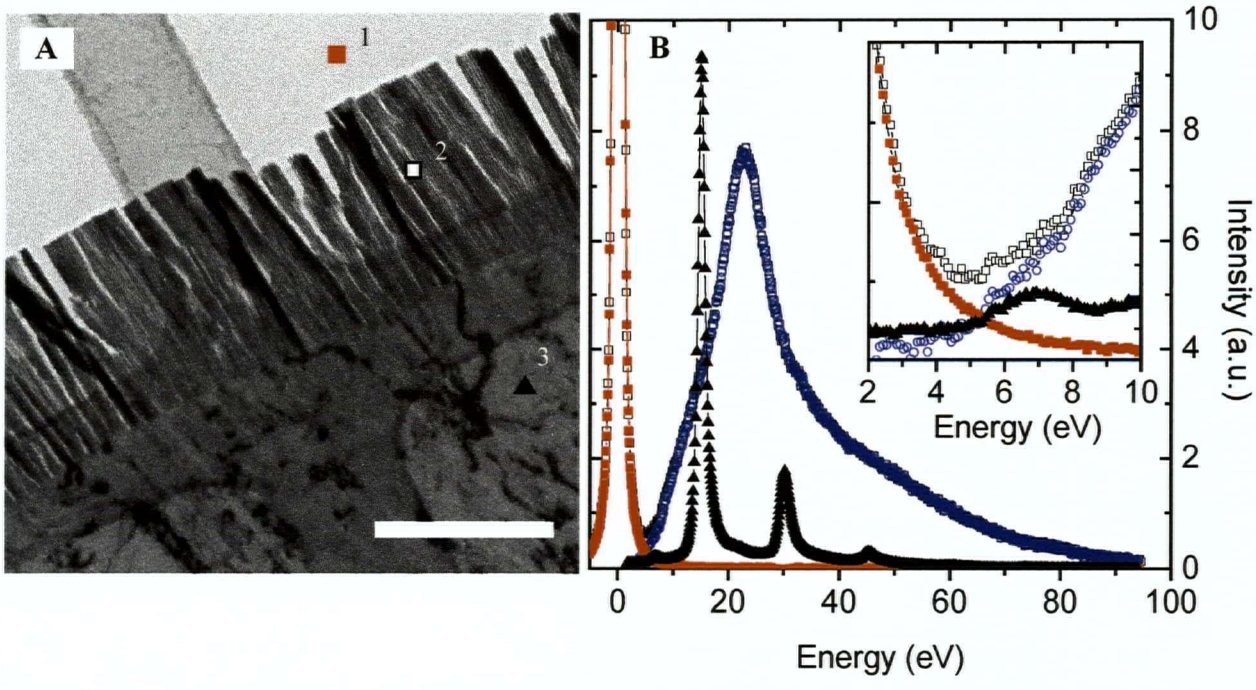

Figure 7.17 (a) TEM image (scale bar is 2 μm) and (b) EELS of thin section of empty porous alumina host: (■) zero-loss peak, porous alumina (□) before and (○) after zero-loss peak subtraction, (▲) aluminum.

plasmon losses at multiples of 15 eV, in agreement with the known aluminum plasmons.[48]

The minimum in the alumina spectrum occurred near 5 eV; an attempt was therefore made to filter on this energy with a 2 eV slit. The energy-filtered images of the empty and centrifuged sample are compared in Figure 7.18: both samples show substantial losses at 5 eV. The presence of small tubules of ~20 nm diameter in defect areas showed that some polymer was present, but the alumina losses at 5 eV appear to mask the polymer distribution in the host. Other areas on the section were similar. Subtraction of the 25 eV image (due mostly to the alumina bulk plasmon) from the 5 eV image did not provide any improvement.

There are two possible causes. First, it is possible that the sectioning process has altered the centrifuged sample: the polymer may have been displaced from the pores in the observed sections. Thus the empty and centrifuged samples appear identical.

The second possible cause may be related to Cherenkov effect in the loss spectrum, as discussed in chapter 6. It appears that there are sufficient losses in alumina below 10 eV such that the presence of polymer is masked by thickness variations in the alumina host. A previous literature report has shown by EELS measurements at 100 kV that losses in amorphous alumina thin films are negligible below 8 eV, in agreement with optical measurements of the dielectric function.[47] The results obtained here differ from this markedly since measurable losses can be observed even below 4 eV (Figure 7.17(b)).

For a 100 kV electron travelling through alumina, the real part of the dielectric function ($\varepsilon_1(\omega)$) must be above 3.3 (Table 6.1). For alumina, the value of $\varepsilon_1(\omega)$ is below this threshold up to 5 eV (Figure 6.2). This suggests that the use of an accelerating voltage of 100 kV or lower is more suitable for the investigation of alumina-based composite materials by low-loss EELS and EFTEM, especially for small amounts of conjugated material.

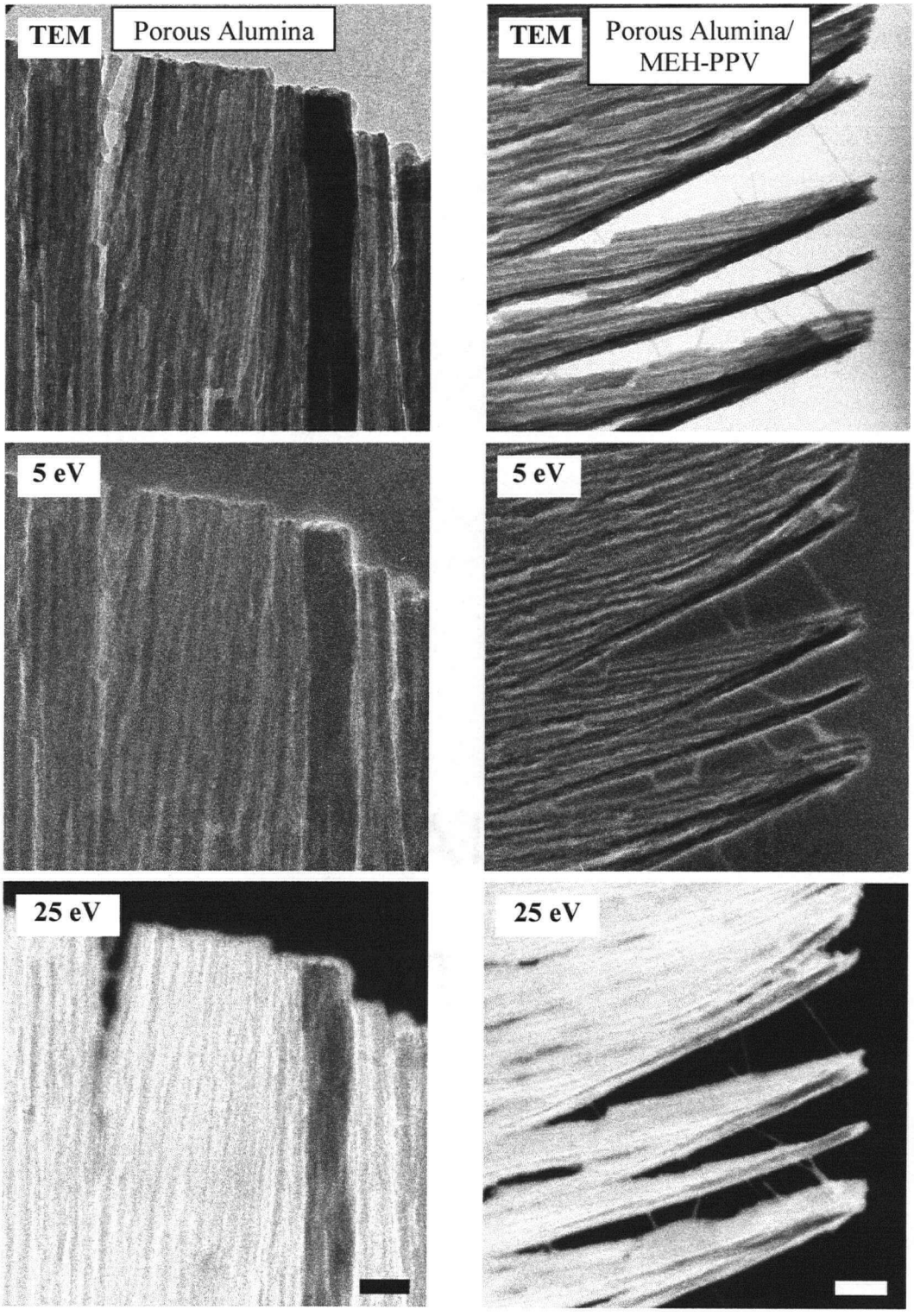

Figure 7.18 Unfiltered (TEM) and energy-filtered (5, 25 eV) images of empty porous alumina and centrifuged MEH-PPV/porous alumina composite. The scale bars are 100 and 200 nm, respectively.

However, it cannot be excluded that some of the features in the low-loss spectrum of porous alumina are due to anion-contamination of the pore walls. Further study at different accelerating voltages would establish which effect is predominant.

For silica-based composite materials (e.g. PPV/MCM-41), there is more flexibility in the choice of accelerating voltage. The dielectric function of an all-silica zeolite, silicalite, has been reported.[49] These results show that $\varepsilon_1(\omega)$ is below 2 up to 5 eV for silicalite and has a maximum value of 3. This suggests the losses due to the Cherenkov effect will be less prominent for silica-based materials even at 200 kV, in agreement with the observed loss spectrum of empty MCM-41 (Figure 3.11).

These issues associated with the low-loss spectrum might have been avoided altogether by filtering on carbon ionization edge at 284 eV instead. This was not attempted because of time constraints. This signal is also expected to be weaker than the plasmon loss, which would entail longer collection times and the associated beam damage to the specimen.

7.4.5 STEM/EELS

Attempts to measure the loss spectrum distribution on thin sections in STEM mode resulted in substantial damage to the alumina host. The image in Figure 7.19(a) shows the damage associated with earlier spectrum acquisitions. The loss spectra recorded in this way showed a new peak near 9 eV (Figure 7.19(b)). Such a feature has been observed previously in a study on electron-beam hole drilling in alumina.[50] It was assigned to molecular oxygen trapped in the material, as drilling proceeds by preferential removal of aluminum atoms.

The loss spectrum acquired directly on a tubule showed substantial losses below 10 eV, suggesting that it was composed of conjugated polymer.

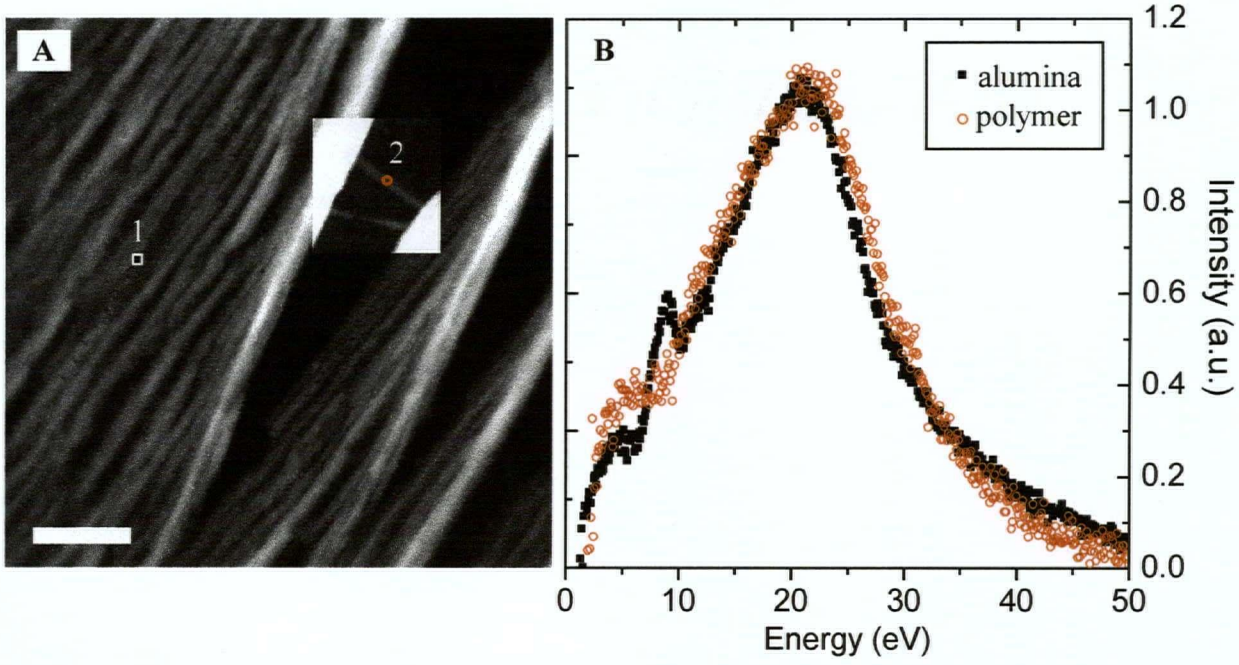

Figure 7.19 (a) STEM image of thin section of centrifuged sample. The contrast has been increased in the inset to show the polymer tubules. (b) EELS associated with (■) drilling in alumina and (○) a polymer tubule. The zero-loss peak has been subtracted.

Nevertheless, it may still be possible to determine the polymer distribution in STEM mode. This has certainly been demonstrated in the core-loss regime[51] and may also be possible in the low-loss regime with careful analysis of the spectra. Such an approach would require a cryogenic sample holder to minimize beam damage to the alumina host, and this was not available for this study.

7.5 Conclusion

Two general approaches to polymer introduction into a porous host were described. The surface-grafted synthesis of conjugated oligomers appears to be a promising route and should be explored in more detail. The synthetic approach described here should be readily applicable to the preparation of larger conjugated molecules on the silicon surface. However, its usefulness can only be confirmed once the structure of the surface-grafted species is established in more

detail, possibly through scanning tunnelling microscopy. These structures would represent a junction between a molecular semiconductor and a bulk semiconductor; the electrical behaviour of such a junction is of fundamental interest.

The use of centrifugal force in conjunction with solvent evaporation has also been explored as a method to introduce a soluble conjugated polymer in porous alumina films. Characterization of the resulting composite clearly showed polymer penetration. However, the polymer could not be located with high resolution by EELS and EFTEM, possibly due to interference from Cherenkov losses in the alumina host. Further experiments at different accelerating voltages would also be required in this direction.

Experimental Details

1. Surface Chemistry

Surface derivatization of porous silicon substrates followed a literature procedure.[30] As silicon is transparent to IR, FT-IR spectra were acquired in transmission. Chemicals were purchased from Sigma-Aldrich, Inc. and used as-received. Carbon tetrachloride and ethylene glycol were dried over molecular sieves. Methylene chloride was dried by passing through activated alumina. NMR spectra were acquired on a Bruker AC-200 at 200 MHz. FT-IR spectra were recorded on a BOMEM MB 155S spectrometer. Photoluminescence spectra were acquired on a Cary spectrophotometer.

2-(4-ethynylphenyl)1,3-dioxolane: Starting from 4-[(trimethylsilyl)ethynyl]benzaldehyde, the ethynyl group was first deprotected following a literature procedure.[52] The aldehyde was then protected by refluxing with excess ethylene glycol in carbon tetrachloride over acidic alumina for 24 h.[53] TLC in 6:1 hexanes/ethyl acetate indicated a single product. The mixture was washed twice with water and dried over magnesium sulfate. Solvent removal under reduced

pressure yielded a light orange solid. After purification by sublimation, a white product was obtained.

FT-IR (KBr): 3270, 3241 (H-C≡C), 2890 (HCOO), 2103 (C≡C), 1424, 1384, 1222, 1074, 941 (1,3-dioxolane), 836 cm^{-1}. ^{1}H NMR (acetone-d^6): δ7.4 (q, 4 H, aromatic), 5.6 (s, 1 H, benzylic), 3.9 (m, 4 H, OCH_2CH_2O), 3.5 (s, 1 H, C≡CH). Mass spectroscopy indicated a parent M/z of 173 ($M^{+\cdot}$ - H).

1,4-xylylenebis(diethylphosphonate): α,α'-dichloro-*p*-xylene was reacted with 2.1 equivalents of triethylphosphite at 140 °C for 5 h. Excess triethylphosphite was removed under reduced pressure. The remaining white powder was purified by recrystallization from methylene chloride/hexanes at -20 °C to form white needle-like crystals. ^{1}H NMR (acetone-d^6): δ7.2 (s, 4 H, aromatic), 4.0 (p, 8 H, $MeCH_2OP$), 3.1 (d, 4 H, CH_2P), 1.2 (t, 12 H, CH_3); ^{31}P NMR: δ26.2. FT-IR (KBr) : 2963, 2907 (CH), 1514, 1480, 1439, 1391 (aromatic), 1261 cm^{-1} (P=O).

Porous silicon: substrates were prepared from n-type silicon wafers as reported in the literature and stored under nitrogen. FT-IR: 1100 cm^{-1} (Si-O framework), 2240 and 2090 cm^{-1} (Si-H). These were present through all the surface modifications below.

Cathodic electrografting on porous silicon: The electrografting cell consisted of a porous silicon substrate clamped down to an aluminum support with a #9 glass joint, and capped with a rubber septum. A Viton O-ring was used to form the seal to the substrate. A platinum mesh counter-electrode was inserted through the septum. A syringe needle was also inserted through the septum to allow evacuation of the cell. The electrografting was carried out under nitrogen atmosphere. The electrolyte, consisting of 0.1 M tetrabutylammonium hexafluorophosphate and 0.2 M protected aldehyde in methylene chloride, was prepared separately under nitrogen and introduced into the cell through the septum. A current density of ~4 mA cm^{-2} was passed through the cell for 3 min. The substrate was then washed with methylene chloride, acetone, water and

ethanol, then dried under a stream of nitrogen. FT-IR (not including silicon surface bands): 2968, 2930, 2884 (C-H), 1606, 1388, 1510 (aromatic), 943 cm^{-1} (1,3-dioxolane).

Aldehyde deprotection on surface: The aldehyde was deprotected by soaking in dilute HCl for 30 min. The substrate was washed with water and dried. FT-IR (not including silicon surface bands): 2969, 2933, 2874 (C-H), 2732 (H-CO), 1700 (C=O), 1603, 1510 (aromatic), 1307 cm^{-1} (aromatic).

WHE reaction on surface: The substrate, 55 mg bis(diethyl phosphonate ester) (0.15 mmol) and a stir bar were added to a round bottom flask and placed under nitrogen. This was followed by the addition of 2.0 mL THF and 0.13 mL of 1.0 M potassium *tert*-butoxide/THF (0.13 mmol). A yellow colour first developed then changed to deep orange. The mixture was refluxed for 5 h. The substrate was then washed with ethanol and acetone, followed by drying under streaming nitrogen. FT-IR (not including silicon surface bands): 2969, 2930, 2869 (C-H), 1510 (aromatic), 1260 cm^{-1} (P=O). Photoluminescence: Emission maximum at 400 nm and a shoulder at 370 nm with excitation at 300 nm; excitation maximum at 322 nm with detection at 400 nm.

2. Vacuum Loading

MEH-PPV was prepared according to a literature procedure.[14] Commercial porous alumina membranes (Anopore by Whatman, Inc.) with a nominal pore diameter of 200 nm on one side and 20 nm on the other side were used. The membrane thickness was 60 μm. It was placed on top of a stainless steel tube, through which vacuum was applied. MEH-PPV polymer solution drops (0.038 to 0.8 wt % in THF) were placed on top of the membrane. Once the solution was drawn through, the membrane was removed for analysis. A Hitachi S-4100 field-emission SEM was used for observation of the composite structure.

3. Centrifuged Samples

Porous alumina hosts were prepared by anodizing aluminum foil samples in 1.2 M sulfuric acid at 15.0 V or in 0.3 M oxalic acid at 40.0 V at room temperature, as described in chapter 4. Some films were also prepared on silicon substrates by anodizing electron-beam evaporated aluminum films. These allowed convenient cross-section preparation by cleavage of the silicon substrate. The anodization time was generally between 2 min and 8 min, resulting in film thicknesses of 0.5 to 2 μm. The pore walls were etched for 5 to 10 min in 5% H_3PO_4, then soaked in distilled H_2O. The samples were then rinsed with ethanol, dried with a heat gun and further dried under vacuum.

Centrifugation was carried out in a standard laboratory centrifuge with a speed of 1700 RPM, using a substrate holder described above. The approximate centrifugal force at the substrate was 3×10^3 N.

MEH-PPV was prepared according to a literature procedure.[14] A 0.038 wt % solution of MEH-PPV in THF (typically 15 – 20 μL) was deposited into the holder by syringe and spun for 5 min. Pure THF was then added (again ~20 μL) and the holder sealed to reduce the evaporation rate. After 15 min of spinning, the seal was removed and the uncovered holder spun again for 5 min.

A Hitachi S-4700 field emission SEM was used to observe the samples, typically with an accelerating voltage of 20 kV for high resolution work.

For XPS analysis of the pore bottoms, a layer of Au/Pd was first deposited onto the top surface. This prevented epoxy penetration into the sample during embedding of the top surface. Due to the need for conductivity, a silver-filled epoxy was used as the embedding medium (Epotek, Inc.). The remaining aluminum substrate was removed by treatment with $HgCl_{2(sat)}$.

Analysis was carried out on a Leybold MAX200 using the Al K_α radiation as the excitation source.

Thin sections were obtained by ultramicrotomy of samples embedded in epoxy (302-3M, Inc.). A diamond knife (Microstar, Inc.) with a 45° included angle was used. The knife clearance angle was set to 4°, and sectioning speeds as low as 0.2 mm s^{-1} were used. The thin sections were floated in a water bath and collected either with lacey carbon-coated Cu grids (Ted Pella, Inc.) or similar Quantifoil-coated Cu grids (Qantifoil Micro Tools GmbH). These grids allowed investigation of the sections by EELS without any interference from a support film, due to the presence of holes in the coatings.

Initial sample observation was carried out on a Hitachi H-7600 TEM at an accelerating voltage of 80 kV. EELS and EFTEM were carried out on a Tecnai F20 TEM equipped with a Gatan Imaging Filter. The accelerating voltage was 197 kV (200 kV nominally, offset by 3 kV by the GIF). Loss spectra were recorded in TEM mode by placing the particle of interest above the GIF entrance aperture (diameter 2.0 mm). The zero-loss peak was recorded separately by moving to an empty area on the grid, immediately before or after spectrum collection. A collection time of 5 s was used. Subtraction was carried out by shifting and scaling the zero-loss peak. EFTEM images were acquired with a 2 eV slit. In STEM mode, a camera length of 150 mm was used, and spectra were collected using a 50 ms dwell time.

The system energy resolution, given by the FWHM of the zero-loss peak, was 0.96 eV. The energy dispersion of the spectrometer was 0.10 eV/pixel.

References

1. Martin, C. R. *Acc. Chem. Res.* **1995**, *28*, 61.

2. Wu, C.-G.; Bein, T. *Science* **1994**, *264*, 1757.

3. Yu, B. Z.; Li, H. L. *Mater. Sci. Eng., A* **2002**, *325*, 215.

4. Yu, B. Z.; Li, M. K.; Lu, M.; Li, H. L. *Appl. Phys. A* **2003**, *76*, 593.

5. Kim, K.; Jin, J. I. *Nano Lett.* **2001**, *1*, 631.

6. Wagaman, M. W.; Grubbs, R. H. *Macromolecules* **1997**, *30*, 3978.

7. Boyd, T. J.; Geerts, Y.; Lee, J. K.; Fogg, D. E.; Lavoie, G. G.; Schrock, R. R.; Rubner, M. F. *Macromolecules* **1997**, *30*, 3553.

8. Scherf, U. *Carbon Rich Compounds Ii* **1999**, *201*, 163.

9. Juang, A.; Scherman, O. A.; Grubbs, R. H.; Lewis, N. S. *Langmuir* **2001**, *17*, 1321.

10. Harada, Y.; Girolami, G. S.; Nuzzo, R. G. *Langmuir* **2003**, *19*, 5104.

11. Li, Z. F.; Ruckenstein, E. *Macromolecules* **2002**, *35*, 9506.

12. Liu, J.; Lin, Y. H.; Liang, L.; Voigt, J. A.; Huber, D. L.; Tian, Z. R.; Coker, E.; Mckenzie, B.; Mcdermott, M. J. *Chem. Eur. J.* **2003**, *9*, 605.

13. Fabre, B.; Lopinski, G. P.; Wayner, D. D. M. *Chem. Commun.* **2002**, 2904.

14. Neef, C. J.; Ferraris, J. P. *Macromolecules* **2000**, *33*, 2311.

15. Jones, L.; Schumm, J. S.; Tour, J. M. *J. Org. Chem.* **1997**, *62*, 1388.

16. Strehmel, B.; Sarker, A. M.; Malpert, J. H.; Strehmel, V.; Seifert, H.; Neckers, D. C. *J. Am. Chem. Soc.* **1999**, *121*, 1226.

17. Pfeiffer, S.; Horhold, H. H. *Macromol. Chem. Phys.* **1999**, *200*, 1870.

18. Sugiono, E.; Metzroth, T.; Detert, H. *Adv. Synth. Catal.* **2001**, *343*, 351.

19. Egbe, D. A. M.; Cornelia, B.; Nowotny, J.; Gunther, W.; Klemm, E. *Macromolecules* **2003**, *36*, 5459.

20. Johnson, C. R.; Zhang, B. R. *Tetrahedron Lett.* **1995**, *36*, 9253.

21. Salvino, J. M.; Kiesow, T. J.; Darnbrough, S.; Labaudiniere, R. *J. Comb. Chem.* **1999**, *1*, 134.

22. Warrass, R.; Lippens, G. *J. Org. Chem.* **2000**, *65*, 2946.

23. Buriak, J. M. *Chem. Commun.* **1999**, 1051.

24. Wayner, D. D. M.; Wolkow, R. A. *J. Chem. Soc., Perkin Trans. 2* **2002**, 23.

25. Sailor, M. J.; Lee, E. J. *Adv. Mater.* **1997**, *9*, 783.

26. Song, J. H.; Sailor, M. J. *J. Am. Chem. Soc.* **1998**, *120*, 2376.

27. Song, J. H.; Sailor, M. J. *Comments Inorg. Chem.* **1999**, *21*, 69.

28. Song, J. H.; Sailor, M. J. *Inorg. Chem.* **1999**, *38*, 1498.

29. Buriak, J. M.; Stewart, M. P.; Geders, T. W.; Allen, M. J.; Choi, H. C.; Smith, J.; Raftery, D.; Canham, L. T. *J. Am. Chem. Soc.* **1999**, *121*, 11491.

30. Robins, E. G.; Stewart, M. P.; Buriak, J. M. *Chem. Commun.* **1999**, 2479.

31. Schmeltzer, J. M.; Porter, L. A.; Stewart, M. P.; Buriak, J. M. *Langmuir* **2002**, *18*, 2971.

32. Stewart, M. P.; Buriak, J. M. *Comments Inorg. Chem.* **2002**, *23*, 179.

33. Boukherroub, R.; Morin, S.; Wayner, D. D. M.; Lockwood, D. J. *Physica Status Solidi a-Applied Research* **2000**, *182*, 117.

34. Boukherroub, R.; Morin, S.; Wayner, D. D. M.; Lockwood, D. J. *Solid State Commun.* **2001**, *118*, 319.

35. Wojtyk, J. T. C.; Morin, K. A.; Boukherroub, R.; Wayner, D. D. M. *Langmuir* **2002**, *18*, 6081.

36. Crouse, D.; Lo, Y. H.; Miller, A. E.; Crouse, M. *Appl. Phys. Lett.* **2000**, *76*, 49.

37. Glusac, K. D.; Schanze, K. S. *Polymer Preprints* **2002**, *43*, 87.

38. Wu, J. J.; Gross, A. F.; Tolbert, S. H. *J. Phys. Chem. B* **1999**, *103*, 2374.

39. Hornyak, G.; Kroll, M.; Pugin, R.; Sawitowski, T.; Schmid, G.; Bovin, J. O.; Karsson, G.; Hofmeister, H.; Hopfe, S. *Chem. Eur. J.* **1997**, *3*, 1951.

40. Marinakos, S. M.; Brousseau, L. C.; Jones, A.; Feldheim, D. L. *Chem. Mater.* **1998**, *10*, 1214.

41. Vanderbeek, G. P.; Stuart, M. A. C.; Fleer, G. J.; Hofman, J. E. *Macromolecules* **1991**, *24*, 6600.

42. Mathur, S.; Moudgil, B. M. *Miner. Metall. Process* **1998**, *15*, 24.

43. Elias, H. G. *Polymere*; Hüthig & Wepf Verlag: Heidelberg, 1996.

44. Treverton, J. A.; West, R.; Johnson, D.; Thornton, M. *Appl. Surf. Sci.* **1993**, *72*, 349.

45. Rehim, S. S. A.; Hassan, H. H.; Amin, M. A. *J. Appl. Electrochem.* **2002**, *32*, 1257.

46. P. Wong, personal communication.

47. French, R. H.; Mullejans, H.; Jones, D. J. *J. Am. Ceram. Soc.* **1998**, *81*, 2549.

48. Egerton, R. F. *Electron energy-loss spectroscopy in the electron microscope*; 2nd ed.; Plenum Press: New York, 1996.

49. McComb, D. W.; Howie, A. *Nucl. Instrum. Methods Phys. Res., Sect. B* **1995**, *96*, 569.

50. Berger, S. D.; Salisbury, I. G.; Milne, R. H.; Imeson, D.; Humphreys, C. J. *Philos. Mag. B* **1987**, *55*, 341.

51. Arayasantiparb, D.; McKnight, S.; Libera, M. *J. Adhes.* **2001**, *76*, 353.

52. Austin, W. B.; Bilow, N.; Kelleghan, W. J.; Lau, K. S. Y. *J. Org. Chem.* **1981**, *48*, 2280.

53. Kamitori, Y.; Hojo, M.; Masuda, R.; Yoshida, R. *Tetrahedron Lett.* **1983**, *26*, 4767.

CHAPTER 8 Comments on Device Fabrication

A substantial amount of effort was directed at fabricating a functioning light-emitting device (LED) based on the composite materials described in this thesis. The preparation of an LED based on conjugated polymer inside a porous alumina host involves three key steps: (1) preparation of porous thin film host, (2) introduction of the conjugated polymer guest, and (3) application of electrodes. The first step was the subject of chapter 4 and will be elaborated upon here in consideration of the third step, the need for electrodes to make an electrical device. The processes described here also assume that the conjugated polymer insertion proceeds by centrifugation (chapter 7), which requires a host film with a supporting substrate.

The devices prepared in this work either did not show any electrical conductivity or failed rapidly because of electrical short circuits. There were no substantially new results in these endeavours but many processing issues were recognized. This chapter is intended to summarize these results and discuss possible routes to the creation of devices based on the porous alumina host.

8.1 Device Structure

The structure of a polymer-based (LED) is constrained by the requirements of two key processes: the field-assisted injection of charges at the polymer-electrode interfaces, and the recombination of charges within the polymer (Figure 1.4). The high electric fields required for

charge injection[1,2] can be obtained at moderate applied potentials (< 50 V) by minimizing the thickness of the polymer layer between the electrodes. The higher hole mobility causes charge recombination to occur close to the electron-injecting electrode. Non-radiative quenching of the excited state has been found to be important near this electrode, which effectively enforces a minimum device thickness of ~90 nm.[3] Above this threshold, the efficiency of a polymer LED remains effectively constant with thickness, up to several hundred nanometres.[3]

The ideal structure is shown in Figure 8.1: the central requirement for a functional device is the existence of the contact surfaces to the anode and cathode materials. Indium tin oxide (ITO) and gold are commonly used as anode materials for MEH-PPV-based devices, whereas a number of different low-workfunction metals (calcium, silver, aluminum) may be applied as the cathode.

The anodization procedure for porous alumina hosts leaves one surface immediately accessible for the application of an electrode. The second surface is usually capped by the alumina barrier layer, which may be over 20 nm thick (Figure 4.11). This barrier layer must be

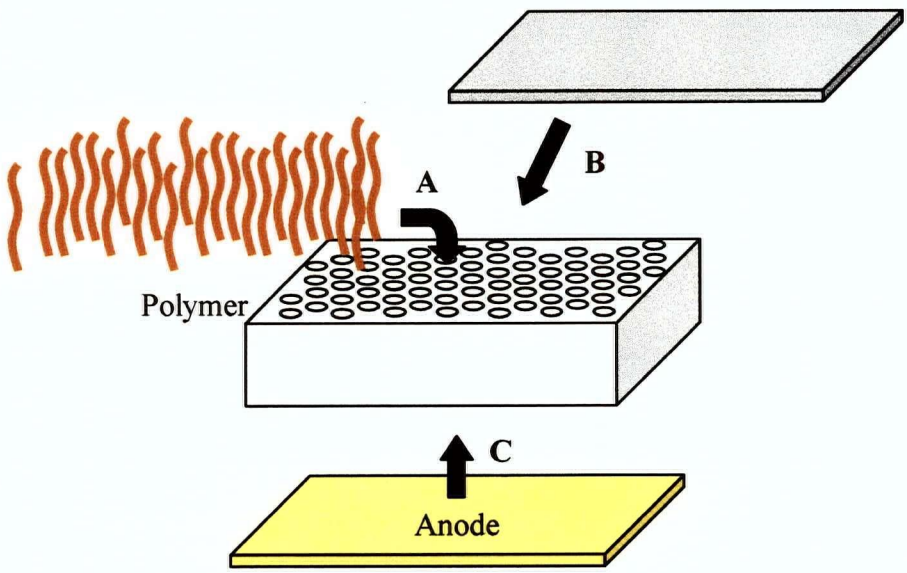

Figure 8.1 Ideal conjugated polymer device components and their assembly: (a) polymer insertion into host, (b) cathode evaporation and (c) anode deposition.

removed in all cases to create functional devices.

8.2 Devices from Porous Alumina Films on Aluminum Foil

A device fabrication sequence utilizing a porous alumina film grown on an aluminum foil is shown in Figure 8.2. Equivalent structures may be produced by partially anodizing thick aluminum films on suitable substrates (silicon wafer, glass slide). These substrates can be cleaved easily, which provides a convenient method for obtaining cross-sections for SEM. The barrier layer is thinned by reducing the potential at the end of the anodization process (Figures 8.3 and 8.4).

After polymer introduction, an ITO anode is deposited on the polymer by RF sputtering. A lead is attached to the ITO layer with silver epoxy, and the top surface is embedded in epoxy to provide support for the device.

At this stage, the aluminum substrate can conceivably act as the electron-injecting contact for the device. This was tested on several different devices but no electroluminescence was observed. All devices eventually failed under the applied potential. The obstacle to device operation in this form is probably the remaining barrier layer at the bottom of the pores.

Further processing to remove this barrier layer was not possible, as the structure proved too fragile for removal of the aluminum substrate: the host film readily separated from the deposited ITO layer during the $HgCl_{2(sat)}$ etching step (Figure 8.2(f)). A solution to this problem was not found

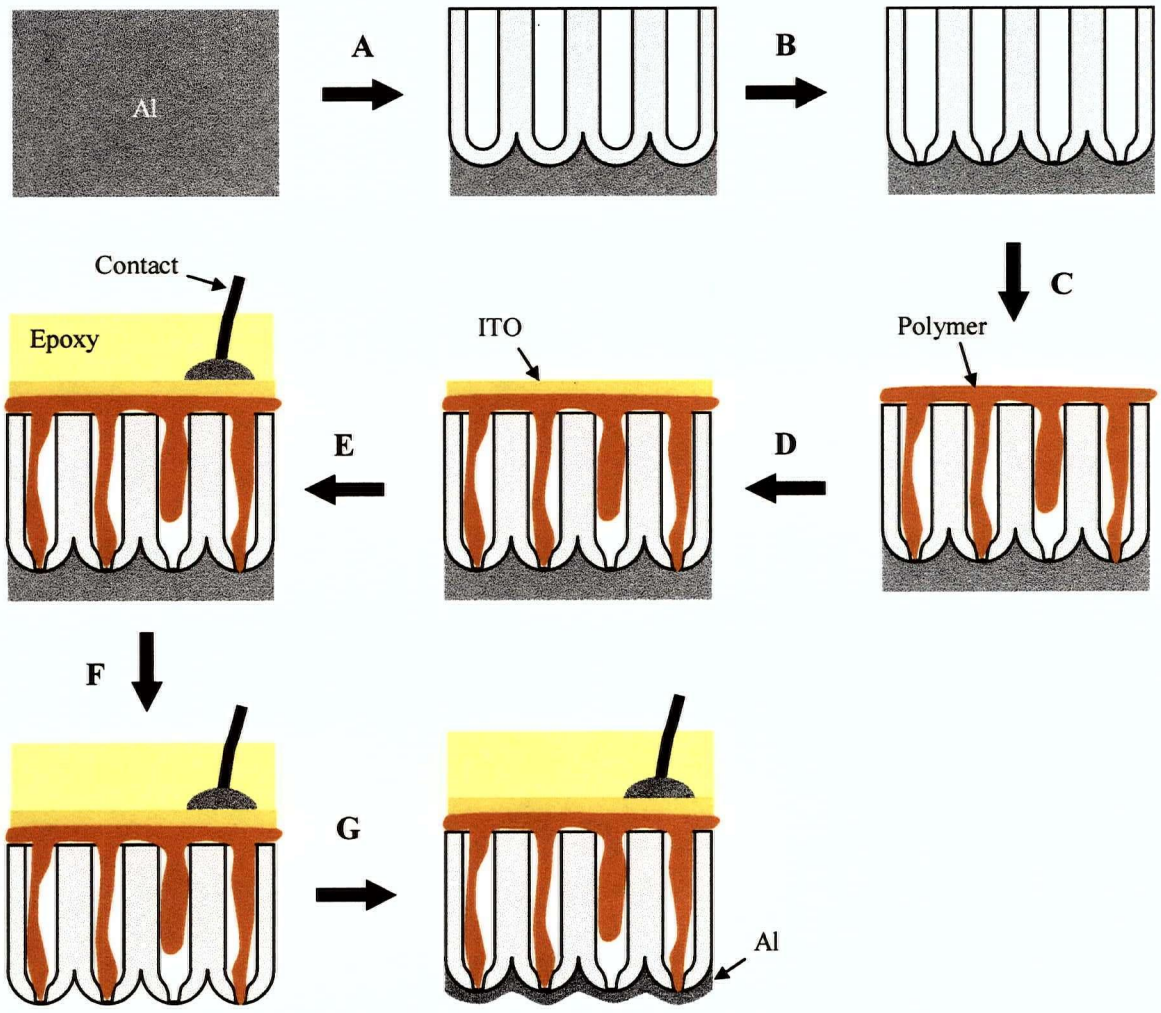

Figure 8.2 Device fabrication sequence from porous alumina film on aluminum foil: (a) anodization of aluminum foil, (b) barrier layer thinning by potential reduction, (c) polymer introduction by centrifugation, (d) ITO deposition by RF sputtering, (e) contact lead bonding with silver epoxy and epoxy embedding of upper surface, (f) aluminum foil removal by chemical etching, (g) aluminum cathode deposition by thermal evaporation.

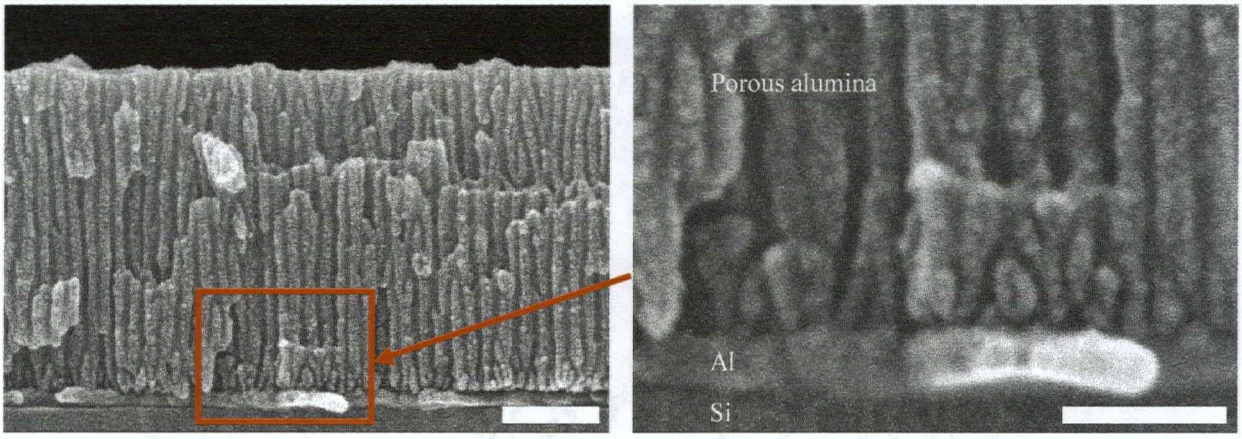

Figure 8.3 SEM images of porous alumina film on a n-type silicon wafer with the barrier layer eliminated by the potential reduction method. The film was anodized at 15 V in 1.2 M sulfuric acid at 20°C followed by a potential reduction to 9 V over 30 s, then a reduction to 0 V over 5 s. The scale bars are 200 nm and 100 nm, respectively.

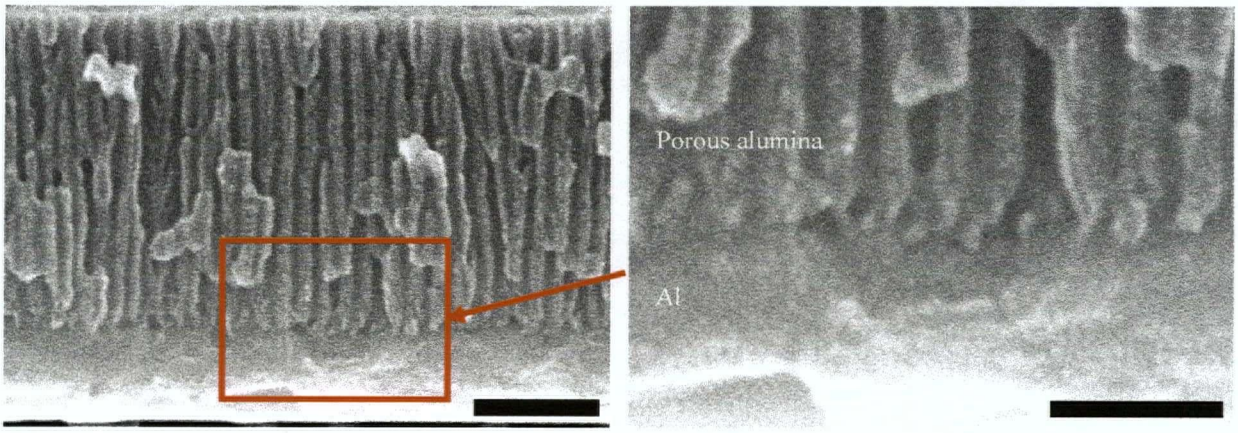

Figure 8.4 SEM images of porous alumina film, showing elimination of barrier layer by rapid potential reduction (from 15 V to 0 V over 8 s). The scale bars are 200 nm and 100 nm, respectively.

8.3 Devices from Thin Films on Conducting Substrates

The integrity of the polymer/porous alumina composite film may be better retained if the porous alumina host is formed directly from an aluminum film on a conductive substrate. Substrates of interest would include any material that can serve as anode in an LED: silicon, ITO and gold. The device fabrication sequence is illustrated in Figure 8.5.

The initial step involves deposition of aluminum thin films. The different physical vapour deposition methods are reviewed below. The anodization step proceeds normally until the substrate interface is reached, at which point the electrolyte may or may not react with the substrate material. Aluminum films on silicon, ITO and gold were investigated, but no suitable structures could be produced. The results and difficulties encountered are described below.

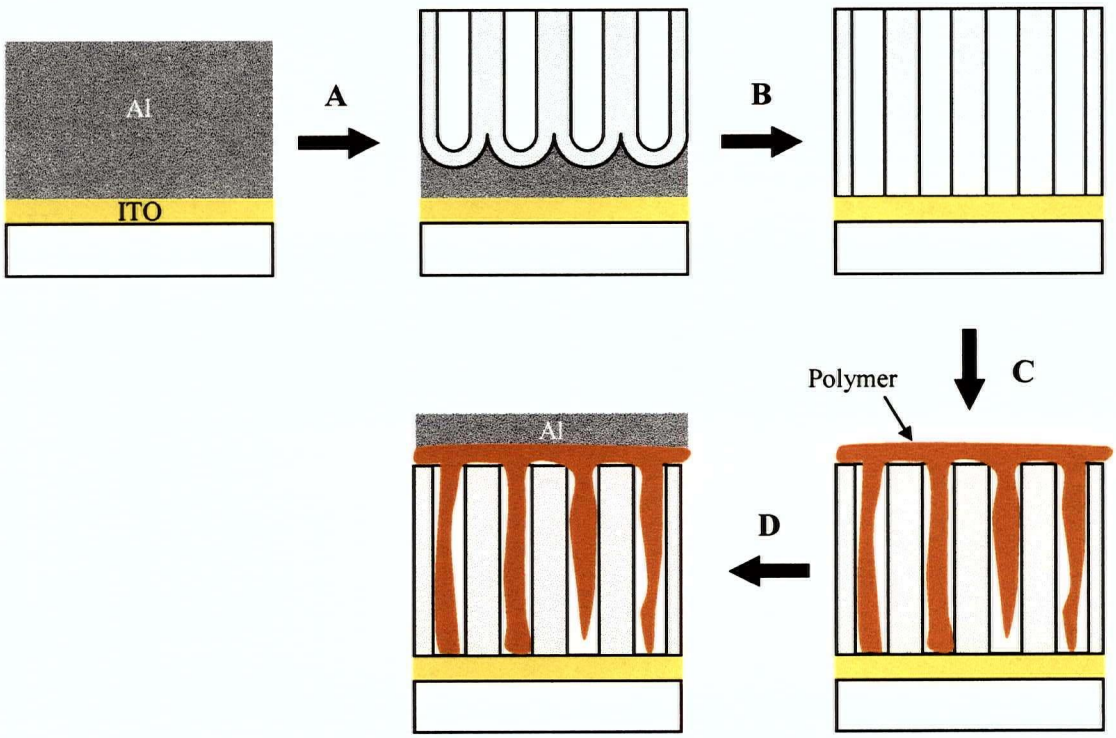

Figure 8.5 Device fabrication sequence from an aluminum film on a conductive substrate: (a) initial aluminum film on substrate, (b) porous alumina film growth, (c) final porous alumina film with barrier layer removed, (d) complete device with conjugated polymer sandwiched between cathode and anode.

8.3.1 Aluminum Film Deposition

The aluminum deposition step must also be carefully controlled for the preparation of defect-free films. Proper cleaning of the substrate was necessary to obtain good adhesion. A simple protocol consisting of two 10 min sonication steps (detergent solution, methanol) was found to be suitable for most substrates.

A number of different film deposition methods available at UBC were investigated. RF sputtering and electron-beam evaporation were available in the AMPEL cleanroom. DC sputtering was available in the Department of Physics, while thermal evaporation was available in the Department of Electrical Engineering.

DC sputtering of aluminum allows convenient deposition of thicker films (> 1 μm, rate > 0.5 nm s^{-1}). However, the setup available at UBC was found to produce contaminated films, as evidenced by gas evolution during the anodization process. It was not used for any further work.

RF sputtering is normally used for the deposition of dielectric materials. It may also be used to deposit aluminum, however hillock formation is known to occur (Figure 8.6). The resulting surface roughness lowers the reflectivity of the aluminum film. The addition of a small

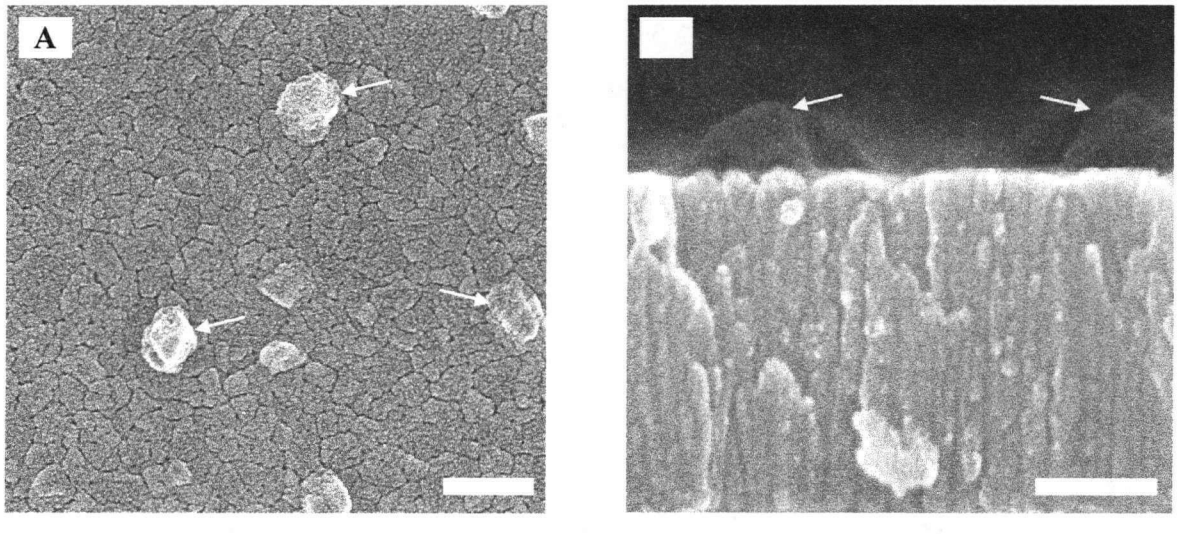

Figure 8.6 SEM images of hillocks on porous alumina films prepared from RF sputtered aluminum films, showing (a) top surface and (b) cross-section. The scale bars are 200 nm.

amount of copper (~1%) is used in the semiconductor industry to prevent hillock formation. This was not attempted here, as the effect of copper impurities on the anodization step was not known. Nevertheless, RF sputtering produced continuous films with good adhesion. The deposition rate was typically 0.2 nm s^{-1}.

Electron-beam evaporation is also commonly used to deposit aluminum. The only difficulty was the presence of pinholes in the resulting film if the deposition process is too rapid. The associated surface roughness again causes a lower reflectivity in the deposited films. The anodized films then contain defects as shown in Figure 8.7. Defect-free films were achievable by keeping the deposition rate below 0.5 nm s^{-1}.

Thermal evaporation was found to produce films with pinholes as well. In this case, the effect of deposition rate was not investigated in more detail. Since the physical process is almost identical to electron-beam evaporation, it is expected that control of the deposition rate would produce similar pinhole-free films.

8.3.2 Porous Alumina/Silicon

The possibility of directly using silicon wafers as an electrode for an organic electroluminescent device has been explored in the literature.[4-6] Parker and Kim showed that both degeneratively doped *n*- and *p*-type silicon wafers can be used as anode or cathode in devices made with MEH-PPV.[4] Wunsch *et al.* found that *p*-type silicon was a better hole-injecting material than either gold or ITO.[6]

Crouse *et al.* investigated the fabrication of porous alumina films on silicon wafers for the purpose of hexagonal pattern transfer to the wafer.[7] They found that *n*-type silicon could be used readily as a substrate, as there were no unfavourable reactions with oxalic, sulfuric or phosphoric acid up to potentials of 110 V. It was observed that the barrier layer could be readily removed by

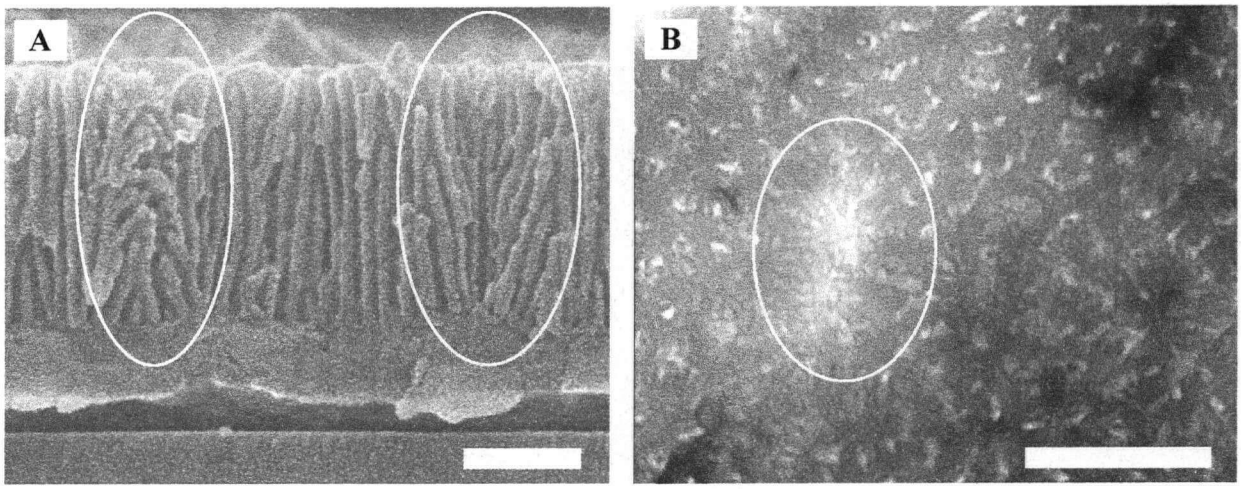

Figure 8.7 Defects in porous alumina films anodized from electron-beam evaporated aluminum film, showing (a) SEM image of cross-section of a film anodized at 20 °C in 1.2 M sulfuric acid and (b) TEM image in plan view of a film anodized at -39 °C. The scale bars are 200 nm long.

a short etching step with 5% phosphoric acid. On the other hand, *p*-type silicon was not suitable without an insulating coating of silicon dioxide.

As degeneratively doped silicon wafers were not readily available, this approach was not pursued any further but may be a promising avenue for future work.

8.3.3 Porous Alumina/ITO

The preparation of porous alumina films on ITO-coated glass substrates has been reported by Chu *et al.*[8] The anodization process normally consumes the ITO layer if it is not halted once the aluminum layer is fully oxidized. If anodization is halted at the right point, the ITO layer is preserved and the desired structure is obtained. These results were obtained with a 10 vol. % phosphoric acid electrolyte and 130 V. The pore size in the resulting film was 80-100 nm.

Protection of the ITO layer by deposition of a thin layer of silicon dioxide or aluminum oxide between the ITO and aluminum layers is also possible. One literature report indicated that a thin silicon dioxide layer above the ITO layer was even beneficial to LED efficiency, through a

better balance of the hole and electron injection rates.[9] An optimal thickness near 2 nm was reported.

Attempts were made to reproduce these results with aluminum deposited on ITO-coated glass and poly(ethylene terephthalate) substrates. The latter is advantageous for obtaining cross-sections by ultramicrotomy. However, pinholes were always present in the aluminum film, as evidenced by immediate gas evolution (i.e., reaction of the ITO) at the beginning of the anodization process. It is believed that deformation of the plastic substrate under the thermal load of the evaporation process was the cause of the pinholes.

On ITO-coated glass substrates, both sulfuric and oxalic acid electrolytes (for pore sizes of ~21 and 60 nm respectively; see chapter 4) were used to anodize the deposited aluminum film. However, the anodization process, using the cell depicted in Figure 4.10, did not proceed uniformly across the substrate, with the outer edge being anodized faster. This produced structures in which the ITO layer was consumed at the edges (Figure 8.8), and aluminum remained in the centre.

The deposition of thin silicon dioxide and alumina layers (up to 4 nm in thickness) was not

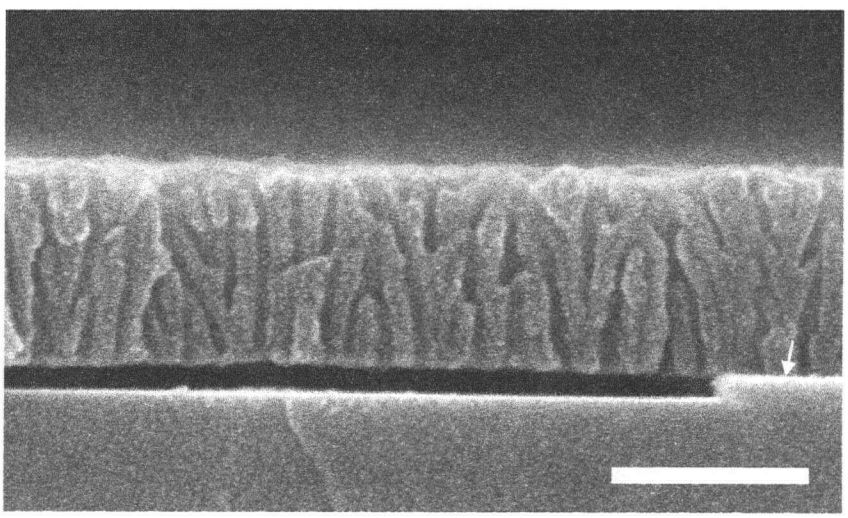

Figure 8.8 SEM image of porous alumina film on ITO-coated glass substrate, showing an area where most of the ITO was consumed. The scale bar is 200 nm.

found to provide any significant protection to the ITO layer during anodization. Thicker layers may have provided more protection but would then have required removal by a different process (e.g., reactive-ion etching). It is also possible that stirring of the electrolyte would have created a more uniform anodization on the substrate. Lowering the electrolyte temperature would reduce the anodization rate, which may allow better control over the end point. As these difficulties were not resolved, this approach did not provide any suitable host films for further processing.

8.3.4 Porous Alumina/Gold

Gold is also commonly used as hole-injecting electrode in polymer-based devices. However, there are two difficulties associated with fabricating porous alumina films over gold. First, aluminum and gold interdiffuse readily to create an intermetallic compound.[10] This proceeds rapidly at 100 °C, with films deteriorating within 1 h. Room-temperature degradation proceeds at a slower rate, which necessitates immediate processing of deposited films. The second difficulty, as with ITO, is in the anodization process: gas evolution occurs at the gold interface once the aluminum is consumed. A literature report indicated that it was again possible to obtain useful structures by stopping the anodization at the correct time.[11] Efforts to reproduce this result were unsuccessful due to immediate reaction evolution of gas from the substrate, which suggested that pinholes were present in the aluminum film. No further attempts were made to prepare porous alumina hosts in this manner.

8.4 Conclusion

The fabrication of a device based on the conjugated polymer/porous alumina composite material revealed a large number of processing issues. The current results indicate that some of

these may be overcome with further effort. In the case of films on aluminum foil, more careful processing to remove the aluminum substrate is necessary to preserve the integrity of the structure. As for films on silicon, ITO and gold, control of the deposited aluminum morphology appears to be key for obtaining the desired structure without causing gas evolution from the underlying substrate during anodization. Devices on *n*-type silicon should still be investigated in more detail, as it is known that it shows no reaction with the electrolyte.

The efforts described here were aimed at relatively crude devices in which conjugated polymer chain confinement was not really possible. However, once the obstacles identified here are resolved, the use of low temperature anodization should produce the desired structure for such confinement and allow the study of single chain electrical properties.

Experimental Details

ITO-coated glass and poly(ethylene terephthalate) substrates were obtained from Delta Technologies, Inc. Silicon wafers (*n*-type) were obtained from Monsanto, Inc.

Substrates were cleaned prior to deposition by sonicating for 10 min in a detergent solution (10% FL-70, Fisher Scientific) and for 10 min in methanol, which was followed by drying in streaming nitrogen.

Gold substrates were prepared by thermal evaporation on silicon with a thin chromium adhesion layer (~10 nm). Aluminum thin films on silicon, gold and ITO were prepared as described in chapter 4. SEM images were acquired on a Hitachi S-4700 field-emission SEM.

ITO films were prepared by RF sputtering at 100 W with 6 mTorr argon (120 sccm flow). Some film darkening was observed due to reduction of metallic impurities. This may be avoided by mixing a small oxygen flow (< 0.1 sccm) to the chamber during deposition. Silicon dioxide

and aluminum oxide protective films were prepared by electron-beam evaporation in the same process as aluminum evaporation.

For device testing, electrical contacts were attached to the ITO layer using silver epoxy (Epotek, Inc.) The ITO layer was further embedded in optical epoxy (302-3M, Epotek, Inc.). Direct contact was made to the aluminum substrate by an alligator clip. Current-voltage characteristics were investigated with a DC power supply and a multimeter. The measurements were in general difficult to reproduce, presumably due to the presence of electrical short circuits in the device that would degrade with time. Conditioning at high voltage (>50 V) improved the stability somewhat but all devices eventually burned out.

References

1. Parker, I. D. *J. Appl. Phys.* **1994**, *75*, 1656.

2. Arkhipov, V. I.; Emelianova, E. V.; Tak, Y. H.; Bässler, H. *J. Appl. Phys.* **1998**, *84*, 848.

3. Cao, Y.; Parker, I. D.; Yu, G.; Zhang, C.; Heeger, A. J. *Nature* **1999**, *397*, 414.

4. Parker, I. D.; Kim Helen, H. *Appl. Phys. Lett.* **1994**, *64*, 1774.

5. Zhou, X.; He, J.; Liao, L. S.; Lu, M.; Xiong, Z. H.; Ding, X. M.; Hou, X. Y.; Tao, F. G.; Zhou, C. E.; Lee, S. T. *Appl. Phys. Lett.* **1999**, *74*, 609.

6. Wunsch, F.; Chazalviel, J. N.; Ozanam, F.; Sigaud, P.; Stephan, O. *Surf. Sci.* **2001**, *489*, 191.

7. Crouse, D.; Lo, Y. H.; Miller, A. E.; Crouse, M. *Appl. Phys. Lett.* **2000**, *76*, 49.

8. Chu, S. Z.; Wada, K.; Inoue, S.; Todoroki, S. *J. Electrochem. Soc.* **2002**, *149*, B321.

9. Deng, Z. B.; Ding, X. M.; Lee, S. T.; Gambling, W. A. *Appl. Phys. Lett.* **1999**, *74*, 2227.

10. Hunter, W. R.; Mikes, T. L.; Hass, G. *Appl. Opt.* **1972**, *11*, 1594.

11. Yang, Y.; Chen, H. L.; Mei, Y. F.; Chen, J. B.; Wu, X. L.; Bao, X. M. *Solid State Commun.* **2002**, *123*, 279.